Nanophotonic point-of-care biosensors for innovative clinical diagnosis of respiratory diseases

Olalla Calvo Lozano

Universitat Autònoma
de Barcelona

Doctorat en Biotecnologia

Departament de Genètica i de Microbiologia – Facultat de Biociéncias

Nanophotonic point-of-care biosensors for innovative clinical diagnosis of respiratory diseases

Doctoral Thesis – 2022

Olalla Calvo Lozano

Author

Prof. Laura M. Lechuga
Supervisor

Prof. Antonio Villaverde
Tutor

CSIC
CONSEJO SUPERIOR DE INVESTIGACIONES CIENTÍFICAS

ICN2
Institut Català
de Nanociència
i Nanotecnologia

EXCELENCIA
SEVERO
OCHOA

Abstract

The conventional methods for the diagnosis of respiratory diseases rely mainly on the clinical evidence by imaging. Complementing such analysis with a molecular evaluation can provide a more suitable and exhaustive diagnosis. However, all these technologies imply long times-to-result and sophisticated techniques and laboratories.

This Doctoral Thesis has as main objective to offer novel evanescent wave-based biosensors as a valuable alternative solution for the clinical diagnosis of several respiratory diseases. We have implemented a surface plasmon resonance biosensor (SPR) and a bimodal waveguide (BiMW) interferometric biosensor, which both offer direct, sensitive, and rapid analysis of specific biomarkers using a reduce sample volume. Their potential for integration into point-of-care (POC) analytical platforms positions them as excellent technologies for a more effective disease diagnosis. Along the Thesis, several biosensor methodologies have been designed and implemented allowing the direct detection of lung-related biomarkers in biological fluids. Bioreceptor immobilisation, antifouling properties of the bioreceptor layer and biomarkers detection have been optimised and evaluated in terms of sensitivity, specificity and reproducibility. In this Thesis, we have developed: (i) a rapid and quantitative serological assay for the detection of anti-SARS-CoV-2 antibodies; (ii) an amplification-free genetic assay for Pneumocystis pneumonia identification in respiratory specimens; and (iii) a novel approach to the early detection of lung cancer based on a biomarker panel combining protein and epigenetic analytes present in human plasma.

The work in this thesis has opened the door to innovative analytical approaches for the diagnosis of lung-related disorders, overcoming some of the limitations of the conventional analytical techniques and exhibiting an enormous potential for their implementation in POC devices applicable in the real clinical practice.

Resumen

Los métodos convencionales para el diagnóstico de las enfermedades respiratorias se basan principalmente en las pruebas clínicas por imagen. Complementar este análisis con una evaluación molecular puede proporcionar un diagnóstico más adecuado y completo. Sin embargo, las técnicas moleculares implican largos tiempos de espera y sofisticadas técnicas e instalaciones.

Esta Tesis Doctoral tiene como objetivo principal ofrecer avanzados biosensores basados en ondas evanescentes como una interesante alternativa para el diagnóstico clínico de diversas enfermedades respiratorias. Hemos implementado un biosensor de resonancia de plasmón superficial (SPR) y un biosensor interferométrico de guía de onda bimodal (BiMW), que ofrecen un análisis directo, sensible y rápido de biomarcadores específicos utilizando un volumen de muestra reducido. Su potencial de integración en las plataformas analíticas de *point-of-care* (POC) los sitúa como excelentes tecnologías para un diagnóstico más eficaz de las enfermedades. A lo largo de la tesis, se han diseñado e implementado varias metodologías de biosensores que permiten la detección directa de biomarcadores relacionados con el pulmón en fluidos biológicos. La inmovilización del biorreceptor, las propiedades *antifouling* de la capa de biorreconocimiento y la detección de los biomarcadores se han optimizado y evaluado en términos de sensibilidad, especificidad y reproducibilidad. En esta Tesis, hemos desarrollado: (i) un ensayo serológico rápido y cuantitativo para la detección de anticuerpos anti-SARS-CoV-2; (ii) un ensayo genético sin amplificación para la identificación de Pneumocystis pneumonia en muestras respiratorias; y (iii) un enfoque novedoso para la detección temprana del cáncer de pulmón basado en un panel de biomarcadores que combina analitos proteicos y epigenéticos presentes en el plasma humano.

El trabajo de esta tesis ha abierto la puerta a enfoques analíticos innovadores para el diagnóstico de trastornos relacionados con el pulmón, superando algunas de las limitaciones de las técnicas analíticas convencionales y mostrando un enorme potencial para su implementación en dispositivos POC aplicables en la práctica clínica real.

Agradecimientos

Quiero agradecer a mi directora de tesis, la profesora Laura Lechuga, por brindarme la oportunidad de iniciarme en el ámbito de los biosensores y realizar el doctorado en su grupo de investigación. También quiero darle las gracias por su guía, su confianza y su apoyo durante todo este tiempo. También me gustaría agradecer al Ministerio de Economía, Industria y Competitividad y al ICN2 por darme la posibilidad de desarrollar mi tesis en un lugar idóneo.

Debo agradecer a M. Carmen la orientación y el soporte desde mis comienzos en el grupo. Gracias por enseñarme a trabajar con los sensores cuando no sabía nada de este mundo. Por otra parte, gracias por la ayuda y los consejos a María y especialmente a César, que aún estando a kilómetros de distancia siempre has contando conmigo y estabas dispuesto a asesorarme.

Dar las gracias a todos los compañeros que forman o han formado parte de NanoB2A, haciendo más ameno el día a día del laboratorio: Daniel, Cristina, Priyanka, Berto, Roger, Denise, M. Cruz, Bernat, Mireia, Razia, Alejandro, Juliana, Medhi, Martalu, Beatriz, y Bárbara... Gracias a Patricia y Jessica por compartir los momentos diarios, sobre todo por el club cultureta, las fiestas, las escape rooms y cualquier plan que se propusiera. Gracias a los dos compañeros que, al comienzo y en mi etapa final en este grupo, me han ayudado sobremanera en el desarrollo de esta tesis, Nuria y Pablo. Mención especial a Miquel y Blanca, con vosotros este camino ha sido una aventura divertida, apasionante y gratificante. Por último, gracias a Laura "Nanoup" por darme huequitos de tiempo para contarnos la vida y reiniciar la mente.

Many thanks to Dr. Revzin for giving me the opportunity to work at such a prestigious institution as the Mayo Clinic. I would also like to thank my lab mates Gulnaz, Jack, Daheui, Seon, Kihak and Ellen. No hay ninguna palabra que pueda utilizar para agradecer a mis "famigos" del team México el cuidado, cariño y diversión que me disteis en Rochester. Gabi, Alan y Manolo, millones de gracias, sois hogar. Lastly, Michelle and Trevor thank you for your kindness. You gave me warmth and light in the harsh Minnesota winter.

Graciès a les meves bèsties de l'Handbol Sant Joan Despí, especialment el front fort amb Laia, Claudia, Anna Sancho i a les meves “germanes petites” Júlia i Marcel·la. Gràcies a Sandra Piqué, Anna Nin, Irene i les seves famílies per fer que em sentís part d'elles res més arribar a Catalunya. A mis santanderinas incondicionales, Andrea y Almudena; a mis compañeras de universidad, Elena, María, Luis, Raquel y Paula; a la liga superior, Sandra Tomás y Mónica; y a mi manchega Elvira.

Por último, esta tesis se la quiero dedicar a mi familia. A mis primas, mi hermano, mi cuñada y mis sobrinas, pero en especial a mis padres. Gracias por apoyarme siempre para crecer profesionalmente. Os quiero.

Motivation and objectives

Respiratory diseases embrace all the disorders related to the lung, one of most exposed and vulnerable internal organs. According to the World Health Organization (WHO), several respiratory diseases such as lower respiratory tract infections and cancer are the fourth and sixth causes of death worldwide, respectively, leading to more than 8 million deaths in 2019. Conventional techniques for the diagnosis of pulmonary disorders are well-established techniques (e.g. microscopic analysis, imaging techniques, immunoassays and polymerase chain reaction (PCR)-based methodologies) but they require lengthy procedures, trained personnel and sophisticated facilities. The emergence of innovative analytical tools that enable simpler, faster and more user-friendly analysis is decisive to ensure prompt diagnosis and the application of efficient therapies.

POC biosensor platforms emerge as bright tools for straightforward clinical diagnostics and/or therapeutic follow-up monitoring. These platforms offer miniaturised laboratory analysis in compact, portable and integrated devices. Among the different biosensor configurations, optical evanescent wave (EW) biosensors stand out as the most promising candidates. EW-based biosensors are an extraordinary choice due to their sensitivity, robustness and capabilities of multiplexing and miniaturization in POC devices.

The main goal of this thesis has been the design, optimisation and evaluation of advanced nanophotonics biosensor methodologies capable of improving the traditional analytical techniques regurlaly used for the clinical diagnosis of three respiratory diseases (Coronavirus Disease 2019 (COVID-19), Pneumonia pneumocystis and lung cancer).

The partial objectives derived from this main goal are the following:

1. Development of a quantitative SPR-based serological biosensor assay for the diagnosis of COVID-19.

    - Selection of the most effective bioreceptor layer (SARS-CoV-2 viral antigens) to obtain the highest sensitivity, specificity and antifouling properties.

- Optimisation of an antibody quantitative biosensor assay in human serum and comparison of its performance with established methodologies.
- Biosensor validation with clinical serum samples and definition of diagnostic parameters (sensitivity, specificity and predictive values).

2. Development of a genetic plasmonic biosensor for Pneumocystis pneumonia detection in lung fluids.

- Optimisation of the DNA probe-based biosensor strategy for the detection of *Pneumocystis jirovecii*.
- Evaluation of the analytical parameters of the biosensor in standard buffer and respitatory samples, assessing their effect on the sensor surface.
- Analysis of the sensor performance by evaluating lung samples from patients infected with various microorganisms.

3. Development of an advanced nanophotonic biosensor for the diagnosis of lung cancer using an innovative biomarker panel.

- Definition of a comprehensive and novel lung cancer biomarker panel based on proteins and epigenetic analytes (microRNAs and DNA methylation) present in human plasma.
- Optimisation of the biosensors assays for each biomarker, assessing the main analytical parameters such as sensitivity, specificity and reproducibility.
- Evaluation of theeffect of human plasma on the nanophotonic biosensor performance.

Table of Contents

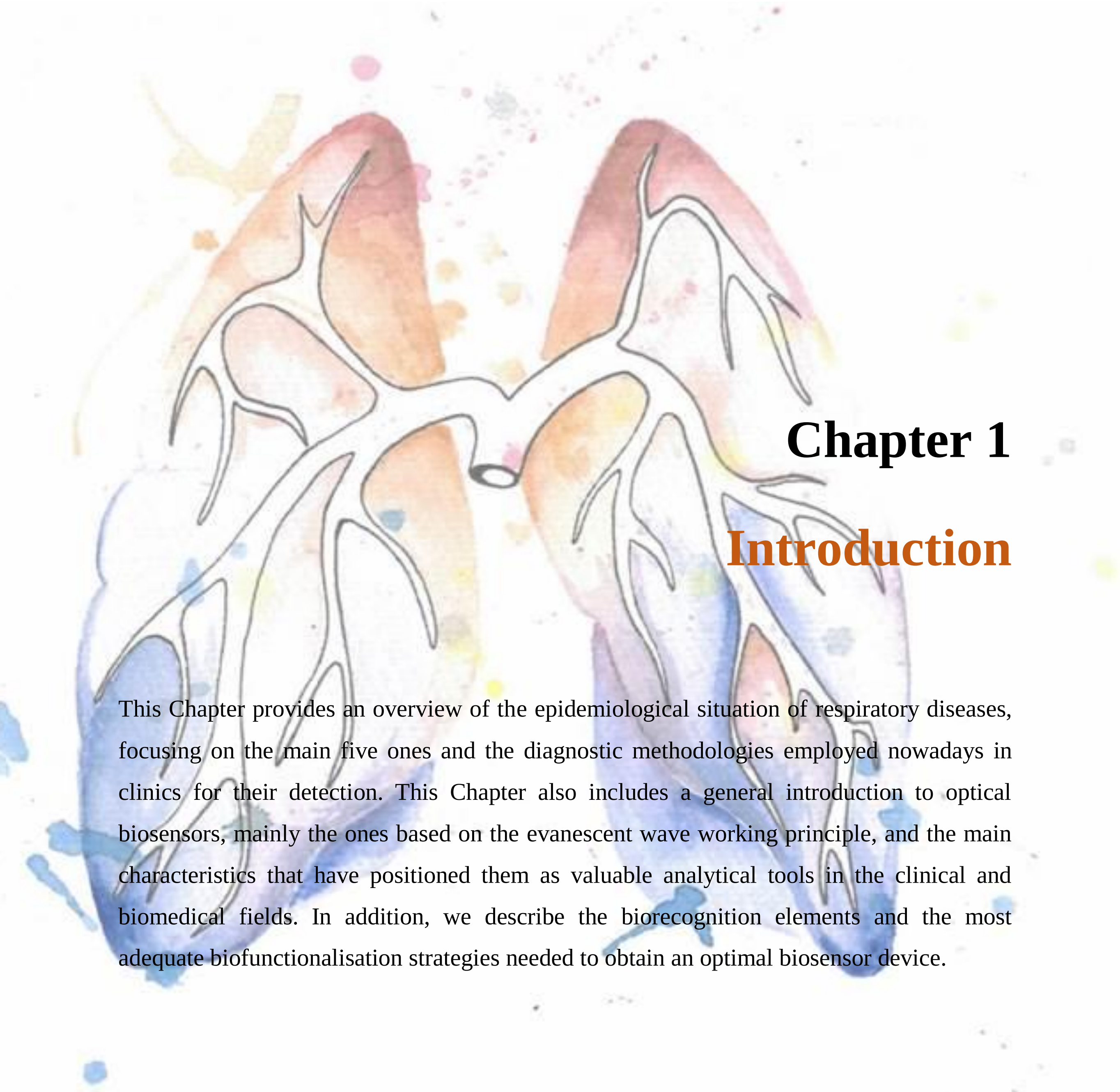

Chapter 1

Introduction

This Chapter provides an overview of the epidemiological situation of respiratory diseases, focusing on the main five ones and the diagnostic methodologies employed nowadays in clinics for their detection. This Chapter also includes a general introduction to optical biosensors, mainly the ones based on the evanescent wave working principle, and the main characteristics that have positioned them as valuable analytical tools in the clinical and biomedical fields. In addition, we describe the biorecognition elements and the most adequate biofunctionalisation strategies needed to obtain an optimal biosensor device.

1. Introduction

1.1. Respiratory diseases

The human lung is the internal organ most exposed to particles, chemicals, and infectious organisms from ambient air, being extremely vulnerable to infection and injury from the external environment. According to the WHO, in 2019 respiratory diseases lead to more than 8 million deaths worldwide and they comprised three of the top 10 causes of death in 2019, being chronic obstructive pulmonary disease (COPD) the third-leading cause of death, the lower respiratory tract infections the fourth, and cancers of the trachea, bronchi, and lungs the sixth, respectively[1] (**Figure 1.1)**. However, other respiratory conditions such as sleep-disorder breathing, pulmonary hypertension and occupational lung diseases affects millions of people each[2]. Risk factors such as exposure to biomass fuel and outdoor pollution affect more than 3 billion people at worldwide level. Moreover, approximately 1 billion people are smokers, causing equal-magnitude risks to second-hand smokers[3].

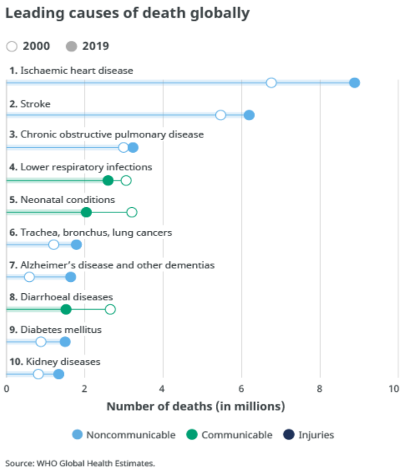

Source: WHO Global Health Estimates.

Figure 1.1. Top ten leading causes of deaths worldwide[1].

From a prevalence standpoint, the Forum of International Respiratory Societies considers pneumonia, asthma, COPD, lung cancer and tuberculosis the five most relevant lung diseases worldwide [2] (**Figure 1.2**). These Big Five can be classified into two main groups:

1.1.1. Chronic respiratory diseases

- ***Obstructive pulmonary disease (COPD)***. This disease includes lung conditions related to a decline in lung function due to the inflammation in the small airways and progressive destruction of lung parenchyma[4]. COPD is the third-leading cause of death globally, affecting around 200 million people, from which about 3.2 million die each year[3,5]. Clinical diagnosis is based on pulmonary function tests, being spirometry the gold standard technique[4].

- ***Asthma***. It is characterized by irregular airway function, specifically with variation in airflow limitation over short periods[6]. Asthma affects more than 350 million people worldwide[7], causing more than 1,300 deaths per day. Currently, the most employed diagnostics methods are spirometry and airway responsiveness, although sputum cell counts could also be included[6].

- ***Lung cancer***. Cancer is a heterogeneous disease characterized by abnormal growth of cells, generating tumours that can expand and spread to other organs (metastasis)[8]. Lung cancer is the most lethal cancer-related mortality with 1.8 million deaths in 2020[9]. Established methods for its diagnosis are based on imaging (e.g. chest radiography, contrast-enhanced computed tomography (CT)), histology and cytology of small biopsies[10].

1.1.2. Infectious respiratory diseases

- ***Tuberculosis***. This lung condition is caused by the infection of the Mycobacterium tuberculosis bacteria. In 2019, 10 million people developed TB and 1.4 million people died[11]. Diagnostics methods are based on direct smear, culture, or sputum examination. Technologies based on molecular techniques such as PCR for the bacteria identification are employed in developed countries[12].

- ***Acute respiratory infections***. This disorder can be caused by bacterial, fungal, or viral pathogen agents. The usual responsible microorganisms are *Streptococcus pneumoniae*, *Mycoplasma pneumoniae*, *Coxiella burnetii* and *Legionella sp.*[13]. However, this condition is extremely challenging due to emerging drug resistance, the immune-depressed patients affected by innocuous microorganisms such as *Pneumocystis jirovecii*[14] and the appearance of new pathogens such as SARS-CoV-2 virus. Lower respiratory tract infection causes more than 2.4 million estimated deaths annually[2] of which about 290,000 to 650,000 are caused by influenza, which affects about 3 to 5 million people[15]. Furthermore, the COVID-19 pandemic has affected nearly 300 million worldwide and resulted in more than 6 million people's deaths[16,17], although there are suspicions that this number is underestimated and many millions more have died from COVID-19[18]. At present, the methods employed for the diagnosis of acute respiratory infection are based on microbiological or molecular tests, as lower respiratory tract culture, antigen test in serum or urine and PCR in combination with chest radiography and pulmonary tests[13,14].

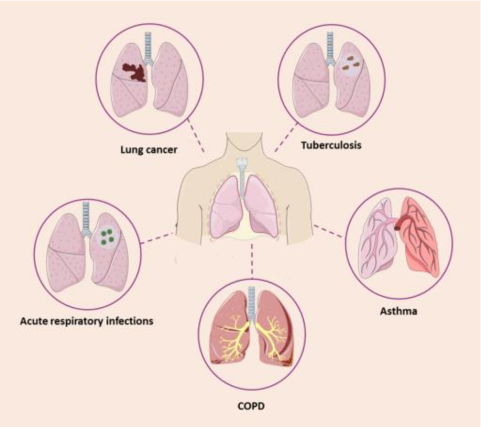

Figure 1.2. The Big Five respiratory diseases[19].

Respiratory diseases imply an elevate burden for the global healthcare system, and this burden is increasing pressing the economies of all nations. In 2019, the economic losses generated exclusively by COPD disease were about 380 € billion annually among 28 European states[20].

It is clear that the development of new diagnostics technologies capable of provide a prompt, precise and reliable result would ensure an accurate treatment and control of the symptoms. Additionally, the new tools would improve patients' quality of life, reducing risks of death and overall healthcare costs[3].

Main clinical diagnoses of lung-related disorders are based on a combination of physical analysis and biomolecular techniques. These techniques rely on the identification of biomarkers such as proteins or DNA mutations by employing tedious, long and sophisticated biomolecular analysis as enzyme-linked immunosorbent assay (ELISA), PCR and sequencing. However, the aggressiveness and high mortality rate of lung cancer, the outbreak of the COVID-19 pandemic affecting the health and economic situation worldwide, and the emergence of new diseases due to infection by emerging microorganisms highlight the crucial need for innovative and more effective diagnostic techniques. In this Thesis, photonic biosensors and particularly, evanescent wave-based sensors are proposed as an excellent alternative for the clinical diagnosis of COVID-19, Pneumocystis pneumonia and lung cancer diseases. Evanescent wave biosensors have reported outstanding sensitivity, fast time-to-results with minimum samples volume and they can be fabricated in multiplex and minituarise format for on-site clinical diagnosis.

1.2. POC and biosensors devices for clinical diagnosis

In recent years, the development of fully integrated, compact, user-friendly, and portable POC biosensor platforms has been an upward trend. Advances in numerous disciplines such as microfluidics, material science, nanophotonics, miniaturization, have boosted the blooming of sophisticated POCs[21] including even wearable sensors and e-textiles whose readout system is connected to a smartphone.

Point-of-care devices aim at performing all analytical steps for diagnostic assays near the patient[22–24]. They should provide rapid and precise results without the need for laboratory staff or specialized facilities[25] and in a way that is easy to handle and interpret, requiring minimal instructions.

The ideal POC platform is composed of: (i) a microfluidic to bring the sample to the sensing area (e.g. disposable strip, chip or cartridge); (ii) chemical or biological components for the selective sensing of the analyte; (iii) a sensor transducer able to detect the interaction (iv) detectors and processing electronics to collect and display the readout (e.g. digital screen or wireless communication with smartphone or tablet) (**Figure 1.3**). The integration of all the above components in a miniaturized sensor device offers extraordinary benefits such as design versatility, multiplex analysis and portability. Additionally, the no need for trained personnel and laboratory facilities reduces manufacturing and analysis costs[22–24,26–28]. The fast turnaround time together with a minimal sample and reagents volume provided by POC platforms enables proper diagnosis and prompt treatment. Thus, the implementation of the POC devices in clinical practice would not only improve patient outcome but also lead to enhancements in the healthcare systems.

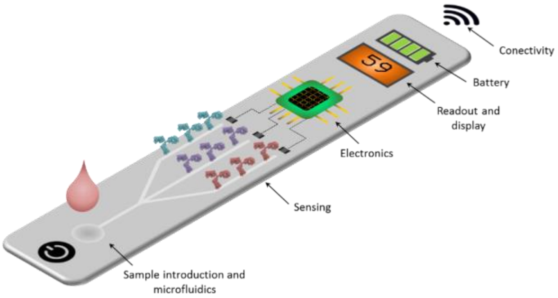

Figure 1.3. Ideal POC platform integrating microfluidics, sensing elements, electronic and data processing, among others. Additional features include low sample processing and real-time display of the results.

The ideal POC device should comply with the requirements of the ASSURED criteria established by the WHO[29]:

- **A**ffordable for those who need the device.
- **S**ensitive, reporting the lowest false negative rates possible.
- **S**pecific, achieving the minimal false positive rate.
- **U**ser-friendly, being easily used by non-trained personnel.
- **R**apid and Robust, displaying results in less than 60 min after sample collection without additional steps (transport and storage).
- **E**quipment-free, avoiding additional equipment
- **D**eliverable to end-users

1.2.1. Optical biosensors

A biosensor as defined by the International Union of Pure and Applied Chemistry (IUPAC) is an integrated analytical device capable of providing specific quantitative or semi-quantitative information using a biological o biomimetic receptor, which is in direct contact with a transducer[30]. Biosensors are composed of a biological receptor, a transducer, and an electronic system, which after data processing, displays the sensor result (**Figure 1.4**). Biological receptors usually employed include nucleic acids, antibodies, enzymes, or even whole cells, designed to selectively interact with the target analyte containing in the sample. Bioreceptors can effectively and selectively bind the analytes through a wide range of biomolecular affinity interactions. Otherwise, the transducer detects the biochemical interaction by the physicochemical changes produce in the medium or at the sensor surface and converts the specific biointeraction into a continuous or discrete measurable signal proportional to the analyte concentration[31].

The combination of the biological receptor layer and the transducer in one single device confers to the biosensors high sensitivity and selectivity in a fast one-step assay. Moreover, the large diversity of biological receptors available offer a broad range of different analyses, and hence, the possibility to employ the biosensors for a broad variety of applications ranging from clinical practice to food quality control and environmental monitoring, among others[32–34]. Additionally, biosensors can be integrated into low-cost, compact, portable, and user-friendly POC platforms, overcoming limitations associated with conventional techniques, such as analyte purification or additional equipment for signal readout, which is usually conducted by trained personnel.

Two of the most representative examples of biosensors are the glucose biosensor and the pregnancy test, which are used worldwide by millions of people. The glucose biosensor is an electrochemical sensor that uses the enzyme glucose oxidase to report the glucose concentration in less than a minute in a drop of blood[35]. The pregnancy test is based on a lateral flow assay (LFA) which detects the presence of the human chorionic gonadotropin (hCG) hormone in women’s urine using specific antibodies labelled with colour tags (colloidal gold particles, dyed polystyrene or latex spheres)[36].

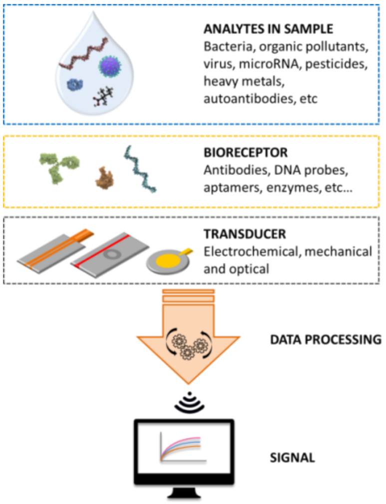

Figure 1.4. Schematic representation of a biosensor including the heterogeneous sample, the biological receptor, the transducer, and the data processing to display a signal.

Biosensors can be classified depending on the transducer, being the most employed ones the electrochemical, mechanical and optical sensors. Each transducer employs different working mechanisms such as electrochemical changes (current or voltage), mass changes or light properties variations (intensity, phase, wavelength…), respectively.

Together with the electrochemical sensors, the optical ones are the most employed because they can provide a direct, rapid, highly sensitive and real-time sensing. Optical sensors identify variations of an optical property of the propagated light (intensity, wavelength, polarisation…)[37] leading to a wide family of sensors based on diverse phenomena including fluorescence, luminescence, absorption, refractive index (RI) variation, among others. The most employed optical sensors are based on the evanescent wave detection principle.

Evanescent wave sensors exploit the confinement of an electromagnetic field in a dielectric and/or metal structure, creating a propagated or localised electromagnetic mode. Part of the confined light penetrates the external medium, resulting in an evanescent wave (**Figure 1.5**). The evanescent wave is extremely sensitive to changes in the RI of the external medium, inducing changes in the optical properties of the exciting electromagnetic mode *via* the evanescent wave tail. If a biological receptor is coupled to the sensor surface, the exposure to the specific analyte and the subsequent biomolecular interaction generates a RI change.

RI variations are correlated to the analyte concentration and kinetics parameters like affinity, providing quantitative values of the biomolecular interaction[38,39]. The evanescent wave penetrates up to hundreds of nanometres into the external medium and exponentially decays, thus, only changes taking place close to the sensor surface will be sensed, minimising the background disturbances from the surrounding media.

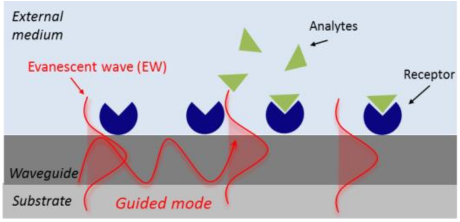

Figure 1.5. Schematic representation to illustrate the sensing principle of an evanescent wave biosensor.

Both the biorecognition layer and the transducer determine the main analytical characteristics of a biosensor.

One of the most relevant parameters to define the performance of a biosensor is the sensitivity. Sensitivity (S) represents the magnitude change of the transducer response to any change in the analyte concentration. Depending on the selected optical transducer, it could be expressed in different units such as nm·RIU^{-1} or rad·RIU^{-1} for wavelength or phase light interrogation, respectively. The limit of detection (LOD) considers not only the sensitivity but also the resolution which depends on the noise of the system employed (e.g., light source variations, microfluidics noise, thermal fluctuations, etc). Therefore, LOD corresponds to the minimum amount of analyte (or refractive index variation) that can be accurately measured or quantified by the biosensor and it is usually estimated as three times the standard deviation of the total system noise (3σ) divided by the sensitivity (**Equation 1.1**).

$$LOD = \frac{3\sigma}{S} \qquad \textbf{(1.1)}$$

Other analytical characteristics of a biosensor include:

- Dynamic range. The ideal biosensor should be able to detect a wide range of concentrations of the target analyte. In particular, the operational or linear range is a key parameter. It reflects the sensor response in a concentration-dependent manner, obviating bioreceptor saturation (absence of sensor response despite increasing analyte concentration).

-Selectivity, determined by the affinity of the bioreceptor towards the analyte. The biorecognition element must be able to detect exclusively the target analyte even if it is in a complex matrix.

-Reproducibility between different biosensor devices, which must equally detect the same concentration of analyte. Reproducibility is evaluated by the coefficient of variation, expressed in %.

-Accuracy to identify the real concentration of the analyte in complex samples. To analyse the accuracy, a comparison of the concentration with other analytical techniques or an evaluation of spike samples can be performed.

-Stability, ensuring a suitable and solid performance even under different storage conditions (time, temperature, humidity…).

-Repeatability and reusability. Biosensors must guarantee the measurement of the same (or different) analyte concentration during consecutive measurements using the same sensor device and the same sample. The removal of the analyte after recognition without modifying the bioreceptor layer is called regeneration, and is a key factor in biosensor assays. An optimised regeneration protocol offers a stable and reusable bioreceptor layer for repeated analysis under the same conditions.

Since the evanescent wave decays exponentially, it is important to distinguish the bulk sensitivity in the surrounding medium from the surface sensitivity at the nanometric vicinity of the sensor surface. Thus, the bulk sensitivity analyses changes in the refractive index (n_1 and n_2) of the external medium in contact with the sensor surface (**Figure 1.6A**). LOD related to bulk sensitivity can be expressed in refractive index units (RIU) by evaluating solutions with different RI and chemically inert to the material of the sensor waveguide. Otherwise, the surface sensitivity represents the ability of the transducer to detect variations in the refractive index (n_1 and n_2) due to the biomolecular interactions occurring in the proximity of the sensor surface (**Figure 1.6B**). Surface sensitivity can be calculated by De Feijter's formula[40] and is expressed as surface mass density in pg·mm^{-2}. Although LOD related to this sensitivity can also be expressed as the analyte concentration (e.g., ng·mL^{-1} or nM), this value is not comparable among sensors because it is directly associated with the affinity between the biological receptor and the specific analyte.

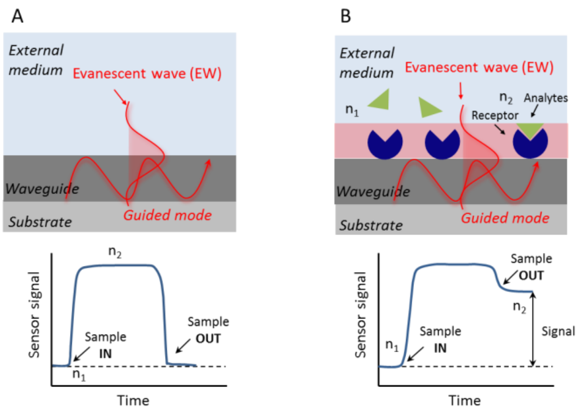

Figure 1.6. Schematic representation to illustrate the sensing principle and the responses for (A) bulk sensitivity and (B) surface sensitivity.

Table 1.1 shows a comparison in terms of bulk and surface sensitivity (RIU and pg mm^{-2}) between several evanescent wave-based optical sensors[41].

Table 1.1. Comparison of the limit of detection of different EW-based sensors.

Device	RI detection limit (RIU)	Mass detection limit (pg·mm^{-2})	Reference
Surface Plasmon Resonance	10^{-5} - 10^{-7}	1 - 5	42
Grating couplers	10^{-6}	0.3 – 5	43
Microring resonators	10^{-5} - 10^{-7}	0.3 – 3	44
Photonic crystals	10^{-4} - 10^{-6}	0.5 – 7.5	38,45

Interferometers	10^{-7} - 10^{-8}	0.02 - 1	38,45

Given all the described-above advantages of the EW-based sensors, and the reported sensitivity by plasmonic and interferometric sensors ranging from 10^{-5} to 10^{-8} RIU, this Thesis focused on the study of the potential application of these two types of evanescent wave biosensors for the diagnosis of respiratory diseases.

1.2.1.1. Plasmonic biosensors

Plasmonic systems benefit from the optical phenomenon firstly noticed by Wood in 1912 based on light-metal (e.g. gold, silver, or aluminum) interactions[46]. The most representative and used plasmonic biosensor is the Surface Plasmon Resonance (SPR) sensor, although other configuration can be employed such as SPR imaging (SPRi), localised surface plasmon resonance (LSPR) or fiber-optic configuration.

SPR is a mature and robust technique widely employed in the characterisation of biomolecular interactions and biomolecules monitoring, mainly for clinical applications. SPR offers label-free, rapid (few minutes), and direct detection of analytes, without compromising analytical parameters (sensitivity and specificity) compared to conventional techniques[47]. Additionally, SPR sensors have been employed not only in clinical diagnostics but also in a diverse range of applications such as food quality and environmental monitoring, among others[48,49] .

The surface plasmon resonance relies on coherent oscillations of charge density that take place in the interface between two media with dielectric constants of opposite signs, such as a thin metal film and a dielectric medium. By coupling an incident polarized light, surface plasmons are excited and can propagate along the metal-dielectric interface as surface plasmon polaritons (SPPs). SPP generates an electromagnetic field called evanescent wave whose intensity exponentially decays into both media[50,51]. Considering Maxwell's equations, the SPP propagation component can be described as a function of the metal and the dielectric permittivity[46] (**Equation 1.2**):

$$k_X^{SPP} = \frac{\omega}{c}\sqrt{\frac{\varepsilon_m \varepsilon_d}{\varepsilon_d+\varepsilon_m}} \qquad \textbf{(1.2)}$$

where ω is the angular frequency, c is the light speed in vacuum; ε_m is the dielectric function of the metal ($\varepsilon_m = \varepsilon'_m + i\varepsilon''_m$) and ε_d is the dielectric constant of the medium, directly related to the refractive index ($\varepsilon d \approx n^2 d$). Working principle of refractometric sensing platforms is based on this direct reliance between the propagation vector and the refractive index of the dielectric.

The excitation of the SPR can be achieved by coupling the light to the metal surface in such a way that the component parallel to the interface of the light wavevector matches the propagation vector of the SPP. Diverse techniques can be employed to couple the incoming light into the metal film, such as prisms, waveguides, and gratings[52]. Prism coupler is the predominant technique employed for this optical excitation, relying on the well-established Kretschmann configuration. In this configuration, the light passes through a high RI glass prism and is totally reflected at the prism base. The excitation of the surface plasmon generates the evanescent wave that penetrates the metal film and propagates along the interface with a specific propagation vector. A plasmon resonance occurs when at a specific angle of incidence (θ), the evanescent wave propagation vector matches the SPP vector (**Figure 1.7**).

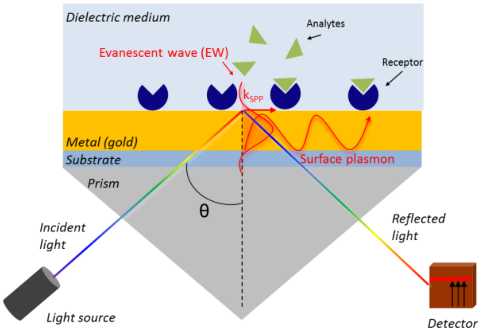

Figure 1.7. Schematic representation of an SPR biosensor employing Kretschmann configuration to couple a monochromatic light into the thin metal layer**.**

SPR sensors can be classified according to the detection scheme employed, which monitors changes or displacements of the spectral reflectivity dip and can be based on the angle, intensity, wavelength and phase interrogation (**Figure 1.8**). Angle-based interrogation is one of the most applied in commercial SPR biosensors, where a quasi-monochromatic light source, hence a fixed wavelength strategy, is used. On the other hand, wavelength-based interrogation uses broadband light for SSP excitement at a fixed angle of incidence[46,53]. Regardless of the detection method, any change in the RI, such as a biomolecular interaction, occurring at the metal-dielectric interface will generate a shift in the reflected light intensity and hence, in the sensor signal. Thus, mass changes on the sensor surface, directly related to RI changes, can be easily monitored in a label-free and real-time approach, achieving sensitivities in the 10^{-5} - 10^{-7} RIU range (**Table 1.1**).

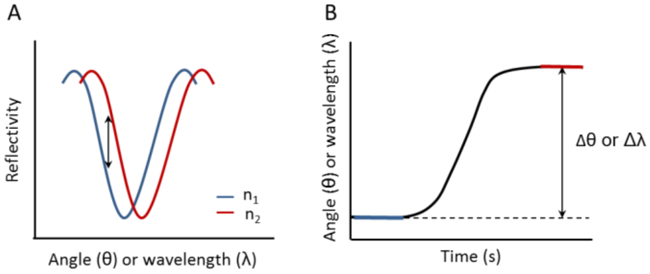

Figure 1.8. (A) Spectral reflectivity dip and (B) sensorgram curve from the SPR measurement methodology by angular or wavelength-based interrogation.

The use of commercial SPR-based biosensors is widespread, from miniature SPR devices to robust laboratory units. Biacore (Cytiva)[54] was the first commercial system in 1990 and since then, a large list of companies from all over the world has been offering different SPR instruments, such as Biosensing Instrument[55], XanTec Bioanalytics[56] and Bionavis[57], among others.

Despite the many advantages of the SPR biosensors such as high sensitivity, label-free and rapid results, they also have some limitations. Its sensitivity is a critical factor for some analyses such as the direct identification of small analytes at extremely low concentrations and single molecule detection. Moreover, SPR-based biosensors offer reduced multiplexing capabilities hindering their integration into POC devices[58]. To overcome such limitations, integrated waveguides photonic sensors appear as an attractive solution due to the higher sensitivity, multiplexing capabilities, and strong potential for mass fabrication using silicon-based technologies[38].

1.2.1.2. Waveguide photonic sensor

An optical waveguide is a structure made of a dielectric material capable of guiding electromagnetic waves with minimal loss by total internal reflection (TIR). A waveguide consists of a high refractive index material (n_1) corresponding to the core, surrounded by lower refractive index materials (n_2 and n_3), referred to as the bottom and top claddings, respectively. Light propagates in the form of guided modes, which are determined by the electromagnetic field distribution and the velocity of propagation. Both parameters depend on the waveguide structure (dimensions of the core (d) and refractive index of the core and cladding materials (n_1, n_2, n_3, respectively), and the working wavelength (λ). Waveguides that guide only one mode of propagation are named single-mode, whereas the ones guiding more than one propagation mode are called multi-mode. A schematic representation of a so-called slab or planar waveguide, the simplest optical waveguide, is shown in **Figure 1.9**. Any refractive index change taking place in the sensor surface when the core is in contact with an external medium will affect the propagating wave mode through the evanescent wave, altering the guided light characteristics.

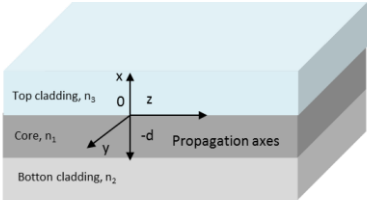

Figure 1.9. Scheme of an asymmetric slab waveguide configuration.

Waveguide biosensors are fabricated using silicon photonics technology. Silicon or silicon-related materials are compatible with complementary metal-oxide semiconductor (CMOS) processes enabling highly reproducible mass production. The use of silicon and CMOS manufacturing facilitates the miniaturisation into compact devices and multiplexing capabilities due to the fabrication of an array of sensors (waveguides) in one chip[59]. Additionally, silicon-based sensors offer robustness, excellent signal-to-noise ratio, and low absorption and light losses. These sensors have already shown extraordinary potential in several applications such as biomedical applications and environmental monitoring[60,61].

A variety of silicon-based sensors have been proposed as biosensors candidates. All of them are evanescent wave-based biosensors but they differ in the configuration and the detection scheme, leading to different sensitivities (**Table 1.1**). Depending on the detection configuration, sensors can be classified in grating couplers, microring resonators, photonic crystals and interferometric waveguide sensors[62]. Among all of them, interferometers have reported the most competitive limit of detection.

Interferometric sensor

The interferometric sensor working principle is based on the interference pattern generated by the superposition of two light beams that travel through different optical paths[40]. For biosensing applications, one of the optical paths is considered as the reference arm while the other constitutes the sensing area, in which the core waveguide is exposed to the external medium. Any change in the refractive index (biomolecular interaction) which takes place in the sensing area, generates a phase change in the interference pattern that can be measured in real-time[45]. The interference variation is proportional to the length of the interaction of the evanescent field with the sample. Therefore, by enlarging the path in the sensing area, the sensitivity can be improved. Different structures for interferometric sensors have been reported, and the most common interferometric sensors are the Mach-Zehnder Interferometer and the Young Interferometer.

In a Mach-Zehnder Interferometer (MZI), a laser beam is firstly coupled in a single mode waveguide. Then, through two integrated Y-junctions, the light is split into the two arms and after a certain distance both beams are recombined into a single waveguide. Finally, the interferometric signal is collected by a photodetector or charge-coupled device (CCD) camera (**Figure 1.10A**). Young Interferometer presents a similar configuration (**Figure 1.10B**), but in this case, the two arms are not recombined by a Y-junction before the output.

Thus, the output light from the two waveguides is collected individually and the interference pattern is generated off-chip by a CCD camera[45].

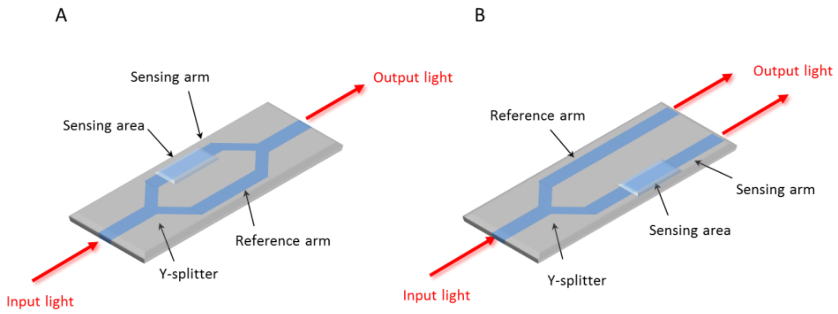

Figure 1.10. Schematic representation comparing Mach-Zehnder and Young Interferometers.

BiMW interferometer

Our group proposed an alternative interferometric sensor, the Bimodal Waveguide Interferometer (BiMW). BiMW sensor maintains an interferometric behaviour while avoiding the light beam splitting and recombination by Y-junctions[63]. Compared to the cited-above inteferometric sensors, the sensitivity level reported for BiMW is ranging from 10^{-7} to 10^{-8} RIU[38,63]. The working principle of the BiMW sensor relies on the properties of a waveguide in which only the fundamental and first modes of transverse electric polarized light can be propagated. Briefly, monochromatic light from a polarized diode laser ($\lambda = 660$ nm) is confined in a rib waveguide designed to support a single (fundamental) mode through the waveguide core (150 nm thickness). After a certain distance, this fundamental mode is coupled into a bimodal section (300–350 nm thickness) through a step junction that permits the additional excitation of the first propagating mode. A sensing window is opened along the bimodal section of the waveguide where the bioreceptors are immobilised and detection takes place (**Figure 1.11**). The two modes travel until the end of the waveguide, generating different evanescent field profiles that decay within the external medium. Any change in the refractive index taking place in the sensing area (η and η') affects the refractive index of the fundamental an first propagating modes (n_{TE00} and n_{TE10}, respectively) and results in an interferometric phase shift between the two modes, which is collected by a two-sectional photodetector at the end of the sensor device. The two-sectional photodetector collects intensities (I_{up} and I_{down}) in real-time, which can define the sensitivity parameter, S_R through **Equation 1.3** and **Equation 1.4.** In these equations, φ is the light phase difference between both propagating modes, L_{SA} is the length of the sensor area (optimised in 15 mm to ensure a high sensitivity), λ is the working wavelength and n_{TE} are the refractive indexes of the propagating modes. Addtionally, A and B are real constants and, I_{up} and I_{down} are the intensities collected by the upper and lower sections of the detector, respectively. Changes in the RI, as the ones due to a biomolecular interaction, generate variations in the light propagation (I_{up} and I_{down}) which is directly related to the concentration of the target analyte, affecting its phase φ and the signal S_R, which presents a sinusoidal form.

$$\Delta\varphi = 2\pi \frac{L_{SA}}{\lambda}(\Delta n_{TE10} - \Delta n_{TE00}) \qquad \textbf{(1.3)}$$

$$S_R = \frac{I_{up} - I_{down}}{I_{up} + I_{down}} = A + B\cos\varphi \qquad \textbf{(1.4)}$$

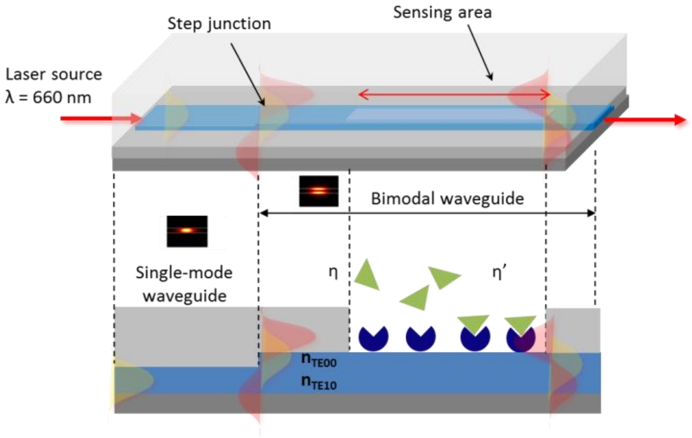

Figure 1.11. Schematic representation of a BiMW biosensor. Light is coupled in the single mode waveguide and after a modal splitter, two modes are excited and propagated until the sensor output.

The periodic nature of the interferometric read-out could generate ambiguities, hindering their commercialisation and application in clinical scenarios. In order to overcome these ambiguities, all-optical phase modulation methods can be incorporated. For the BiMW interferometer, the all-optical phase modulation is based on the modulation of the incident wavelength and the Fourier Series deconvolution. Fourier Series transform the periodic interference signal into a linear one, being able to quantify the phase shifts ($\Delta\varphi$, rad) between both modes continuously[64] (**Figure 1.12**).

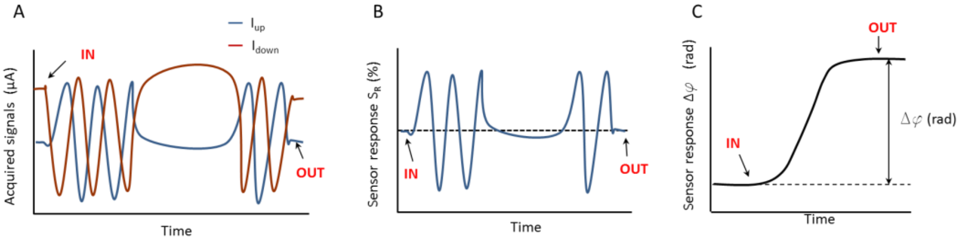

Figure 1.12. Typical BiMW sensor signal. (A) Acquired I_{up} and I_{down} signals (B) Periodic sensor signal from interferometric read-outs corresponding to S_R during the detection of a RI change (C) Linear sensor signal after all-optical modulation.

The BiMW biosensor has previously demonstrated its potential for environmental monitoring[65,66] and for clinical diagnostics in several areas including infectious diseases[67], cancer diagnosis[68], and endocrinology[69], enabling direct, sensitive, and reliable detection of pesticides, bacteria, miRNAs, and hormones, respectively.

1.2.2. The bioreceptor layer

In label-free optical biosensors, the sensitivity relies on the transducer sensing principle but also the biorecognition layer over the sensor surface. The biorecognition layer must be reproducible and provide high selectivity and specificity. Additionally, it should avoid non-specific adsorptions from other components present in the samples. There are two key factors in the assembly of a biofunctionalised surface: (i) the selection of the biorecognition element, responsible for the target affinity and, hence, the sensor sensitivity and selectivity; and (ii) the surface functionalisation chemistry. The functionalisation chemistry must be robust and assuring enough bioreceptor density, proper accessibility of the target to the immobilised biolayer and the rejection of non-specific adsorptions[70].

Bioreceptors can be classified regarding their nature and biochemical interaction with the analyte. Catalytic bioreceptors recognise a specific analyte (substrate) and transform it into a product, altering chemically their structure. The most employed catalytic bioreceptor are enzymes (**Figure 1.13A**). For biosensing applications, the catalytic reaction is monitored by the reduction of the substrate or the identification of the final product[71].

Among affinity biological receptors, antibodies are widely employed (**Figure 1.13B**). They are proteins generated by the immune system with extraordinary affinity and specificity against their specific target molecule[72].

There are several affinity bioreceptors based on nucleic acid composition. Nucleic acids recognise complementary DNA or RNA sequences with extremely high affinity (**Figure 1.13C**). The bond strength will depend on the length and nucleotide sequence (guanine-cytosine content (GC %)) complementary to bioreceptor[73].

Finally, other nucleic acid-based biological receptors are aptamers. Aptamers are single-stranded oligonucleotide sequences (DNA or RNA) that present secondary structures capable to recognise analytes such as proteins or small organic compounds with outstanding affinity (**Figure 1.13D**). These bioreceptors are synthesized by SELEX protocol (Systematic Evolution of Ligands by Exponential Enrichment). This procedure employs a large library of random sequences that are exposed to the analyte of interest. The unbound sequences are removed and the attached ones are eluted, amplified and sequenced. After several cycles of selection under increasingly stringent conditions, only the tightest-binding sequences are chosen[74].

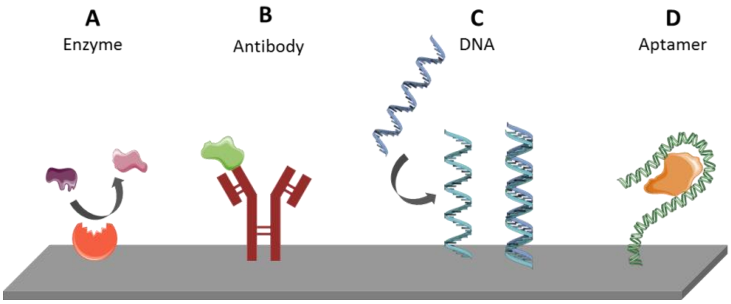

Figure 1.13. Summary of common biological receptors employed in biosensors.

1.2.2.1. Antibodies

Antibodies (Ab), or immunoglobulins (Ig), are proteins produced by the B cells of the adaptive immune system to recognise and neutralize foreign molecules in the body, known as antigens. An antibody is a Y-shaped molecule composed of four polypeptide chains, two heavy (H) and two smaller light (L) chains with a molecular weight of 50 and 25 kDa, respectively, linked by a disulfide bonding (**Figure 1.14**). Each chain contains a variable (V) and a constant (C) region. Antigen recognition is mediated by the variable light and heavy domains also known as fragment antigen-binding (Fab) region, placed at the Y arm ends[72]. Since Fab region is involved in recognizing the specific antigen, it differs in sequence and structure among antibodies. On the other hand, the H chain constant domains constitute the Fragment crystallizable (Fc) region, which plays a relevant role in activating the immune system by interacting with other components of the system[75].

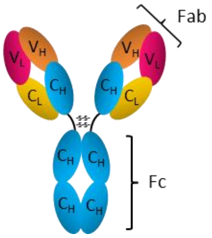

Figure 1.14. The basic structure of an antibody.

In mammalian cells, there are five antibody isotypes characterized by different H chains structure: IgA, IgD, IgE, IgG, and IgM. IgG is the most generated immunoglobulin during an immune response and, hence, the principal and most used in immunoassay-based biosensors[76]. The bond established between the antibody and the antigen is due to several non-covalent bonds such as electrostatic and hydrophobic interactions, ionic and hydrogen bonds, and van der Waals forces. Despite the weakness of these bonds, the association can persist for a long time. The strength and duration of the union will be determined by the structural closeness between the Fab region of the antibody and the antigen, leading to a possible cross-reactivity with structurally similar antigens.

Antibodies are produced in laboratories for a wide range of applications, not only biosensing ones. According to the number of B-lymphocyte lines employed for their production, antibodies can be classified into monoclonal and polyclonal antibodies[72]. The production of polyclonal antibodies (pAb) involves the repeated immunisation of an animal (rabbit, goat, mouse, etc) with the desired antigen. The host immune system reacts to the specific antigen and its B lymphocytes start producing antibodies. Different B lymphocyte clones generate antibodies that can be directly collected from the animal serum, obtaining a heterogeneous mixture of polyclonal antibodies. This mixture recognises different binding sites of a single antigen, showing different affinity and specificity. It is an easy procedure however, it only can be carried out for a limited amount of time for the same animal and antibodies properties can vary between animals[77].

In the case of monoclonal antibodies (mAb), its production is reached through the fusion of identical B cells with immortal myelomas (cancer cells), resulting in a hybrid cell known as hybridoma. The resulting hybridoma produces identical antibodies that recognise explicitly only one binding site of the antigen with high affinity. Hybridomas can produce unlimited antibodies but they require sophisticated materials and trained personnel[77].

The recognition capabilities of the antibodies to identify a specific antigen, their assortment and at the same time exclusivity position antibodies as outstanding biomolecules for the development of immunoassays. Antibodies are not only required for clinical diagnosis, but also for environmental monitoring and food analysis, among other fields[72].

1.2.2.2. Nucleic acid probes

Traditionally in nucleic acid biosensors, the biorecognition element is a single-stranded DNA (DNA probe) with a specific sequence of nucleotides (9–50 bases) complementary to the target sequence (RNA or DNA). Whereas antibody production implied the injection of a specific antigen into animals and/or cells and their eventual recovery, DNA is an easily synthesizable biorecognition element. Current biotechnological methods permit the *in-vitro* production of synthetic nucleic acid probes with the desired sequence in large amounts and with a high degree of purity[78]. Depending on the biosensor application, nucleic acid probes can be designed and customised adding different functional groups in both 5' and 3' DNA ends or even in the middle of the sequence.

For the selection of the probe sequence, there are available many commercially manufactured and well-understood codes that help to verify the probe-target stability[79]. Essential factors for DNA probe synthesis are the length (15 and 25 bases permit strong hybridisation) and guanine-cytosine content (GC, %). Long targets or probes might self-hybridise, hiding the recognition sequences and hindering the hybridisation event. Otherwise, around 40–60% GC content, promotes a stronger hybridisation due to the higher contribution of stacking interactions providing the stability of the formed hybrid. However, excessive CG content may lead to non-specific hybridisation from non-complementary sequences[79,80].

In addition to conventional DNA probes, innovative DNA probes have been reported to enhance target capture efficiency and increase the sensitivity of label-free optical sensors. The incorporation of modified nucleotides exhibiting restricted conformation that promotes the base stacking and backbone pre-organization, such as locked- nucleic acids (LNA)[81,82], Peptide nucleic acids (PNAs)[83,84], Phosphorodiamidate morpholino oligos (PMO)[85] and new DNA configuration in DNA clamps[86] have revolutionized the world of nucleic acid-based sensors. The main characteristics and advantages of these novel DNA probes are described in **Table 1.2**.

Table 1.2. Nucleic acid-based biorecognition elements. Main characteristics and advantages.

Probe	Main characteristics	Advantages
DNA	Conventional sequence	Simple synthesis
LNA	Ribonucleotide homolog 2’-O, 4’-C-methylene bridge	Increase melting T^a by 2–8°C per subunit, affinity and mismatch discrimination. Decrease nuclease digestion

PNA	DNA/RNA analogues N-2-aminoehtylglycine backbone (neutral charge, no electrostatic repulsion)	Increase hybrids’ complex stability, affinity and solubility
PMO	Synthetic DNA analogues Morpholine rings backbone	Increase solubility, length and flexibility
DNA clamp	Polypurine/Polypyrimidine-rich antiparallel sequences with 8-aminoG modifications	Increase hybridisation efficiency

1.2.3. Immobilisation of biorecognition elements

The biofunctionalisation of an optical sensor relies on the surface chemistry immobilisation. Surface chemistry functionalisation ensures the attachment of biological receptors to the sensor surface and largely determines the performance of the biosensor (sensitivity, selectivity, non-specific adsorptions from complex matrix, etc). Biofunctionalisation is a process of paramount importance in which some key factors must be considered[87,88]:

(i) Suitable bioreceptors orientation and density over the sensor surface to ensure accessibility for the analyte recognition.

(ii) Conservation of the bioreceptors structure and functionality over the course of analysis.

(iii) Prevention of non-specific adsorptions from other components present in real samples such as urine, blood or saliva.

In order to couple the biological receptors to the sensor surface and obtain an optimal biosensor analytical performance, an extensive variety of biofunctionalisation strategies have been reported.

Physical adsorption, based on the direct adsorption of the bioreceptor over the sensor surface, is the most straightforward strategy. The attachment involves interactions such as hydrogen bonds, van der Waals forces and electrostatic and hydrophobic interactions[88] (**Figure 1.15A**). The weakness of these bonds makes this strategy extremely sensitive to environmental changes such as pH, ionic strength, and temperature. Additionally, the bioreceptors couple to the surface in an aleatory orientation in order to reduce repulsive forces with the surface and other molecules over the sensor surface. The randomized formation of the bioreceptor layer might hinder the receptor-analyte recognition, minimising the affinity and specificity of the assay[89].

Physical entrapment is another usual strategy for biofunctionalisation. It consists of creating a uniform polymer matrix that enables the bioreceptor to be locked in (**Figure 1.15B**). This one-step method does not modify the conformation of the bioreceptors, ensuring its biological activity for longer periods due to its enclosure and protection from the environment. However, the polymer layer might modify the diffusion and mass transport to the sensor surface, hampering the analyte accessibility. Polyaniline, dextran-based polymers, polythiophene and polypyrrole are the most employed polymers[90].

Other biofunctionalisation strategies exploit the extraordinary bioaffinity between certain biomolecules such as the biotin-avidin proteins, cofactors or other site-directed proteins (**Figure 1.15C**). Contrary to previous approaches, this strategy enables an oriented bioreceptor layer, without affecting the binding sites of the bioreceptor and guaranteeing the analyte accessibility. However, this strategy requires the conjugation of the native bioreceptors with the selected molecules (biotinylation) which might lead to stability issues[91,92].

Finally, in order to overcome some of the above-described limitations, a covalent biofunctionalisation is normally selected. The covalent strategy implies the irreversible bond between exposed functional groups over the sensor surface and the bioreceptors (**Figure 1.15D**). This approach is the most extensively employed due to the wide variety of functional groups ($–NH_2$, $–COOH$, $–SH$, $–N_3$) and the reproducibility, sensitivity and durability of the covalent binding. As main inconvenience, covalent binding requires a previous chemical activation to ensure enough functional groups on the sensor surface.

Additionally, binding can take place on the active sites of bioreceptors, reducing their biological activity[93].

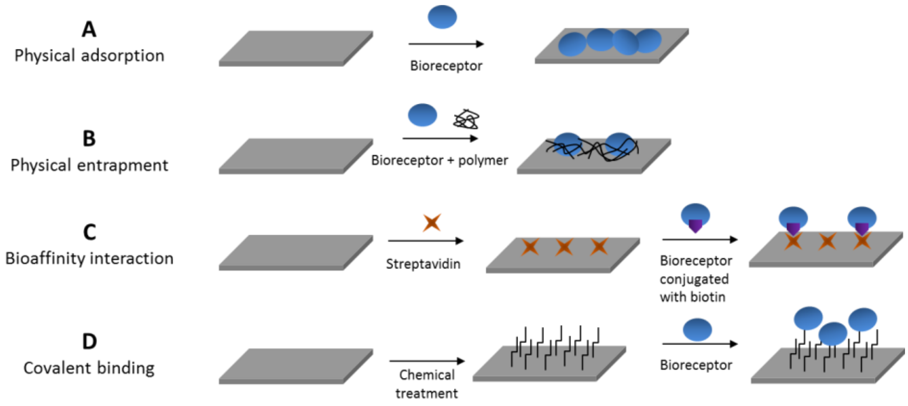

Figure 1.15. Main procedures for surface biofunctionalisation: (A)Physical adsorption, (B)Physical entrapment, (C) Bioaffinity interaction and (D) Covalent binding.

1.2.3.1. Bioreceptor immobilisation in gold surfaces

In metal-based biosensors (gold), the most widely employed biofunctionalisation strategy relies on the adsorption of thiolated molecules (R-SH) on this metal. This process is called chemical adsorption (i.e. chemisorption) and exploits the exceptional and strong affinity between the thiol atoms and gold surfaces. Thus, molecules with exposed thiol groups are spontaneously and irreversibly adsorbed to the gold surface, generating highly ordered and compact Self- Assembled Monolayers (SAM)[93,94]. SAMs are generally achieved with aliphatic or aromatic chains composed of a sulfhydryl group and functional groups at other positions (-COOH, $-NH_2$, biotin, -OH, maleimide, etc) to allow further chemical reactions such bioreceptor cross-linking over the sensor surface[95]. Moreover, other highly stable and compact molecules such as dextran-based polymers (carboxymethylated dextran) can form hydrophilic layers exposing functional groups (COOH) for bioreceptor attachment[96].

The formation of the SAM on the gold surface involves two steps (**Figure 1.16**). In the first step, the gold sensor surface is immersed in an organic solvent (commonly ethanol) containing the thiolated compounds and the alkanethiols adsorb to the sensor surface. The alkanethiols are then ordered and oriented, generating the compact monolayer. This second step can take between 2 to 24 hours at room temperature, depending on the terminal functional group (e.g. kinetics of SAMs of polar groups, such as carboxylic acids, can be considerably slower)[97].

The concentration and composition of the alkanethiols determine the analytical parameters of the biosensor. The selected SAM might directly affect the stability and density of the bioreceptor, which can be modulated by the combination of reactive alkanethiols with lateral spacers such as polyethylene glycol[98] or other alkanethiols with non-reactive alcohol groups such as 6-mercapto-1-hexanol (MCH) and 11-mercaptoundecanol (MUOH)[99,100]. Additionally, SAM can interfere with steric hinderance and thus, with the non-specific interactions on the sensor surface.

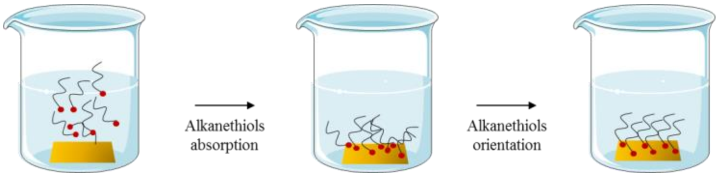

Figure 1.16. SAM formation on an immersed gold-coated substrate.

Among the variety of chemical compound for gold surfaces modification, alkanethiols with carboxyl (-COOH) as therminal functional group are widely used. Carboxyl groups enable the covalent bonding of native (antibodies) or amine-modified bioreceptor such as DNA probes through an amide bond. The amine bond is formed between the primary amine of the bioreceptor and the carboxyl terminated monolayer after the layer activation by the well-established carbodiimide-mediated chemistry (**Figure 1.17**). Usually, a solution of 1-Ethyl-3-(3-dimethylaminopropyl)-carbodiimide/N-hydroxysuccinimide (EDC/sulfo-NHS) is employed to activate the -COOH groups by producing an NHS-ester intermediate highly reactive to the primary amine in the bioreceptors[101].

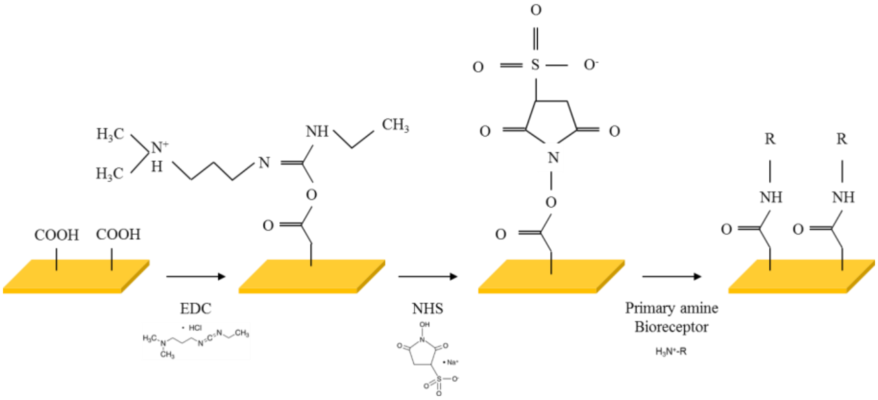

Figure 1.17. Mechanism of reaction of EDC/sulfo-NHS.

The affinity between thiol groups and gold surfaces has been exploited in this Thesis for the development of the SPR biosensor methodologies. Different bioreceptor such as DNA probes and antibodies or viral antigens were attached to the gold surface by direct covalent bond or covalent carboxyl SAMs, respectively.

1.2.3.2. Bioreceptor immobilisation in silicon photonic sensors

In the case of silicon-based biosensors such as the BiMW interferometer, the most employed biofunctionalisation strategy is also the covalent one. Covalent binding is performed through organofunctional alkylsilanes due to their stability and rapid covalent linkage[102].

The alkylsilanes consist of an organic component corresponding to the functional group (-R) in charge of the bioreceptor attachment and an inorganic part that chemically interacts with the sensor surface. The alkylsilane monolayer is generated by the reaction of silane with the hydroxyl groups of the oxidized silicon-based surface. This reaction is called silanisation and implies two steps (**Figure 1.18**). In the first step, hydrogen bonds are stablished between the alkylsilanols and the free hydroxyl groups or adsorbed water molecules on the surface. The second step involves the condensation and release of water molecules, generating the covalent siloxane bonds (Si-O-Si) which are thermally and relatively chemically stable. Due to the nature of the silanisation procedure, it is influenced by the experimental conditions such as the nature of the silane and the solvent, the silane concentration, the water content, the temperature and the incubation time[70].

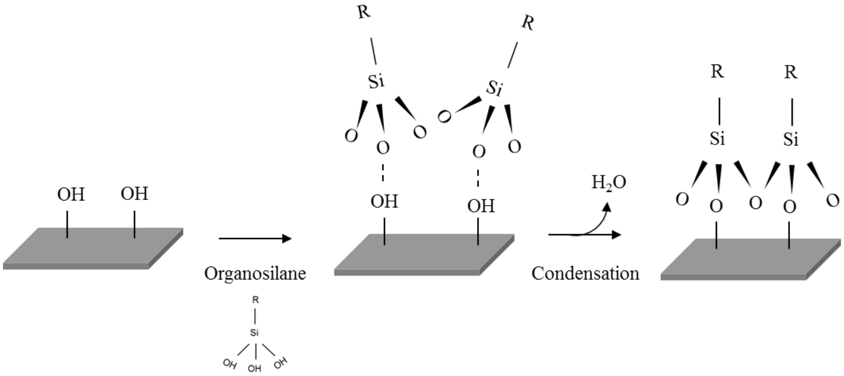

Figure 1.18. Scheme of the reaction of organosilanes with the silicon surface.

Organosilanes with different functional groups might be employed, being the most used 3-aminopropyltriethoxy silane (APTES, with an amino group), carboxyethylsilanetriol sodium salt (CTES, with a carboxylic acid group), 3- glycidyloxypropyltrimethoxysilane (GOPTS, with an epoxy group), isocyanatepropyltriethoxysilane (ICPTS, with a isocyanate group) and (3- mercaptopropyl) trimethoxysilane (MPTMS, with a thiol group)[70].

In EW-based biosensors, the evanescent field exponentially decays as it penetrates the outer medium. For this reason, it is crucial the proximity of the bioreceptor to the sensor surface. All the above-cited silanes have around three carbons in length, coupling the bioreceptors as close as possible to the sensor surface. Therefore, the selection of the silanes and the silanisation reaction determine the biofunctionalisation procedures and the analytical performance of the biosensor.

For biosensor assays using the BiMW interferometer, different functionalisation protocols based on chemical silanisation have been tested. The silanes selected were APTES and triethoxysilane polyethylene glycol carboxylic acid (silane-PEG-COOH). APTES provides a surface with amine groups, being one of the most employed silanes due to the versatility to incorporate different corsslinkers for the biofunctionalisation of molecules. On the other hand, silane-PEG-COOH allows a carboxylic surface that can be activated by the robust and previously described EDC/sulfo-NHS chemistry. As in the case of the SPR methodologies, different bioreceptors as DNA probes and antibodies were covalently coupled for the identification and analysis of lung cancer-related biomarkers (miRNAs, DNA methylation and proteins).

1.2.4. Antifouling properties of the biolayer

Evanescent wave-based biosensors are able to monitor in real-time any changes in the RI caused, for example, by the binding of the target analyte to the immobilised bioreceptor on the sensor surface. However, these optical biosensors are also sensitive to RI changes unrelated to the analyte recognition. The interactions over the sensor surface due to non-specific analytes are called fouling effects. These fouling effects are extremely severe in clinical samples where the analyte is dissolved in complex biological matrices such as blood, plasma, serum, urine or saliva. These biological matrices consist of a combination of chemical and biologal components such as proteins, hormones, fats, etc which can be adsorbed non-specifically on the sensor surface through interactions such as hydrogen, electrostatic, van der Waals, and hydrophobic bonds. These non-specific adsorptions could affect the sensor response, generating a background signal that modifies the real value of the specific binding. In addition, the presence of these compounds could hinder or even inhibit the analyte-bioreceptor recognition[103]. Therefore, the control of these fouling effects is crucial for the use of biosensor devices in real clinical scenarios to ensure an accurate and reliable detection of the analytes. Considering the composition of the biological fluids, different antifouling strategies should be designed and performed to reduce or completely eliminate the fouling effect.

In order to create antifouling properties in the sensor surface, numerous antifouling compounds can be used. These blocking agents have different physicochemical characteristics that prevent or eliminate undesired interactions from complex matrices[103]. These antifouling compounds can be incorporated in the biosensor assay following different strategies: (i) introduction of a surface blocking agent over the sensor surface after the bioreceptor attachment; (ii) addition of antifouling compounds in the employed buffer; and (iii) dilution of the biological fluid.

Among blocking agents, non-ionic and zwitterionic surfactants such as Tween 20 and 3-[(3-cholamidopropyl) dimethylammonium]-1-propanesulfonate (CHAPS) are commoly used[104,105]. Surfactants are able to prevent undesirable hydrophobic or electrostatic interactions by solubilising biological macromolecules.

Other additives, such those based on proteins can reduce the adsorption of other proteins on the sensor surface. Casein and milk are some examples, being bovine serum albumin (BSA) the most employed[104].

Polymers and copolymers are also widely used for the reduction of fouling effects. Polymers such as dextran and its derivatives (e.g. amino-dextran, dextran-sulfate…) are characterised by high hydrophilicity, showing remarkable resistance to protein adsorption[106]. Otherwise, blocking agents composed of copolymers such as polyethylene glycol (PEG) attract attention not only due to their antifouling properties but also due to their biocompatibility. Poly-L-Lysine-graft-PEG (PLL-g-PEG) is the major representative of PEGs compounds. PLL-g-PEG interacts electrostatically with the sensor surface and side-chains form a dense protective monomolecular coating. Additionally, the poly-lysine chains confer high hydrophilicity[103,107]. Other PEGs-based agents such as thiolated PEGs molecules with other functional group (SH-PEG-CH_3, SH-PEG-NH_2, SH-PEG-COOH, etc) is an efficient and practical strategy to incorporate antifouling agents in the sensor surface (mainly in plasmonic sensors) and remain a reactive layer to attach the bioreceptors[108].

For each particular application, antifouling properties should be studied and analysed to reduce or eliminate non-specific interaction from complex matrices and guarantee reliable and accurate analyte detection. In this thesis, different antifouling strategies have been used for the clinical analysis of biological fluids such as blood, plasma and pulmonary specimens. **Figure 1.19** shows some of the blocking agents used for the human fluids evaluation such as detergents (Tween 20 (**Figure 1.19A**) and CHAPS **Figure 1.19B**), dextran derivates (sulfate dextran **Figure 1.19C**) and PEGs-based agents (SH-PEG-CH_3 **Figure 1.19D**).

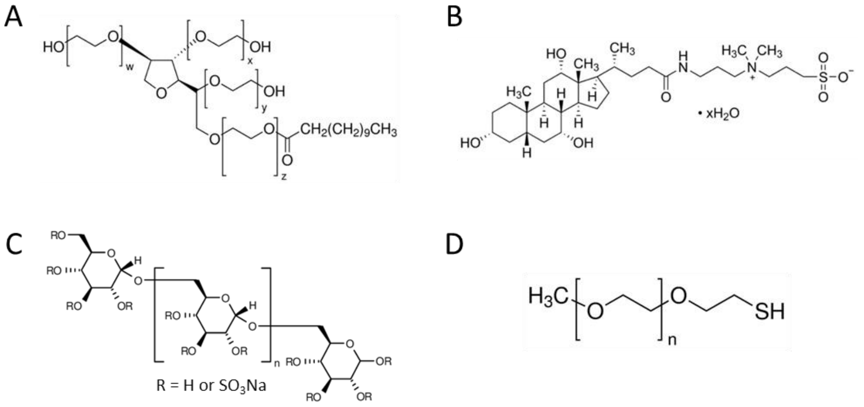

Figure 1.19. Blocking agents used in this thesis for the analysis of human fluids such as serum and plasma. (A) Tween20, (B) CHAPS, (C) dextran sulfate and (D) SH-PEG-CH_3.

Chapter 2

Evanescent wave sensor platforms description

This chapter includes a description of the SPR and the BiMW interferometer biosensor platforms, followed by the fabrication of the sensor chips based on gold layers and silicon nitride waveguides, respectively. The optical, microfluidic and electronical components are also detailed.

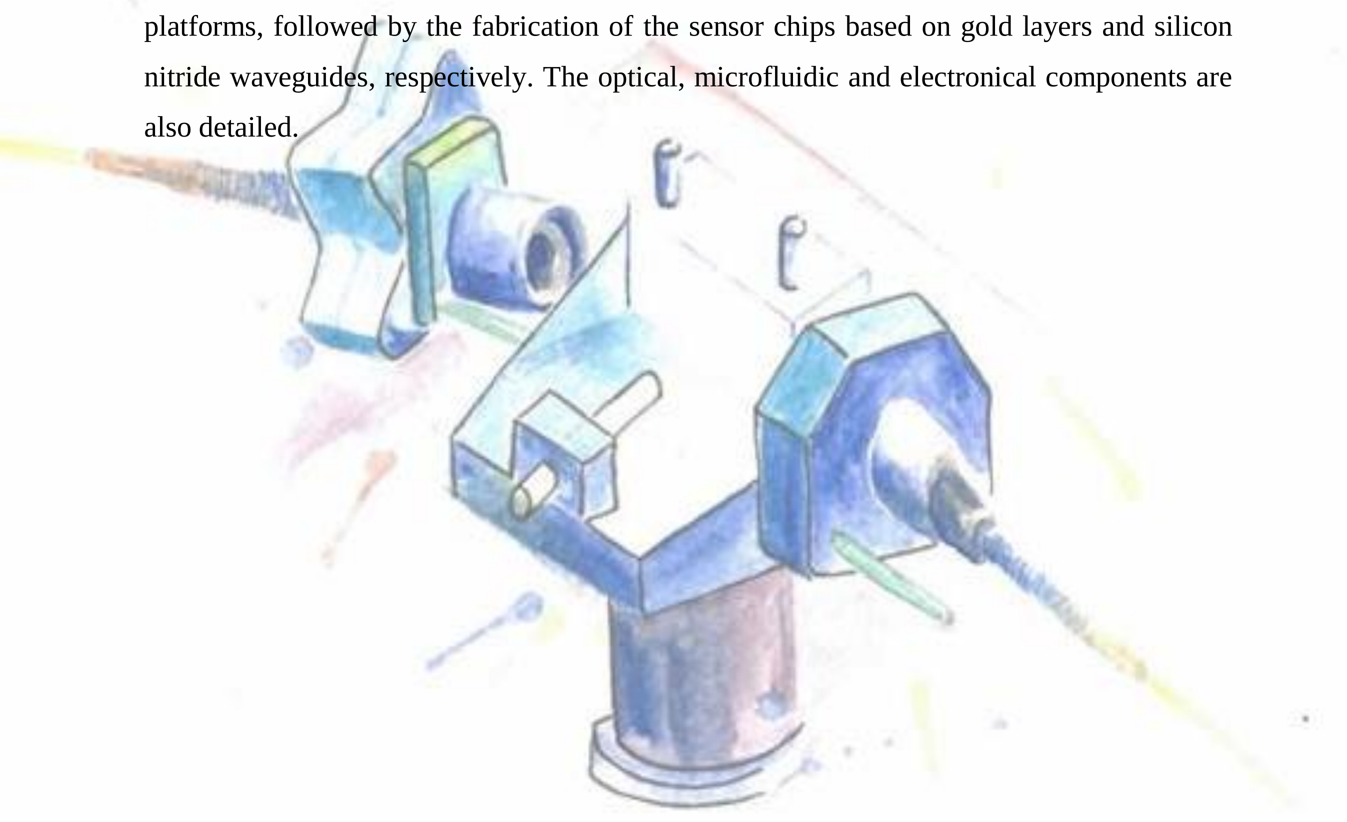

2. Evanescent wave sensor platform description

2.1. Surface plasmon resonance device

The components generally employed in an SPR biosensor based on a Kretschmann configurationare are: (i) a light source (monochromatic or broadband) for SPP excitation; (ii) the plasmonic transducer, which normally consists of a thin layer of gold (≈ 50 nm); (iii) a detector (angle, wavelength, intensity or phase-based) for SPP interrogation and (iii) a microfluidic system for flowing the liquid samples over the sensor surface.

2.1.1. Sensor chips fabrication and cleaning

Gold sensor chips were fabricated by metal evaporation employing an electron beam-deposition system (AJA International Inc. ATC-8E, Orion, USA) where 1 nm of titanium and 49 nm of gold are deposited on glass substrates (No. 4, 22 x 22 mm, Thermo Scientific Menzel-Glaser (Braunschweig, Germany)). Before gold surface biofunctionalisation, sensor chips should be cleaned by consecutive heating at 80° C and sonicating for 1 min with solvents of increasing polarity (acetone, ethanol and Milli-Q water). Then, sensor chips are dried with an N_2 flow and placed in a UV/Ozone Procleaner Plus (Bioforce Nanosciences, Utah, US) for 20 min for surface activation. The sensor chips were finally rinsed with ethanol and dried with N_2 flow for chemical modifications over the gold surface.

2.1.2. Surface plasmon resonance platform

In this Thesis, we have employed an in-house designed and fabricated plasmonic sensor based on the Kretschmann configuration (TIR, prism-coupled, set at a fixed angle) which works at a fixed angle of $\theta=70^{o}$. The platform contains all the optical components in a portable 20 x 20 cm^2 breadboard, which reflects its potential portability and integration. A photograph of the sensor platform can be seen in **Figure 2.1**.

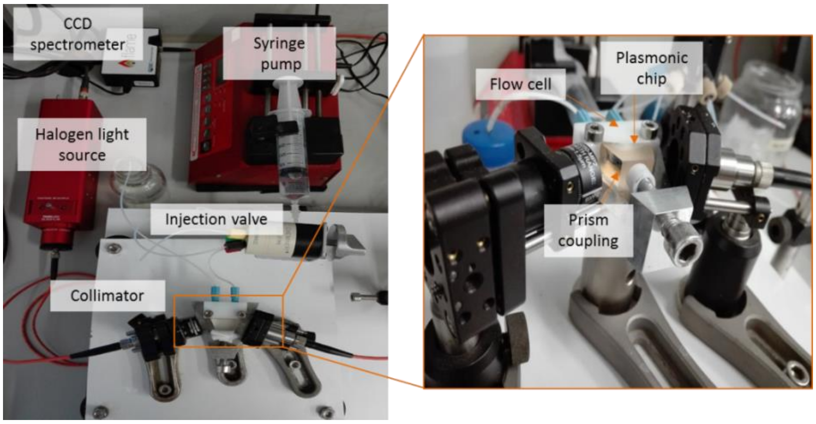

Figure 2.1. Photograph of the experimental SPR sensor set-up.

The SPR biosensor monitors the binding events in real-time by tracking the SPR-wavelength displacements (Δλ, nm). Plasmonic sensor chips are clamped between a trapezoidal glass prism through RI matching oil (n≈1.512) and a custom-made flow cell of Delrin (volume = 4 µL). The flow cell is connected to a microfluidics system consisting of a syringe pump (Darwin microfluidics, Paris, France) with adjustable pumping speed that provides a constant liquid flow and a manually operated injection valve (CHEMINERT®, VICI, Houston, TX, USA) incorporating a 100 µL loop to deliver the liquid samples into the microfluidic cell. The sensor surface is excited by a collimated (C330TMEB, Thorlabs, Germany) halogen light source (THORLABS, Newton, NJ, USA) set in transverse-magnetic (TM) polarization mode, using a linear polarized (LPVIS050, Thorlabs, Germany). The polarized light reaches the substrate through the prism coupling, generating an evanescent field at the sensor surface which is very sensitive to refractive index changes. The reflected light is collected and fiber-coupled to a CCD spectrometer (Flame, Ocean Optics, Largo, FL, US).

Biomolecular interactions occurring at the gold sensor surface result in an increment in the mass, which translates in an increase in the RI (shifting the resonance curve to higher wavelengths), whereas desorptions from the sensor surface decrease the RI, shifting the curve to lower wavelengths. The tracking of the resonance peak position (Δλ) can be followed in real-time *via* polynomial fit using a custom-made readout software (National

Instruments, Labview, US), being possible to detect interactions or desorptions instantaneously (**Figure 2.2**). Reflectivity spectra are acquired every 3 ms and 300 consecutive spectra are averaged to generate the resonant spectrum.

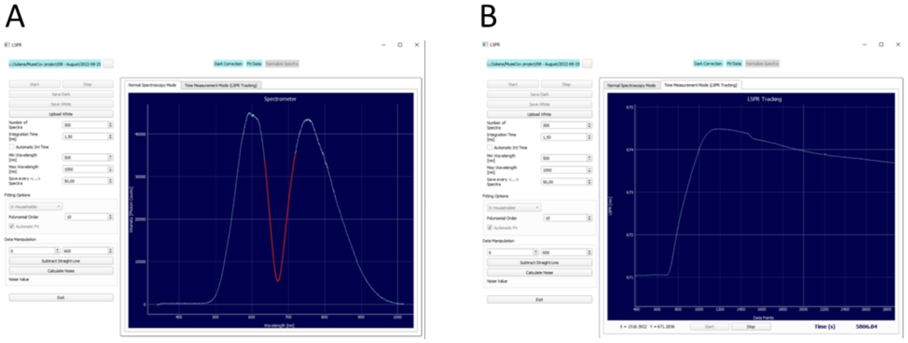

A:
Number of Spectra: 300
Integration Time [ms]: 1,50
Min Wavelength [nm]: 500
Max Wavelength [nm]: 1000
Save every <...> Spectra: 50,00
Polynomial Order: 10
Data Manipulation: 0 – 600

B:
Number of Spectra: 300
Integration Time [ms]: 1,50
Min Wavelength [nm]: 500
Max Wavelength [nm]: 1000
Save every <...> Spectra: 50,00
Polynomial Order: 10
Data Manipulation: 0 – 600
X = 1518.3922 Y = 671.2836
Time (s) 5806.84

Figure 2.2. Screenshots of the home-made readout software showing in real-time (A) the wavelength spectra and (B) the sensorgram tracking the SPR signal in nm (Δλ).

2.1.3. Sensitivity evaluation

The bulk sensitivity of the plasmonic biosensor was assessed by a calibration curve. Gold sensor chips were evaluated by injecting successive solutions with different refractive index (HCl solutions, 0.025M, 0.05M, 0.1M, 0.025M and 0.5M) which do not affect the sensor surface (deposition by residues nor oxidation). First, HCl solution were analysed with a refractometer J57 (RUDOLPH, Hackettstown, USA) to determine the refractive index of each sample. Then, the HCl solutions were injected to measure the wavelenght variation (Δλ) caused by the refractive index change from water (running buffer) to the solution of HCl (**Table 2.1 and Figure 2.3A**). This wavelength variation (Δλ) was evaluated *versus* the refractive index change (Δη) (**Figure 2.3B**).

Figure 2.3B shows the calibration curve fitted in linear regression and its equation with a correlation coefficient of R^2=0.9998 and a bulk sensitivity of S_{bulk} = 2832 nm·RIU^{-1}.The limit of detection (LOD) of the SPR biosensor can be calculated using the **Equation 1.1**. The SPR sensor reflects excellent LOD = $4.24.10^{-6}$ RIU (SD noise σ= 0.004), reaching sensitivities in the same range than other reported SPR sensors[42].

Table 2.1. Refractive index change induced by a set of HCl soluctions and corresponding wavelength changes evaluated on a SPR sensor.

HCl concentrations (M)	Δn (RIU)	Δλ (nm)
0.025	$2.2\text{x}10^{-4}$	10.80
0.05	$4.5\text{x}10^{-4}$	5.48
0.1	$8.2\text{x}10^{-4}$	2.17
0.25	$1.97\text{x}10^{-3}$	1.27
0.5	$3.85\text{x}10^{-3}$	0.48

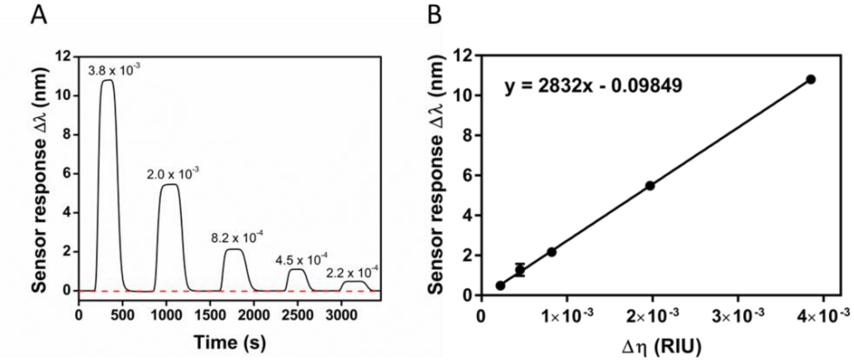

Figure 2.3. Bulk sensitivity (A) Real-time sensorgram for different refractive index solutions measured in the SPR platform (B) Calibration curve showing the relationship between the variation in the refractive index (Δn) and the sensor response (Δλ).

2.2. Bimodal waveguide interferometer platform

In this Thesis we have employed a home-customed BiMW interferometer platform composed by: (i) a monochromatic light from a polarized diode laser (λ = 660 nm) (ii) the interferometric transducer, which consists of a rib Si_3N_4 waveguide designed to support the propagation of the fundamental and first modes; (iii) a photodetector for interferometric phase shift between the two modes and (iii) a microfluidic system for flowing the liquid samples over the sensor surface.

2.2.1. Sensor chip fabrication and cleaning

Silicon-based BiMW sensor chips are fabricated at the Infraestructura Científica y Técnica Singular (ICTS) Clean Room facilities of the Microelectronic National Center (IMB-CNM-CSIC) in Barcelona (Spain). The fabrication process is based on a standard microelectronic technology including photolithography and etching processes over a silicon wafer substrate. The resulting wafer has a total of 12 BiMW chips, each of them containing 20 BiMW sensors, 6 BiMW references (without sensor area) and 6 single-mode waveguides, all of them separated by 250 μm from center-to-center (**Figure 2.4**). The dimensions for each BiMW chip are 3 cm x 1 cm and the dimensions for the rib waveguide are 3 μm in width by 1.5 nm in height. The simple BiMW design without light splitters such as the Y-type dividers or more complex structures, and the wafer-scale fabrication, increase the precision and reproducibility of the fabrication process and reduce fabrication time and costs allowing mass production. Finally, the high homogeneity of the waveguide material and hence, the reproducibility and reliability of each waveguide sensor enable multiplexed analysis and integration in compact portable platforms.

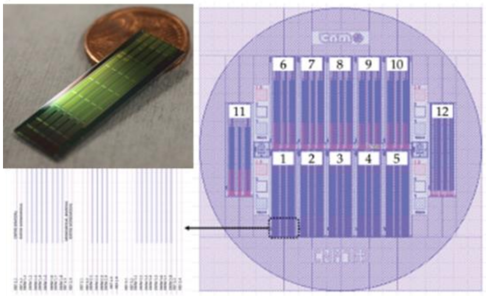

Figure 2.4. Photograph of the BiMW chip containing 20 sensors and BiMW wafer mask layout with 12 chips containing 240 sensors in total.

In the BiMW sensor chips, the waveguide core material is silicon nitride (Si_3N_4) due to its high refractive index (n_{core}=2.00), and high density and chemical inertness to ion species, oxygen or moisture permeation[109]. The Si_3N_4 core is surrounded by an upper and lower cladding made of silicon oxide (SiO_2) with a lower refractive index (n_{cladd}=1.46) to ensure light guides through the core with minimal loss of energy (**Figure 2.5**). In the bimodal section, the cladding is etched to create the sensing area (15 mm) in which the core is exposed to the external medium. BiMW sensor works with TE polarized light of a $\lambda = 660$ nm coupled into the rib waveguide, then Si_3N_4 and SiO_2 are both perfect materials for BiMW sensor because of their transparency for a broad spectral range (≈ 200 — 2000 nm). Additionally, most of the biomolecules are non-absorbent in the visible, avoiding light absorption. Si_3N_4 material is an ideal candidate for integrated optics waveguide-based sensors in the visible spectra.

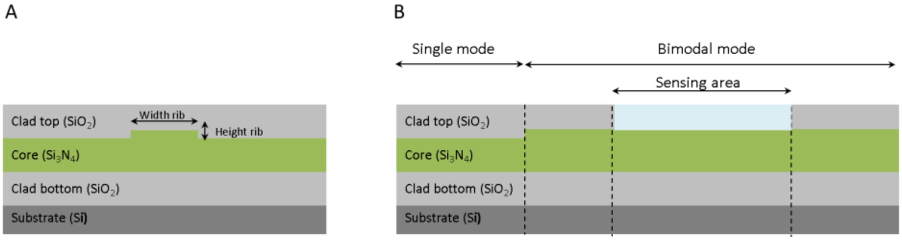

Figure 2.5. Schematic representation of the BiMW interferometric sensor chips in the (A) cross section and (B) the longitudinal section.

The Si_3N_4-based BiMW sensor chips must be cleaned before the biofunctionalisation process. Firstly, the chips were cleaned by sonicating them sequentially in acetone, ethanol, and water for 5 min at 60 ^{o}C, followed by a 10 min sonication in 1:1 (v/v) methanol:hydrochloric acid (MeOH:HCl) solution to remove organic contamination. The chips were rinsed with milli-Q H_2O and dried under an N_2 stream. Then, a layer of active hydroxyl group was generated on the surface by O_2 plasma activation (Electronic Diener, Ebhausen, Germany) for 5 min at 45 sccm gas flow, followed by immersion in a 15 % HNO_3 solution at 95 °C for 25 min. Finally, rinsed and dried chips can be silanized *ex-situ* to biofunctionalise the sensor surface.

2.2.2. BiMW interferometer platform

The BiMW devices employed in this thesis are shown in **Figure 2.6**. The sensor chip is placed on a custom-made holder with a 3- axis translation platform for the proper coupling of the input light beam. A Peltier thermoelectric cooler (Peltier element TEC3-2.5, Thorlabs, New Jersey, US) and a temperature controller behind the sensor chip avoid temperature fluctuations that affect the intrinsic sensitivity of the BiMW biosensor, providing stabilization with an accuracy of 0.01 °C.

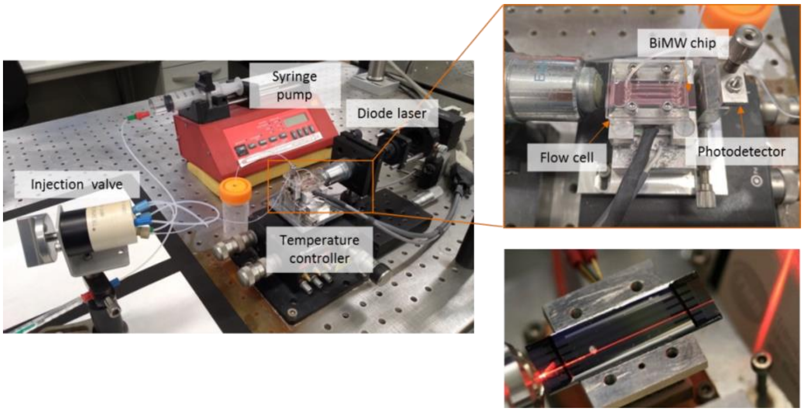

Figure 2.6. Photograph of the experimental BiMW sensor set-up and a light coupled BiMW waveguide.

Input light from a transverse-electric (TE) polarized diode laser (λ = 660 nm) (Hitachi, Tokyo, Japan) is coupled into the BiMW sensor through a lenses system consisting of a collimated lens (C240TME-D, Thorlabs, New Jersey, US), a polarization-dependent isolator (IO-3D-660-VLP, Thorlabs, New Jersey, US) and a coupling objective 40x (Achro, Leica, Wetzlar, Germany). The intensity is recorded by a two-sectional photodetector (Hamamatsu Photonics, Hamamatsu, Japan) and processed through an acquisition card. Signal acquisition is performed in real-time using a homemade LabVIEW software (National Instruments, US) where an all-optical phase modulation method based on a trigonometric algorithm is applied to transforms the interference signal into a linear one[64]. Thus, the phase shifts (Δφ, rad) between both modes can continuously be monitored and quantified (**Figure 2.7**).

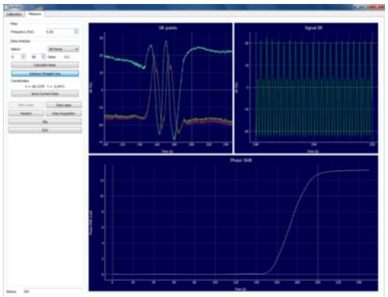

Figure 2.7. Screenshots of the home-made readout software showing in real-time (up) the interferometric signal and S_R values and (down) the sensorgram tracking the BiMW signal in radians ($\Delta\varphi$).

A fluidic system composed of a five-channel polydimethylsiloxane (PDMS) microfluidic cell (channel dimensions = 1.25 mm width x 500 µm height x 18.5 mm long), a syringe pump (Darwin, Paris, France) and a 6-port injection valve (CHEMINERT®, VICI, Texas, US), guarantee a continuous flow rate of the running buffer and the injections of the different solutions (**Figure 2.6**).

2.2.3. Sensitivity evaluation

As we describes previously for SPR platform, the bulk sensitivity of the BiMW biosensor was assessed through a calibration curve by injecting successive solutions with different refractive index (HCl solutions, 0.025M, 0.05M, 0.1M, 0.025M and 0.5M). The phase variation ($\Delta\varphi$) caused by the refractive index change from water (running buffer) to the solution of HCl (**Table 2.2**) was monitored in real-time (**Figure 2.8A**). This phase variation ($\Delta\varphi$) was evaluated *versus* the refractive index change (Δn) (**Figure 2.8B**).

Figure 2.8 shows the calibration curve fitted in a linear relation and its equation with a correlation coefficient of $R^2=1$ and a bulk sensitivity of S_{bulk} = 14413 rad·RIU^{-1}. Using the **Equation 1.1**, the limit of detection of the BiMW biosensor can be calculated as LOD = 4.16 x 10^{-7} RIU (SD noise σ= 0.002). The reported sensitivity matches that of other interferometric waveguide devices[45].

Table 2.2. Refractive index change induced by a set of HCl soluctions and corresponding phase changes evaluated on a SPR sensor.

HCl concentrations (M)	Δn (RIU)	Δφ (rad)
0.025	$2.2\mathrm{x}10^{-4}$	54.45
0.05	$4.5\mathrm{x}10^{-4}$	27.53
0.1	$8.2\mathrm{x}10^{-4}$	10.77
0.25	$2.0\mathrm{x}10^{-3}$	5.36
0.5	$3.8\mathrm{x}10^{-3}$	2.28

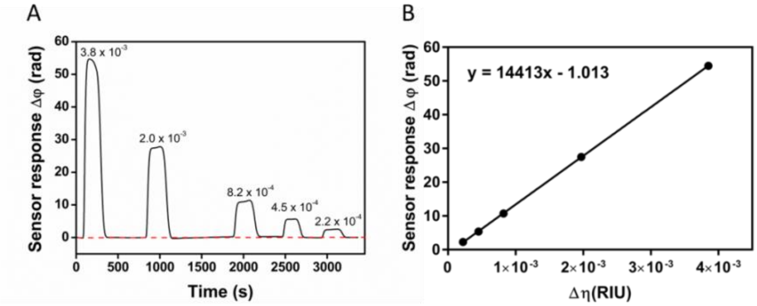

Figure 2.8. Bulk sensitivity. (A) Real-time sensorgram for different refractive index solutions measured in the BiMW interferometer (B) Calibration curve showing the relationship between the variation in the refractive index (Δη) and the sensor response (Δφ).

2.2.4. BiMW interferometer in a multiplex configuration

As discussed above, EW-based biosensors and specially BiMW interferometers stand out among conventional biosensors not only because of their high sensitivity, but also because of their miniaturised and multiplexed capabilities. Althoug BiMW interferometer sensors are designed to cointain up to 20 waveguides, technical and engineering improvements in the optical platform are needed to ensure simultaneous and individual analysis of several analytes.

We are currently focused on the development of a multiplexed BiMW device, including the modelling testing and optimisation of several designs of the multiplexed version of the BiMW sensor chips, as well the corresponding microfluidics and the light detectors (CCD cameras and photodetector array). **Figure 2.9** shows some examples of the proposed designs and the evaluation of one of the multiplexed sensor chip after their fabrication at the Clean Room facilities. Additionally, this figure illustrates the custom-designed microfluidics and the software used for the simultaneous measurements. For example, the dimensions of the multiplexed BiMW sensor chip in **Figure 2.9A** are 5 cm x 0.67 cm. It has several splitters integrated to achieve light propagation through 8 waveguides sensors, which are separated by 150 µm from center-to-center.

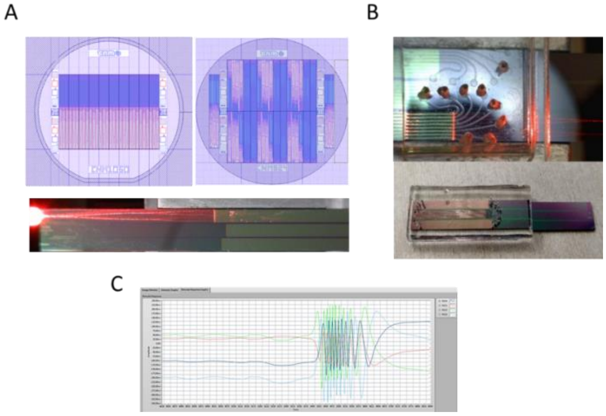

Figure 2.9. Multiplex configuration of the BiMW interferometer. (A) Photograph of multiplexed BiMW sensor chips and (B) designed microfluidic. (C) Screenshot of the home-made readout software showing the multiplex and real-time interferometric signal of two waveguides.

Studies focused on improving the multiplex configuration of the BiMW interferometer are still on-going. The ultimate goal involves the possibility of integrating several functionalities (antigen, miRNAs, DNA mutation detection...) on a single chip for simultaneous detection of these biomarkers using a single patient sample. Multiple and instantaneous detection of numerous analytes in a patient's samples would not only extremely improve diagnostic sensitivity and specificity, but also provide a more accurate and efficient diagnosis. The implementation of this type of POC together with the development of artificial intelligence in clinical practice would revolutionise personalised medicine, offering more efficient therapies.

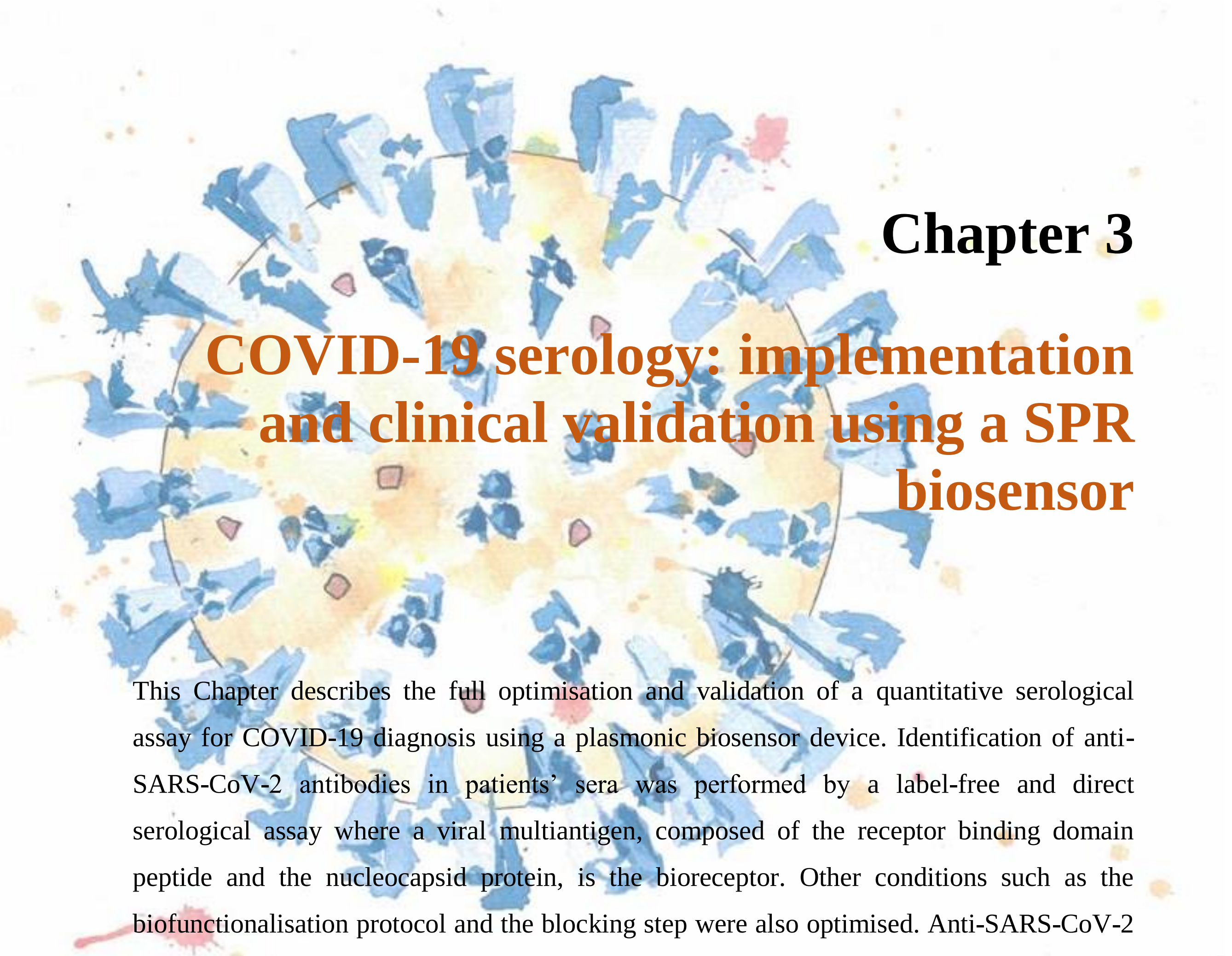

Chapter 3

COVID-19 serology: implementation and clinical validation using a SPR biosensor

This Chapter describes the full optimisation and validation of a quantitative serological assay for COVID-19 diagnosis using a plasmonic biosensor device. Identification of anti-SARS-CoV-2 antibodies in patients' sera was performed by a label-free and direct serological assay where a viral multiantigen, composed of the receptor binding domain peptide and the nucleocapsid protein, is the bioreceptor. Other conditions such as the biofunctionalisation protocol and the blocking step were also optimised. Anti-SARS-CoV-2 antibodies quantification in diluted serum using the first WHO International Standard is described, providing a limit of detection within the clinical range. Finally, serological assay validation is carried out with 125 clinical serum samples from COVID-19 patients and pre-pandemic samples, showing the potential of the biosensor device as an effective point-of-care platform. This device would have an added value to manage the COVID-19 pandemic (epidemiological studies, acquire immunity knowledge, ICU bed management, vaccine development).

3. COVID-19 serology: implementation and clinical validation using a SPR biosensor

3.1. Introduction

3.1.1. COVID-19

In 2019, the COVID-19 was declared a pandemic by the WHO. The outbreak of this infectious disease originated in December 2019 and was rapidly spread worldwide generating devastating consequences at health, social, and economic levels. To date, COVID-19 has affected more than 560 million people, with more than 6 million deaths[17]. This disease is caused by the SARS-CoV-2 virus (Severe Acute Respiratory Syndrome Coronavirus 2). This virus belongs to the family of Coronaviridae, subfamily Coronavirinae and the genera Betacoronavirus. SARS-CoV-2 is composed of four structural proteins (spike protein (S), envelop protein (E), membrane protein (M), and nucleocapsid protein (N)) and sixteen non-structural proteins (nsp1−16). Spike protein is a relevant antigen since it is in charge of recognizing and entering the human host cell. The S protein consists of two subunits S1 and S2. S1 contains the Receptor Binding Domain (RBD) to bind the receptor on the host cell. Otherwise, S2 contains some domains to fuse the membranes of viruses and host cells (**Figure 3.1**). The genome of SARS-CoV-2 is a single-stranded positive-sense RNA (+ssRNA) of 29.9 kb[110].

The COVID-19 disease singularities such as varied symptomatology or non-symptomatology in a significant percentage of the infected people, long incubation times, high transmission rate, etc., allowed the fast and quietly spread of the SARS-CoV-2 virus. In addition, the lack of (i) knowledge about the emerged virus(ii) population's immunity against the disease and (iii) accurate diagnostic methods, have facilitated its uncontrolled spread[111–113].

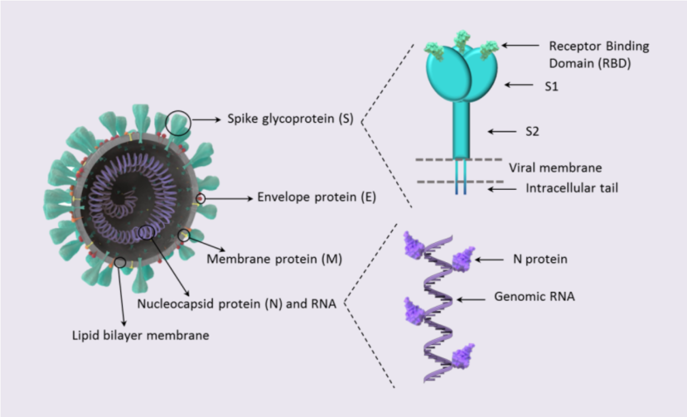

Figure 3.1. SARS-COV-2 virus structure. Schematic representation of the viral antigens used in this thesis: spike and nucleocapsid protein.

3.1.2. Established methods for SARS-CoV-2 virus detection

Standard diagnosis methods for COVID-19 can be classified depending on infection time (active or past infection) and the SARS-CoV-2 virus component identified (**Figure 3.2**). Active infection can be diagnosed through the gold standard technique based on the amplification of the viral genetic material from respiratory samples, the reverse transcription polymerase chain reaction (RT-PCR)[114,115]. RT-PCR provides excellent levels of sensitivity and specificity, but requires centralized and specialized laboratories and long turnaround times (between 3 to 48 hours) to deliver results. Moreover, during the pandemic the time-to-result of the PCR was a bottleneck, as thousands of samples needed to be analysed everyday. To overcome the RT-PCR limitations mainly related to extensive time to result, rapid antigen tests were developed. Rapid antigen tests detect SARS-CoV-2 antigens (N or S proteins, mainly) from viral fragments in 15 - 30 minutes. Antigen tests are used as point-of-care and can be self-used although their sensitivity and reliability do not reach the levels of the genomic molecular assays[116,117]. Complementary to the detection of the active infection, a past infection can be diagnosed through serological tests. These tests detect the presence in the blood of immunoglobulins (Ig) generated by the infected host. Serological tests have played an important role in pandemic management, providing information about the prevalence of the virus, disease surveillance and the dynamics of acquired immunity.

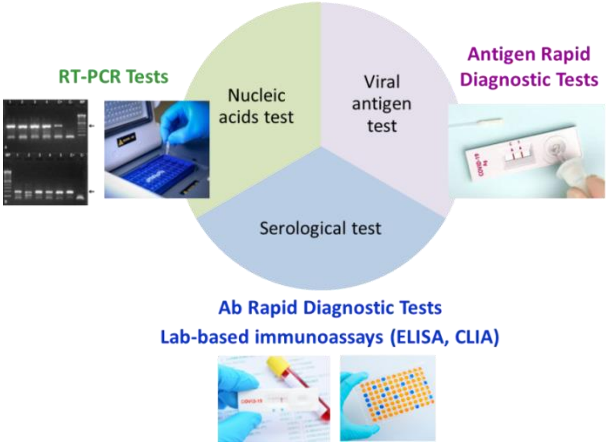

Figure 3.2. COVID-19 diagnosis techniques. Molecular diagnosis can be based on the identification of viral nucleic acids, viral antigens or host immunoglobulins.

3.1.2.1. Serological biosensor assays of anti-SARS-CoV-2 antibodies

In the case of SARS-CoV-2, during the active infection, only the viral components (RNA and structural proteins) can be detected. However, the immune response is soon triggered, and antibodies are detectable in the blood after a few days post-infection (**Figure 3.3**). The immune response starts with the appearance of IgMs during the acute infection phase which peak at two weeks to five and decline after a few days or even weeks. Then, IgGs and IgAs are generated. IgGs are long-lasting immunoglobulins that peak at week three to seven and they remain in the bloodstream at constant concentrations for at least two months after infection, conferring immunity to the SARS-CoV-2 virus[118–120].

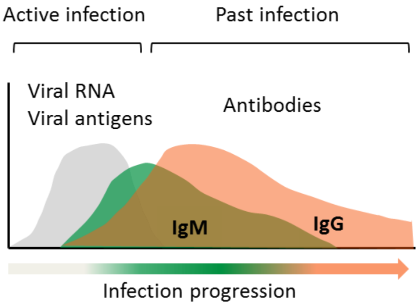

Figure 3.3. Serology timeline. Detectable immunoglobulins in the course of the SARS-CoV-2 infection.

Although serology assays are not direct diagnosis methods of the infection, they are indirect tests extremely helpful for the diagnosis of past infections and pandemic management. In ICU and hospitals, they are immensely useful for bed management and the deisolation of post-COVID-19 patients (PCR-positive patients with a positive serological test). These tests also identify asymptomatic and suspected patients with negative PCR results. In addition, they provide valuable information for the development of new vaccines or treatments[119,121,122]. Finally, they are a key component to study the emergence of SARS-CoV-2 variants resistant to antibodies induced after vaccination or primary infection.

COVID-19 serological assays identify immunoglobulins specific for the most abundant and relevant viral antigens such as the S protein (S1, S2 and RBD) and the N protein. In the clinic, traditional microplate-format immunoassays, such as ELISA and chemiluminescence immunoassay (CLIA) are widely used since they offer high sensitivities, multiplexed capabilities and automation. However, they require long incubation times, sophisticated equipment and trained personnel[123]. In addition, immunochromatographic LFAs have been commercialized as point-of-care platforms. LFAs identify immunoglobulins in a fast way (15-min assay) providing qualitative results, but they exhibit moderate sensitivity (90-94%)[124–126]. In addition, some of them can differentiate the IgG and/or IgM, giving information about the stage of the infection (acute phase or past infection). Advantages and inconveniences of microplate and LFA-based assays are summarised in **Table 3.1**.

The development of quantitative serological assays is crucial for potentially useful scenarios such as monitoring and predicting acquired immunity over time, managing the hospital beds and COVID-19 patient’s isolation and/or understanding the relationship between antibody levels and severity of the symptoms, among others[122,127–129].

Table 3.1. Advantages and drawbacks of the established methods for COVID-19 serological assays .

Serological assay	Advantages	Inconveniences
Lateral Flow Assay	✓ fast (15 min) ✓ commercialized ✓ user-friendly	X limited sensitivity, specificity

	✓ information about infection status	X qualitative result
Microplate Assay (CLIA/ELISA)	✓ high sensitivity, specificity, ✓ well-established, high scalability ✓ multiplex capabilities	X time-consuming (2-5 h), X trained personnel X centralized, price

Optical biosensors and, specifically, SPR sensors have been reported as a powerful tool for multiple clinical applications in virology, including serological assays related to dengue virus[130,131], Hepatitis B virus[132], Epstein-Barr virus[133], and the first SARS-CoV[134]. After SARS-CoV-2 outbreak, novel works and perspectives have been reported[135–137], highlighting the capabilities of this technology as a diagnostic device since SPR biosensors can ensure sensitive and specific detection of the immunoglobulins rapidly and quantitatively. Based on this, we have used a home-mode plasmonic biosensor platform as a potential portable device able to quantify levels of anti-SARS-CoV-2 immunoglobulins in patients' sera in less than 15 min. A label-free direct assay using a viral multiantigen has been implemented. We have assessed the feasibility of the assay through a large clinical validation, paying special attention to the diagnostic sensitivity and specificity reported by the plasmonic biosensing platform compared to established serological techniques.

This work was done under the umbrella of the H2020 Research and Innovation Programme of the European Commission (H202-SC1-PHE-Coronavirus-2020, CONVAT Project, No. 101003544).

3.2. Materials and methods

3.2.1. Chemical and biological reagents

Solvents used for sensor chips cleaning (acetone 99.5% and ethanol 99%) were purchased from Panreac Applichem (Barcelona, Spain). All the buffer compounds, PBS 10 mM (NaCl 0.137 M, KCl 2.7 mM, Na_2HPO_4 10 mM, KH_2PO_4 1.8 mM, pH 7), MES 0.1 M (2-(N-morpholino) ethanesulfonic acid), HEPES (10 mM 4-(2-hydroxyethyl)piperazine-1-

ethanesulfonic acid, 300 mM NaCl, pH 8), Tween 20, dextran sulfate sodium salt (DS) (MW~40000 g·mol^{-1}), commercial serum, 16-mercaptohexadecanoic acid (MHDA), (1-ethyl-4(3-dimethylaminopropyl)carbodiimide hydrochloride (EDC), nickel (II) chloride ($NiCl_2$), ethanolamine and N-hydroxysulfosuccinimide (sulfo-NHS) were purchased from Sigma-Aldrich (Steinhem, Germany). HS-$(CH_2)_{11}$-EG_3-NTA was purchased from ProChimia Surfaces (Sopot, Poland). Poly-L-lysine-graft-PEG (PLL-g-PEG) was purchased from SuSoS (Dübendorf, Switzerland). Recombinant RBD domain, S1 subunit and their respective polyclonal IgG antibodies (pAb-RBD, pAb-S1) were obtained from SinoBiological (Eschborn, Germany). A polyclonal IgG antibody specific for N protein (pAb-N) was purchased from GeneTex (Irvine, CA, US). Recombinant N protein was synthesized in the Unité Des Virus Émergents (Aix-Marseille Université, Marseille, France). WHO International Standard Anti-SARS-CoV-2 immunoglobulin (code: 20/136) was purchased from National Institute for Biological Standards and Control (NIBSC, Hertfordshire, United Kingdom). Control monoclonal IgG antibody against CRP C7 (anti-CRP) was acquired from HyTest (Turku, Finland).

3.2.2. Gold surface biofunctionalisation procedures

The analytical parameters of the assay (sensitivity, reproducibility, specificity, reusability…) directly rely on the biofunctionalisation strategy since it determines the bioreceptors density, the target accessibility, the non-specific interactions and the robustness. Self-assembled monolayers (SAM) based on thiolated compounds are the most reported methodologies for chemical gold surface modifications. We evaluated two different SAMs approaches: carboxyl-SAM and nitrilotriacetic acid (NTA)-SAM.

3.2.2.1. Carboxyl-Self Assembled Monolayer

Covalent binding for bioreceptor immobilisation onto the sensor surface is the most reliable and robust strategy. The formation of a carboxylic SAM and the posterior activation by EDC/sulfo-NHS, allow the covalent binding of the viral antigens to the sensor surface. For the carboxyl SAM formation, the cleaned gold chips were immersed in a solution of MHDA 1 mM dissolved in ethanol overnight at RT in dark conditions. After rising and drying, the sensor chips were placed on the SPR instrument for *in-situ* covalent immobilisation of 20 μg·mL^{-1} of the viral antigens (N protein, S1 protein, RBD peptide or multiantigen (N+RBD (1:1)) to carboxyl groups through EDC/sulfo-NHS chemistry. Using Milli-Q as running buffer and a constant rate of 15 μL·min^{-1}, EDC/sulfo-NHS were dissolved in MES buffer 0.1 M pH 6 at a final concentration of 0.2/0.05 M respectively and injected over the sensor surface at a constant rate. Finally, ethanolamine 1M pH 8.5 was flowed for 2 min in order to block the non-reactive carboxylic groups (**Figure 3.4**). For optimal antigen immobilisation, viral antigens were immobilised in different buffers such as PBS (S1 and RBD peptide) and HEPES (N protein and multiantigen).

To avoid non-specific adsorptions from serum samples, after the immobilisation step, a blocking step was included by injecting 0.5 mg·mL $^{-1}$ of PLL-g-PEG dissolved in HEPES at a constant flow rate. Finally, the sensor chips were kept under a continuous flow of PBST+DS (PBS 10 mM + 0.5% Tween 20 + 2 mg·mL^{-1} DS) at 15 μL·min^{-1}.

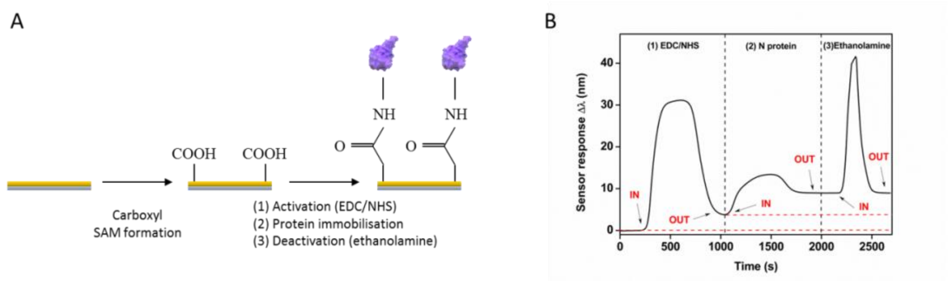

Figure 3.4. (A) Scheme of the covalent immobilisation of viral antigens through carboxyl-SAM and EDC/sulfo-NHS activation to the gold sensor chip. (B) A sensorgram of the three-step reaction (activation, immobilisation and deactivation) of N protein is also shown.

3.2.2.2. NTA-Self Assembled Monolayer

The addition of 6 histidine tags (His-tag) is a common and highly sensitive method for the purification of recombinant proteins. This approach is based on chelation chemistry. The use of NTA-Nickle (Ni) columns enables the purification of protains containing His-tags. NTA-Ni strategy can also be easily applied to immobilise His-tagged proteins on the gold sensor surface[138]. For the NTA -SAM formation, the cleaned gold chips were immersed in a solution of $HS\text{-}(CH_2)_{11}\text{-}EG_3\text{-}NTA$ 1 mM dissolved in ethanol overnight at RT in dark conditions. After rising and drying, the sensor chips were placed on the SPR instrument for *in-situ* immobilisation of the viral proteins to NTA groups through nickel activation. Using Milli-Q as running buffer at a constant rate of 15 µL·min^{-1}, 600 µM $NiCl_2$ dissolved in HEPES was flowed over the sensor surface and followed by a solution of 20 µg·mL^{-1} of viral antigens also dissolved in HEPES 10 mM (**Figure 3.5**).

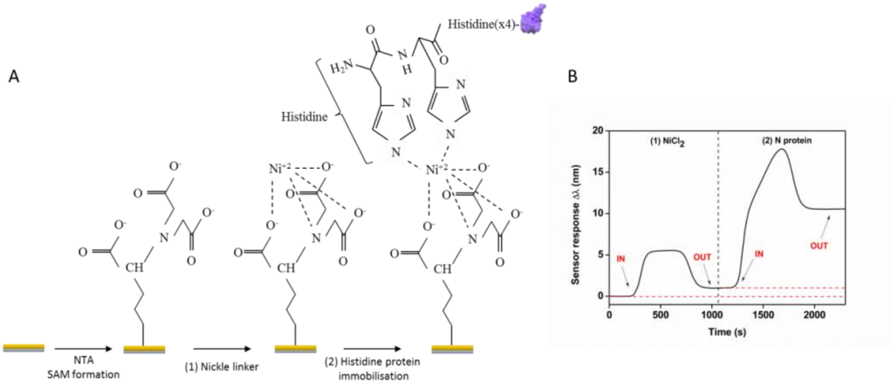

Figure 3.5. (A) Scheme of the immobilisation of viral antigens through NTA-SAM and $NiCl_2$ activation to the gold sensor chip. (B) A sensorgram of the two-step reaction (activation and immobilisation) of N protein is also shown.

3.2.3. Antibody detection biosensor assays

For the serological biosensor assay, polyclonal antibodies were used since they can mimic the pool of antibodies with different antigen affinities produced by a host individual after infection. The experiments were performed with polyclonal antibodies, pAb-N, pAb-S1 and pAb-RBD, specific for N protein, S1 subunit and the RBD domain, respectively, and with the first WHO International Standard Anti-SARS-CoV-2 human immunoglobulin. Real-time sensorgrams of the antibodies (100 µL) were obtained in all the cases, monitoring the specific binding in each case (shift in the position of the resonance peak (Δλ, nm) to higher wavelengths). For single-antigen gold sensor chips, calibration curves were obtained by injecting different concentrations of the corresponding specific antibody (ranging from100 ng·mL^{-1} to 10 µg·mL^{-1}) in standard buffer (PBST+DS) or in commercial serum 10% diluted. For the RBD/N sensor chips, several mixtures of pAb-RBD and pAb-N antibodies (ratio 1:1) (from 100 ng·mL^{-1} to 10 µg·mL^{-1}) were spiked in diluted serum and evaluated.

Calibration curves from the first WHO-approved standard for serology assays were obtained by assessing several concentrations of binding antibody units (BAU) (ranging from 1.25 to 500 BAU·mL^{-1}) in standard buffer (PBST+DS) or in commercial serum diluted to 10 % on the RBD/N co-immobilised sensor chip (stock solution 1000 BAU·mL^{-1}. All the antibody solutions were injected over the sensor chip at a constant flow of 15 µL·min^{-1}. In all the cases, antigen-antibody interaction was disrupted by injecting a 20 mM NaOH regeneration solution for 1 min at a constant flow rate.

3.2.4. Data analysis

Biosensor data were analyzed and processed using Origin 8.0 software (OriginLab Northampton, MA). Data and statistical analysis (Kruskal-Wallis, correlation, etc) were performed using Graphpad Prism (Graphpad Software, Inc., California, US). The mean sensor response ($\Delta\lambda$) and its standard deviation (SD) were plotted as a function of the polyclonal antibodies concentration to obtain calibration curves fitted to a linear regression model (**Equation 3.1**).

$$y = mX + b \tag{3.1}$$

where y is the sensor response, X is the concentration of polyclonal antibody, m is the slope of the linear regression curve and b is the intercept. The experimental LOD was determined as three times the SD of the wavelength shift obtained from a blank signal using only the running buffer. The coefficients of variation were obtained as the ratio of the standard deviation of the mean, expressed in percentages (% CV).

The differences between groups were analyzed with the Kruskal-Wallis test, considering a p-value < 0.05 to be statistically significant. The correlation between immune response and clinical severity was analyzed by the non-parametric Spearman test considering p-value < 0.05. Threshold values (cut-off values) to determine positive samples were calculated from the mean + 2SD of control negative samples. A value < 0.9xMean +2SD was considered negative; a value > 1.1xMean + 2SD as positive; and between 0.9 - 1.1xMean + 2SD as indeterminate. Threshold values and test results are described in **Table 3.2**.

Table 3.2. Threshold calculation from negative sample signals

TS calculation (Mean + 2SD)	Result
< 0.179	Negative
0.179 – 0.219	Indeterminate
> 0.219	Positive

The diagnostic sensitivity (SE), diagnostic specificity (SP), positive predictive value (PPV) and negative predictive value (NPV) were obtained from the number of false positives (FP), false negatives (FN), true positives (TP) and true negatives (TN) (**Equations 3.2-3.5**).

$$SE = \frac{TP}{TP+FN} \tag{3.2}$$

$$SP = \frac{TN}{TN+FP} \tag{3.3}$$

$$PPV = \frac{TP}{FP+TP} \tag{3.4}$$

$$NPV = \frac{TN}{FN+TN} \tag{3.5}$$

3.2.5. Clinical serum samples

A total of 125 clinical samples were collected from two hospitals in Barcelona (Spain) in three different batches. Two batches were provided by Vall d'Hebron University Hospital (VH.1 n=15, and VH.2 n=70), and a third batch was provided by the Clinic Hospital of Barcelona (CH.1 n=40). Negative samples were collected pre-pandemic in 2016. Positive samples were confirmed by PCR and other serological methodologies depending on the hospital (ELISA, CLIA or LFA). Positive samples from Clinic Hospital (CH.1) were stratified according to the patients severity and symptomatology: mild (symptomatic with no hospitalization), moderate (required hospital admission), and severe (required ICU admission). Serum samples were stored at a local at -80^{o} C until analysis. Clinical serum samples information is summarised in **Table 3.3**.

Table 3.3. COVID-19 clinical samples classification/characterization.

	Total	Positive*	Negative	Characterisation
Vall d'Hebron Hospital (VH)	85	60	25	**VH.1** (n=15) ELISA (15/15) LFA (15/15)
				VH.2 (n=70) CLIA (50/70)
Clinic Hospital (CH)	40	40	0	**CH.1** (n=40) LFA (40/40)
				mild (n=14) *moderate* (n=14) *severe* (n=12)
Total	125	100	25	

*Samples from patients with a positive PCR

3.3. Design, optimisation and analytical performance of the anti-SARS-CoV-2 biosensor assay

In the case of COVID-19 serological assays, key aspects to maximize both specificity and sensitivity are the biofunctionalisation approach and the viral antigen used for the detection of the antibodies. The N protein and S protein (specifically the S1 subunit or the RBD peptide) are highly specific targets[119,123,139,140]. Thus, we have evaluated two SAM functionalisation strategies employing the N, the S1 and the RBD viral antigens in order to capture the antibodies generated by the host.

3.3.1. Comparison of the SARS-COV-2 antigens immobilisation protocols

In **section 3.2.2.**, two different gold chemical modifications based on SAM were described. One of the approaches was based on the covalent immobilisation of the virals antigens through carboxyl-SAMs and EDC/sulfo-NHS chemistry. This strategy is one of the most employed in plasmonic biosensors for bioreceptor immobilisation. On the other hand, a NTA-SAMs approach was carried out taking advantage of the His-tags added to the viral antigens for the supplier for their purification. Both strategies were compared in terms of sensitivity, reusability and rejection of non-specific adsorptions in order to select the most robust and reliable strategy for COVID-19 serological biosensor assays.

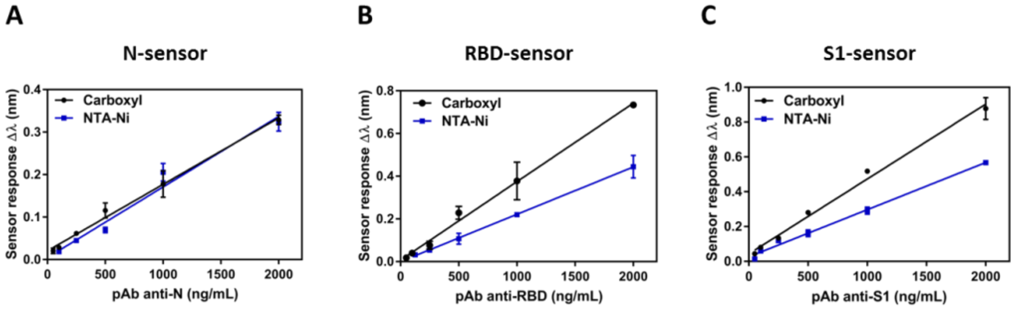

Figure 3.6. Self-assembled monolayers comparison. Calibration curves were obtained from (A) N-sensor (B) RBD-sensor and (C) S1-sensor on modified gold surfaces with carboxyl (COOH) (black line) and NTA-SAMs (blue line).

For each viral antigen (N, S1 proteins and RBD domain), a calibration curve showing the sensor signal as a function of different concentrations of p-Ab against the corresponding bioreceptor were analysed. **Figure 3.6** shows these calibrations cruve for the two biofunctionalisation strategies by coupling different viral antigen. The limit of detection achieved for each viral antigen was: for N protein (Carboxyl) LOD = 31.95 ng·mL^{-1}; (NTA) LOD = 30.08 ng·mL^{-1}, for RBD peptide (Carboxyl) LOD = 13.60 ng·mL^{-1}; (NTA) LOD = 22.52 ng·mL^{-1} and for S1 subunit (Carboxyl) LOD = 11.62 ng·mL^{-1}; (NTA) LOD = 18.46 ng·mL^{-1}. The sensitivity was similar or slightly better for the carboxyl strategy in all cases, reflecting LOD in the same order (**Figure 3.6**).

The reusability of the biosensor was also evaluated depending on the SAM condition. **Figure 3.7** shows the sensor signal corresponding to the recognition of 500 ng·mL^{-1} S1 p-Abs after succesive cycles of regeneration with 20 mM NaOH on carboxyl-SAMs. The NTA-based strategy utilised chelation chemistry through the nickle metal ion to attach the His-tag of the viral antigen. This interaction is mainly electrostatic, generating a binding more sensitive to the regeneration step. Otherwise, using carboxyl-SAM, the viral receptors were covalently attached to the sensor surface, creating a stronger and more stable bond. However, both sensor surfaces could be reused 15-20 times without altering or modifying the immobilised viral proteins and assay performance.

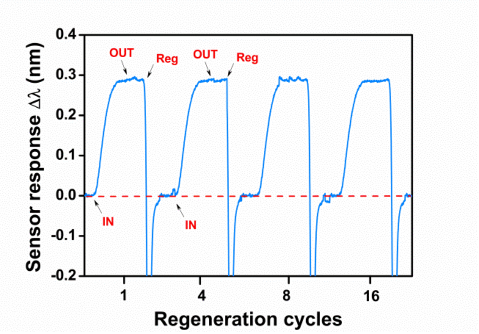

Figure 3.7. Detection-regeneration cycles after consecutive recognition of S1 p-Abs (500 ng·mL^{-1}) with the immobilised viral antigen and subsequent surface regeneration (Reg) with NaOH 20 mM.

In addition to sensitivity and reusability, non-specific binding interactions were also evaluated to sort out the most adequate approach.

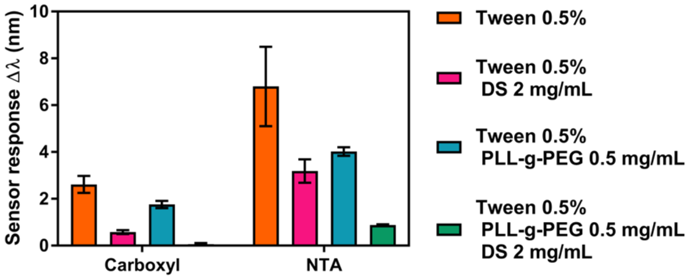

Figure 3.8. Non-specific adsorptions in carboxyl- and NTA-based SAMs due to serum matrix.

In order to apply the described methodologies to the analysis of patient's serum samples, we decided to test a combination of blocking agents including PLL-g-PEG and detergents (Tween 20 and DS). These blocking agents are reported to reduce non-specific interactions from serum in plasmonic devices[100]. For this study, PLL-g-PEG was immobilised on the sensor surface after viral antigens attachment and detergents were incorporated in the running buffer. Then, samples of 10 % diluted serum were flowed over the sensor surface. We tested four blocking conditions and, in all cases, the non-specific interactions due to the serum samples were lower in the carboxyl-based SAM (**Figure 3.8**). The absence of non-specific adsorptions from serum matrix was only observed on the carboxyl surface when a combination of all the blocking agents (PLL-g-PEG, Tween 20 and DS) was employed.

Comparison between NTA-based and carboxyl-based SAMs showed slight differences in terms of sensitivity, reusability and antifouling properties. However, we selected the covalent binding approach for the development of the quantitative detection of anti-SARS-CoV-2 antibodies. Covalent strategy is a simple, robust and well-know strategy which has given the best results in surface blocking against serum. In addition, carboxyl-based strategy does not depend on the presence of the His-tag on the bioreceptors for immobilisation.

3.3.2. Analytical parameters: sensitivity, specificity, reproducibility

To evaluate the performance of the biosensor, we perform calibration curves for three different biofunctionalised surfaces (N, RBD and S1) (**Figure 3.9)**. In all cases, the sensor signal increases as the polyclonal antibody concentrations increased. Thus, a direct and linear relationship between the pAb concentration and the sensor signal was observed, being possible to determine the limit of detection: 45.6 ng·mL^{-1} for anti-N (R^2=0.994), 19.9 ng·mL^{-1} for anti-RBD (R^2=0.992), and 12.42 ng·mL^{-1} (R^2=0.985) for anti-S1, respectively. Considering that the clinical concentration of antibodies in serum from COVID-19 patients is in the range of µg·mL^{-1}[141], the plasmonic biosensor device provides enough analytical sensitivity for COVID-19 serological testing with the all three sensor chips.

To guarantee the absence of non-specific interactions of antibodies with the sensor chip surface, the specificity of the assay was assessed. As we can observe in **Figure 3.9**, neither polyclonal antibodies against other viral antigens nor a SARS-CoV-2 non-related antibody (anti-CRP) interacted with the antigen surface. These results confirm the absence of cross-reactivity, observing with the biosensor only the specific antigen-antibody interactions.

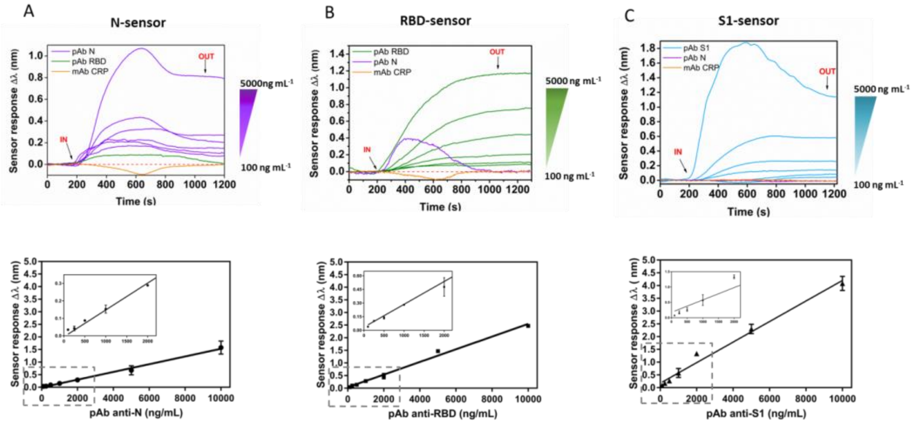

Figure 3.9. Real-time sensorgrams and calibration curve in standard buffer conditions for different antibody concentrations over an (A) N-coated sensor chip, (B) RBD-coated sensor chip and (B) S1-coated sensor. Each signal corresponds to the mean ± SD of triplicate measurements. Non-specific antibodies were measured at a concentration of 2 μg·mL^{-1}.

In order to apply the biosensor methodology to the analysis of clinical samples, the performance of the assays was evaluated with serum diluted at 10%. The good sensitivity of the biosensor assay (LOD in the ng·mL^{-1}) and the clinical range in the μg·mL^{-1} level ensure the detectability despite the dilution. The limit of detection obtained for the N-coated sensor was twice as higher than in standard buffer conditions (from 45.6 ng·mL^{-1} to 86 ng·mL^{-1}) (R^2=0.901), which might indicate antigen-antibody hindrance from the serum matrix. For RBD and S1-coated sensors, the LOD remained very similar to those obtained in standard buffer conditions, 22.1 ng·mL^{-1} (R^2=0.999) for RBD and 15.4 ng·mL^{-1} (R^2=0.996) for S1, respectively. In these cases, the serum did not affect the interaction antigen-antibody.

The reproducibility of the biosensor assays in serum dilution was analyzed through the inter-assay variability expressed as CV % (**Table 3.4**). The values obtained for N-protein and RBD-domain were below the maximum variability recommended for clinical analysis (15%)[142], confirming the good reproducibility and suitability of these serological assays.

Table 3.4. Inter-assay variability for diluted serum (10%) calibration curves (CC)

Viral antigen	Parameter	CC1	CC2	CC3	Mean±SD	CV (%)

N	**LOD (ng·mL^{-1})**	70.67	84.21	86.02	80.3 ± 8.39	10
RBD	**LOD (ng·mL^{-1})**	26.66	22.14	22.98	23.9 ± 2.40	10
S1	**LOD (ng·mL^{-1})**	15.37	16.13	18.26	16.59±1.49	9
RBD + N	**LOD (ng·mL^{-1})**	11.09	13.98	13.18	12.7 ± 1.49	12

3.3.3. Preliminary real samples assessment

The excellent sensitivity and reproducibility for the analysis in serum described above indicate that the RDB and S1 are promising viral antigens for the development of a serological biosensor assay. However, for a most exhaustive and rigorous optimisation of the serological assay, the three antigen-based assays were evaluated with real serum samples. In addition, a novel assay based on a multireceptor approach was designed. This multiabioreceptor consists of the combination of both N and RBD viral antigens on the sensor surface to capture antibodies targeting both proteins.

We first evaluated a set of 15 clinical serum samples (VH.1: 10 COVID-19 positive samples and 5 negative samples). The samples were analyzed with N-coated, S1-coated, RBD-coated and multireceptors -coated sensor chips and statistical comparison of the four serological biosensor assays was carried out. As can be observed in **Figure 3.10**, the N-and S1-based biosensor assays showed poor differentiation between sample groups, not being statistically significant ($p > 0.9999$). RBD-based assay performed better as the p-value ($p=0.0053$) indicates statistical significance for the discrimination between positive and negative samples. The multi-receptor sensor capture both N and RBD antibodies, revealing higher responses and discriminating anti-SARS-CoV-2 positive samples from negative ones with the most relevant statistical significance ($p=0.0002$), notably improving the performance of the individual assays.

This result is in concordance with the respective calibration curves (**Figure 3.10 and Table 3.4**) and the better sensitivity and detectability levels reached with the multireceptor-based biosensor assay, which reported a LOD of 12.7 ng·mL^{-1}($R^2=0.997$), a better LOD than when using the receptor antigens individually. The reproducibility study, which was done for viral antigens receptors individually, was also performed for the multireceptor (**Table 3.4**) showing CV values also below 15% and supporting the excellent reproducibility of the biosensor assay and the ability of the multireceptor format for SARS-CoV-2 serological biosensor test.

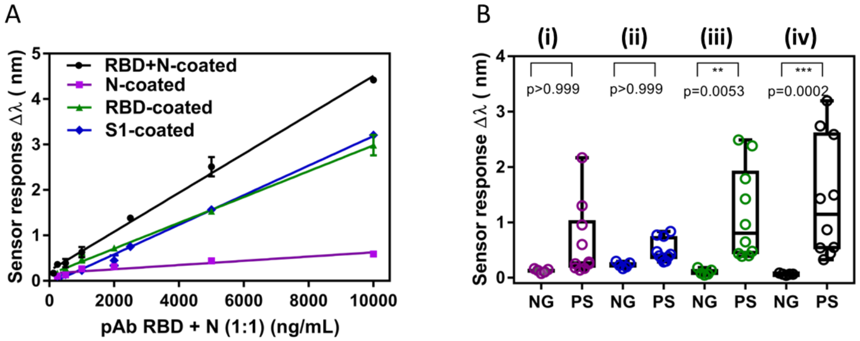

Figure 3.10. A) Calibration curves in 10% diluted commercial serum using four different biofunctionalised sensor surfaces (N, RBD, S1 and RBD+N). Sensor response represents the mean ± SD of three measurements. B) Statistical comparison between the positive (PS) and negative (NG) clinical samples: (i) N-coated sensor chips; (ii) S1-coated sensor chip; (iii)RBD-coated sensor chips; (iv) RBD+N –coated sensor chip. Kurskal-Wallis test.

3.3.4. Evaluation of the WHO international standard

During the pandemic, the WHO launched the first WHO International Standard for Anti-SARS-CoV-2 immunoglobulin. It is a useful tool to reach a consensus in the reading of serological assays, facilitating the interpretation of the results independently of the test. This WHO International Standard allows the expression of the Ig concentration in arbitrary units called Binding Antibody Units (BAU· mL^{-1}). It was obtained from pooled plasma from individuals recovered from SARS-CoV-2 infection with an inticial anti-SARS-Cov-2 antibody concentration of 1000 BAU·mL^{-1}.

To prove the quantification performance of the SPR serological biosensor and ease its comparison with other serology assays, we carried out a calibration curve with the first WHO International Standard for Anti-SARS-CoV-2 immunoglobulin (stock concentration 1000 BAU·mL^{-1}). Calibration curves were generated in both standard buffer conditions

(PBST+DS) and 10% diluted serum, measuring antibody concentrations from 500 BAU·mL^{-1} to 2.5 BAU·mL^{-1} (minimum concentration that triggered a sensor response) over the RBD+N-sensor surface. **Figure 3.11A** shows the sensorgram of the increasing direct relationship between the sensor signal and the International Standard concentration, increasing proportionally. As we can observe in Figure **3.11B**, no differences between the calibration curves regardless of the buffer conditions (standard and diluted serum), achieving similar limits of detection, 0.098 BAU·mL^{-1} for PBST+DS and 0.137 BAU·mL^{-1} for diluted serum, respectively. The WHO International Standard also included a negative standard from non-infected individuals. **Figure 3.11** shows no sensor signal independly of the negative standard concentration (from 500 to 2.5 BAU·mL^{-1}). These results confirmed the good performance of the biosensor assay, being specific for anti-SARS-CoV-2 antibodies and avoiding non-specific interaction from sera of non-infected patients.

The novelty of the International Standard, the pressure on clinical laboratories due to the excess of samples during the pandemic and the appearance of new qualitative serological techniques make it difficult to analyze and compare these results with other methodologies. However, in this thesis, serum samples from patients were analyzed and their immunoglobulin concentration was expressed by applying the standardised calibration curve in order to be able to perform the corresponding studies in the future.

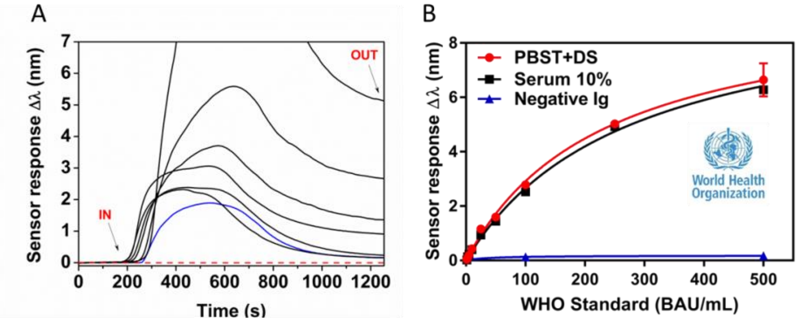

Figure 3.11. (A) Real-time sensorgram using the WHO Standard in 10 % diluted serum. Black lines correspond to standard concentrations ranging from 250 BAU·mL^{-1} to 2.5 BAU·mL^{-1}. The blue line corresponds to the negative standard at 500 BAU·mL^{-1} (B) Calibration curves obtained using the WHO Standard anti-SARS-CoV-2 immunoglobulin in PBST+DS and 10% diluted commercial serum over the RBD+N-coated sensor. Biosensor response represents the mean ± SD of three evaluations.

3.3.5. SPR biosensor performance compared to conventional serological techniques

As we commented previously, ELISA and LFA are the most established methodologies used in clinical practice for the serological analysis realted to COVID-19. In order to compare the SPR methodology with the conventional techniques, a set of 15 clinical serum samples (VH.1) was evaluated. We have compared qualitatively the RBD/N-based serological biosensor assay to standard ELISA Euroimmun (Lübeck, Germany) and two different commercial LFA (Wondfo Biotech (Luogang, China) and FaStep (Hangzhou, China)) employed in clinics. Results are summarised in **Figure 3.12**, where quantitative results from SPR, semi-quantitative results from ELISA and qualitative results from commercial LFAs are shown. Additionally, detection results confirming the positive o negative COVID-19 infection are also shown.

Although ELISA provides semi-quantitative information, we observed a significant correlation between the cut-off index (COI) (arbitrary ELISA values related to antibody concentration) and the sensor response obtained with the SPR biosensor. For example, samples number 7 and 8 reported the highest SPR signals ($\Delta\lambda \approx 2.5$nm) and also the highest ELISA values (COI>9). Similar correlation can be observed for low concentrated samples such as sample number 2, which reported a SPR signal of $\Delta\lambda \approx 0.3$ nm and ELISA value of COI ≈ 3. The identification of positive samples by the SPR serological assay completely matched the outcomes provided by the commercial ELISA assay. The result reflects the good accuracy of the plasmonic biosensor assay, which has achieved excellent diagnostic sensitivity and specificity concurring ELISA performance. Otherwise, LFA tests failed to identify some of those COVID-19 positive samples. Commercial FaStep tests reported an incorrect result (false negative) for positive COVID-19 samples number 1, 3 and 4 and Wondfo tests failed to identify sample number 1. In addition, FaStep test identified as positive one negative sample (negative COVID sample number 1), manifesting a false positive detection result. Although LFA assays provide rapid results in less than 15 min, the above-described results demonstrate their limited diagnostic sensitivity and specificity, reporting false detection outcomes.

The SPR biosensor could establish itself as a promising candidate for the serological assay of COVID-19 in clinical practice. This biosensor offers significant advantages over conventional ELISA and LFA methodologies, exhibiting similar diagnostic sensitivity and specificity to ELISA and comparable speed to LFA assays. In addition, SPR can provide quantitative results related to anti-SARS-CoV-2 antibody concentrations in serum samples.

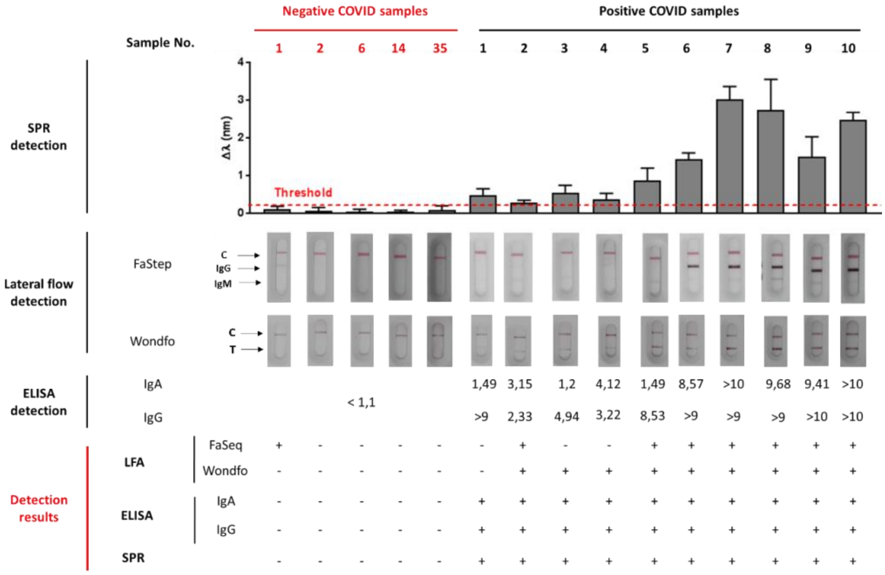

Figure 3.12. Comparison of results of different COVID-19 serological assays. COVID-19 patients were firstly tested by PCR-based methodolies. LFA tests were considered positive after the appearance of a coloured band with regular or strong intensity in the IgG and/or IgM line, and negative for very weak or not coloured bands. ELISA tests were considered positive for COI > 1.1of IgG and/or IgA. SPR biosensor assays were considered positive for samples above the set threshold (red dotted line $\Delta\lambda = 0.219$). The detection results show the numbers of positive (+) and negative (-) samples for each serological technique.

3.3.6. Clinical validation of the SPR-based COVID-19 serology

The results achieved with the preliminary clinical evaluation triggered a larger clinical validation study. A total of 120 clinical samples were analyzed (100 COVID-19 positive clinical and 20 negative samples). The serum samples were evaluated by the SPR biosensor as well as different commercial techniques such as ELISA, CLIA and LFA (**Table 3.5**).

The SPR results are shown in **Figure 3.13.**, which reflects the distribution of the sensor response obtained by the SPR biosensor assay for each of the samples. Positive samples showed a variable distribution of Ig levels which might go from a few BAU·mL^{-1} to thousands of BAU·mL^{-1}. Considering the threshold (0.219 nm), all the 20 negative samples studied gave signals below this value and only one of the PCR positive samples was considered not positive (indeterminate).

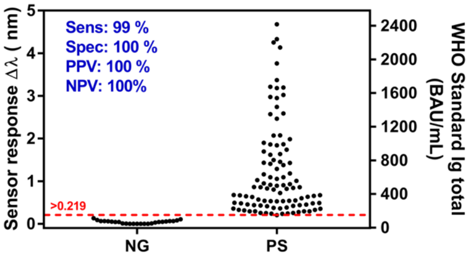

Figure 3.13. Sensor response distribution of 100 COVID-19 positive (PS) and 20 negatives (NG) clinical samples. Total Ig concentration calculated from the WHO Standard calibration curve is shown on the right axis. Sensitivity, specificity, PPV, NPV and threshold are also shown.

The SPR-based serological test shows sensitivity and PPV of 99% and 100%, respectively, and specificity and NPV of 100% both. The SPR biosensor results were compared to the techniques employed in the Vall D'Hebron and Clinic Hospitals. **Table 3.5** summarizes the diagnostic results obtained for the clinical samples when analyzed by ELISA (Euroimmun,), CLIA (Liaison, (DiaSorin, Italy) and Elecsys (Roche Diagnostics, US)), LFAs (Wondfo, FaStep, Vazyme (Vazymebiotech Co, Nanjing, China) and Quick Profile (Quick Profile, USA)) and SPR biosensor.

LFAs, regardless of the provider, were the serological methodologies that reported the most false negatives or indeterminate results. They provided up to 50 % of failed results in batch CH.1 batch, demonstrating their limited sensitivity. On the other hand, CLIA and ELISA techniques, as well as SPR, reported a few false or indeterminate analyses, without ever decreasing 92 % sensivity (CLIA Liaison in batch VH.2).

Beyond the results shown in **Table 3.5**, commercial LFAs manufacturers reported sensitivities between 90-95% and specificities between 97-99.8%. The manufacturers of CLIA and ELISA reported sensitivities higher than 95%, achieving values of 100% in many cases, and specificities between 97-99.8%. These results confirm the outperformance of the plasmonic biosensor providing highly precise detection of anti-SARS-CoV-2 antibodies in a rapid manner (15 min) which is the same as with LFA preserving a diagnostic sensitivity, specificity and reliability equivalent to ELISA and CLIA.

Table 3.5. Summary of COVID-19 clinical samples validation

VH.1	***PCR***	***SPR***	***ELISA Euroimmun***	***LFA Wondfo***	***LFA FaStep***
Positive	10	10	10	9	7
Indeterminate	0	0	0	0	2
Negative	0	0	0	1	1
VH.2	***PCR***	***SPR***	***CLIA Liaison***	***CLIA Elecsys***	
Positive	50	49	46	48	
Indeterminate	0	1	4	0	
Negative	0	0	0	2	
CH.1	***PCR***	***SPR***	***LFA Vazyme***	***LFA Quick Profile***	
Positive	40	40	18	18	
Indeterminate	0	0	4	4	
Negative	0	0	18	18	

3.3.7. Relationship between humoral immunity in SARS-CoV-2 infection and clinical severity

Quantification of the humoral response in patients with COVID-19 may be a useful tool for understanding the human body's response to the virus. In addition, a possible association between antibody production and the severity of patients' symptoms would provide a more accurate prognosis of the disease.

As preliminary study to decipher a possible correlation between the severity of symptomatology and the concentration of SARS-CoV-2 antibodies in sera was carried out. A total of 40 serum samples (CH.1) confirmed by PCR and LFA and stratified according to severity and symptomatology of the patients (mild (n=14), moderate (n=14) and severe (n=12)) were evaluated.

Plasmonic biosensors detected immunoglobulins in all three conditions, showing higher antibody concentrations in the moderate and severe groups *versus* the mild ones. However, the levels of immunoglobulins did not differ statistically between groups (0.87[0.36-3.02], 1.44[0.50-1.83] and 1.07[0.92-1.80]]) p=0.548 (**Figure 3.14**). Correlation analysis neither reported a relationship between levels of antibodies and severity of COVID-19 outcome (r=0.175 and p=0.279).

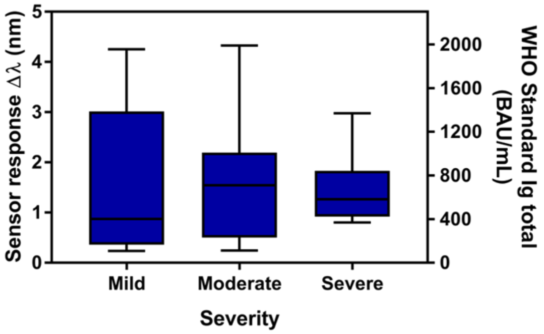

Figure 3.14. Correlation outcome severity *vs* antibodies level. Sensor signal of 40 COVID-19 positive samples from individuals with different degrees of severity (mild, moderate and severe symptoms). Spearman test (p-value=0.279) and Kruskal-Wallis test (p-value=0.548). Total Ig concentration calculated from the WHO Standard calibration curve is shown on the right axis

The plasmonic biosensor provides controvertible information regarding a possible correlation between the severity outcome of COVID-19 patients and the SARS-CoV-2 antibodies concentration in serum. In the first stages of the pandemic, other publications neither were able to confirm this association[143–145]. However, as it occurs after Middle East Respiratory Syndrome (MERS) virus infection, there is a strong relationship between acquired immunity and symptomatology gravity after SARS-CoV-2 infection[146–149]. Our preliminary study presents limitations as the number of samples, the time from symptoms onset until samples collection (more than 3 months for extremely severe patients), and other factors that could hinder the confirmation of the relationship.

3.4. Conclusions

The emergence of a novel coronavirus, which has caused millions of deaths together with social and economic repercussions, brought to light the necessity to develop diagnosis technologies for a rapid and direct diagnosis of COVID-19. In this Chapter, a serological assay using a plasmonic biosensor has been fully developed and validated. The SPR technology can detect and quantify the total amount of anti-SARS-CoV-2 antibodies in serum in a rapid – less than 15 min – manner. During the optimisation process, we explored different strategies depending on the viral antigen selected to identify SARS-CoV-2 immunoglobulins, being a multireceptor strategy (combination of N protein and RBD peptide) the most sensitive and specific approach. An in-depth optimisation of the serological assay allowed outstanding limits of detection of anti-SARS-CoV-2 antibodies in serum of 12.7 $ng \cdot mL^{-1}$, and excellent discrimination between positive and negative samples (p-value=0.0005). To provide quantitative SPR biosensor results able to be compared with other serological techniques, we have implemented the serological biosensor assay with the first WHO International nti-SARS-CoV-2 Immunoglobulin Standard.

The biosensor methodology was validated with 100 COVID-19 positive and 20 negative pre-pandemic samples (n=120) from two Spanish Hospitals. The results showed an excellent diagnostic sensitivity of 99% and diagnostic specificity of 100%, outperforming established serological techniques like ELISA, CLIA and rapid tests.

A preliminary study of the correlation between the humoral immune response and the clinical severity outcome was also performed although a larger cohort would be required to obtain more irrefutable results.

The described results demonstrate that label-free plasmonic biosensors are precise, robust, and easy-to-use tools, providing a COVID-19 serology analysis rapidly and reliable. Additionally, the possibilities to integrate and miniaturize the biosensor platform in a user-friendly point-of-care pave the way to a smooth technological transfer with great perspectives in clinical practice.

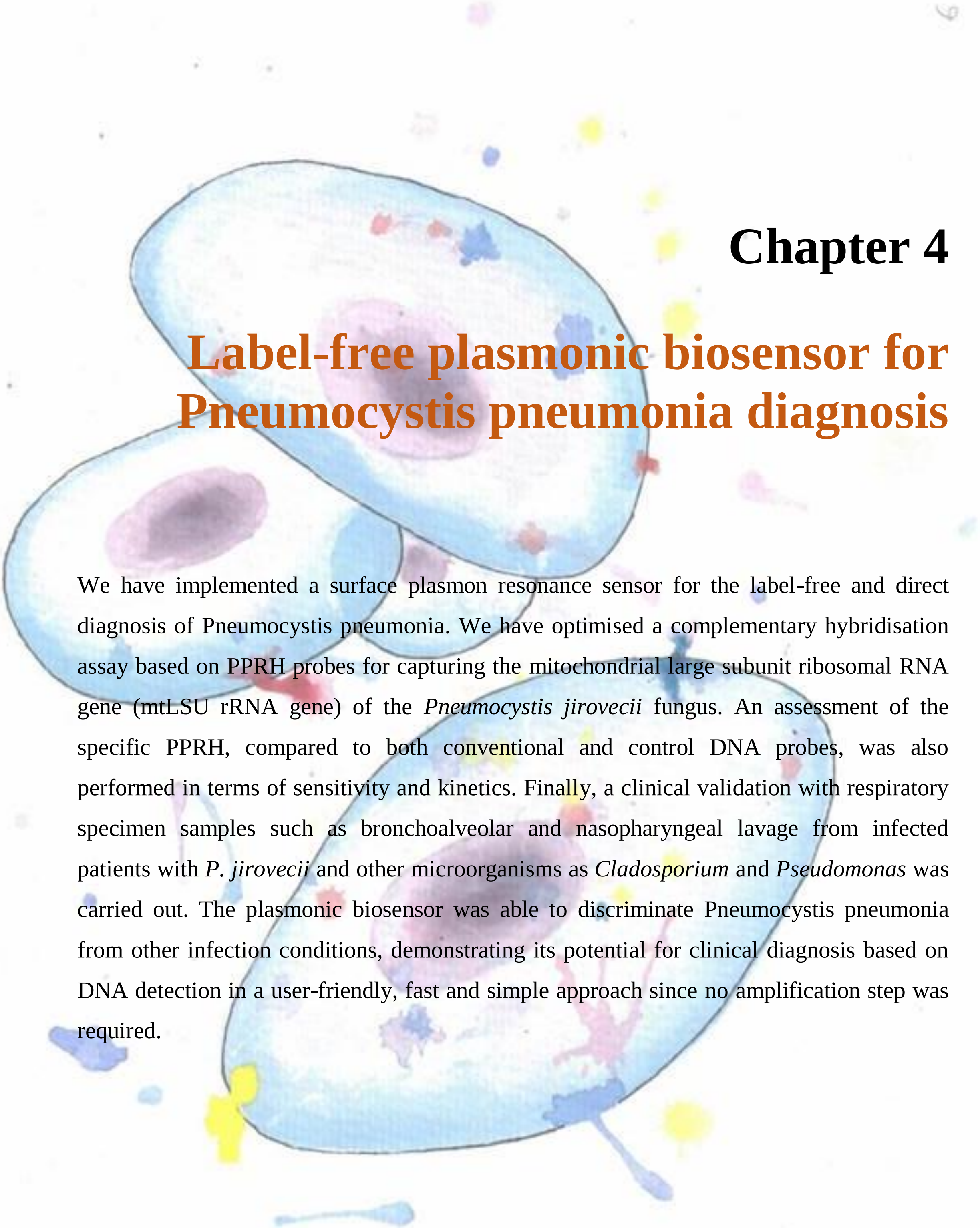

Chapter 4

Label-free plasmonic biosensor for Pneumocystis pneumonia diagnosis

We have implemented a surface plasmon resonance sensor for the label-free and direct diagnosis of Pneumocystis pneumonia. We have optimised a complementary hybridisation assay based on PPRH probes for capturing the mitochondrial large subunit ribosomal RNA gene (mtLSU rRNA gene) of the *Pneumocystis jirovecii* fungus. An assessment of the specific PPRH, compared to both conventional and control DNA probes, was also performed in terms of sensitivity and kinetics. Finally, a clinical validation with respiratory specimen samples such as bronchoalveolar and nasopharyngeal lavage from infected patients with *P. jirovecii* and other microorganisms as *Cladosporium* and *Pseudomonas* was carried out. The plasmonic biosensor was able to discriminate Pneumocystis pneumonia from other infection conditions, demonstrating its potential for clinical diagnosis based on DNA detection in a user-friendly, fast and simple approach since no amplification step was required.

4. Label-free palsmonic biosensor for Pneumocystis pneumonia diagnosis

4.1 Introduction

4.1.1. Pneumocystis pneumonia

Pneumocystis pneumonia (PcP) is an infectious respiratory disease caused by *Pneumocystis jirovecii* (**Figure 4.1**). This microorganism is a ubiquitous and opportunistic fungus that does not cause any problem in individuals with a functional immune system. Otherwise, PcP is one of the most serious and potentially fatal infections encountered in AIDS patients and it is becoming more common in non-HIV immunosuppressed patients due to malignancies such as haematological cancer, allogeneic organ transplantations and autoimmune diseases[150]. Epidemiologically, PcP is an important cause of morbidity and mortality worldwide with a mortality rate ranging between 11 and 53% in HIV-infected patients[151,152].

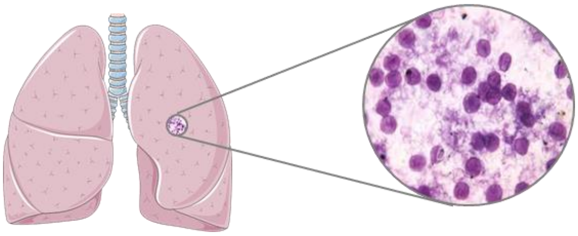

Figure 4.1. Pulmonary infection caused by *Pneumocystis jirovecii*.

The diagnosis of PcP continues to be challenging. The clinical presentation of PcP may differ from HIV-infected patients to other immunocompromised patients (Chest-X results, colonization rate, the burden of fungus), and there are no specific symptoms or signs (high fever, cough, and dyspnea)[153,154]. There is no global diagnosis approach to the initial management of patients with suspected PcP. Many physicians treat patients empirically, while others chase a decisive microbiological diagnosis[155].

4.1.2. Current methods for *P. jirovecii* detection

Clinical diagnosis of PcP relies on clinical (pulmonary auscultation) and radiological (Chest X-ray) analysis but confirmation requires microscopic visualization of the microorganism in stained respiratory specimens such as bronchoalveolar lavage (BAL) since *P.jirovecii* cannot be grown in vitro[151,153,154,156]. All the microscopic staining methods might lead to false-negative results[157]. To detect *P. jirovecii*, a serological assay might be performed for the identification of (1 → 3)-β-D-glucan in serum. (1 → 3)-β-D-glucan is a component of the cellular wall of *P. jirovecii* but it is also present in the cell wall of most fungi. Even though this technique is not specific to *P.jirovecii*, it is a highly sensitive test and could be used to obtain a most complete diagnosis of PcP[158].

PCR-based techniques have demonstrated high effectiveness to identify *P. jirovecii* in clinical respiratory specimens such as BAL, nasopharyngeal aspirates samples (NPA) and biopsy specimens, among others[157,159]. A comparison between PCR-based methodologies and a staining method (immunofluorescence) showed that PCR results were more sensitive and closer to the histological evidence, although the PCR sensitivity and specificity depend on the selected genes[160]. The most commonly employed gene for PcP diagnosis is the mitochondrial large subunit ribosomal RNA (mtLSU rRNA) gene[161], but many other sequences have been reported such as the major surface glycoprotein, internal transcribed spacers, thymidylate synthase, dihydrofolate reductase, heat-shock protein 70, among others[151,153,157]. An analytical comparison depending on the targeted sequence is challenging. Results from PCR-based techniques show high variation rates due to sample collection, DNA extraction methods and different analysis strategies[157]. The lack of standardization hinders the determination of a specific limit of detection but some publications consider $<10^3$ copies$\cdot$mL^{-1} as the clinical value for the diagnosis of Pneumocystis pneumonia[160,162]. Additionally, PCR-based methodologies require long turnaround times, trained personnel and precise instruments. Main advantages and drawbacks of the diagnostic techniques for PcP aresummarised in **Table 4.1.**

Table 4.1. Established methods for *P.jirovecii* diagnosis. Advantages and inconveniences

Methodology	Advantages	Drawbacks
Microscopy	✓ Specificity	X Depending on the P.jirovecci burden X Some patients cannot produce respiratory samples X False-negative results
(1 → 3)-β-D-glucan	✓ High sensitivity	X Fungi biomarker X No specific for *P.jirovecii*
PCR	✓ High sensitivity and specificity	X Time-consuming X Centralized and trained personnel

The rapid identification of suspected PcP patients could ease the prompt and most suitable selection of the treatment[163]. Although PCR is a well-established technique, new approaches have been developed to diagnose PcP in a fast, accurate and specific manner such as flow-cytometry[164]. Using optical biosensors, different strategies have been performed. A. L. Tomás *et al.* reported a serological biosensor assay for the detection of *P.jirovecii* immunoglobulins in sera from infected patients[165]. On the other hand, and based on DNA-gated nanomaterials and fluorescence spectroscopy were able to detect *P.jirovecii* mtLSU rRNA gene with a LOD of 1 nM without amplification steps[166]. Here, we propose a surface plasmon resonance biosensor based on PPRH probes for the detection of mtLSU rRNA gene as a competitive candidate for the diagnosis of this infectious disease.

4.2 Materials and methods

4.2.1. Chemicals

Organic solvents for sensor chip cleaning (acetone and ethanol) were purchased from Panreac (Barcelona, Spain). Buffer compounds, PBS 50 mM (50 mM phosphate buffer, 0.75 M NaCl, 2 mM ethylenediaminetetraacetic acid (EDTA), pH 7), 2.5 X SSC (Saline-sodium citrate buffer) (0.375 M NaCl, 0.0375 M sodium citrate, 2 mM EDTA, pH 7), diethylpyrocarbonate (DEPC) and formamide (FA) were purchased from Sigma-Aldrich (Steinheim, Germany). Bond-Breaker™ TCEP Solution was purchased from ThermoFisher (Massachusetts, US). Thiol-polyethylene glycols (SH–PEGs) with functional groups (amine ($–NH_2$), methyl ($–CH_3$) and carboxyl (–COOH)) were purchased from Laysan Bio (Alabama, US).

Buffers and other solutions for DNA detection were prepared using DEPC-H_2O (Milli-Q water incubated overnight with 0.1% DEPC and autoclaved for 1 h at 121° C). All solid plastic and glass materials were autoclaved for 1 h at 121° C.

4.2.2. DNA polypurines hairpin probes and nucleotide sequences

Oligonucleotide sequences listed in **Table 4.2** were synthesized by the group of Prof. R. Eritja from the Department of Chemical and Biomolecular Nanotechnology at the Institute of Advances Chemistry of Catalonia (IQAC), CSIC (Spain). Sequences were prepared on an Applied Biosystems 3400 (Applied Biosystems, California, US) synthesizer using controlled-pore supports (scale 1µM) according to the protocols of the manufacturer. Thermal UV denaturation and CD studies were carried out to assess the triplex structure.

The PPRHs were designed to carry two antiparallel polypurine sequences complementary to the pyrimidine region of the mtLSU rRNA gene to displace the ds-DNA and form the antiparallel triplex structure. All the DNA probes were modified with a T_{15} vertical spacer and a thiol group to ensure the biorecpetors immobilisation and a good accessibility of the target sequence.

Table 4.2. Nucleotide sequences employed in the Pneumocystis pneumonia biosensor

Name	Sequence
Triplex	5’Thiol-PolyT15-GACAAAGGGAAAG-TTTT-GAAAGGGAAACAGCCCAG 3’
Duplex	5’Thiol-PolyT15-GAAAGGGAAACAGCCCAG 3’
Control	5’Thiol-PolyT15-AGAGCAGAAAGGA-TTTT-

	GAAAGGGAAACAGCCCAG 3’
mtLSU gene	5′-CTGGGCTGTTTCCCTTTC-3′
Control gene	5′-TTCCGTGGCTGTTCTCCT-3′

4.2.3. PPRH immobilisation onto the gold sensor surface

For *in-situ* PPRH biofunctionalisation, clean gold sensor chips were biofunctionalised *via* thiol-gold chemistry. Using DEPC-H_2O as running buffer, a solution of 1 µM DNA probes combined with 1 µM CH_3–PEG–SH (ratio 1:1) diluted in PBS 50 mM was flowed over the sensor surface at a constant rate of 18 µL·min^{-1}. The immobilisation solution was previously incubated at 70 °C, 650 rpm for 20 min with 1 µM TCEP to reduce possible disulfide bonds. During the immobilisation process, thiolated bioreceptors and lateral spacers arrange themselves spontaneously into a so-called self-assembled monolayer (SAM).

4.2.4. mtLSU rRNA gene detection

Calibration curves in standard buffer conditions were performed by injecting different concentrations of the mtLSU rRNA analyte (5–200 nM) diluted in 2.5 X SSC buffer + 5% formamide (FA) over the SPR sensor device at a constant flow rate 18 µL·min^{-1}. 2.5 X SSC + 5 % FA was the running buffer.

In order to dissociate the hybrids and regenerate the sensor surface for furtherevaluations, a solution of NaOH 5 mM was injected for 60 s at the same rate of 18 µL·min^{-1}.

The calibration curve for the clinical validation of respiratory specimens was performed by flowing different concentrations of mtLSU rRNA analyte (50–1000 nM) dissolved in DEPC-H_2O at a constant flow rate of 18 µL·min^{-1} and employing as running buffer 2.5 X SSC + 5 % FA.

4.2.5. Pneumocystis pneumonia in real samples

Extracted DNA from bronchoalveolar lavage (BAL) and nasopharyngeal aspirates (NPA) from patients and synthesised DNA (fragments and pGEM-T Easy Vector System plasmids containing mtLSU rRNA sequence) were collected, treated or synthetized in the Group of Enrique J. Calderón at University Hospital Virgen del Rocío and the Institute of Biomedicine of Seville (IBiS) (Seville, Spain). Clinical samples were also validated by nested-PCR for the mtLSU rRNA gene or other fungi genes (e.g. gene oprl for *Pseudomonas aeruginosa*). Once collected, samples were stored at −80 °C until analysis.

4.2.6. Data Analysis

The sensor data were analyzed and processed using Origin 8.0 software (OriginLab, Massachusetts, US). Calibration curve fitting and statistical analysis were performed using Graphpad Prism (Graphpad Software 7, Inc., California, US). Calibration curves were obtained by plotting the mean sensor signal (Δλ) and standard deviation (SD) as a function of the mtLSU rRNA analyte concentration. The data were fitted to the following one-site specific binding equation (**Equation 4.1**):

$$y = \frac{Bmax + X}{Kd + X} \tag{4.1}$$

where *y* is the sensor response, *X* is the concentration of the target analyte, *Bmax* is the extrapolated maximum number of bioreceptors on the surface and *Kd* is the equilibrium binding constant, which corresponds to the mtLSU rRNA concentration needed to achieve half-maximum bioreceptors occupied at equilibrium.

The experimental LOD was determined as three times the SD of the sensor response obtained from a blank signal using only the running buffer. The coefficients of variation were obtained as the ratio of the standard deviation of the mean, expressed in percentages (% CV).

Statistical differences between clinical samples infected with different microorganisms were analysed with the non-parametric Kruskal-Wallis test, considering a $p\text{-value} < 0.05$ to be statistically significant.

4.3. Design and optimisation of the genomic biosensor assay and analytical performance

4.3.1. Optimisation of the PPRH probes layer

The optimisation of the bioreceptor layer is a key component in the development of optical biosensors. For nucleic acid-based sensors, the design and density of the bioreceptor and even the buffer solution can affect dramatically the capture of the target sequence[87].

Generally, the selected bioreceptor used for the development of genetic biosensors are based on conventional DNA probes composed of a linear sequence of nucleotide. In the last years, advanced DNA-based bioreceptors have been studied to enhance DNA analyte detection efficiency and increase the sensitivity of sensors. In our biosensor assay, we have employed PPRH probes for the detection of the mtLSU rRNA gene in ds-DNA. These probes are composed of two antiparallel polypurine sequences complementary to a polypirimidine sequence in the target gene, forming nucleic acid triplexes[167]. One polypurine sequence can recognise the complementary polypyrimidine sequences in ds-DNA through Watson-Crick bonds (WC track). The polypurine antiparallel sequence hybridises by reverse-Hoogsteen hydrogen interactions (RH track), generating the displacement of the ds-DNA and forming a triplex structure with the analyte sequence (**Figure 4.2**).

Due to the ability to create the triplex structures and the displacement of ds-DNA, PPRH probes have been gaining increasing attention in biosensing and gene inhibition applications[86,168]. Reported studies have shown marked improvement for the detection of nucleid acid analytes when using the triplex structure approach compared with the conventional duplex one (detection of miRNAs for cancer diagnosis[169] or Listeria innocua RNAs with predicted secondary structures[170,171]. More recently, the ability of PPRH probes for ds-DNA displacement was exploited for the development of a plasmonic biosensor for DNA methylation analysis[172].

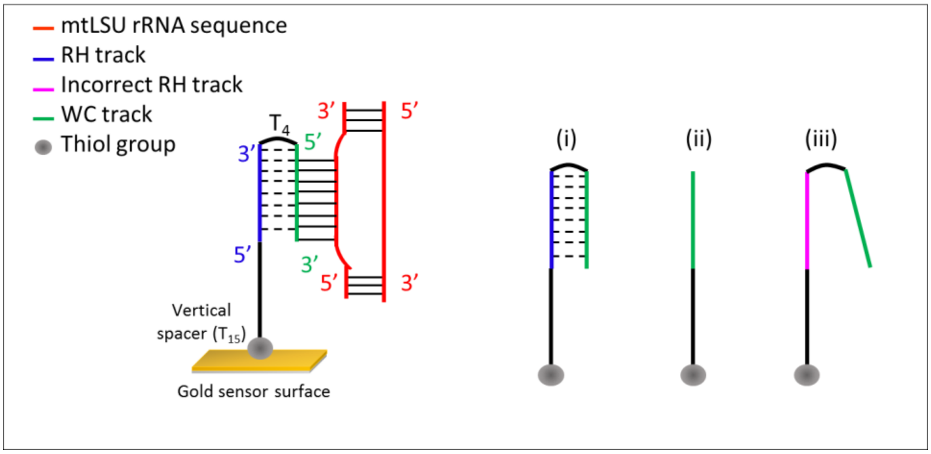

Figure 4.2. Schematic representation of the mtLSU rRNA gene capture using the PPRH probe, forming an antiparallel triplex structure. In addition, different bioreceptors employed in the SPR biosensor are shown: (i) PPRH probe, (ii) duplex probe, (iii) control PPRH probe.

Regarding the design, PPRH probes incorporate a thiol group for gold sensor immobilisation and a PolyT$_{15}$ to separate the recognition sequence from the sensor surface, easing the accessibility of the target sequence.

As a first step, we optimised the biosensor assay and evaluated the selectivity and efficiency of the PPRH probe for the detection of the mtLSU rRNA sequence by employing a single strand DNA (ss-DNA) of mtLSU gene. To study and control the density of the bioreceptors and, therefore, the target accessibility, different combinations of the PPRH probes and lateral spacers (SH-PEG-COOH, SH-PEG-NH$_2$ and SH-PEG-CH$_3$) where tested. These PEG might also avoid non-specific interactions from other sequences or complex matrices. In all cases, after the bioreceptor layer immobilisation, an evaluation of the sensor capability to capture mtLSU 100 nM was carried out (**Figure 4.3**).

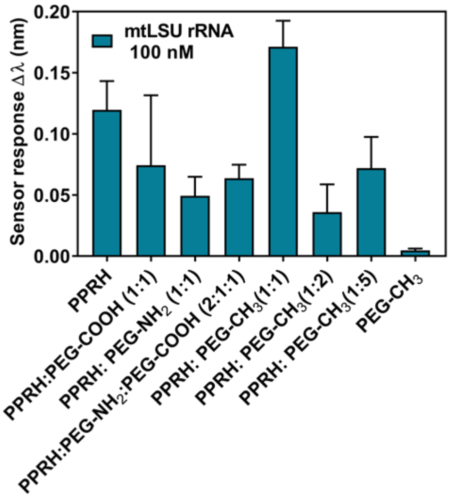

Figure 4.3. Effect of SAMs with different DNA probes and lateral spacer combinations on the capture of mtLSU rRNA gene 100 nM

As can be appreciated from **Figure 4.3**, monolayers containing only DNA probes without SH-PEGs showed a significant sensor response, whereas the negative control monolayer, containing only SH-PEG-CH$_3$, did not show any response to the target at 100 nM, corroborating the specificity of the PPRH probes for the target. DNA: PEG-CH$_3$ (1:1) monolayer showed the highest sensor response for the target, increasing the sensor performance by 40%. The presence of net groups such as methyl in the surface improved the sensor signal compared to a surface full of DNA probes. However, increasing concentrations of SH-PEG-CH$_3$ in the mixed monolayers decreased the signal, indicating that 1:1 ratio provided the appropriate lateral spacing for the target accessibility while maintaining an adequate concentration of the bioreceptor. Monolayers with charged functional groups (-NH$_2$ and -COOH) showed the lowest sensor response, decreasing by 60% and 40%, respectively. These results suggest that a monolayer with a net charge, such as the one provided by the methyl groups, did not affect the accessibility of the target DNA sequences, which are characterized by a negative charge. The introduction of charges in the PEG spacers dramatically affects the target accessibility and confirms that the presence of negative or positive charges in the monolayer can hinder the hybridisation due to repulsion forces. In addition, a combination of both charged PEGs (NH_2: COOH) at 1:1 ratio, did not offset the charge effect and it did not show a higher signal.

Regarding the buffer composition, the ionic strength of the employed solution might affect the hybridisation, as well as the use of several agents as formamide (FA) that reduce the melting temperature (the temperature corresponding to the midpoint in the transition from helix to the random coil) increasing the hybridisation efficiency[87]. Different SSC buffer concentrations and FA percentages were evaluated for the improvement of the capture and selectivity of the biosensor assay (**Figure 4.4**). Increasing the ionic strength of the buffer by using solutions with higher concentrations hindered the capture of the mtLSU gene, avoiding the hybridisation at elevated concentrations (**Figure 4.4A**). On the other hand, the addition of a certain percentage of FA (higher than 5 %) to the buffer, avoids non-specific interaction of the PPRH with the control sequence, which has the same GC% as mtLSU rRNA target, without compromising the capture of the mtLSU gene (**Figure 4.4B**). Thus, 2.5 X SSC buffer + 5% FA was selected as the optimised buffer for mtLSU rRNA gene detection.

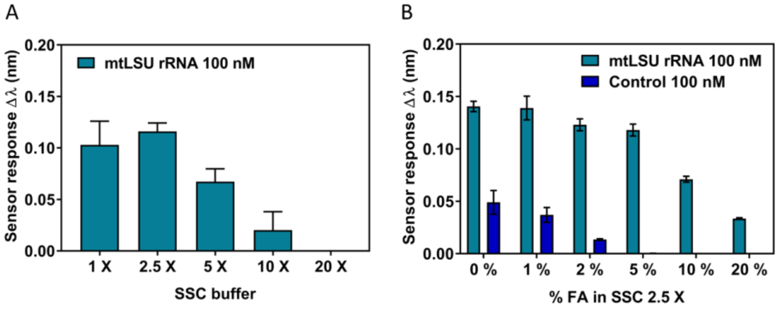

Figure 4.4. (A) Effect of hybridisation buffer ionic strength on the hybridisation mtLSU rRNA recognition using PPRH probes. (B) Formamide effect on the cross-hybridisation response of PPRH probes.

4.3.2. Analytical parameters of the genomic SPR biosensor

To validate the PPRH bioreceptor-based biosensor strategy, we compared the performance of PPRH probes (triplex approach) with conventional oligonucleotide probes (duplex approach) and control PPRH probes. All three were compared in terms of sensitivity and kinetic parameters. In control PPRH, one of the polypurine sequences did not contain the right sequences and the triplex could not be formed properly.

To evaluate each bioreceptor, they were immobilised *in-sit*u (DNA probe: CH_3–PEG–SH 1:1 ratio) on the sensor surface and we monitored their response to the flow of samples containing different ss-DNA mtLSU rRNA concentrations (**Figure 4.5**). As can be observed in **Figure 4.5A**, for the triplex PPRH probe, an increase in the mtLSU rRNA concentrations generated a higher sensor response, demonstrating the capabilities of the biosensor for quantitative analyses.

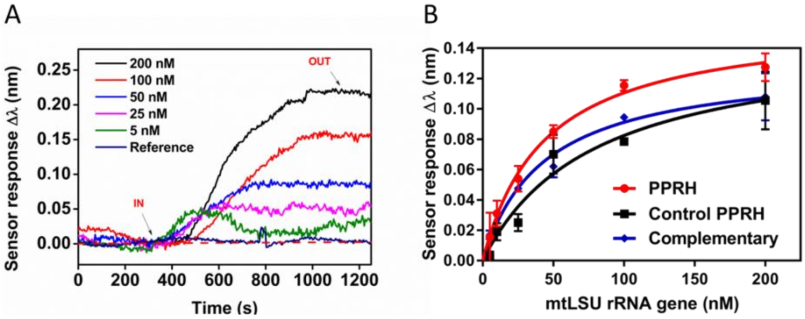

Figure 4.5. mtLSU rRNA gene detection. (A) Real-time sensorgram corresponding to different mtLSU rRNA concentrations (200, 100, 50, 25 and 5 nM) in standard buffer conditions. DNA control (reference) sequences were analysed at 100 nM. (B) Calibration curves of mtLSU rRNA on SSC 2.5 X + 5% FA buffer. Sensor response represents the mean ± SD of three measurements**.**

The limit of detection (LOD) achieved for each condition was 2.11 nM (R^2 = 0.9706) for triplex PPRH; 3.14 nM (R^2 = 0.9576) for the duplex probe and 4.40 nM (R^2 = 0.9246) for the control PPRH probe, respectively. According to these results, the formation of the triple helix enabled a more sensitive recognition of the mtLSU rRNA gene. Although the duplex probe also detected ss-mtLSU rRNA analyte fairly, hybridisation achieved only through Watson-Crick bonds, was not as strong as the one achieved by the triplex approach. Finally, the control PPRH probe showed a poorer performance, showing the worst limit of detection due to the presence of non-symmetrical two-polypurines sequences. The complementary polypurine sequences were able to detect mtLSU rRNA gene but the mismatching with the antiparallel one impeded the formation of the triple helix. The specificity of the triple PPRH biosensor assay was confirmed by evaluating a similar sequence with identical length and CG content. As commented previously, the incorporation of a certain percentage of formamide (5 %) in the buffer, avoided the non-specific interaction from non-complementary sequences.

The fitting formula used in **Figure 4.5B** not only informed about the sensitivity, but also provided data related to kinetics parameters such as the number of saturated bioreceptors in the sensor surface (*Bmax*) and their affinity with the analyte (*Kd*, equilibrium binding constant).

Table 4.3 shows the *Kd* and *Bmax* values for each DNA probe. A lower equilibrium binding constant implies a faster recognition event and a higher receptor-analyte affinity. The reported *Kd* for triplex PPRH (*Kd* = 44.06 nM) and the duplex probe (*Kd* = 43.36 nM) were similar, indicating that both probes presented the same capabilities to capture ss-DNA mtLSU rRNA. Otherwise, the control PPRH (*Kd* = 78.76 nM) achieved the worst affinity, almost twice times higher as the previous ones. Regarding *Bmax*, there was not a substantial difference in all the cases, meaning that the biofunctionalisation methodology is reproducible ensuring the same amount and density of bioreceptors onto the sensor surface regardless of the DNA probe.

Table 4.3. Kinetics parameters, equilibrium binding constant (*Kd*) and extrapolated maximum number of bioreceptors in the sensor surface (*Bmax*), corresponding to the hybridisation interaction mtLSU rRNA sequence—DNA probes.

	PPRH Probe	**Control PPRH Probe**	**Duplex Probe**
Kd (nm)	44.06	78.76	43.36
Bmax (nm/nM)	0.1593	0.1473	0.1306

Finally, the detection reproducibility of the biosensor assay was assessed through the coefficient of variation (CV) intra- and inter-sensor chips (**Table 4.4**). CV values for the triplex PPRH and duplex probe were close to the maximum variability recommended for clinical analysis (15%)[142], which reflected an acceptable reproducibility of these bioreceptors. Otherwise, the inter-sensor chip CV in the control PPRH case was twice as higher as the recommended values, indicating the poor accuracy and reproducibility of this probe for mtLSU rRNA recognition. Considering the ability of PPRH probes to generate ds-DNA displacement and given these results, we verified that triplex PPRH is the most suitable bioreceptor for mtLSU rRNA detection and, hence, for the diagnosis of Pneumocystis pneumonia.

Table 4.4. Variability of the SPR sensor signal intra- and inter-assays for mtLSU rRNA detection. The mean ± SD are from three replicates performed in the same or different biofunctionalised sensor chips, respectively.

nM	PPRH Probe		Control PPRH Probe		Duplex Probe	
	Mean ± SD	**% CV**	**Mean ± SD**	**% CV**	**Mean ± SD**	**% CV**
	Intra-chip					
LOD	2.8 ± 0.5	16	4.2 ± 0.6	14	3.1 ± 0.2	8
	Inter-chip					
LOD	1.9 ± 0.3	14	3.6 ± 1.3	37	3.4 ± 0.3	9

4.3.3. Analysis of mtLSU rRNA gene in human samples

To demonstrate the capabilities of the SPR biosensor for clinical analysis, an evaluation of real human samples was performed. As previously described, usually *Pneumocystis jirovecii* is detected in pulmonary fluids such as BAL and NPA. DNA from these respiratory samples was extracted, purified and diluted in highly pure water (milli-Q water) in a very low volume (30–50 µL), where the concentration is close to the limit of detection of the SPR biosensor. To avoid the dilution of the purified samples and ensure proper detection conditions (buffer salt concentration, detectable analyte concentration…), different strategies for sample preparation have been evaluated:

1. Use sterile milli-Q water as running buffer to perform the hybridisation assay without treating the purified samples.
2. Use the optimised hybridisation buffer SSC2.5X + 5% FA as running buffer. The purified samples did not suffer any dilution or pre-treatment.
3. Dilute the pufied samples with a high concentration of SSC and FA. We included a low volume of these compounds to reach the same concentration in the sample as the concentration in the optimised hybridisation buffer (2.5 X SSC + 5 % FA).

Figure 4.6 and Figure 4.7 show the results of the three strategies. The first and second strategies are similar, differing only in the running buffer. As we can observe in **Figure 4.6A**, the detection of mtLSU rRNA target (1000 nM in Milli-Q water) is higher using SSC2.5X + 5% FA than Milli-Q water as running buffer. The complete elimination of salts and FA content in strategy 1, dramatically affected the hybridisation efficiency, obtaining negligible sensor responses and reducing the signal by 80% compared to the second strategy.

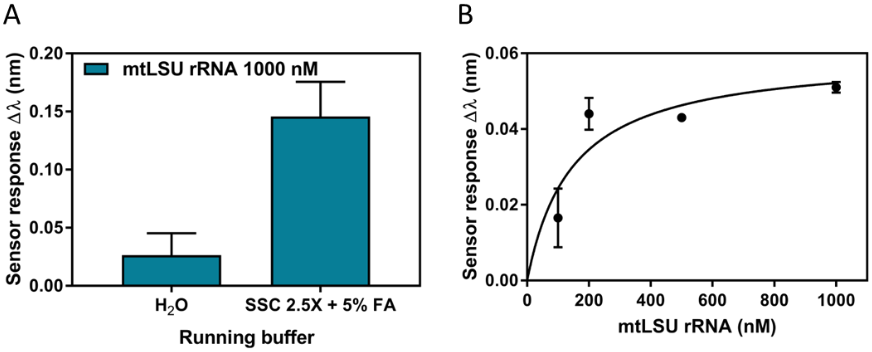

Figure 4.6. mtLSU detection when dissolved in water. (A) Sensor response to the detection of mtLSU target 1000 nM dissolved in water by using H_2O and SSC 2.5 x + 5 % FA as running buffer, respectively. It represents mean ± SD of four measurements. (B) Non-linear calibration curves of DNA target on water and enriched with a high concentration of FA and SSC and using SSC 2.5 x + 5 % FA as running buffer. Sensor response represents the mean ± SD of two measurements.

The lack of optimised hybridisation conditions related to SSC and FA compounds affected extraordinally the biosensor assay. The thrid strategy tried to achieve similar conditions of the hybridisation buffer, however the salt and FA content was not accurate enough and the calibration curve reflected an inadequate $R^2 = 0.7264$ and a deficient limit of detection LOD = 32.89 nM (**Figure 4.6B**). Moreover, comparing the sensor response to 1000 nM mtLSU rRNA, the second strategy increased the sensor signal by 60% compared to the last strategy. As shown in **Figure 4.4A,** an excess of SSC can reduce the signal response by 40% due to the overabundance of salts interfering in the hybridisation event, which explains the low sensor response in these conditions.

In all three above-described strategies, a decrease in the sensor sensitivity compared to the buffer circumstrances was observed. A higher mtLSU rRNA concentration had to be used to evaluate their performance. As a summary, the sensor responses for each strategy detecting 1000 nM of the genetic analyte were: strategy 1 ≈ 0.025 nm; strategy 2 ≈ 0.150 nm; strategy 3 ≈ 0.055 nm. The use of the optimised buffer in a constant flow may enhance the stability and conformation of the monolayer, maintining suitable conditions for hybridisation. Strategy 2 showed the best performance, however, the absence of salts and FA in the injected sample affected the detection capabilities of the PPRH probes.

To evaluate purified samples with the new biosensor assay conditions, it was required to obtain a new calibration curve. We used SSC2.5X + 5% FA as running buffer and mtLSU rRNA ss-DNA as analyte dissolved in Milli-Q water. We analysed the effect of the water on the sensor signal and the hybridisation event. We decided to assess more mtLSU rRNA ss-DNA concentrated samples, from 1000 nM to 50 nM, to counteract the limited sensitivity due to the absence of the optimised hybridisation buffer conditions (**Figure 4.7**).

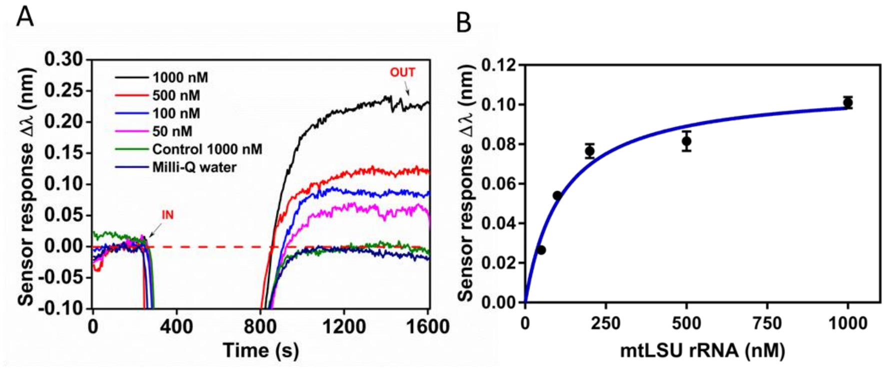

Figure 4.7. mtLSU rRNA gene detection. (A) Real-time sensorgram corresponding to the hybridisation of different mtLSU rRNA concentrations (1000, 500, 100 and 50 nM, respectively)

diluted in water. A control DNA sequence of 1000 nM and water were used as negative controls (B) Calibration curves of mtLSU rRNA on water using SSC 2.5 X + 5% FA as running buffer. Sensor response represents the mean ± SD of three measurements.

First of all, we evaluated the water effect on the plasmonic biosensor. The difference in the refractive index between the water used for sample solutions (RI = 1.33299) and the running buffer SSC 2.5X + 5% FA (RI = 1.34235), led to a decrease in the sensor signal during the sample flow over the sensor surface. In **Figure 4.7A** we can observe a drop in the real-time sensor signal since the water has a refractive index lower than the running buffer. Finally, the sensor signal returned to the baseline, indicating no interaction with the sensor surface or the monolayer. Similar behaviour was observed in the case of the control sequence (**Figure 4.7A**). Regarding the hybridisation event, the absence of salts and formamide in the samples hindered the hybridisation event, worsening the sensitivity of the plasmonic biosensor, which was reduced by five times, from 2.11 nM to 10.14 nM (R^2 = 0.9413). Despite the limited sensitivity in water-assay conditions, the reproducibility continued to be extremely adequate, as shown in **Table 4.4** where CV values for inter- and intra-sensor chips are below or near to recommended values of 15%.

Table 4.4. Variability of the SPR biosensor signal intra- and inter-assays for mtLSU rRNA detection using PPRH probes. The mean ± SD are from three replicates performed in the same or different biofunctionalised sensor chips, respectively.

mtLSU rRNA	**Intra-chip**		**Inter-chip**	
(nM)	**Mean ± SD**	**% CV**	**Mean ± SD**	**% CV**
1000	0.10 ± 0.003	3	0.11 ± 0.013	12
500	0.08 ± 0.005	6	0.08 ± 0.003	3
200	0.08 ± 0.003	5	0.07 ± 0.004	6
100	0.05 ± 0.002	3	0.05 ± 0.006	11
LOD	10.17 ± 0.69	7	12.03 ± 2.64	22

4.3.4. Clinical evaluation of Pneumocystis pneumonia

Pulmonary clinical specimens were pre-treated for purification and extraction of DNA. Additionally, these samples were dissolved in low volume of Milli-Q water (30 - 50 µL) in which the DNA concentration was close to the limit of detection of the biosensor. Due to the absence of salts in the sample and the limitations of sensitivity and volume, it was crucial to optimise the clinical evaluation by avoiding loss of volume sample and ensuring good sensitivity using the plasmonic biosensor. For this reason, previously to pulmonary specimens evaluation, an analysis of purified and synthetised DNA samples dissolved in Milli-Q water was carried out. We evaluated the PPRH-based assay in ds-DNA sequences and more complex DNA structures such as plasmids or ds-DNA fragments containing mtLSU rRNA sequence dissolved in Milli-Q water (**Figure 4.8**).

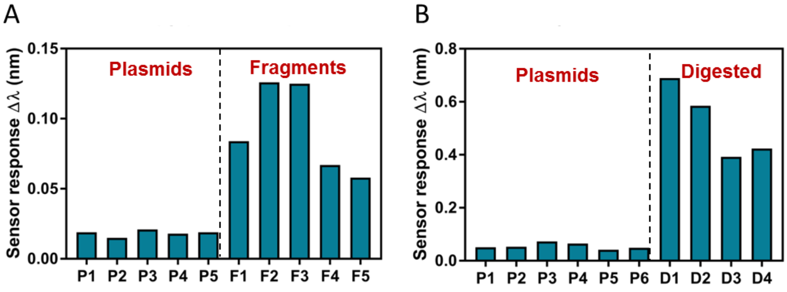

Figure 4.8. Detection of mtLSU rRNA gene contained in synthetic pGEM-T Easy plasmids and DNA fragments. (A) Sensor signals corresponding to pGEM-T Easy plasmids (P) and ds-DNA fragments (F). (B) Sensor signals corresponding to pGEM-T Easy plasmids (P) and digested ones by EcoRI enzyme (D).

As we can appreciate in **Figure 4.8**, PPRH probes were only able to detect DNA fragments and digested plasmids but not whole plasmids. The last ones have a large molecular weight (3400 bp) and a circular conformation that in the absence of FA in the hybridisation buffer allowed the presence of secondary structures. In these conditions, the accessibility to the mtLSU rRNA sequence by PPRH probes was nearly impossible, reporting responses around zero. The digestion of the plasmids enabled shorter, simpler and lighter sequences (i 346 bp or 260 bp) with a linear DNA configuration, as well as DNA fragments. Despite the possible presence of secondary structures, PPRH probes were able to displace DNA strands and form a triple helix with the ds-mtLSU rRNA sequence, providing higher sensor responses.

Finally, a clinical validation with clinical patients samples from BAL and NPA collected in the Hospital Virgen del Rocío (Seville, Spain) was carried out. The clinical validation included four samples from *P. jirovecii* infected individuals and eight control samples from patients infected by other microorganisms (*Pseudomonas* and *Cladosporium*) (**Figure 4.9**). BAL or NPA samples were collected and DNA was extracted, purified and dissolved in highly pure Milli-Q water.

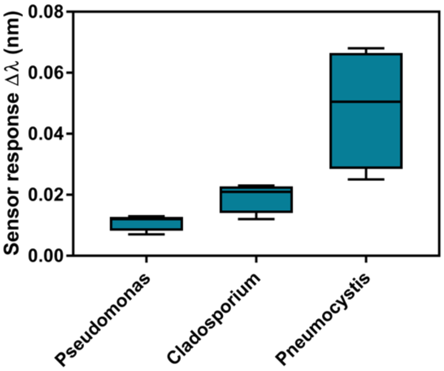

Figure 4.9. Analysis of mtLSU rRNA in clinical samples from patients infected by (i) *Pseudomonas aeruginosa* (*n* = 4), (ii) *Cladosporium* (*n* = 4) and (iii) *Pneumocystis* (*n* = 4). Representation of Kruskal-Wallis test where median, maximum and minimum values are shown. Kurskal-Wallis test, *p*-value = 0.0012.

Figure 4.9 compares the plasmonic biosensor results obtained for each infection condition. The result indicated that mtLSU rRNA levels were statistically higher in *P. jirovecii* infected patients (mean = 0.0485 nm) compared to controls ones infected by *Cladosporium* (mean = 0.01925) and *Pseudomonas* (mean = 0.011 nm). The Kruskal-Wallis test result with a p-value= 0.0012 below 0.05, confirmed the specific capabilities of the PPRH probes to detect and discriminate mtLSU rRNA from other DNA sequences, without cross-reactivity.

The plasmonic PPRH-based biosensor shows a satisfactory performance for Pneumocystis pneumonia diagnosis but more extended studies should be performed to transfer this methodology to the clinical practice. The addition of a pre-treatment procedure such as an enzymatic digestion to short and ease mtLSU rRNA accessibility could greatly boost the sensitivity of the biosensor assay. Moreover, the optimisation of the sensor biosurface for a direct BAL and NPA samples evaluation in a DNA extraction-free format would reduce turnaround times and avoid standardization complications from these DNA process. In this case, a thorough analysis should be performed with respect to surface blocking agents. The addition of blocking agents such as BSA, pLL-g-PEG or detergents (Tween 20 and dextran) on the sensor surface or in the running buffer, could avoid non-specific interactions of proteins and other components present in these lung samples. The optimisation of the blocking step would allow the direct analysis of BAL and NPA samples in an amplification- and extraction-free format, decreasing the described limitations related to volume and sensitivity.

4.4. Conclusions

Pneumocystis jirovecii is an opportunistic fungus that can cause a severe and mortal condition called Pneumocystis pneumonia in immunosuppressed individuals. The ambiguous diagnosis and the heterogeneous symptomatology depending on the patient condition, transform the diagnosis of Pneumocystis pneumonia into a hard challenge. We have demonstrated the efficiency of an SPR biosensor for the label-free, direct and rapid detection of Pneumocystis pneumonia in human fluid samples without amplification in a reduced sample volume (30 -50 µL). We employed a triplex helix approach to detect ds-DNA, specifically the mtLSU rRNA gene of *P. jirovecii*, using PPRH probes as capture bioreceptors. Sensitivity and kinetics studies highlighted the better and stronger capture capabilities of the triplex approach over the traditional duplex approach. PPRH probes ensured better and tougher capture of the mtLSU rRNA gene detecting it with a LOD of 2.11 nM. A preliminary study with plasmids and fragments containing the gene sequence revealed the necessity to establish a pre-treatment step (cleavage protocol) of the samples to obtain shorter DNA fragments. The shortening of the DNA length decreases the presence of secondary structures, generating linear fragments and easing the accessibility of mtLSU rRNA by the PPRH probes. The pre-treatment could improve the sensitivity of the SPR biosensor for the detection of *P. jirovecii* and could allow the DNA quantification able to be compared to conventional techniques such as PCR-based ones.

A clinical validation reflected the sensor ability to discriminate clinical samples for patients infected with *P. jirovecii* from samples infected by other microorganisms such as *Pseudomonas* or *Cladosporium*.

The developed SPR biosensor has demonstrated its efficiency and potential for clinical diagnosis of Pneumocystis pneumonia in an amplification-free, direct and fast manner. This format could enable reduced diagnosis time and the rapid adoption of the adequate treatment, increasing the survival possibilities of the patients.

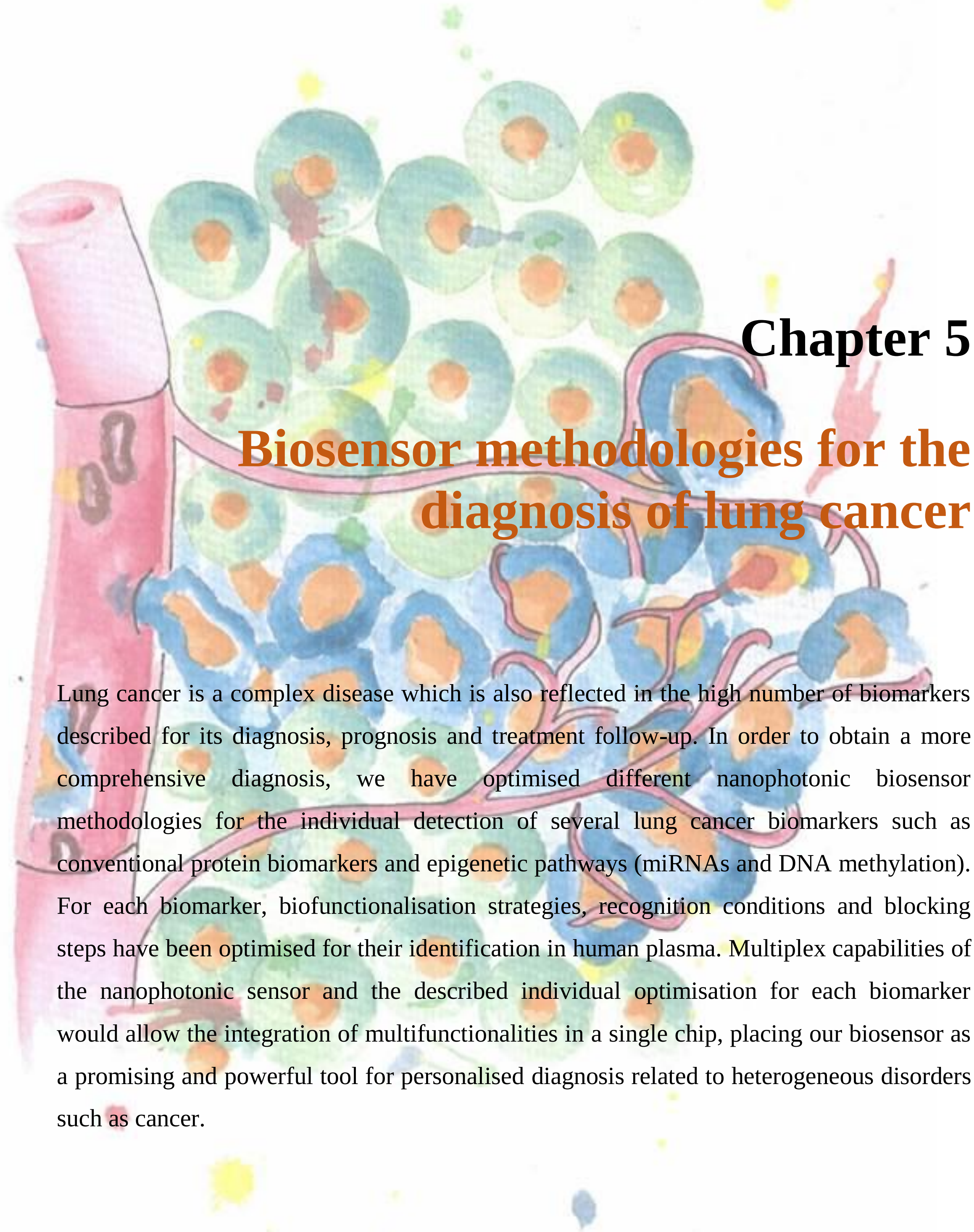

Chapter 5

Biosensor methodologies for the diagnosis of lung cancer

Lung cancer is a complex disease which is also reflected in the high number of biomarkers described for its diagnosis, prognosis and treatment follow-up. In order to obtain a more comprehensive diagnosis, we have optimised different nanophotonic biosensor methodologies for the individual detection of several lung cancer biomarkers such as conventional protein biomarkers and epigenetic pathways (miRNAs and DNA methylation). For each biomarker, biofunctionalisation strategies, recognition conditions and blocking steps have been optimised for their identification in human plasma. Multiplex capabilities of the nanophotonic sensor and the described individual optimisation for each biomarker would allow the integration of multifunctionalities in a single chip, placing our biosensor as a promising and powerful tool for personalised diagnosis related to heterogeneous disorders such as cancer.

5. Biosensor methodologies for the diagnosis of lung cancer

5.1. Introduction

5.1.1. Lung cancer

Lung cancer (LC) is the cancer with the highest incidence and mortality rates globally. In 2020, 2.206.771 new cases and 1.796.144 deaths were reported, representing close to 1 in 5 (18.4 %) cancer-related deaths[173] (**Figure 5.1.**). In the last years, lung cancer-related deaths exceed in number the combination of the deaths caused by the most relevant cancer (breast, prostate, colorectal and brain). In men, lung cancer is the top cancer death and in females, the second one behind breast cancer. Lung cancer usually has a late diagnosis due to the non-symptomatology or the presence of common symptoms like cough, anorexia, fatigue or dyspnea[10], leading to advanced cancer stages characterized by metastasis. In these advanced stages, the treatment might not be enough effective against the tumour and the patient's survival rate decays[174]. Lung cancer is considered one of the cancers with the poorest prognosis since it reports a 5-years survival rate of 19%, second only to pancreatic cancer[175].

Lung cancer is classified by pathological criteria into small cell lung cancer (SCLC), which corresponds to 15 % of the cases, or non-small cell lung cancer (NSCLC) affecting the remaining 85 %. In turn, NSCLC is classified into adenocarcinoma, squamous cell carcinoma, and large cell carcinoma[10,176].

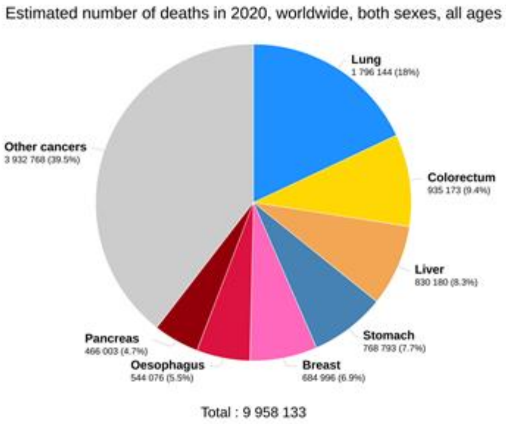

Figure 5.1. Cancer-related mortality in 2020. Lung cancer is the first cancer-related death comprising 18 % of the deaths[173].

5.1.2. Conventional clinical techniques for the diagnosis of lung cancer

Nowadays, clinical techniques for lung cancer diagnosis rely on imaging methodologies such as chest radiography, contrast-enhanced computed tomography (CT), magnetic resonance imaging (MRI) and positron emission tomography (PET). The main drawbacks associated with these techniques are a low sensitivity (they are only useful when the tumour is visible enough), the high costs and the generation of radiation[177]. To offer a better diagnosis and treatment, physicians combine imaging techniques with molecular ones such as cytology samples and small biopsies[10]. Among molecular approaches, the gold standard procedure for lung cancer diagnosis is histological or cytological analysis by microscopic techniques. These methodologies can provide relevant information on the histological type of cancer based on morphological and immunohistochemical features. However, the size of the biosy is a key factor and the identification of these features may not be conclusive in small biopsies and early stages of cancer[176]. Thus, clinical diagnosis based on the detection of specific biomarkers (proteins or genetic material) in body fluids such as urine, saliva or blood could constitute an excellent alternative to improve the lung cancer diagnosis. Biomolecular analysis has demonstrated its capabilities to identify cancer events in a non-invasive and inexpensive approach, even in the early stages before tumour appearance[176,178] allowing a rapid treatment and increasing cancer survival rate. Currently, clinical molecular tests are based on the human exhaled breath for volatile organic compound analysis[178], genetic diagnosis (e.g. mutation in *EGFR*[179] and rearrangements in *ALK* and *ROS* genes[180,181]) and/or liquid biopsies. Main techniques for clinical lung cancer diagnosis are summarised in **Table 5.1**.

Table 5.1. Clinical diagnosis methods employed for lung cancer diagnosis

LC diagnosis	Technique
Medical exploration	Pulmonary function test
Imaging	Chest X-Ray, MRI, CT Scan
Lung biopsy or cytology	Tissue immunohistochemistry and microscope
Biomolecular test	Human exhaled breath Genetic test Liquid biopsy

Lung cancer biomarkers

Liquid biopsies take advantage of the presence of several biomarkers in cancerous cells and biological fluids (plasma, urine, saliva, sputum…)[178]. The ideal biomarker must provide information about the tumour existence but also it should have prognosis and predictive value[182]. A wide variety of biomarkers have been reported for lung cancer diagnosis and they can be classified depending on their nature in protein and genetic biomarkers.

-*Proteins biomarkers*. A vast number of proteins have been described as lung cancer biomarkers although their levels can vary depending on the type of lung cancer. Most relevant protein biomarkers are carcino embryonic antigen (CEA)[183] and neuro-specific enolase (NSE)[184] due to their diagnostic sensitivity and specificity. Other proteins such as cancer antigen 15-3 (CA15.3), cytokeratin 19 fragment (CYFRA21-1), annexin A2 (ANX-

A2), etc have been described[182,185], although they do not show enough diagnostics sensitivity and specificity individually and they should be combined[186,187].

-*Genetic biomarkers*. Among genetic biomarkers, two different subtypes can be distinguished. One subtype corresponds to genetic changes in the DNA sequence or chromosomal configuration such as DNA mutations in *EGFR*, *K-ras*, *p53*, *COX2* and *PIK3CA* genes[181,182,188]. In the second subtype, genetic biomarkers also include changes in the gene expression without the need of nucleotide alteration. These are called epigenetic events which englobe DNA methylation (e.g.*CDO1* and *RARβ* genes)[189–191], miRNAs (miRNA-21-5p, miRNA-205-5p, miRNA-210-3p, miRNA-212-3p, miRNA-27a-3p and miRNA-132-5p,…)[192] and alternative splicing (*actinin-4*, *Bcl-x*, *CD44* genes)[193,194], among other events.

A list of described lung cancer biomarkers and the established detection techniques for their analysis are shown in **Table 5.2**.

Table 5.2. Lung cancer biomarkers and their corresponding analysis techniques

Type of biomarker	**Type of Biomarkers**	**Biomarkers**	**Diagnostics technique**
Protein	**Proteins**	CA15.3, CEA, CYFRA 21-1, NSE, ANX-A2	ELISA, protein array, mass spectroscopy, chromatography, immunohistochemistry
Genetic and epigenetic	**miRNAs**	miRNA-21-5p, miRNA-205-5p, miRNA-210-3p, miRNA-212-3p, miRNA-27a-3p, miRNA-132-5p	PCR-based technologies, Northern-Blot, microarray
	DNA methylation	*APC*, *CDH13*, *KLK10*, *DLEC1*,	Chromatin immunoprecipitation

		RASSF1A, *EFEMP1*, *SFRP1*, *RARβ*, *p16INK4A*, *CDO1*, *ZNF177*, *TRIM50*, *BRAC1*	(ChIP) assays, bisulfite conversion, methyl-sensitive restriction enzymes
	DNA mutations	*EGFR*, *K-RAS*, *p53*, *COX2*, *PIK3CA*	PCR-based technologies, microarray, sequencing, FISH
	Alternative splicing	*actinin-4*, *Bcl-x*, *CD44*, *XAGE-1*, *VEGF*, *APP* NUMB	RNASeq Microarray profiling, RT-PCR

The simultaneous detection of a variety of biomarkers can increase the sensitivity and specificity of the cancer diagnosis. The analysis of the biomarkers involves a myriad of laboratory techniques of high sensitivity and specificity, reliability and feasibility, but these techniques also require rigorous experiments with long turnaround times, sophisticated equipment and trained personnel and adequate installations. Additionally, large amounts of purified patient samples might be needed, introducing a high variability and leading to inaccurate analyses due to the lack of standardization in the extraction protocols[195]. It is clear that the development of efficient and easy-to-use diagnostics technologies capable of evaluate multiple biomarkers simultaneously could be a landmark for the rapid and simple diagnosis of any type of cancer in general and, in particular, for those types of cancer difficult to be detected in an early phase, as the lung cancer.

In this Chapter, we described a novel biosensor approach for lung cancer diagnosis. This approach combines the analysis of several biomarkers such as NSE protein, and epigenetic biomarkers as miRNAs (miRNA-21-5p, miRNA-210-3p and miRNA-205-5p), and DNA methylation profiling (*CDO1* and *ZNF177* genes). Design and optimisation of individual biosensor assays are detailed for a future simultaneous analysis of lung cancer biomarkers with our multiplexed BiMW biosensor.

5.2. Label-free detection of lung cancer-related miRNAs levels using biosensors

Mature miRNAs are short and single-stranded non-coding RNAs (≈ 22 nucleotides), which play an important role in gene expression via post-transcriptional regulation of messenger RNA (mRNA) (**Figure 5.2**)[192]. It is well-known that miRNAs can identify and hybridise to complementary sites present in the 3′untranslated region (UTR) of target mRNA resulting in post-transcriptional gene silencing either by mRNA degeneration or translation inhibition[196]. Some studies have reported that miRNAs can also bind the 5'UTR region and/or the open reading frame (ORF) for mRNA transcription allowing gene translation activation. However, these models are not universally accepted due to the weak bond between the miRNA and the mRNA region and the ribosome action, which usually removes the miRNAs[197].

MiRNAS have been reported to regulate the translation of more than 60 % of protein-coding genes and to be implicated in many diseases such as cardiovascular, inflammatory, autoimmune and neurodevelopmental diseases, among others[198]. They are also involved in regulating many processes, including cellular proliferation, differentiation, apoptosis and development and therefore, the tumourigenesis process[192].

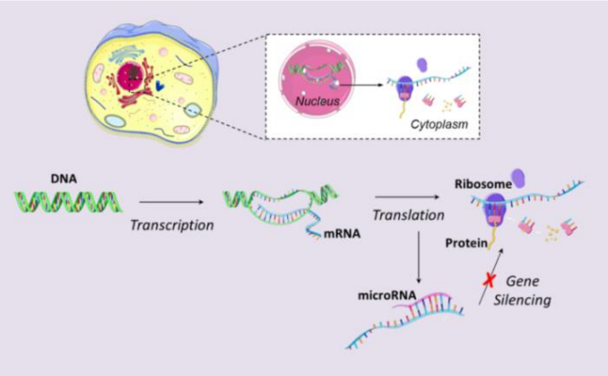

Figure 5.2. miRNAs role in protein translation

miRNAs are promising biomarkers for non-invasive cancer diagnosis due to their presence in biological fluids such as urine, saliva, blood, etc…[178]. Moreover, miRNAs do not only offer diagnosis but also prognosis and predictive values. The expression of a specific miRNA (upregulated or downregulated) signature can determine the type of cancer according to the tissue[199] and its development and progression stage (early or late stage, metastasis…)[200].

The clinical values of miRNA biomarkers in body fluids are still a controversial topic due to the lack of standardization in RNA extraction and quantification techniques for RNA analysis. Even though there is not a consensus about the concentration of miRNA in human plasma, some studies estimate that the miRNA concentration in clinical samples might lie in the range of $10^5 – 10^8$ copies·mL^{-1} (fM – nM)[201].

MiRNA detection is based on laboratory techniques such as RT-qPCR, Northern Blot and high-throughput sequencing as microarrays. Despite the suitability and accuracy of these techniques, they require laborious protocols and stringent conditions[195]. Optical biosensors are an alternative for the rapid and direct detection of miRNAs biomarkers. Several optical biosensors have been proposed to detect miRNAs for clinical diagnosis, mainly the surface plasmon resonance biosensor, reaching LOD in the pM - fM range after an amplification step with antibodies[202], gold nanoparticles[203] or catalytic reactions[204]. Within silicon photonics biosensors, microring resonators[205] and Mach Zehnder interferometer[206] have been also developed for miRNAs identification, reaching limits of detection in the nM range.Our BiMW have been also employed for miRNA detection involved in cancer, reaching aM range as limit od detection[68].

5.2.1. Lung cancer-related miRNAs

A large variety of miRNAs is involved in lung cancer like miRNA-25-3p, miRNA-224-5p miRNA-31-5p, miRNA-155-5p, miRNA-Let-7 family…[192]. Among them, miRNA-21-5p, miRNA-205-5p and miRNA-210-3p have been the ones selected in this work since all of them are upregulated during the lung cancerous process. The cited miRNAs can modulate several genes, miRNA-21-5p represses tumour suppressor PTEN[207], miRNA-205-5p negatively affects p53 inducible nuclear protein 1 (TP53INP1), a tumour suppressor[208] and miRNA-210-3p is related to the expression of hypoxia-inducible factor-1 (HIF-1), indispensable for cancer environment[209].

In this thesis, SPR-based and BiMW-based biosensor assays have been designed, developed and implemented for diagnosing lung cancer in clinical plasma samples using miRNAs as epigenetic biomarkers.

5.2.2. Materials and methods

5.2.2.1. Chemical reagents

Solvents used for sensor chips cleaning (acetone 99.5%, ethanol 99% and methanol 99%, hydrochloric acid (HCl, 37 %), nitric acid (HNO_3) were purchased from Panreac Applichem (Barcelona, Spain). All the buffer compounds, sodium citrate buffer (SSC) 20X (3 M NaCl, 0.3 M sodium citrate, EDTA 4 mM, pH 7.4), phosphate immobilisation buffer PBS 50 mM (NaCl 0.84 M, KCl 13.5 mM, Na_2HPO_4 50 mM, KH_2PO_4 9 mM, EDTA 10 mM, pH 7.1), phosphate buffer saline PBS 10 mM (NaCl 0.137 M, KCl 2.7 mM, Na_2HPO_4 10 mM, KH_2PO_4 1.8 mM pH 7), 0.5 M NaCl/Tris-EDTA buffer and $MgCl_2$, anhydrous toluene 99.8%, N, N-dimethylformamide anhydrous ≥99.8%, (DMF), anhydrous pyridine 99.8%, crosslinking molecule p-phenylene diisothiocyanate 98% (PDITC), 3-aminopropyltriethoxy silane ≥98%, (APTES), N, N-diisopropylethylamine (DIPEA), diethyl pyrocarbonate (DEPC), bovine serum albumin (BSA), Tween 20, (1-ethyl-4(3-dimethylaminopropyl)carbodiimide hydrochloride (EDC), ethanolamine hydrochloride (1 M, pH 8.5) and N-hydroxysulfosuccinimide (sulfo-NHS) were acquired from Sigma-Aldrich (Darmstadt, Germany). Lateral spacers SH-PEG-COOH, SH-PEG-NH_2, SH-PEG-CH_3, SH-PEG-OH (MW 2000 $g \cdot mol^{-1}$) were purchased from Laysan Bio (Alabama, US). 3-[3-Cholamidopropyl)dimethylammonio]-1-propane sulfonate (CHAPS) was purchased from Avanti Polar Lipids (Alabama, US). Bond-Breaker™ TCEP Solution (tris(2-carboxyethyl)phosphine hydrochloride solution) was purchased from ThermoFisher (Massachusetts, US). Human pooled plasma was purchased from Innovative Research (Michigan, US). Triethoxysilane polyethylene glycol carboxylic acid (silane-PEG-COOH, 600 Da) was supplied by Nanocs (New York, US).

To work under RNase-free conditions, all the labware used was sterilized, and buffer solutions were prepared with milli-Q H_2O treated with 0.1% DEPC and autoclaved at 121° C for 1 hour.

5.2.2.2. DNA probes and miRNA sequences

MiRNA sequences for probe and analyte design were extracted from the miRBase database (http://www.mirbase.org). DNA probes sequences are complementary to miRNA-21-5p, miRNA-210-3p and miRNA-205-5p, respectively, and they incorporate a thiol (SH-) or amine ($-NH_2$) functional group at the 5'-end to enable coupling with an activated sensor surfaces. In addition, a spacing region that consists of a 15 thymines (polyT15) sequence is placed between the functional group and the recognition sequence to push away it from the sensor surface and for enhancing target accessibility.

DNA probes and synthetic miRNAs employed for the optimisation of the hybridisation complementary assay were purchased from IBIAN technologies (Zaragoza, Spain) and are summarised in **Table 5.3**.

Table 5.3. Nucleotide sequences employed for lung cancer diagnosis based on miRNA detection

miRNA name	DNA probe (5'→3')	miRNA sequence(5'→3')
miRNA-210-3p	[Thiol]TTT TTT TTT TTT TTT TCA GCC GCT GTC ACA	CUG UGC GUG UGA CAG CGG CUG A
miRNA-21-5p	[Amine]/[Thiol]TTT TTT TTT TTT TTT TCA ACA TCA GTC TGA	UAG CUU AUC AGA CUG AUG UUG A
miRNA-205-5p	[Thiol]TTT TTT TTT TTT TTT CAG ACT CCG GTG GAA TGA AGG A	UCC UUC AUU CCA CCG GAG UCU G

5.2.2.3. DNA probe biofunctionalisation

DNA probe immobilisation in gold surface

DNA probes with a thiol functional group in the 5’ end were directly attached to the gold sensor surface via thiol-gold chemisorption (**Figure 5.3**). For the *in-situ* immobilisation of the DNA probes, the cleaned sensor chips were placed in the experimental setup under a constant flow (10 µL·min^{-1}) of DEPC–H_2O. An immobilisation solution composed of DNA probes and lateral spacers (SH-PEG-COOH) in a ratio of 1:1 at a final concentration of 2 µM prepared in PBS 50 mM was flowed at a constant rate. Previous to the immobilisation step, the DNA probe was incubated with 0.1 µM TCEP in constant agitation for 20 min at 37° C to reduce eventual disulfide bonds formed between thiol groups.

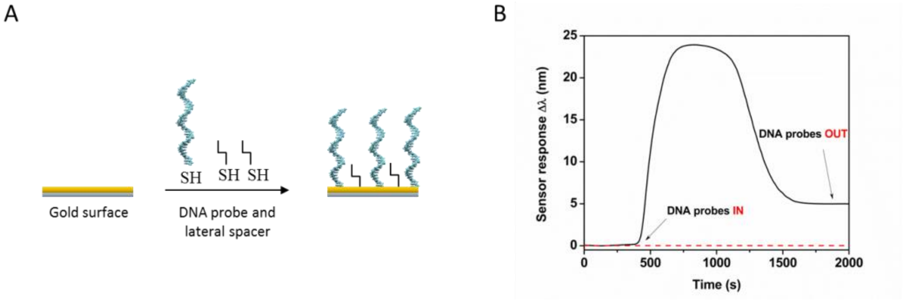

Figure 5.3. DNA probe immobilisation in the gold sensor surfaces. (A) Schematic representation of the immobilisation process by chemisorption of the thiols groups. (B) Real-time sensorgram of the one-step reaction of DNA-immobilisation

DNA probe immobilisation in silicon nitride surface

Many organic silanes can be employed for silicon photonic sensors biofunctionalisation. Taking into account the idea of a multiplex device where different bioreceptors (DNA probes and antibodies) can be immobilised, two silanes ended with different functional groups (PEG-Carboxyl) and APTES (amine) have been employed. APTES is one of the most used organic silanes for biosensors assays. Otherwise, PEG-COOH silane was evaluated in order to mimic the robust and stable carboxyl-SAM surface commonly used for SPR biosensor assays.

- **PEG-Carboxyl (COOH).** Clean and hydroxyl-activated sensor chips were immediately incubated with a 25 mg·mL^{-1} silane-PEG-COOH solution in ethanol/water 95:5 (v/v) for 2 h at 4° C. After rising with ethanol and water and drying with N_2, the sensor chips were cured in an autoclave for 90 min at 120° C and 1.5 bars. Finally, the immobilisation of the amine-DNA probe was carried out *ex-situ* and *in-situ*. For *ex-situ* conditions, the carboxyl groups on the sensor surface were activated with a solution of 0.4 M EDC/0.1 M sulfo-NHS in MES buffer for 3 h. Then, a solution of 20 μM amino-modified DNA probe in 10 mM PBS containing 1 mM MgCl2 was incubated over the sensor surface overnight at RT. For *in-situ* conditions, the silanized chips were placed in the experimental set-up. Using DEPC-H_2O as running buffer at a constant rate of 3 μL·min^{-1}, the carboxyl groups on the sensor surface were activated with a solution of 0.4 M EDC/0.1 M sulfo-NHS in the MES buffer. Then, the 20 μM amino-modified DNA probe solution was injected and flowed at the same flow rate (**Figure 5.4**).

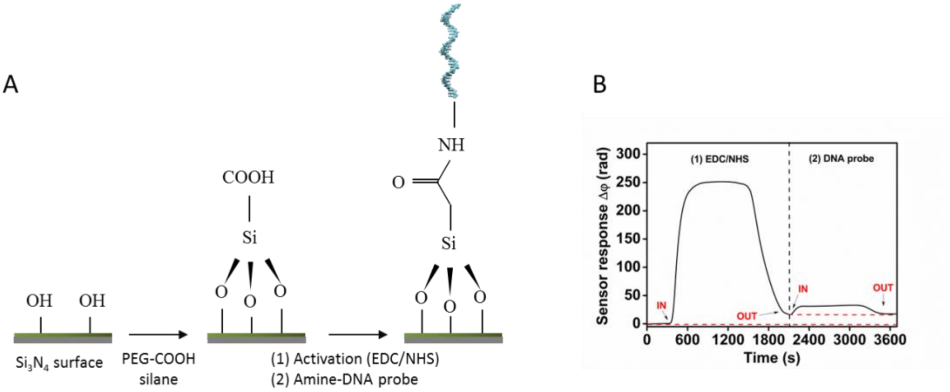

Figure 5.4. DNA probe coupling in PEG-COOH silanized surface. (A) Scheme of the functionalisation process performed for amine-DNA probe attachment. (B) Real-time sensorgram of the EDC/sulfo-NHS surface activation and DNA probe immobilisation over a PEG-COOH surface.

- **APTES (NH_2).** Clean and hydroxyl-activated sensor chips were immediately immersed into a toluene solution containing silane APTES 1 % (v/v) and catalyser

DIPEA 0.3 % (v/v) for 1 h under an N_2 atmosphere. After the incubation, the sensor chips were rinsed with ethanol and dried with an N_2 stream. Then, sensor chips were placed in a conventional oven and a curing step was carried out at 110° C for 1 h. Finally, APTES-modified sensor chips were incubated with 20 mM PDITC solution in DFM containing 10 % anhydrous pyridine for 1 h in darkness at RT. PDITC is a homobifunctional cross-linker with two isothiocyanates (R-NCS) groups that can interact with APTES primary amine groups through thiourea bonds and with thiol groups through the thiocarbamate bonds.

The PDITC-activated sensor chip was placed on the experimental set-up for the *in-situ* immobilisation of the thiol-DNA probe (**Figure 5.5**). The PDITC monolayer was biofunctionalised by flowing the immobilisation solution at a constant rate of 3 $\mu L \cdot min^{-1}$ and employing DEPC-H_2O water as running buffer. The immobilisation solution contained a mixture of SH-DNA probe and SH-PEG-COOH spacer in a 1:1 ratio at a final concentration of 2 μM in 50 mM PBS. Before injection, the immobilisation solution was incubated with 0.1 μM TCEP compound in constant agitation for 20 min at 37° C.

To avoid non-specific adsorptions from plasma samples, a blocking step was included after DNA attachment. BSA 20 $mg \cdot mL^{-1}$ diluted in 10 mM PBS was injected over the sensor chip at 5 $\mu L \cdot min^{-1}$. Finally, the sensor chips were kept under a continuous flow of SSC-P (SSC 2.5X + 0.5 % Tween 20 + 10 mM CHAPS) at 10 $\mu L \cdot min^{-1}$.

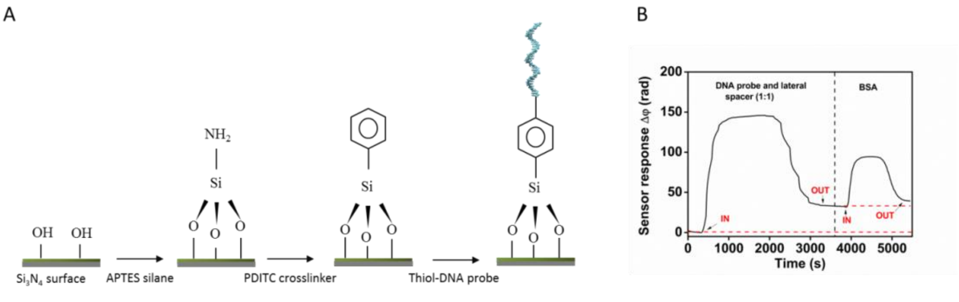

Figure 5.5. DNA probe coupling in APTES silanized surface. (A) Scheme of the functionalisation process performed for thiol-DNA probe attachment. (B) Real-time sensorgram of the DNA probe and lateral spacer (SH-PEG-COOH) immobilisation and BSA blocking over a PDITC-activated surface.

5.2.2.4. miRNA hybridisation

Different miRNA solutions (from 0.5 nM to 200 nM) were dissolved in SSC 5X buffer (0.75 M NaCl, 0.075 M sodium citrate) and flowed over the biofunctionalised sensor surface at a constant 10 µL·min^{-1} rate, using SSC 5X as running buffer. Calibration curves in plasma were generated by flowing different concentrations of miRNA (ranging from 0.5 nM to 100 nM) spiked in undiluted human plasma over the BiMW sensor surface at a 10 µL·min^{-1} rate, using SSC2.5X + 0.5 Tween + 10 mM CHAPS as running buffer. In all cases, DNA probe-miRNA hybrids were disrupted by injecting a 5 mM NaOH regeneration solution for 30 s at a constant flow rate.

5.2.2.5. Data analysis

Biosensor data were analyzed and processed using Origin 8.0 software (OriginLab, Massachusetts, US). Data and statistical analysis (Mann-Whitney, Kruskal-Wallis, ROC curves, and correlation tests) were performed using Graphpad Prism (Graphpad Software, Inc., California, US). The mean sensor response ($\Delta\lambda$ or $\Delta\varphi$) and its standard deviation (SD) were plotted as a function of the miRNA concentration to obtain calibration curves. Calibration curves were fitted to a linear regression model (**Equation 3.1**) or one-site specific binding equation (**Equation 4.1**).

The experimental LOD was determined as three times the SD of the sensor signal obtained from a blank signal using only the running buffer. The coefficients of variation were obtained as the ratio of the standard deviation of the mean, expressed in percentages (% CV).

Statistical analysis assessing the differences between healthy and cancer groups was analyzed with the Mann-Whitney test, considering a p-value < 0.05 to be statistically significant. The correlation between BiMW biosensor and qRT-PCR was analyzed by the Spearman test considering a p-value < 0.05. To evaluate the diagnosis capabilities of both, the BiMW biosensor and qRT-PCR, ROC curves were also performed. Statistical analysis to discover any significant relationship between sensor response and cancer stages was analyzed with the Kruskal-Wallis test, considering a p-value < 0.05.

5.2.2.6. Clinical plasma samples

A total of 20 patients from the "Leon Daniello" Pneumophtisiology Clinical Hospital Cluj-Napoca, Romania with a diagnosis of NSCLC were studied in our assay. Lung cancer patients were stratified according to the TNM classification for cancer stage, where the size and extent of the primary tumour (T), the number of nearby lymph nodes invasion (N), and the absence or presence of metastasis (M) are analysed. **Table 5.4** shows the cancer stage of the NSCLC patients analysed in this miRNA study

Table 5.4. Cancer stage of NSCLC patient samples used for miRNA study according to TNM classification.

Samples	Cancer stage	T*	N+	M‡
1	IIIA	3	2	0
2	IIIA	2	2	0
3	IIIA	3	2	0
4	IIIA	3	2	0
5	IIIB	4	2	0
6	IIIB	3	2	0
7	IIIB	3	2	0
8	IIIB	3	3	0
9	IIIA	2	2	0
10	IIIB	4	2	0
11	IIIB	4	2	0
12	IV	3	3	1
13	IV	4	3	1
14	IIIB	4	2	0
15	IIIB	4	3	0
16	IV	4	2	1
17	IIIB	4	2	1
18	IV	2	2	1
19	IIIB	4	2	0
20	IV	4	2	1

*T Scale 1-4, 1-inner layer, 2-muscle layer, 3-into outer lining, 4-through outer lining
+N Scale 1-3, 1- none, 2-three, 3-four or more
‡M Scale 0= no metastasis; 1= metastasis

Additionally, 20 healthy subjects from blood sample donation were employed as plasma controls (**Table 5.5**). Plasma samples were collected and stored at -80° C until biosensor analysis.

Table 5.5. Lung cancer patients and healthy subjects included in the miRNA-based BiMW biosensor assay

Plasma sample	No. of samples	Cancer stage
NSCLC	20 (50 %)	IIIA- (25 %) IIIB- (50 %) IV - (25 %)
Healthy subjects	20 (50 %)	-

For miRNA-21-5p validation, RNA was extracted from plasma samples and analysed by qRT-PCR at the Research Center for Functional Genomics, Biomedicine and Translational Medicine (Cluj-Napoca, Romania). The relative expression level was expressed as –ΔΔCT/Fold change.

5.2.3. Design, optimisation and detection of miRNAs by SPR biosensor

5.2.3.1. Optimisation of the DNA bioreceptor layer

The analytical parameters of a biosensor depend directly on the quality of the bioreceptor layer. In the case of nucleic acid-based sensors, a good coverage and a correct density of DNA probes are crucial since these determine the accessibility of the target sequence.

For the attachment of the DNA-based bioreceptor to the gold sensor surface, we opted for the simplest and more straightforward immobilisation strategy. Taking advantage of the high affinity between gold atoms and thiols, we attached the thiolated DNA probes to the sensor surface. In order to control the bioreceptor density, thiolated lateral spacers with different functional groups might be employed. Usually, these lateral spacers have a thiol group in the 5’end for their attachment to the gold sensor surface and another functional group such as amine, carboxyl or hydroxyl in the 3’end. These functional groups generate a monolayer of different characteristics (ionic strength) that facilitate or hinder the capture of the target and avoid or promote the non-specific interactions from other miRNAs or compounds in complex matrices like plasma, urine or saliva.

To optimise the complementary miRNA assay in the SPR biosensor, miRNA-21-5p was used as a model. The similarities between miRNAs enable the transference and application of the optimised miRNA biosensor assay to any other miRNA.

Firstly, analysis of the optimal amount of the DNA probe immobilised and the effect of laterals spacers in the miRNA capture and the antifouling properties were carried out (**Figure 5.6**).

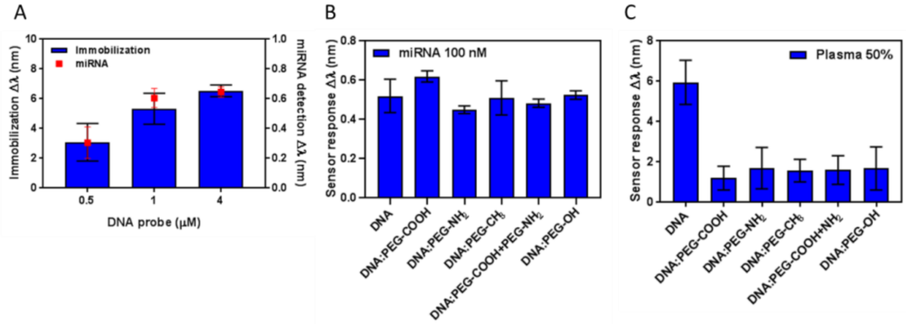

Figure 5.6. Optimisation protocol for the bioreceptor layer. Sensor response obtained depending on (A) concentration of the DNA probe immobilised and detection of the miRNA-21-5p 100 nM (B) the composition of the SAM layer, using lateral spacers with different functional groups (C) analysis in plasma 50% depending on the SAM layer composition.

As can be observed in **Figure 5.6A**, a concentration of DNA probes 1 µM (Δλ = 5.7 nm) ensures a complete coverage of the sensor surface, showing a immobilisation signal up to 2 nm compared to 0.5 µM and close to the signal corresponding to a four times higher concentration (Δλ ≈ 6 nm). Additionally, the sensor response for the detection of miRNA-21-5p using the 1 µM layer, was almost two times higher than the 0.5 µM condition and similar to the most concentrated layer. The attachment of 1 µM DNA probes assures an optimal biorecognition layer formation and plasmonic biosensor performance.

Regarding the effect of the introduction of lateral spacers in the biorecognition layer, **Figure 5.6B** shows the result ofthe miRNA-21-5p capture and **Figure 5.6C** the effect of avoiding non-specific interactions from plasma diluted 50 % depending on the combination of different spacers and ratios. Lateral spacers did not affect the miRNA-21-5p hybridisation since the DNA probe concentration is the most adequate. Otherwise, the presence of PEGs components on the sensor surface reduced the non-specific interaction from plasma samples. Although non-statistical differences were observed depending on the lateral spacer coupled, a monolayer consisting of DNA probes and SH-PEG-COOH in a ratio of 1:1 and a thiol concentration of 2 µM were employed for the miRNA biosensor assays. SH-PEG-COOH showed slightly better performance for miRNA-21-5p identification and non-specific interaction removal.

5.2.3.2. Plasmonic biosensors assay and analytical characterisation

To demonstrate and evaluate the performance of the SPR biosensor for miRNA detection, an assay based on direct hybridisation was designed. The simple design of the biosensor assay, based on hybridisation recognition, and the versatility of SPR, this approach could be easily transferred to other miRNA assays. Thus, we employed a DNA probe complementary to the miRNA-21-5p, miRNA-205-5p and miRNA210-3p to the analysis of those miRNAs, providing the required specificity. **Figure 5.7A** shows how the plasmonic biosensor signals ($\Delta\lambda$, nm) gradually increased as the miRNA (miRNA-21-5p) concentrations were higher. In the three cases, the same sensor behaviour was observed. **Figure 5.7B** reflects that possible bioreceptor saturation could be assumed above 200 nM, whereas a linear behaviour was observed for the lower miRNA concentrations analyzed (from 1–50 nM). Calibration curves allowed the determination of the limit of detection for each miRNA, resulting in a LOD = 1.29 nM (R^2=0.9402) for miRNA-21-5p, a LOD= 2.35 nM (R^2=0.9141) for miRNA-205-5p and a LOD= 2 nM (R^2=0.9302) for miRNA-210-3p. Despite the lack of consensus on miRNA concentration in clinical samples, some publications suggest that the concentration might lie in the range of $10^5 – 10^8$ copies·mL^{-1} (fM – nM)[201]. Considering the clinical values for miRNA, the SPR biosensor could not provide enough analytical sensitivity for lung cancer miRNA-based diagnosis in a amplification-free format and the methodology had to be transferred to a more sensitive sensor, the BiMW interferometric biosensor for a label-free detection of the miRNAs.

The biosensor assay specificity was also evaluated to guarantee the absence of non-specific interactions from other miRNAs involved in the lung cancer diagnostics based on miRNA (using miRNA-210-3p as control). As we can observe in **Figure 5.7A**, miRNA-210-3p interacted neither with the sensor surface nor with the DNA probe showing a null sensor response, which confirms the absence of cross-reactivity.

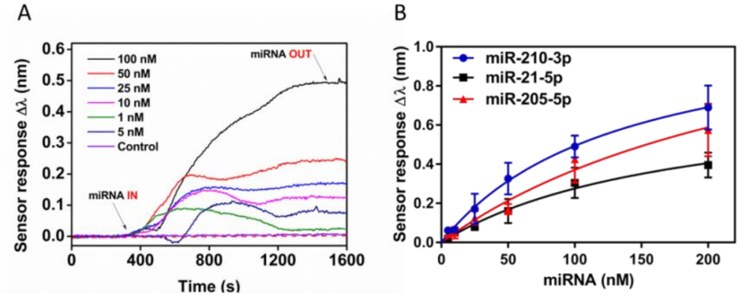

Figure 5.7. SPR-based hybridisation assay in buffer conditions. (A) Real-time sensorgrams showing the specific interaction of DNA probes with different miRNA-21-5p concentrations. Non-specific miRNA-210 (control) was evaluated at a concentration of 100 nM. (B) Calibration curve in hybridisation buffer conditions (SSC 5X) for miRNA-21-5p, miRNA-210-3p and miRNA-205-5p, respectively. Each signal corresponds to the mean ± SD of triplicate measurements.

In the three cases, the analysis of the CV values obtained for buffer condition allowed the evaluation of the assay reproducibility. CV values were below the maximum variability recommended for clinical analysis (15 %)[142] (**Table 5.6**) confirming the outstanding reproducibility of the developed miRNA biosensor assay.

Table 5.6. MiRNA inter-assay variability in the plasmonic biosensor for standard buffer conditions

miRNA	Parameter	CC1	CC2	Mean ± SD	% CV
miRNA-21-5p	**LOD, nM**	1.3	1.2	1.2 ± 0.062	5.0
miRNA-205-5p	**LOD, nM**	2.3	2.3	2.3 ± 0.001	0.04
miRNA-210-3p	**LOD, nM**	2.0	1.9	1.9 ± 0.03	1.5

5.2.4 Detection of miRNA-21-5p for clinical diagnosis of lung cancer using a BiMW biosensor

5.2.4.1. Comparison of silanisation procedures

For the DNA functionalisation in the silicon photonic biosensor, two silanes (PEG-COOH and APTES) with different functional groups, carboxyl and amine respectively, were employed. To select the best strategy for miRNA identification in plasma samples, an analysis of the miRNA-21-5p hybridisation after DNA probes immobilisation was carried out.

In the case of PEG-COOH, amine DNA probes were attached *in-situ* by EDC/sulfo-NHS chemistry. However, the sensorgram in **Figure 5.4B** shows a low or even unnoticeable immobilisation signal on the sensor surface. *Ex-situ* coupling was also tested with the idea of improving DNA probes attachment by increasing the reaction time. As we can observe in **Figure 5.8**, a null sensor response was reported after the injection of 100 nM miRNA-21-5p over the sensor surface. Neither *in-situ* nor *ex-situ* biofunctionalisation conditions provided a positive for miRNA detection, confirming that the immobilisation of the DNA probes had not been successful. Thus, the PEG-COOH protocol did not guarantee the immobilisation of the amine-DNA probes and, therefore, the detection of the miRNA-21-5p.

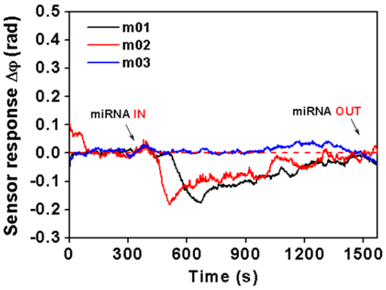

Figure 5.8. PEG-COOH silanisation procedure. Real-time sensorgram of miRNA-21-5p 100 nM detection by amine-DNA probes coupled to PEG-COOH silanized sensor surface in triplicate.

On the other hand, the APTES immobilisation protocol showed a good thiol DNA probes immobilisation ($\Delta\varphi \approx 25$ rad) (**Figure 5.5B**) and this was also confirmed by the capability to capture different concentrations of miRNA-21-5p. **Figure 5.9** reflects the increase in the sensor signal (Δφ, rad) at the same time as the miRNA concentration was higher. This result demonstrated that the thiolated DNA probes were attached over the APTES sensor surface. This biofunctionalisation strategy was carried out as the optimal approach for miRNA-21-5p assay in the silicon-based biosensor.

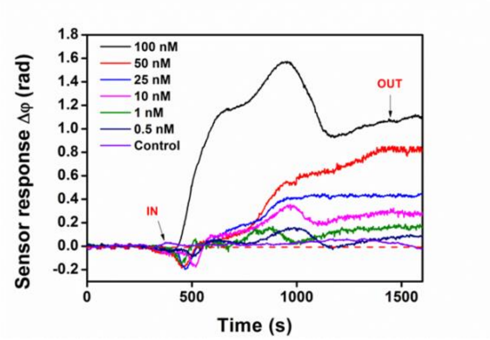

Figure 5.9. APTES silanisation procedure. Real-time sensorgrams showing the specific interaction of DNA probes with different miRNA-21 concentrations. Non-specific miRNA-210 (control) was evaluated at a concentration of 100 nM.

5.2.4.2. BiMW biosensor assay and analytical characterisation

The above-described result demonstrates that the thiol DNA-probes attached over the APTES sensor surface are the optimal approach for miRNA-21-5p assay in the silicon-based biosensor. The analysis of different miRNA-21-5p concentrations by the biosensor showed a linear correlation between miRNA concentrations and the sensor response at the lower miRNA concentrations (from 0.5 – 30 nM) (**Figure 5.10**). Additionally, saturation of DNA probes could be assumed when miRNA concentrations exceed 100 nM. From the calibration curve it is possible to calculate a limit of detection LOD=297 pM (R^2=0.9746). The transference of the methodology from the SPR biosensor to the BiMW biosensor has allowed improving the sensitivity of the assay by one order of magnitude. Considering this LOD and the reported clinical ranges for miRNAs in plasma samples (fM-nM), the BiMW biosensor may provide enough analytical sensitivity for lung cancer miRNA-based diagnosis.

In other to analyse non-specific interactions from other interfering miRNAs i (for example, miRNA-210), the specificity of the biosensor assay was evaluated. As can be observed in **Figure 5.9**, miRNA-210-3p (control) did not interact with the sensor surface or with the DNA probes, verifying that the biosensor responses come exclusively from the specific complementary miRNA to the immobilised DNA probes.

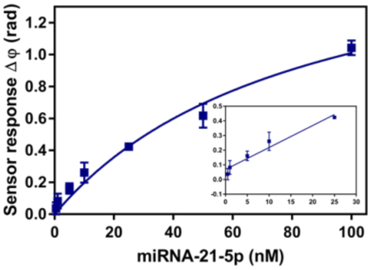

Figure 5.10. BiMW-based miRNA-21-5p hybridisation assay in buffer conditions. Calibration curve in standard hybridisation buffer (SSC 5X) conditions. Each signal corresponds to the mean ± SD of triplicate measurements.

The reproducibility of the biosensor assay was evaluated through the inter-assay variability, expressed as % CV values. The values obtained for the standard hybridisation buffer conditions were lowered than the suggested values for clinical analysis (15 %)[142] (**Table 5.7**), supporting the good reproducibility of this detection protocol.

Table 5.7. Inter-assay variability for miRNA-21-5p capture in standard buffer and undiluted plasma calibration curves (CC).

Matrix solution	Parameter	CC1	CC2	Mean ± SD	%CV
Buffer (SSC 5X)	**LOD, pM**	297	323	310 ± 18.4	5.9
Undiluted plasma	**LOD, pM**	381	416	398.5 ± 24.7	6.2

5.2.4.3. Human plasma effect on the hybridisation biosensor assay performance

To be able to apply the above-described biosensor methodology for the evaluation of lung cancer patients' plasma samples, it is critical to consider the influence of the plasma matrix on the sensor surface and on the hybridisation event. Plasma contains high amounts of proteins and other compounds that could produce non-specific interactions onto the sensor surface or hinder the DNA probe-miRNA recognition. To minimise the plasma effect on the sensor surface and the hybridisation event, different combinations of blocking agents as BSA added to the surface (**Figure 5.11A**) and detergent additives (as Tween 20 and CHAPS, nonionic and zwitterionic surfactants) added to the running buffer (**Figure 5.11B**) were tested. As can be seen in **Figure 5.11**, non-specific adsorption sin an unblocked biofunctionalised sensor chips resulted in extremely high signals (Δφ ≈ 40 rad); the incorporation of BSA over the sensor surface reduced that interaction up to four times (Δφ ≈ 7 rad). Additionally, the presence of detergents in the running buffer also decreased the plasma interaction with the sensor surface up to three times (Δφ ≈ 2 rad) or even eliminated them. Finally, a combination of BSA 20 mg·mL^{-1} as a blocking agent, and Tween 20 0.5% + CHAPS 10 mM, was selected as the most suitable additives mixture that successfully removed all non-specific interactions from human plasma (Δφ ≈ 0 rad).

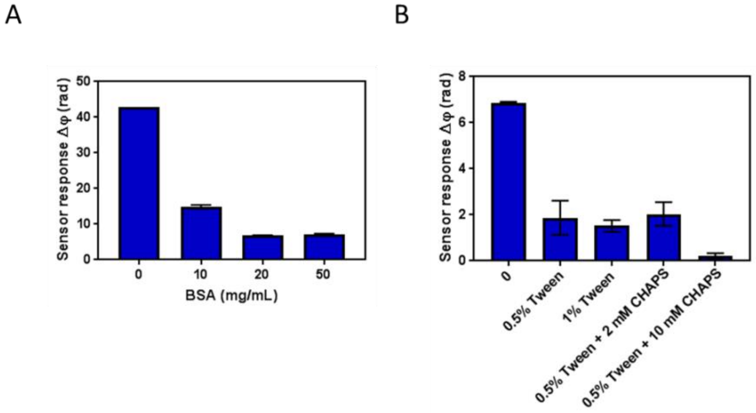

Figure 5.11. Effect of antifouling surfaces for plasma analysis. A) Sensor signals obtained from human plasma after covering the sensor surface with different concentrations of BSA blocking agent. B) Sensor signals were obtained from human plasma after blocking the sensor surface with BSA 20 mg·mL^{-1} and adding different combinations of detergents Tween 20 and CHAPS in the running buffer.

After the optimisation of the blocking step, a calibration curve in plasmawas recorded. Different miRNA-21-5p concentrations in the range from 0.5 nM to 100 nM were spiked in commercial human plasma. **Figure 5.12** shows the calibration curve with a LOD of 381 pM

(R^2=0.9776). MiRNA-21-5p accomplished for plasma conditions were rather similar to the LOD value obtained in standard buffer conditions (297 pM). This result reveals that the plasma matrix did not compromise the biosensor assay sensitivity, keeping the sensor surface and the DNA probes intact. As previously, the assessment of the assay reproducibility reflects a close behaviour in plasma and buffer conditions, reporting a low inter-assay CV (6.2%) value (**Table 5.6**).

Analytical parameters such as sensitivity, specificity and reproducibility confirmed the feasibility and suitability of the BiMW biosensor for the accurate detection of miRNA-21-5p in real clinical samples.

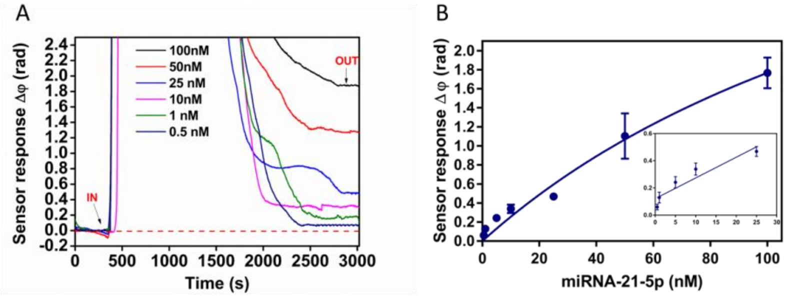

Figure 5.12. BiMW-based miRNA-21 hybridisation assays in plasma. A) Real-time sensorgrams showing the specific interaction of DNA probes with different miRNA-21 concentrations spiked in human plasma. B) Calibration curve in human plasma. Each signal corresponds to the mean ± SD of triplicate measurements.

5.2.4.4. Lung cancer validation with clinical plasma samples for miRNA-21-5p

A set of 40 plasma clinical samples from the Research Center for Functional Genomics, Biomedicine and Translational Medicine (Romania) were evaluated. The set consisted of 20 lung cancer plasma samples and 20 negative samples from healthy donors (**Table 5.5**). Additionally, all samples were previously validated for miRNA-21-5p by qRT-PCR in the collector center.

All the samples were analyzed with the BiMW-based hybridisation biosensor assay. A statistical comparison between healthy and LC individuals, and with qRT-PCR results was carried out. **Figure 5.13A** reflects the distribution of the BiMW sensor response after clinical plasma samples analysis. Sensor response values showed a statistical significance differentiation between healthy [median = 2.37] and LC patient [median = 3.56] (p-value < 0.0001). To evaluate the diagnostic capabilities (specificity and sensitivity) of the BiMW biosensor technology, a ROC curve was accomplished (**Figure 5.13B**). The area under curve (AUC) value reflects the potential of a diagnostic test to discriminate between controls and patients by considering 1 as an excellent and 0.5 as a random diagnosis. BiMW biosensor reported an AUC 0.87 (CI95%, 0.7616-0.9784), confirming an appropriate diagnosis capability, with a sensitivity of 80 % and specificity of 80 %, respectively.

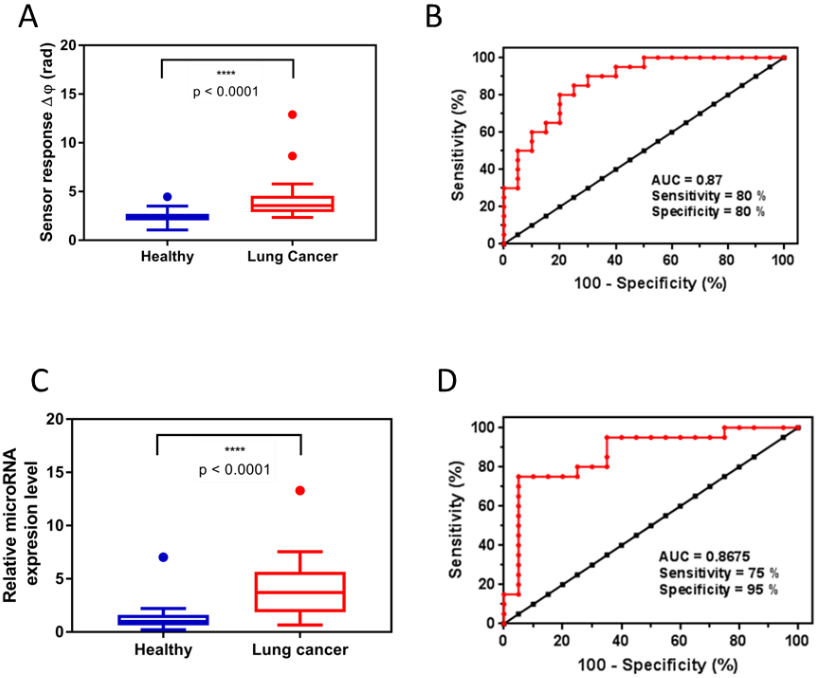

Figure 5.13. MiRNA-21-5p detection in clinical samples based on A) BiMW biosensor and C) qRT-PCR, in 20 healthy and 20 lung cancer individuals. Mann-Whitney test p-value < 0.0001. Outliers are also shown. ROC curves analysis of B) BiMW biosensor and D) qRT-PCR. AUC, sensitivity, and specificity values are reported.

The BiMW biosensor performance was qualitatively compared to the standard technique qRT-PCR. As can be observed in **Figure 5.13C**, the statistical analysis showed that qRT-

PCR was able to discriminate between healthy [median = 0.99] and lung cancer patients [median = 3.70] in a statistically significant manner (p-value < 0.0001, p-value< 0.05). Additionally, ROC curves demonstrated that qRT-PCR technology presented acceptable diagnostics capabilities (AUC 0.8675 (CI95%, 0.75–0.985), sensitivity 75 %, and specificity 95 %) (**Figure 5.13D**).

To compare both methodologies, a statistical correlation analysis was also carried out by the Spearman test. Spearman coefficient = 0.373, p-value= 0.018 showed a significant association between the relative $-\Delta\Delta$CT value obtained with qRT-PCR and the BiMW biosensor. These results corroborate the competitive performance of the BiMW technology compared with the benchmarked qRT-PCR. Our BiMW biosensor offers precise detection of miRNA-21-5p in a fast (in less than 45 min), amplification-free approach with diagnostic reliability equivalent to qRT-PCR for lung cancer identification.

Finally, a small-scale study was carried out to elucidate a possible correlation between the cancer stage and the levels of miRNA-21-5p in the plasma. Some studies reported that the overexpression of miRNA-21-5p and hence, its concentration in plasma, increases according to the TNM stage, being higher in advanced TNM cancers[207].

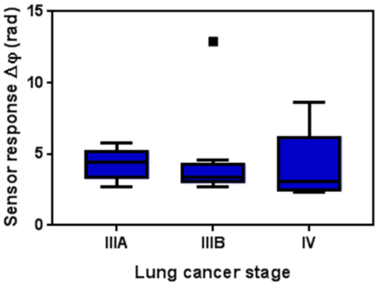

Figure 5.14. Correlation cancer stage *vs* miRNA-21-5p concentration. Sensor signal for the 20 lung cancer plasma samples stratified in different oncological stages (IIIA, IIIB, and IV). Kruskal-Wallis test (p-value = 0.4833). Outliers are also shown.

We analysed 20 lung cancer plasma samples from different lung cancer stages [IIIA (n = 5), IIIB (n = 10), and IV (n = 5)] (**Table 5.4**). **Figure 5.14** represents the statistical analysis of the BiMW biosensor response obtained depending on the patient cancer stage. Despite the capability of the BiMW biosensor to diagnose lung cancer, these results did not offer a statistical significant difference in the miRNA-21-5p concentration between average groups (IIIA [4.290]; IIIB [4.383]; IV [4.074], with a p-value = 0.4833). The limitations of the study such as the limited number of samples, and above all, the difficulty in collecting early-stage lung cancer samples (we only evaluated lung cancer III and IV stages, in which metastasis has started in some cases) offered a non-conclusive correlation between miRNA-21-5p plasma concentration and cancer stage. A more extensive study has to be performed, with a larger number of samples and a more variety of lung cancer samples (if possible from stage 0 to stage IV).

5.2.5. Conclusions

MiRNAs are small molecules that can regulate gene expression affecting a wide variety of cellular processes such as proliferation, differentiation and apoptosis. These features make miRNAs suitable biomarkers for cancer diagnosis and prognosis. We have demonstrated the potential of evanescent wave optical sensors, especially SPR and BiMW biosensors, to identify miRNA-21-5p, miRNA-210-3p and miR205-5p biomarkers for lung cancer diagnosis. Both optical biosensors were developed for complementary hybridisation assays. For gold sensor surfaces, a direct and rapid DNA probes immobilisation was carried out via thiol-gold linkage. However, the limit of detection achieved for each miRNAs were in the nM range (miRNA-21-5p=1.23 nM ; miRNA-205-5p=2.35 nM and miRNA-210-3p= 1.98 nM) not enough for the clinical range reported for miRNA in plasma (fM-nM).

In order to perform an accurate clinical validation, the assay was transferred to the BiMW biosensor. The complementary hybridisation approach was carried out by the covalent immobilisation of thiol-DNA probes over an APTES and PDITC-activated sensor surface. The miRNA assay offered excellent specificity and a limit of detection in plasma of 381 pM. A clinical validation (n=40) was performed with the BiMW biosensor, comparing the performance with the benchmark qRT-PCR methodology. Statistical analysis showed excellent discrimination between healthy and NSCLC cancer samples (p-value<0.0001), with a similar performance to qRT-PCR but without RNA extraction or amplification steps. ROC curves reported a diagnostic sensitivity and specificity of 80 % in both cases. Finally, to evaluate the capabilities of our approach for the early diagnosis of lung cancer, a preliminary study was conducted. However, no conclusive evidence was obtained since clinical samples at stages 0, I or II would be necessary to complete the analysis and to extract relevant conclusions.

The BiMW biosensor allows one-step and real-time quantitative analysis of miRNAs without amplification steps or sample pre-treatment steps. Moreover, it provides a sensitivity and specificity similar to conventional qRT-PCR. The described methodology represents a relevant step towards the implementation of this biosensor for clinical diagnosis, specifically in lung cancer diagnostics.

5.3. DNA methylation profiling for lung cancer diagnosis

5.3.1. DNA methylation and lung cancer

Epigenetic englobe heritable gene expression changes that occur independently of changes in DNA nucleotide sequence. Epigenetic events can control transcriptional activity, chromatin structure, X-chromosome inactivation and genomic imprinting, among other processes[191,210]. The mechanisms that might take place for epigenetic regulation are the methylation of DNA, modifications of histones, and positioning of nucleosomes along the DNA. One of the most relevant epigenetic events is DNA methylation which consists of the covalent addition of a methyl group (–CH_3) at the 5 positions of the nucleotide cytosine (**Figure 5.15A**). 5-Methylcytosines are positioned in dinucleotides repeated along areas of 0.2 to 1 kilobases called CpG islands and found mostly in the promoter and/or the first exon region of the genes[210,211] (**Figure 5.15B**). Nearly 60% of human promoters are estimated to be characterized by high-CpG content[212].

DNA methylation is a dynamic and reversible process mediated by enzymes known as DNA methyltransferases (DNMTs)[191]. The human genome encodes five DNMTs: DNMT1, DNMT2, DNMT3A, DNMT3B and DNMT3L. DNMT1, DNMT3A and DNMT3B are canonical 5-methylcytosine DNMTs that catalyse the addition of methyl group onto cytosine. On the other hand, DNMT2 and DNMT3L do not offer catalytic DNMT activity[213].

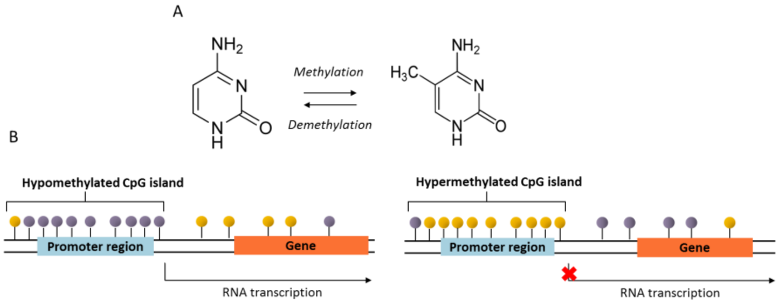

Figure 5.15. DNA methylation. (A) Addition of methyl group in the 5 positions of the cytosine nucleotide and its reversibility (B) RNA transcription regulated by DNA methylation levels in the CpG islands in the promoter region of genes[191].

The capability to regulate the gene expression turns DNA methylation into a relevant mechanism involved in cell development and proliferation, and hence, in cancer. Tumour cells are characterized by a different methylome than normal cells. Interestingly, both hypo- and hypermethylation events can be observed in cancer. Hypomethylation is a genome-wide feature in cancer cells[214], contributing to genomic instability, reactivation of transposable elements, loss of imprinting and, less frequently, activation of silenced oncogenes[215]. Otherwise, hypermethylation in promoter regions of specific genes is a relevant hallmark in many cancer cells and implies gene silencing[211] (**Figure 5.15B**). The mechanism by which hypermethylation silences genes is through the recruitment of methyl-binding proteins (as MeCP2) and associated factors such as histone deacetylases that contribute to chromatin remodeling and non-viable transcription[210,215,216]. Hypermethylation of CpG islands in the promoter regions of tumour-suppressor, cell cycle, apoptosis and DNA repair genes, can lead to a cancerous process[211,217].

The reversibility and dynamism of the CpGs methylation process offers the possibility to identify it in different biologic fluids, pointing DNA methylation as a promising biomarker for non-invasive cancer diagnosis and prognosis[191,218]. Free tumour DNA released after cell lysis or even directly tumour cells can be collected from biological fluids such as blood, stool, saliva or urine samples[219].

In addition, the hypermethylated gene signature varies between cancers from different organs[220]. Certain genes such as *CDKN2A* (also known as *p16INK4A*) show promoter hypermethylation in almost all cancers. However, other genes present high methylation levels only in specific tumour types[221]. In the case of lung cancer , different diagnosis gene signatures have been described[222] and summarised in **Table 5.8**. Moreover, due to the prognosis and therapeutic follow-up capabilities, new signature genes have been reported[223–225].

Table 5.8. Epigenetic signature of DNA methylation related to lung cancer.

Gene signature	References
CDO1, *ZNF177*, *BRAC1* and *TRIM50*	189

SHOX2	226
APC, *CDH13*, *KLK10*, *DLEC1*, *RASSF1A*, *EFEMP1*, *SFRP1*, *RARβ* and *p16INK4A*	190
CDO1, *HOXA9*, and *TAC1*	227
p16, *TERT*, *WT1*, and *RASSF1*	228
p16, *RASSF1A*, *H-cadherin*, and *RARβ*	229

The conventional methodologies to detect DNA methylation are summarised in three types: (1) Bisulfite conversion of DNA, (2) the use of methylation-sensitive restriction enzymes, or (3) chromatin immunoprecipitation (ChIP) assays. The first strategy combines bisulfite conversion with subsequent analytical techniques. Bisulfite treatment converts unmethylated cytosines to uracil, without affecting methylated cytosines. Then, restriction analysis or PCR amplification are performed for the analysis of the DNA methylation level. In the other strategies, methylation-sensitive restriction enzymes which cannot digest methylated nucleosides and specific antibodies against 5-methylcytosines in DNA microarray chips or methyl-CpG binding proteins are employed. However, these biomolecular techniques can provide false results. Bisulfite and restriction enzyme reactions require optimal conditions (temperature, reagent concentration, time…) because failed or inappropiated conversion and cleveage frequencies can distort the methylation analysis. Moreover, they imply sophisticated, time-consuming and laborious techniques[230].

The detection of the methylation status using label-free optical biosensors has attracted attention over the last few years[231]. Different optical sensors such as SPR and silicon photonics sensors have been described. Regarding biofunctionalisation procedures, innovative bioreceptors and methodologies have been employed in SPR biosensing like novel alkylating linker molecules[232], PNAs[233], physical absorption above gold substrates[234], molecular inversion probes[235] and DNA biotinylated bulge[236]. For 5-methylcytosine (5mC) detection, a specific anti-5mC antibody[172,232,236] or the Methyl-CpG-binding domain (MBD) protein[237] have been used. In the case of silicon photonics biosensors, J. Yoon *et al.* reported a lab-on-a-chip device but it requires bisulfite methodology and DNA amplification steps[238]. Also, by using specific antibodies[239] in toroidal resonant cavities were able to discriminate other epigenetic events such as 5-hydromethylcitosines and using a nanowire-transistor achieved a LOD of 2.5 × 10^{-19} mol although magnetic beads procedure off-chip was required[240].

We propose the use of plasmonic and interferometer biosensors for the identification of the methylation profiling of the *CDO1* and *ZNF177* genes, involved in lung cancer since cysteine dioxygenase 1 (CDO1) regulates intracellular cysteine metabolism[241] and zinc finger protein 177 (ZNF177) is a zinc finger transcription factor[189]. Our methodology approach consists of a rapid and reliable strategy based on PPRH probes and a specific anti-5mC antibody, which does not require bisulfite treatment or DNA amplification.

5.3.2. Materials and methods

5.3.2.1. Chemical reagents

Solvents used for sensor chips cleaning (acetone 99.5%, ethanol 99%, methanol 99%, hydrochloric acid (HCl, 37 %), nitric acid (HNO_3, 65 %) were purchased from Panreac Applichem (Barcelona, Spain). All the buffers compounds: sodium citrate buffer (SSC) 20X (3 M NaCl, 0.3 M sodium citrate, EDTA 4 mM, pH 7.4), phosphate immobilisation buffer 50 mM (NaCl 0.84 M, KCl 13.5 mM, Na_2HPO_4 50 mM, KH_2PO_4 9 mM, EDTA 10 mM, pH 7.1), phosphate buffer saline (PBS) 10 mM (NaCl 0.137 M, KCl 2.7 mM, Na_2HPO_4 10 mM, KH_2PO_4 1.8 mM pH 7, anhydrous toluene 99.8%, N, N-dimethylformamide anhydrous ≥99.8%, (DMF), anhydrous pyridine 99.8%, crosslinking molecule p-phenylene diisothiocyanate 98% (PDITC), 3-aminopropyltriethoxy silane ≥98%, (APTES), N, N-diisopropylethylamine (DIPEA), diethyl pyrocarbonate (DEPC), Tween 20 and bovine serum albumin (BSA) were acquired from Sigma-Aldrich (Darmstadt, Germany). Lateral spacer SH-PEG-CH_3 (MW 2000 $g \cdot mol^{-1}$) was purchased from Laysan Bio (Alabama, US). Bond-Breaker™ TCEP Solution (tris(2-carboxyethyl)phosphine hydrochloride solution) was purchased from ThermoFisher (Massachusetts, US). Human pooled plasma was purchased from Innovative Research (Michigan, US). Antibodies specific against 5-

methylcytosines (anti-5mC) and 5-Hydroxymethylcytosine (anti-5hmC) were purchased from Genetex (California, US).

To work under sterile conditions, all the labware used was sterilized, and buffer solutions were prepared with milli-Q H_2O treated with 0.1% DEPC and autoclaved at 121º C for 1 hour.

5.3.2.2. PPRH probes and nucleotide sequences

PPRH sequences were synthesized by the Group of Prof. R. Eritja from the Department of Chemical and Biomolecular Nanotechnology Group at the Institute of Advances Chemistry of Catalonia (IQAC), CSIC (Spain). Sequences were prepared on an Applied Biosystems 3400 (Applied Biosystems, California, US) synthesizer using controlled-pore supports (scale 1 µM) according to the protocols of the manufacturer. Thermal UV denaturation and CD studies were carried out to assess the triplex structure. Methylated and unmethylated sequences of *CDO1* and *ZNF177* genes were purchased from Ibian Technologies (Zaragoza, Spain). All nucleotide sequences are summarised in **Table 5.9**.

Table 5.9. Nucleotide sequences employed for DNA methylation study.

Sequence name	Nucleotide sequence (5’→3’)
PPRH CDO1	Thiol-(T15)-GGAGGCGGGAGA- (T4) GGAGGCGGGAGACCCTGCGGGC
CDO1 (+)	CTT GGG AAG GCG CGG AGC CCG GGG AAG CCG GGG ATG TGC GCG TGA GCC GTG CCC GCA GGG TCT CCC CGC CTC CGC CAC CT
CDO1 (-)	AGG TGG CGG AGG CGG GGA GAC CCT GCG GGC ACG GCT CAC GCG CAC ATC CCC GGC TTC CCC GGG CTC CGC GCC TTC CCA AG
CDO1 (-)x1CpG	AGG TGG CGG AGG CGG GGA GAC CCT GCG GGC ACG GCT CAC* GCG CAC ATC CCC GGC TTC CCC GGG CTC CGC GCC TTC CCA AG

CDO1 (-)x3CpG	AGG TGG CGG AGG CGG GGA GAC CCT GCG GGC AC*G GCT CAC* GCG CAC ATC CCC GGC TTC CCC GGG CTC CGC* GCC TTC CCA AG
CDO1 (-)x6CpG	AGG TGG CGG AGG CGG GGA GAC CCT GCG GGC AC*G GCT CAC* GC*G CAC ATC CCC* GGC TTC CCC* GGG CTC CGC* GCC TTC CCA AG
CDO1 (+)x1CpG	CTT GGG AAG GCG CGG AGC CCG GGG AAG CCG GGG ATG TGC GC*G TGA GCC GTG CCC GCA GGG TCT CCC CGC CTC CGC CAC CT
CDO1 (+)x3CpG	CTT GGG AAG GC*G CGG AGC CCG GGG AAG CCG GGG ATG TGC GC*G TGA GCC* GTG CCC GCA GGG TCT CCC CGC CTC CGC CAC CT
CDO1 (+)x6CpG	CTT GGG AAG GC*G CGG AGC CC*G GGG AAG CC*G GGG ATG TGC* GC*G TGA GCC* GTG CCC GCA GGG TCT CCC CGC CTC CGC CAC CT
PPRH ZNF177	Thiol-(T15)-GAAAGGGGTGGG- (T4) GAAAGGGGTGGGCTGCCCAGCT
ZNF177 (+)	GCG AGC TGG GCA GCC CAC CCC TTT CAG CTG CTG GCC GGA AGC GGA AGT GGG CGT CCG TCG CCT CGC CAT CTC CCA TAG CT
ZNF177 (-)	AGC TAT GGG AGA TGG CGA GGC GAC GGA CGC CCA CTT CCG CTT CCG GCC AGC AGC TGA AAG GGG TGG GCT GCC CAG CTC GC
ZNF177 (-)x1CpG	AGC TAT GGG AGA TGG CGA GGC GAC GGA C*GC CCA CTT CCG CTT CCG GCC AGC AGC TGA AAG GGG TGG GCT GCC CAG CTC GC
ZNF177 (-	AGC TAT GGG AGA TGG CGA GGC GAC* GGA C*GC CCA CTT CC*G CTT CC*G GCC AGC AGC TGA AAG GGG TGG GCT

)x4CpG	GCC CAG CTC GC
ZNF177 (-)x6CpG	AGC TAT GGG AGA TGG C*GA GGC* GAC* GGA C*GC CCA CTT CC*G CTT CC*G GCC AGC AGC TGA AAG GGG TGG GCT GCC CAG CTC GC
ZNF177 (+)x1CpG	GCG AGC TGG GCA GCC CAC CCC TTT CAG CTG CTG GCC GGA AGC GGA AGT GGG C*GT CCG TCG CCT CGC CAT CTC CCA TAG CT
ZNF177 (+)x4CpG	GCG AGC TGG GCA GCC CAC CCC TTT CAG CTG CTG GCC GGA AGC* GGA AGT GGG C*GT CCG TC*G CCT C*GC CAT CTC CCA TAG CT
ZNF177 (+)x6CpG	GCG AGC TGG GCA GCC CAC CCC TTT CAG CTG CTG GCC* GGA AGC* GGA AGT GGG C*GT CC*G TC*G CCT C*GC CAT CTC CCA TAG CT

5.3.2.3. Sensor surface biofunctionalisation with PPRH probes

PPRH probes for the detection of the DNA methylation profiling, were modified in the 5'end with thiol groups for their attachment to the sensor surface. Therefore, the approach used for DNA methylation probes coupling is the same as the above-reported for miRNAs. To optimise the assay for *CDO1* and *ZNF177* detection in double-strand DNA format and CpG island quantification, some parameters such as the lateral spacers and buffer conditions differed.

PPRH probes coupling in gold surface

For the *in-situ* immobilisation of the PPRH probes via chemisorption, the clean sensor chips were placed in the experimental set-up and a constant flow (10 µL·min^{-1}) of DEPC–H$_2$O and a solution of the PPRH and lateral spacer (SH-PEG-CH$_3$) in a ration 1:1 at a final concentration of 2 µM prepared in 50 mM PBS was flowed (**Figure 5.16**). Before the immobilisation, the PPRH probe solution was incubated with 1 µM of TCEP for 20 min at 37^{o} C.

For analysis of the *CDO1* gene in 10 % diluted plasma, an additional blocking step was performed. A solution of BSA 10 mg· mL^{-1} in PBS 10 mM was flowed at a constant rate of 10 µL·min^{-1} over the sensor surface after PPRH immobilisation for blocking the sensor surface and avoiding non-specific adsorptions from the plasma matrix.

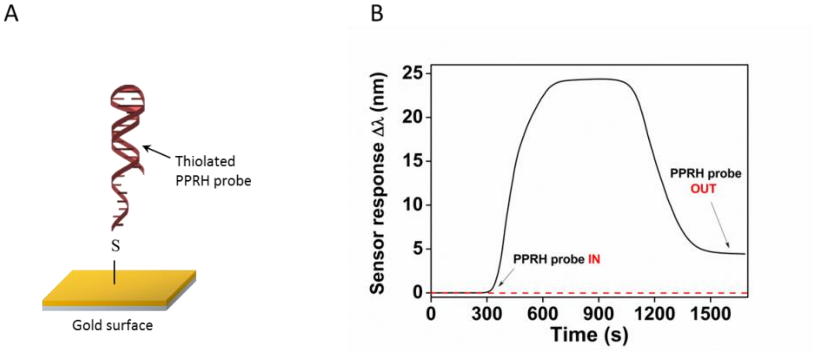

Figure 5.16. Gold SPR surface biofunctionalisation.(A) Scheme of the functionalisation performed for the detection of CpG islands in *CDO1* and *ZNF177* genes. (B) Real-time sensorgram of the one-step coupling of PPRH probe / lateral spacer (SH-PEG-CH_3).

PPRH probe coupling in silicon nitride surface

Following the protocol described in **Section 5.2.2.3** for miRNA assays in BiMW biosensor, PPRH probes were attached to the silicon nitride surface. Briefly, after APTES silanisation and PDITC crosslinker activation, BiMW sensor chips were placed on the experimental set-up for the *in-situ* immobilisation of the thiol PPRH probes (**Figure 5.17**). A solution of PPRH probes and SH-PEG-CH_3 lateral spacer was injected into the sensor at a constant rate of 3 µL·min^{-1} using DEPC-H_2O as running buffer. The immobilisation solution consisted of a combination of PPRH probes and SH-PEG-CH_3 (in a ratio of 1 µM :1 µM) in 50 mM PBS buffer. Additionally, and before the injection, the immobilisation solution was incubated with 1 µM TCEP solution in constant agitation for 20 min at 36° C.

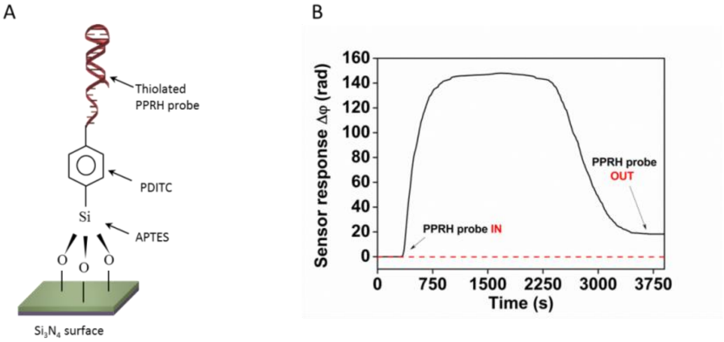

Figure 5.17. Si_3N_4 BiMW surface biofunctionalisation. Scheme of the functionalisation performed for the detection of CpG islands in *CDO1* and *ZNF177* genes. Real-time sensorgram of the PPRH probe/lateral spacer (SH-PEG-CH_3) immobilisation over a PDITC-APTES activated surface.

5.3.2.4. DNA hybridisation

Single-stranded (ss-DNA) and double-stranded DNA (ds-DNA) analyses were performed by injecting different DNA concentrations, ranging from 1 nM to 100 nM at a constant flow rate of 10 µL·min^{-1}. Target DNA sequences were dissolved in 5X SSC buffer with different percentages of formamide depending on the gene (*CDO1* 20% and *ZNF177* 30%).

Analysis in plasma was carried out by spiking 100 nM ds-DNA in 10 % diluted plasma in SSC5X with different concentrations of FA. DNA samples were flowed at a 10 µL·min^{-1} rate using SSC 0.5 X + 0.1 % Tween as running buffer.

Ds-DNA sequences were generated from the hybridisation of single strands. Double-stranded DNA fragments were obtained by incubating both strands (sense (+) and antisense (-)), in a ratio of 1:3 M respectively, of lung cancer genes at 95 °C for 5 min. Excess of (-) strand is added to the incubation solution to avoid free (+) strand without forming ds-DNA and being captured by the PPRH in a single strand mode. After hot incubation, the sequences were cooled down for 1 h at RT.

In all cases, even after 5-mC recognition by a specific antibody, DNA target-PPRH probe interactions were disrupted by employing 20 mM NaOH solution for 2 min.

5.3.2.5. CpG islands detection

For CpG island methylation profiling, anti-5mC and anti-5hmC antibodies were diluted in PBS 10 mM buffer at a final concentration of 2 $\mu g \cdot mL^{-1}$. After DNA hybridisation and using SSC 0.5 X + 0.1% Tween as running buffer, the antibody solution was flowed over the sensor surface at 10 $\mu L \cdot min^{-1}$.

5.3.2.6. Data analysis

Biosensor data were analyzed and processed using Origin 8.0 software (OriginLab, Massachusetts, US). Data and statistical analysis (Kruskal-Wallis test) were performed using Graphpad Prism (Graphpad Software, Inc., California, US). For DNA calibration curves, the mean sensor response ($\Delta\lambda$ or $\Delta\varphi$) and its standard deviation (SD) were plotted as a function of the DNA concentration. Calibration curves were fitted to a linear regression model (**Equation 3.1**) or one-site specific binding equation (**Equation 4.1**). For 5mC quantification, the mean sensor response ($\Delta\lambda$ or $\Delta\varphi$) and its standard deviation (SD) were plotted as a function of the DNA methylation level (number of CpGs).

The experimental LOD was determined as three times the SD of the sensor signal obtained from a blank signal using only the running buffer. The coefficients of variation were obtained as the ratio of the standard deviation of the mean, expressed in percentages (% CV).

5.3.3. Assessment of CpG island quantification in lung cancer genes using SPR biosensor

To develop a biosensor methodology capable of identifying the DNA methylation profiling of promoter region in two lung cancer-related genes (*CDO1* and *ZNF177*), we designed an assay consisting of two recognition steps: (1) capture of ds-DNA fragment through complementary PPRH probe and (2) quantification of the number of methylated cytosine residues through a specific antibody against 5-methylcytosines (**Figure 5.18**).

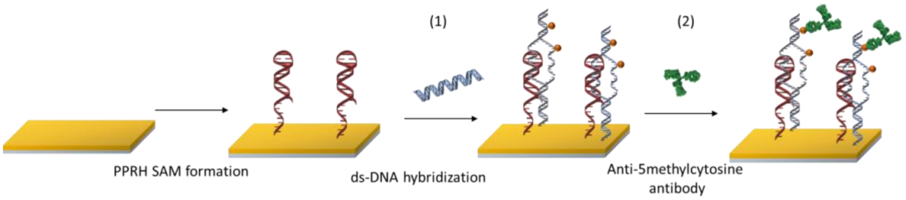

Figure 5.18. CpG island methylation level. Scheme representation of the biosensor strategy performed for ds-DNA capture and 5mC detection.

5.3.3.1. Optimisation of the DNA methylation assay

PPRH probes are ideal for our methodology since they can recognise ds-DNA by DNA displacement in a triple helix approach. In **Section 4.3.1.**, an optimisation of the biorecognition layer with PPRH probes and combinations of different lateral spacers was described. Additionally, C. S. Huertas *et al.* also described a protocol for PPRH probes in SPR biosensor for DNA methylation profiling[172]. Due to the previously described biofunctionalisation process, we only study the effect of uncharged lateral spacer (SH-PEG-CH3) in gene accessibility and capture by PPRH probes. **Figure 5.19** shows the sensor response for the detection of *ZNF177* gene 100 nM in two different biolayers, in the presence and absence of lateral spacers in the biorecognition layer. The incorporation of a lateral spacer with a net charge such as SH-PEG-CH_3 increased the sensor performance up to twice, improving DNA target accessibility and showing a higher sensor response ($\Delta\lambda \approx 0.15$) compared to a layer full of PPRH probes ($\Delta\lambda \approx 0.075$).

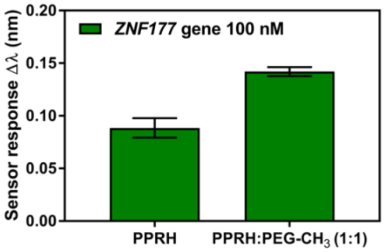

Figure 5.19. Lateral spacer effect. Sensor response to *ZNF177* gene detection with and without SH-PEG-CH_3 lateral spacer. Each signal corresponds to the mean ± SD of triplicate measurements.

In addition to the biorecognition layer, the length of the target sequences is crucial to ensure an adequate hybridisation event. The long length of the *CDO1* and *ZNF177* target sequences, consisting of 80 nucleotides, could originate the self-hybridisation and formation of secondary structures which would hinder the recognition by PPRH probes. To guarantee the capture of the DNA by the hybridisation between the PPRH and the complementary area in the target, different FA percentages in the injected samples were tested. As can be observed in **Figure 5.20**, the capacity of the PPRH to detect *CDO1* and *ZNF177* sequences depended on the concentrations of FA present in the injected samples. Although both sequences share the same number of nucleotides, they required different FA percentage due to their different GC% content. The most recommendable percentages of FA were 20 % for *CDO1* and 30 % for *ZNF177* genes, respectively.

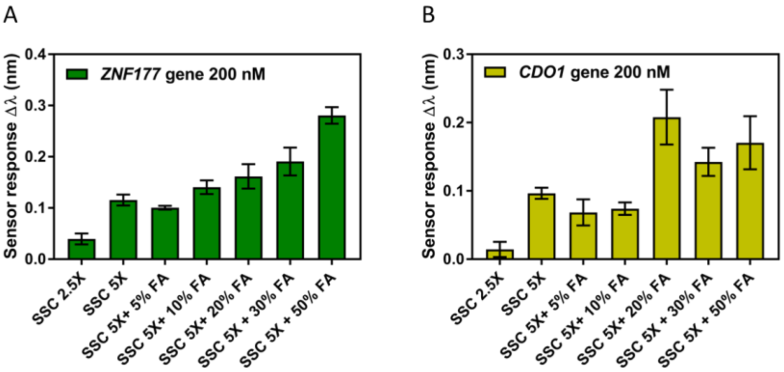

Figure 5.20. Formamide effect for (A) *ZNF177* and (B) *CDO1* genes detection. Sensor response to 100 nM of gene *CDO1* and *ZNF177* dissolved in SSC5X with different concentrations of FA.

As the designed biosensor assay for the DNA methylation profiling was composed of two recognition steps, ds-DNA had to be captured by PPRH probes before 5mC quantification. Firstly, analyses of the biosensor sensitivity for the detection of the ds-DNA were carried out through the elaboration of calibration curves. As we can see in **Figure 5.21A**, the higher *CDO1* ds-DNA concentration, an increase in the sensor response is reflected, indicating a direct and linear behaviour that enables the establishment of calibration curves for both genes (**Figure 5.21BC**) with a limit of detection of LOD = 4.29 nM (R^2=0.9326) for *CDO1* gene and LOD= 3.90 nM (R^2 = 0.9584) for *ZNF177* gene.

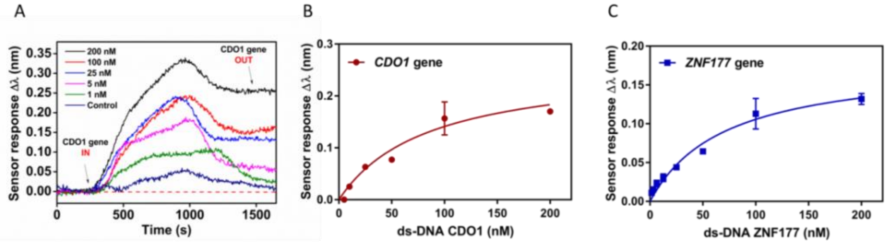

Figure 5.21. SPR-based *CDO1* and *ZNF177* assay in buffer condition. (A) Real-time sensorgrams showing the specific interaction of PPRH probes with different *CDO1* ds-DNA concentrations. (B) Calibration curve of *CDO1* gene in buffer conditions. (C) Calibration curve of *ZNF177* gene in buffer conditions. Each signal corresponds to the mean ± SD of duplicated measurements.

After the capture of the ds-DNA, identification and quantification of the 5-methylcytosines could be performed by employing a specific antibody against this type of cytosines residues. To validate the whole assay and ensure the correct performance of the biosensor, only the antisense sequence (-) of the ds-DNA target was modified with the incorporation of different amounts of cytosines (*CDO1* 1,3,6xCpGs and *ZNF177* 1,4,6xCpGs). However, the sense sequence (+), which is the sequence complementary to the PPRH probe to form the triple helix, did not present any methylation in its cytosine nucleotides. Therefore, if a sensor signal was observed after anti-5mC antibody injection meant that DNA hybrids (ds-DNA) have been formed and the methodology could successfully capture them and identify the level of methylation in their sequences.

To evaluate the performance of the above-described methodology, 100 nM ds-DNA of *CDO1* and *ZNF177* genes with different methylation levels (1, 3 and 6xCpGs for *CDO1* and 1, 4 and 6xCpGs for *ZNF177*, respectively) were flowed over the plasmonic sensor surface, being captures by the PPRH probes. Finally, the specific anti-5mC antibody was able to detect the 5-methylcytosines residues.

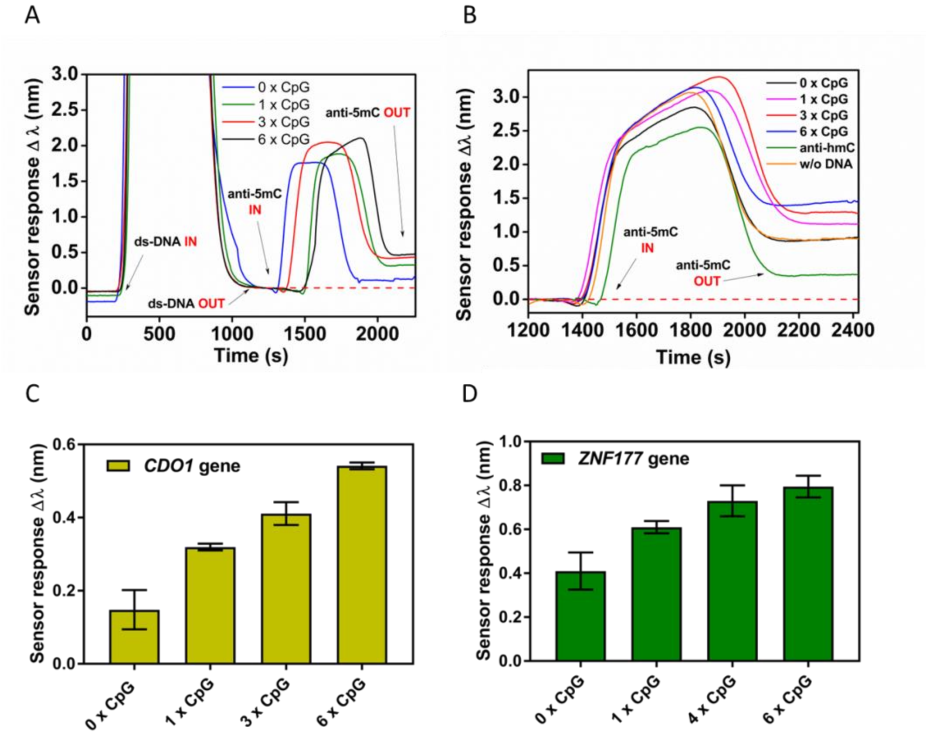

Figure 5.22. DNA methylation profiling of *CDO1* and *ZNF177* genes. Real-time sensorgrams showing the interaction of anti-5mC antibody with ds-DNA hybrids with different amounts of 5mC in the promoter regions of (A) CDO1 and (B) ZNF177 genes. Control conditions such as no DNA hybrids (w/o DNA), unmethylated (0xCpGs) and anti-5hmC antibody were measured. Interaction of anti-5mC antibody with four different methylation profiles (0x, 1x, x3, 4x and x6 CpGs) in (C) *CDO1* (Test Kruskal-Wallis p-value= 0.0095) and (D) *ZNF177* (p-value =0.0381) All data show mean ± SD of duplicated measurements.

Figure 5.22 shows that in both cases the presence of a larger number of 5-methylcytosines produced an increase in thebiosensor response. Even though the anti-5mC antibody produced non-specific interactions with the gold surface ($\Delta\lambda \approx 0.3$ nm), it was capable to discriminate the methylation level of the DNA sequences. The sensor response to the anti-5mC antibody step increased by 50 % or higher in hybrids containing six methyl groups compared with unmethylated ones. Statistical analysis performed through Kruskal-Wallis tests for both genes informed of a p-value = 0.0095 in *CDO1* and p-value=0.031 in *ZNF177* genes, respectively. P-values were lower than the cut-off of 0.05, reflecting significant differences between methylation conditions. These results confirmed the feasibility of the

DNA methylation approach, where ds-DNA was captured through PPRH probes and subsequently 5mC was identified by a specific antibody. Moreover, the simplicity of the assay allowed it to be successfully performed independently of the gene sequence.The described methodology is an outstanding step for the quantification of DNA methylation status in an amplification- and bisulfite-free format.

The specificity of the assay was evaluated by using an antibody specific against other chemical modifications onto the cytosine nucleotides such as the presence of 5-hydroxylmethylcytosines (5hmC). **Figure 5.22B** represents the sensor response after anti-5hmC injection when ds-DNA 6xCpGs target sequences were captured by the PPRH probes. The sensor signal reported for the 5hmC antibody is lower than the sensor signal achieved with the anti-5mC antibody in absence of DNA or the presence of unmethylated hybrids. These results indicate that anti-5hmC did not cross-react with 5mC residues, verifying the specificity of the antibody against the correct epigenetic DNA modification.

The reproducibility of the DNA methylation profiling assay was evaluated through the inter-assay (% CV), in which the reported values were lower than the highest variability advised (15 %)[142] (**Table 5.10**), affirming the excellent suitability of the plasmonic biosensor for the DNA methylome identification.

Table 5.10. Inter-assay variability of *CDO1* and *ZNF177* genes for CpG island quantification

Methylation level	***CDO1***		***ZNF177***	
	Mean ± SD	**%CV**	**Mean ± SD**	**%CV**
0xCpGs	0.15 ±0.04	25.7	0.41±0.06	14.6
1xCpGs	0.32±0.007	2.03	0.61±0.02	3.28
3xCpGs	0.41±0.02	5.35	-	-
4xCpGs	-	-	0.73±0.05	6.84
6xCpGs	0.54±0.006	1.20	0.79±0.03	4.40

5.3.3.2. Preliminary analysis: *CDO1* gene methylation level in plasma

Above-described results corroborated the capacity of the plasmonic biosensor for CpG island quantification. This methodology opens the way to bisulfite and amplification-free analysis, reducing false results, turnaround times and sophisticated protocols.

As a final validation of our methodology, we carried out the analysis of the DNA methylation status in real plasma samples. A preliminary evaluation of the *CDO1* DNA methylation level was performed in 10 % diluted plasma to check the effect of the complex matrix components on the ds-DNA recognition and the 5mC quantification. As previously, 5hmC antibody was used as control.

As we can see in **Figure 5.23**, the sensor response increased as a function of the amount of 5mC present in the ds-DNA *CDO1*. Despite the dissolution of the ds-DNA hybrids in the plasma samples, the plasmonic sensor was able to behave in a similar manner as in the standard buffer conditions, discriminating with statistical significance between DNA methylation levels. The Kruskal-Wallis test afforded a p-value = 0.0138, meaning a slighly limited performance compared to standard buffer conditions (p-value= 0.0095). The 10 % dilution was selected just to minimise non-specific blood component interactions. However, the presence of plasma compounds could somewhat hinder PPRH-ds-DNA hybridisation or anti-5mC recognition. This effect could be also observed comparing the sensor response for the anti-5mC antibody for the same methylation condition. For example, for 6xCpGs in buffer conditions, the sensor signal was Δλ≈0.56 nm, whereas in plasma was Δλ≈ 0.35, verifying the interferences in the biosensor assay due to the presence of plasma.

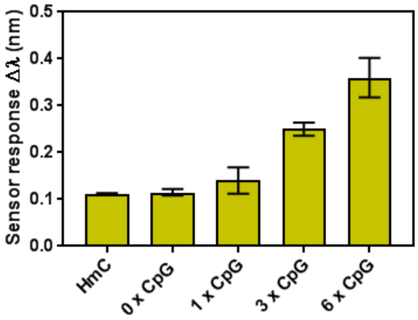

Figure 5.23. DNA methylation profiling of *CDO1* in diluted plasma. Interaction of anti-5mC antibody with four different methylation profiles (0x, 1x, x3, and x6 CpGs) in the *CDO1* gene. Control 5-hmC antibody were also employed. (Test Kruskal-Wallis p-value = 0.0138).

The specificity of the biosensor assay was checked in plasma conditions using an anti-5hmC antibody. This antibody did not interact with 6xCpGs ds-DNA, providing a sensor signal extremely like the response shown for anti-5mC antibody after the unmethylated ds-DNA target capture. Plasma dilution did not affect the specificity of the assay, reporting a good discrimination between DNA epigenetic modifications.

Further studies on antifouling properties should be performed to prevent non-specific interactions of biological fluids, such as plasma. These studies would avoid dilution of plasma samples and even hindrance of recognition events during the assay. In addition, analytical parameters such as sensitivity and reproducibility need to be reanalyzed to ensure a feasible and accurate plaamonic biosensor assay.

On the other hand, the idea of developing a multiplex biosensor for a comprehensive diagnosis of lung cancer biomarkers and the sensitivity limitations previously presented by the plasmonic biosensor for the diagnosis of miRNAs, motivated the transfer of the described methodology to the BiMW biosensor.

5.3.4. Detection of *CDO1* DNA methylation profile using BiMW biosensor

By mimicking the biofunctionalisation strategy employed for the miRNAs assays, we attached thiol DNA probes in an APTES silanised and PDITC activated surfaces. In addition, we followed the methodology optimised for the SPR biosensor for a preliminary pilot analysis of the *CDO1* gene methylation profiling in standard buffer conditions using the BiMW biosensor.

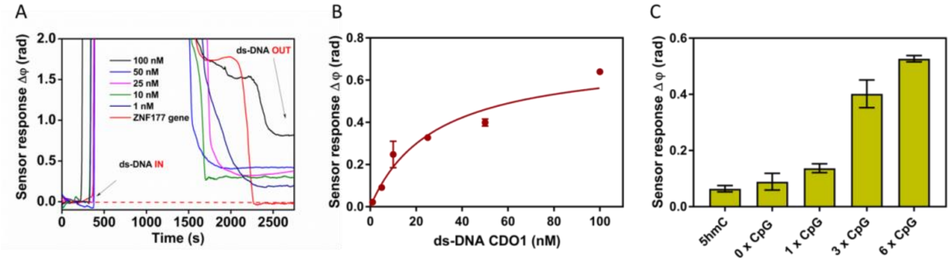

Figure 5.24. DNA methylation profiling of *CDO1*. (A) Real-time sensorgrams showing the interaction of ds-DNA and PPRH probe. (B) Calibration curve of *CDO1*. (C) Interaction of anti-5-methyl-CpG antibody with three different methylation profiles (0x, 1x and 4x CpGs) in *CDO1* (Test Kruskal-Wallis p-value = 0.0032). All data show mean ± SD of duplicate measurements**.**

As previously described for the SPR biosensor, a two-step biosensor assay was carried out to capture the ds-DNA *CDO1* gene and subsequently, the 5mC status was quantified using the specific anti-5mC antibody on the (-) strand of the DNA. **Figure 5.24** verifies the excellent performance of the PPRH probes and the 5mC-antibody strategy, which were able to be reproducible in a different biosensor as is the BiMW one. Regarding ds-DNA capture, the real-time sensorgram and the calibration curve in **Figure 5.24AB** show the capability of the PPRH probes to identify ds-DNA hybrids in a direct association. The limit of detection achieved with the interferometric sensor was LOD= 0.40 nM (R^2= 0.9048). The better sensitivity reported by the BiMW sensor compared to the plasmonic one was again demonstrated, improving the LOD up to one order of magnitude. Concerning the 5mC detection and quantification, the BiMW-based approach also ameliorated the SPR outcome since the statistical Kruskal Wallis test indicated a p-value =0.0032. Additionally, the biosensor assay maintained the specificity, achieving sensor response of the 5hmC antibody for 6xCpGs close to the signal obtained for 5mC antibody after unmethylated DNA-target capturing (**Figure 5.24C**).

Despite the good results in translating the methodology to silicon-based biosensors, additional studies need to be made to fine-tune the strategy in the nanophotonic biosensors. Analytical parameters such as sensitivity and reproducibility must be analysed to ensure that the assay is suitable for clinical practice. Also, optimisation of the blocking steps and evaluation of the sample in diluted or undiluted plasma should be performed to complete the validation of the strategy.

5.3.5. Conclusions

DNA methylation is an epigenetic event that can regulate gene expression without modifying the nucleotide sequence. This epigenetic event is involved in cell processes such as proliferation and development, being a relevant biomarker in cancer. Hypermethylation of specific genes is a hallmark of certain cancer such as *CDO1* and *ZNF177* in the lung cancer process. We have designed and fully developed a biosensing strategy to overcome the inherent disadvantages of traditional methodologies like the use of bisulfite pretreatment and PCR techniques. The designed biosensor assay was based on two recognition steps: (i) ds-DNA capturing by specific PPRH probes and (ii) 5mC detection and quantification by a specific anti-5mC antibody.

This biosensor methodology, applied in plasmonic and interferometric devices, has been demonstrated to be completely successful for DNA methylation profiling. Kruskal-Wallis statistical tests have reported significant discrimination between amounts of cytosine residues in all cases (SPR p-value=0.0095 and BiMW p-value=0.0032). Moreover, the specificity of the biosensor assay was evaluated using other antibodies specific to other DNA modifications such as 5- hydroxymethylcytosines, indicating no cross-reactivity with 5methylcytosines. The versatility of the evanescent wave biosensors would enable the detection of any other epigenetic modification like 5-formylcytosine and 5-carboxylcytosine whereas an antibody could specifically identify them.

To apply the methodology to clinical plasma samples, a preliminary study in the plasmonic biosensor was conducted using 10 % diluted plasma. Even though the sensor retains the ability to discriminate between levels of methylation (p-value= 0.0138), initial results indicated that the plasma matrix could interfere in ds-DNA capture or in the anti-5mC antibody recognition event, slightly worsening the discrimination of the DNA methylation status.

The designed biosensor strategy is a step forward towards introducing a more convenient way for the analysis of DNA methylation in the clinical practice. The biosensor offer a bisulfite and amplification-free analysis that would overcome the limitations associated to those conventional techniques. However, to adapt the biosensor assay to clinical implementation in plasma samples, a re-optimisation of the biofunctionalisation and blocking steps will be required for improving the ds-DNA capture and the 5mC detection while avoiding plasma non-specific adsorptions effects.

5.4. Evaluation of NSE protein for lung cancer diagnosis

5.4.1. Introduction

NSE also known as gamma (γ) enolase or enolase-2 (Eno2), is a glycolytic isoenzyme that catalyzes the decomposition of glycerol in the glycolytic pathway[242]. NSE consists of non-covalently linked dimers of either α, β or γ subunits, each having a molecular weight of 39 kDa[243] (**Figure 5.25**). NSE is mainly expressed in central and peripheral neurons and cellular lineages of the amine precursor uptake and decarboxylation (APUD) such as the thyroid, pancreas, intestine and lung[243,244]. Some studies demonstrate that overexpression of NSE may play a critical role in aerobic glycolysis and malignance proliferation of various tumours such as small-cell lung cancer, neuroblastomas and intestinal carcinoid[243–245]. NSE is clinically acknowledged as a well-established diagnostic, prognosis and therapeutic marker of SCLC and some studies also highlight its association with NSCLC[184].

Although NSE is an accepted biomarker for SCLC patients, its mechanism and biological role remain to be elucidated. Recent publications have reported that NSE could promote the epithelial-mesenchymal transition (EMT) process of SCLC cells by activating the Wnt/β-catenin signalling pathway. The interaction between NSE and β-catenin avoided the degradation of β-catenin protein, thereby promoting cell migration, invasion and distant metastasis[242,246].

The combination of the analysis of several protein biomarkers (CEA, CYFRA21-1, NSE…) continues to be the most accurate diagnosis method for cancer. However, NSE by itself has reported a sensitivity of 81.2 %, being possible to be used in solitude for lung cancer diagnosis[186,247]. Clinical studies differ in the cut-off value for NSE but a NSE concentration in serum above ≈ 11 $ng·mL^{-1}$ is a hallmark of SCLC[247–249]. Additionally, clinical studies have highlighted that NSE offers discrimination on SCLC cancer stages (>16 $ng·mL^{-1}$ limited stage *vs* extensive stage >50 $ng·mL^{-1}$)[246,250]; and cancer subtypes since NSE levels in SCLC can be > 70 $ng·mL^{-1}$, whereas it would be never higher than 20.5 $ng·mL^{-1}$ for NSCLC[249]. NSE has not only diagnostic values but also prognostic and predictive ones[251]. Moreover, NSE levels are correlated to chemotherapy response and survival rate[250,252].

The range of analytical techniques used for the detection of protein biomarkers related to clinical diagnosis is wide. Methodologies such as immunoassay (ELISA, LFA and chemiluminescence) and mass spectroscopy are the gold standard[253]. Some techniques are extremely sensitive and specific but they required trained personnel, arduous protocols and very expensive experimental platforms as in the case of mass-spectrometers. Otherwise, LFA can overcome those drawbacks with commercial and easy-to-use point-of-care devices, but their sensitivity and specificity are not enough.

A few optical biosensors have been employed for the NSE detection as lung cancer biomarker, but the electrochemical ones are the most reported for NSE identification[254]. Some SPR biosensors have been employed including different strategies as using aptamers as bioreceptors[255] or fluorescent detection[256,257], reaching a LOD of 3.9 nM or 0.5 ng·mL^{-1} detection, respectively

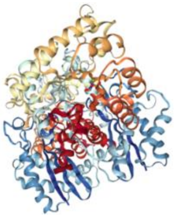

Figure 5.25. NSE protein structure

5.4.2. Materials and methods

5.4.2.1. Chemicals and biological components

Solvents used for sensor chips cleaning - acetone 99.5%, ethanol 99% and methanol 99%, hydrochloric acid (HCl, 37 %), nitric acid (HNO_3) and anhydrous toluene 99.8% were purchased from Panreac Applichem (Barcelona, Spain). All the buffer compounds, phosphate buffer solution PBS 10 mM (NaCl 0.137 M, KCl 2.7 mM, Na2HPO4 10 mM, KH2PO4 1.8 mM pH 7), MES 0.1 M (2-(N-morpholino) ethanesulfonic acid), HEPES (10 mM 4-(2-hydroxyethyl)piperazine-1-ethanesulfonic acid, 300 mM NaCl, pH 7.4), tris-HCl (Tris(hydroxymethyl)aminomethane hydrochloride) (50 mM TRIS-HCl, 150 mM NaCl), acetate (10 mM sodium acetate), bicarbonate buffer 0.1M pH 9.5 (74.2 mM sodium bicarbonate, 25.8 mM anhydrous sodium carbonate), bovine serum albumin (BSA), Tween 20, dextran sulfate sodium salt (DS) (MW~40000 g·mol^{-1}), 16-mercaptohexadecanoic acid (MHDA), 11-marcapto-1-undecanol (MUOH), (1-ethyl-4(3-dimethylaminopropyl)carbodiimide hydrochloride (EDC), ethanolamine hydrochloride (1 M, pH 8.5), N-hydroxysulfosuccinimide (sulfo-NHS), N, N-dimethylformamide anhydrous ≥99.8%, (DMF), anhydrous pyridine 99.8%, crosslinking molecule p-phenylene diisothiocyanate 98% (PDITC), (3-aminopropyl)triethoxysilane ≥98%, (APTES), N, N-diisopropylethylamine (DIPEA)were purchased from Sigma-Aldrich (Steinhem, Germany). Poly-L-lysine-graft-PEG (PLL-g-PEG) was purchased from SuSoS (Dübendorf, Switzerland). Triethoxysilane polyethylene glycol carboxylic acid (silane-PEG-COOH, 600 Da) was supplied by Nanocs (New York, US). Human pooled plasma was purchased from Innovative Research (Michigan, US). Recombinant NSE protein was obtained from OriGene Technologies (Rockville, MD, US) and the control human C-Reactive protein (CRP) from BBI Solutions (Crumlin, UK). Monoclonal antibody specific for NSE protein was purchased from HyTest Ltd. (Truku, Finland).

5.4.2.2. Surface biofunctionalisation

Antibody attachment in gold sensor surface

Anti-NSE antibody was attached to the gold sensor surface through covalent binding after a carboxyl SAM formation. Clean gold sensor chips were immersed in a solution of MHDA: MUOH (ratio 1:5 at 1 mM final thiol concentration) dissolved in ethanol overnight at RT in dark conditions. After rising and drying, the sensor chips were placed on the SPR instrument for *in-situ* covalent immobilisation. Flowing Milli-Q as running buffer at a constant rate of 15 µL·min^{-1}, a solution of EDC/sulfo-NHS was dissolved in MES buffer 0.1 M pH 6 at a final concentration of 0.2/0.05 M, respectively, and injected over the sensor surface for the activation of the carboxyl groups. A solution of 20 µg·mL^{-1} of the anti-NSE antibody dissolved in acetate buffer pH 5 was flowed over the activated surface. Finally, ethanolamine 1M pH 8.5 was injected for 2 min to block remained reactive carboxylic groups (**Figure 5.26**).

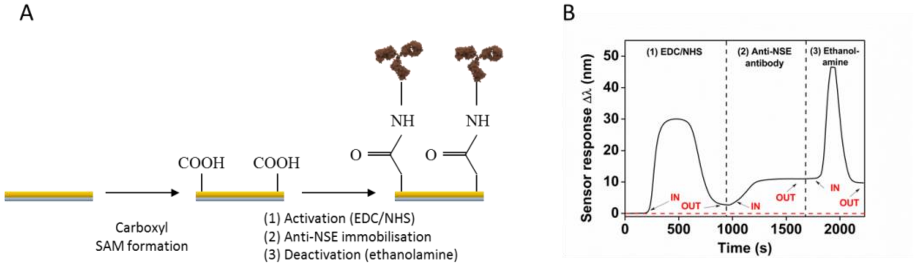

Figure 5.26. Anti-NSE antibody immobilisation in gold surfaces. (A) Scheme representation of the silanisation process by employing EDC/sulfo-NHS chemistry. (B) Real-time sensorgram of the three-step reaction of EDC/sulfo-NHS for anti-NSE antibody immobilisation

Antibody attachment in silicon nitride surface

In the same way as for the biofunctionalisation of silicon sensor surfaces with DNA probes, two organic silanes have been employed for the coupling of the anti-NSE antibody.

- **PEG-Carboxyl (COOH)** Si_4N_3 waveguide surface was silanized following the protocol described in **Section 5.2.2.3.** Once the PEG-COOH was formed over the sensor surface, sensor chips were placed in the experimental set-up and the carboxyl groups were activated by flowing a solution of EDC/sulfo-NHS 0.2/0.05 M in MES 0.1M pH 6, using Milli-Q water as running buffer at 10 µL·min-^{1}. Immediately, anti-NSE antibody 50 µg·mL^{-1} dissolved in acetate buffer 10 mM pH 5 was injected into the sensor. Finally, ethanolamine 1M pH 8 was flowed over the sensor surface for 2 min (**Figure 5.27**).

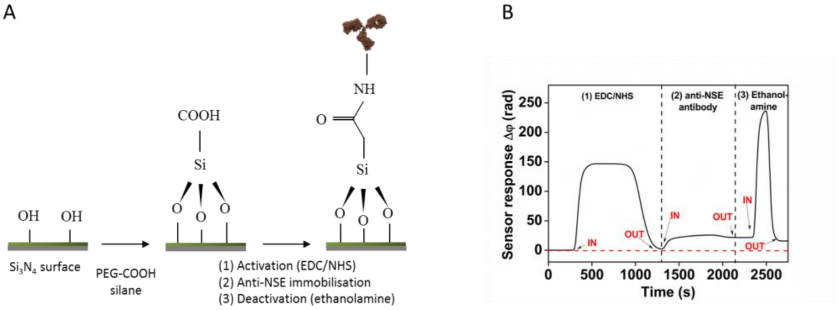

Figure 5.27. PEG silanisation. (A) Scheme representation of the silanisation process by employing PEG-carboxyl silane. (B) Real-time sensorgram of the three-step reaction for anti-NSE antibody immobilisation.

- **APTES. Section 4.2.2.3.2** describes the silanisation and activation surface with APTES silane and PDITC crosslinker respectively for the functionalisation of the BiMW sensor chips. In the case of antibody coupling, PDITC-activated sensor chips were placed in the experimental set-up and antibody attachment was carried out *in-situ*. Flowing Milli-Q water at a constant rate of 5 µL·min^{-1}, a solution of 50 µg·mL^{-1} anti-NSE antibody dissolved in bicarbonate buffer 0.1 M pH9.5 was injected.

  To avoid non-specific adsorptions from plasma samples, a blocking step was included by employing BSA 50 mg·mL^{-1} diluted in PBS 10 mM, which was injected over the sensor chip after the antibody attachment at 5 µL·min-1. Finally, ethanolamine 1 M pH 8 was flowed over the sensor surface (**Figure 5.28**).

  After the biofunctionalisation process, the sensor chips were kept under a continuous flow of MES 50 mM + 0.5 % Tween 20 + 10 mM DS at 10 µL min^{-1} until the analysis.

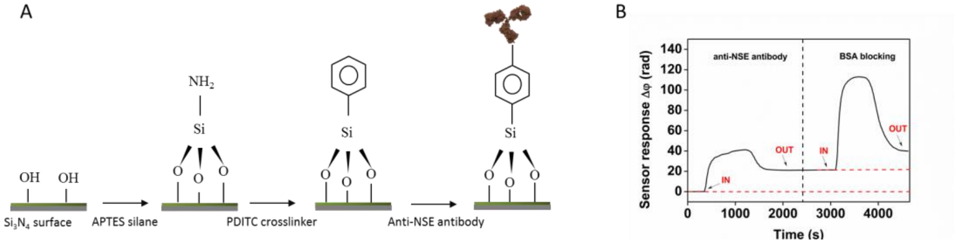

Figure 5.28. APTES silanisation. (A) Scheme representation of the silanisation process by employing APTES silane. (B) Real-time sensorgram of the two-step reaction for anti-NSE antibody and BSA immobilisation.

5.4.2.3. NSE detection

Different concentrations of the NSE protein, ranging from 0.5 ng mL^{-1} to 1000 ng mL^{-1}, were dissolved in MES 50 mM + 0.1 % Tween pH 5.5 and flowed over the sensor surface at a constant rate of 10 µL·min^{-1}. Calibration curves in 25% diluted plasma were accomplished by flowing different concentrations of NSE protein (ranging from 0.5 ng·mL^{-1}

to 1000 ng·mL^{-1}) spiked in 25 % diluted commercial plasma over the sensor surface at 10 µL·min^{-1}, using MES 50 mM + 0.5 % Tween 20 + 10 mM DS as running buffer. Regeneration of the biofunctionalised surface was achieved by flowing NaOH 20 mM for 50 s at a constant rate.

5.4.2.4. Data analysis

Biosensor data were analyzed and processed using Origin 8.0 software (OriginLab, Massachusetts, US) and Graphpad Prism (Graphpad Software, Inc., California, US). The mean sensor response ($\Delta\lambda$ or $\Delta\phi$) and its standard deviation (SD) were plotted as a function of the NSE protein concentration to obtain calibration curves. Calibration curves were fitted to a linear regression model (**Equation 3.1**) or one-site specific binding equation (**Equation 4.1**).

The experimental LOD was determined as three times the SD of the sensor signal obtained from a blank signal using only the running buffer. The coefficients of variation were obtained as the ratio of the standard deviation of the mean, expressed in percentages (% CV).

5.4.3. Design and optimisation of NSE detection using SPR biosensor

5.4.3.1. Optimisation of the bioreceptor layer and the immunoassay

Studies of NSE in plasmonic biosensor were carried by following the conventional carboxyl-SAM strategy and EDC/NHS chemistry. In order to optimise the biorecognition layer and, hence, the analytical parameters of the plasmonic biosensor, several immobilisation buffers (**Figure 5.29A**), MHDA:MUOH combinations (**Figure 5.29B**) and different antibody concentrations (**Figure 5.29C**) have been tested.

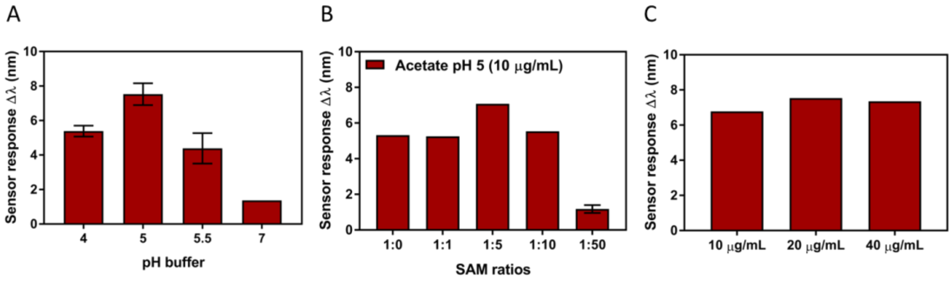

Figure 5.29. Bioreceptor layer optimisation. Sensor response to antibody immobilisation depending on (A) the pH of the immobilisation buffer (acetate pH 4 and 5; MES pH 5.5 and PBS pH 7). (B) MHDA:MUOH ratios and (C) concentrations of the anti-NSE antibody. Each signal corresponds to the mean ± SD of duplicate measurements.

Figure 5.29 shows the immobilisation conditions in which the antibody provided the highest signal and the optimal gold sensor coverage, corresponding to the SAM formation with a 1:5 MHDA:MUOH ratio. Moreover, the immobilisation of the antibody had to be performed by a solution of 20 μg·mL^{-1} in acetate buffer pH 5, ensuring the maximum number of antibodies attached to the sensor surface.

Once the maximum amount of antibodies was attached to the sensor surface, the recognition event between the anti-NSE antibody and the NSE protein was analysed. For this purpose, running buffer solutions with different salts and pHs were assessed (**Figure 5.30A**). In addition, the effect of Tween 20 detergent was also evaluated by adding different concentrations to the selected running buffer (**Figure 5.30B**).

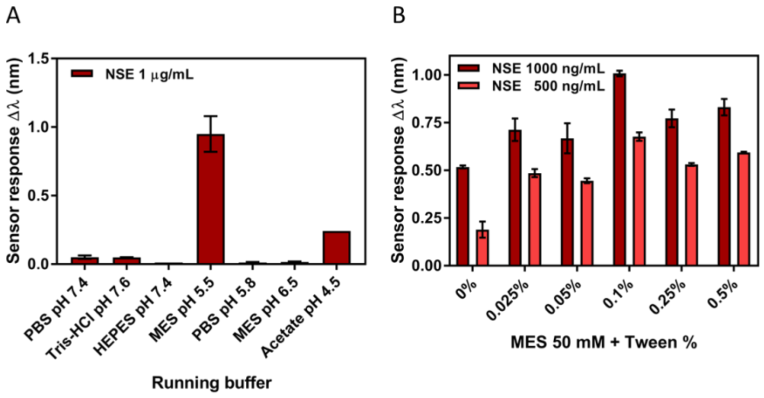

Figure 5.30. Optimisation of the NSE protein recognition biosensor event. Sensor signal obtained for the NSE detection depending on (A) the running buffer composition and pH, (B) the percentage of Tween 20 added to the running buffer (MES 50 mM pH 5.5). Each signal corresponds to the mean ± SD of duplicate measurements.

The salt composition and the pH of the running buffer are crucial parameters for the NSE detection. pH affects the structure of both, protein and antibody, and determines the affinityof the biointeraction. Buffers with a neutral pH (PBS, Tris-HCl and HEPES) shown a low or even unnoticeable detection of NSE ($\Delta\lambda \approx 0.002$ nm). High acidic buffers such as acetate allowed NSE capture ($\Delta\lambda \approx 0.25$ nm) but the highest sensor response was obtained with MES buffer, obtaining a signal four times higher than the acetate one ($\Delta\lambda \approx 1$ nm). Besides, the addition of 0.1% Tween in the running buffer improved two times the NSE detection. Hence, for the detection of NSE we used MES 50 mM + 0.1 % Tween as running buffer.

5.4.3.2. SPR biosensor assay for NSE detection: analytical parameters

To evaluate the performance of the plasmonic biosensor-based assay we carried out a calibration curves. **Figure 5.31** shows the direct relationship between the NSE protein concentration and the sensor signal and enabled to establish the limit of detection LOD= 5.33 ng·mL^{-1} for anti-NSE immunoassay (R^2=0.995). As we commented in the introduction, clinical cut-off values for NSE and lung cancer diagnosis are around 11 ng·mL^{-1}. The LOD accomplished with our plasmonic biosensor could provide enough analytical sensitivity for NSE detection in lung cancer diagnosis.

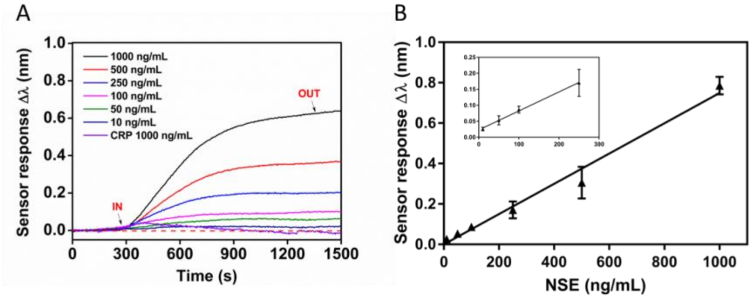

Figure 5.31. NSE detection in SPR sensor. (A) Real-time sensorgrams showing the specific interaction of different NSE concentrations ranged from 10 ng·mL^{-1} to 1000 ng·mL^{-1} in buffer conditions. CRP 1000 ng·mL^{-1} was used as a control. (B) Calibration curve in buffer conditions. Each signal corresponds to the mean ± SD of triplicate measurements.

The specificity of the assay was analysed by the measured of a non-lung cancer biomarkers such as CRP protein. It was flowed over the anti-NSE antibody surface at a constant flow rate and 1000 ng·mL^{-1}.As we can observe in **Figure 5.31A**, CRP reported a null sensor response, reflecting the absence of non-specific interactions with the sensor surface or the antibodies. The result confirmed the good specificity of the biosensor assay, where only NSE protein was detected by the bioreceptor. Finally, inter-assay variability (CV %) showed in **Table 5.11**, corroborated the good reproducibility of the NSE detection in buffer conditions since its value was close or below to the recommended one for clinical analysis (15%)[142].

Table 5.11. SPR-based inter-variability of the NSE assay in standard buffer conditions

NSE (ng·mL^{-1})	CC1	CC2	CC3	Mean ± SD	CV %
500	0.43	0.55	0.36	0.44±0.068	15
250	0.20	0.20	0.24	0.21±0.018	8
100	0.09	0.09	0.11	0.10±0.008	7
50	0.09	0.06	0.08	0.08±0.009	12
10	0.03	0.02	0.03	0.03±0.004	15
5	0.05	0.06	0.04	0.05±0.007	15
LOD	6.68	4.91	5.32	5.64±0.655	11

5.4.4. Design and optimisation of the NSE detection using the BiMW biosensor

The idea of a multiplexed biosensor for the simultaneous detection of miRNAs, DNA methylation profiling and proteins biomarkers related to the diagnosis of lung cancer demands a reliable and sensitive methodology for all the biomarkers. Although the NSE biosensor assay in SPR reflected an excellent sensitivity for the protein detection in plasma samples, NSE detection was also transferred to the BiMW biosensor.

5.4.4.1. Comparison of silicon-based biofunctionalisation procedures

As previously described for the other lung cancer-related biomarkers, different biofunctionalisation approaches were carried for the antibody attachment to the BiMW sensor asurface. To analytically compare PEG-COOH and APTES silanes for the identification of the NSE protein, calibration curves in standard buffer conditions were performed in both cases (**Figures 5.32 and Figure 5.33**). We employed the detection conditions previously optimised for the plasmonic biosensor assay (buffer MES 50 mM + 0.1 % Tween).

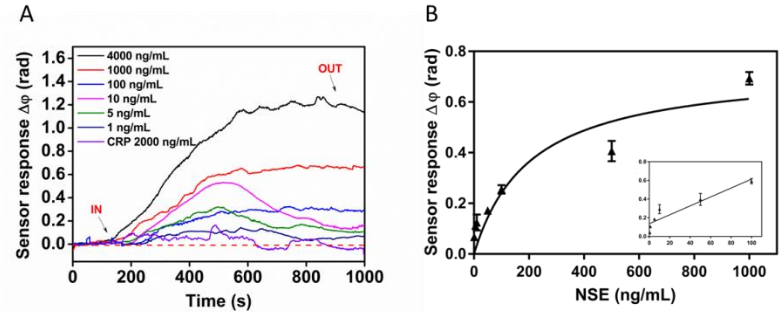

Figure 5.32. NSE detection with the BiMW biosensor. (A) Real-time sensorgrams showing the specific interaction of different NSE concentrations ranged from 1000 ng·mL^{-1} to 1 ng·mL^{-1} in buffer conditions. CRP 2000 ng·mL^{-1} was used as a control. (B) Calibration curve in buffer conditions. Each signal corresponds to the mean ± SD of triplicate measurements.

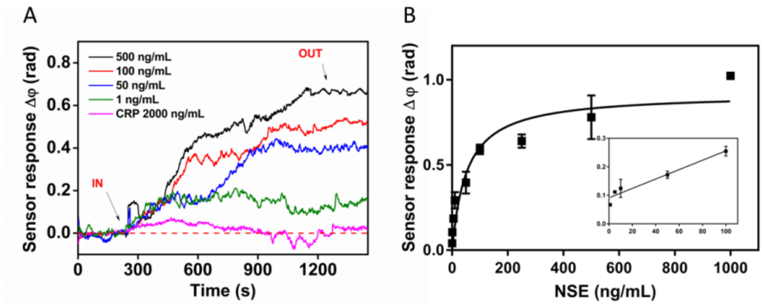

Figure 5.33. NSE detection in an APTES silanized BiMW sensor. (A) Real-time sensorgrams showing the specific interaction of different NSE concentrations ranged from 1000 ng·mL^{-1} to 1 ng·mL^{-1} in buffer conditions. CRP 2000 ng·mL^{-1} was used as control. B) Calibration curve in buffer conditions. Each signal corresponds to the mean ± SD of triplicate measurements.

In both cases, an increase in the sensor signal was observed at the same time the NSE concentrations were higher in buffer conditions (**Figure 5.32A and Figure 5.33A**). The calibration curves obtained in **Figure 5.32B and Figure 5.33B** show a direct relationship between the protein concentration and the biosensor signal, being possible to determine the limit of detection in both cases: 0.84 ng·mL^{-1} for PEG-COOH functionalisation (R^2=0.8584) and 1.22 ng·mL^{-1} for APTES functionalisation (R^2=0.924t). Also, comparing the sensorgrams in **Figure 5.32A and Figure 5.33A**, we can see that the sensor signal from the APTES surface are noisy compared to those from PEG-COOH. Although APTES is the silane par excellence, it is very sensitive to environmental conditions. It requires nitrogen atmosphere or certain water percentage because these conditiones affect its polymerization.Also, PDITC cross-lonker is sensitive to light and moisture. Tiny modifications during the silanisation and biofunctionalisation processes could introduce some variables that affect the immobilisation and detection steps, generating higher background signals. Otherwise, PEG-COOH silane is a well-establised protocol and EDC/sulfo-NHS is a well-know chemistry that guarantees a consistent antibody immobilisation with a low background.

In comparison with the LOD achieved with the SPR biosensor, the silicon photonic biosensor improved the sensitivity almost five times (SPR ≈ 5 mg·mL^{-1} *vs* BiMW ≈ 1 ng·mL^{-1}). Even though the PEG-COOH methodology is slightly more sensitive, stable and reproducible (**Table 5.12**) than the APTES, the necessity of developing a multiplexed device that enables the attachment of different types of bioreceptors (DNA probes and antibodies) with the same strategy, obligate to use the APTES methodology also for the NSE protein detection.

Table 5.12. Inter-assay variability of NSE-based assay in BiMW sensor chips silanized with PEG-COOH and APTES.

Silane	Parameter	CC1	CC2	CC3	Mean ± SD	%CV
PEG-COOH	**LOD, ng·mL^{-1}**	0.76	0.84	1.06	0.89 ± 0.13	14
APTES	**LOD, ng·mL^{-1}**	1.22	0.70	1.14	1.02 ± 0.23	22

5.4.4.2. Plasma effect on the NSE immunoassay

To analyse patients plasma samples, we first need to minimise the non-specific interactions from this complex matrix. Different combinations and concentrations of surface blocking agents (PLL-g-PEG and BSA) and detergents (Tween 20 and dextran sulfate) were tested (**Figure 5.34**). The excellent sensitivity of the BiMW sensor allowed the plasma dilution without compromising the sensitivity of the assay. The biosensor performance was directly evaluated with plasma diluted at 25%, as the detectability range of the assay might certainly tolerate this dilution without compromising quantitative detection as the LOD ofBiMW is in the 1 ng·mL^{-1} range and expected NSE concentrations are in the 11 ng·mL^{-1} level. A combination of blocking agents such as BSA 50 µg·mL^{-1}, detergent Tween 20 0.5 % and sodium sulfate dextran salt 10 mM successfully reduced non-specific interactions from diluted plasma although a slight background signal was always obtained ($\Delta\phi \approx 0.5$ rad).

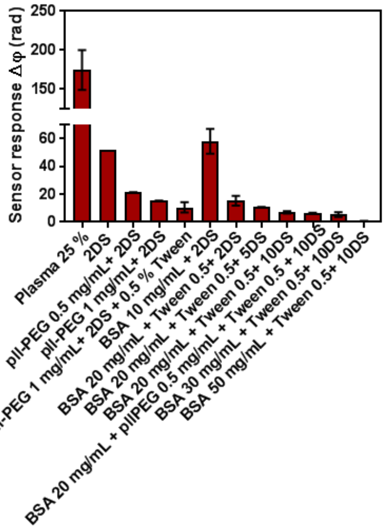

Figure 5.34. Effect of antifouling biosensor surfaces for diluted plasma analysis. Sensor signals obtained from commercial plasma diluted 25 % after covering the sensor surface with different concentrations of blocking agents and detergents.

5.4.4.3. BiMW sensor analytical parameters in plasma conditions

The performance of the NSE biosensor assays was evaluated with plasma diluted at 25% (**Figure 5.35**) by the generation of the calibration curve. For data analysis, sensor signals corresponding to each NSE concentration were normalized considering a background signal due to the plasma of $\Delta\varphi = 0.5$ rad. The limit of detection achieved for NSE in 25 % diluted plasma was 2.18 ng·mL^{-1} (R^2=0.928). The LOD in plasma conditions was twice higher than in standard buffer conditions (from 1.22 ng·mL^{-1} to 2.18 ng·mL^{-1}), which might be related to a possible hindrance of the antibody-antigen interaction due to the plasma matrix. Despite the deterioration in the assay sensitivity due to the plasma effect, the LOD achieved is good enough for real samples validation. To avoid plasma dilution, an optimised blocking step could be designed, although the effect of the plasma on the antibody-protein recognition event should have to be analysed.

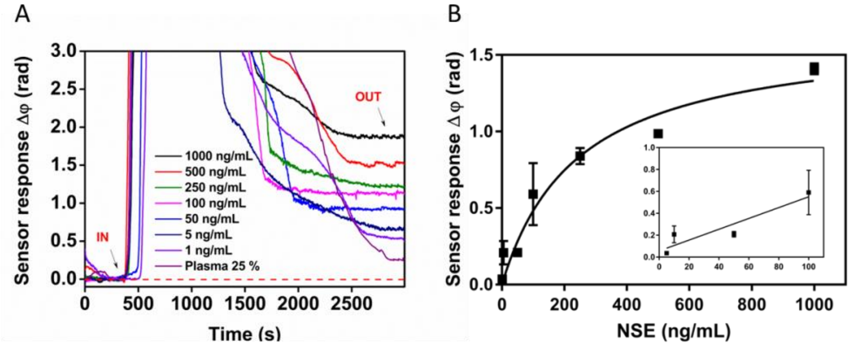

Figure 5.35. NSE detection in an APTES silanized BiMW sensor. (A) Real-time sensorgrams showing the specific interaction of different NSE concentrations ranged from 1000 ng·mL^{-1} to 1 ng·mL^{-1} in diluted plasma conditions. (B) Calibration curve in diluted plasma conditions. Each signal corresponds to the normalized mean ± SD of triplicate measurements.

To study the reproducibility of the assays in diluted plasma, the inter-assay variability was calculated (**Table 5.13**), showing values close to the highest variability recommended[142] and confirming the excellent suitability of this biosensor methodology.

Table 5.13. Inter-assay variability for diluted serum (10%) calibration curves (CC)

NSE (ng·mL^{-1})	CC1	CC2	Mean ± SD	CV
1000	1.38	1.43	1.41 ± 0.02	2
500	0.99	0.98	0.98 ±0.004	0.5
250	0.80	0.85	0.84 ± 0.04	4
100	0.45	0.73	0.59 ± 0.14	24
50	0.19	0.23	0.21 ± 0.02	8
LOD	3.29	2.12	2.70 ±0.58	21

5.4.5. Conclusions

NSE is a well-established biomarker for lung cancer diagnosis, mainly for SCLC, being the cut-off described for clinical analysis around 11 ng·mL^{-1}. We have developed a direct immunoassay in SPR and BiMW biosensors for NSE biomarker for lung cancer diagnosis. Both biosensors reported a sensitivity enough for clinical analysis since they achieved SPR = 5.33 ng·mL^{-1} and BiMW = 1.22 ng·mL^{-1} limits of detection, respectively.

To be able to offer a multiplex biosensor for the simultaneous analysis of the different biomarkers related to lung cancer, the biosensor assay was optimised for plasma analysis in the BiMW biosensor. The anti-NSE antibody biofunctionalisation was carried out by covalent immobilisation over an APTES and PDITC-activated sensor surface. The NSE biosensor assay offered excellent sensitivity in diluted plasma conditions (LOD = 2.18 ng·mL^{-1}). However, further studies related to antifouling properties should be carried out in order to ensure the absence of non-specific adsoprtions and to avoid plasma dilution. All these improvements, would allow a final clinical validation with previously validated real plasma samples.

5.5. Overall conclusions and perspectives for early diagnosis of lung cancer

As it is well known, the identification of several biomarkers boosts immensely the sensitivity and specificity of the diagnosis, especially in heterogeneous and complex diseases such as cancer. The multiplexed capabilities of the described nanophotonic biosensors such as BiMW interferometer, which can detect up to 20 different biomarkers, position it as an outstanding candidate for diagnostic tool for those disorders. In this Chapter, we have individualy optimised and evaluated several biosensor assays for the detection of lung cancer-associated biomarkers in human fuids. A combination of protein biomarkers and epigenetic pathways such as miRNAs and DNA methylation has been proposed for an exhaustive and precise lung-cancer diagnosis. These individuals studies, opens the door to the integration of these multifunctionalities in a single chip for the simultaneous detection of those biomarkers. The final aim will be to include all the biomarkers (and/or novel ones) in the same biosensor chip to perform a multiplexed assay in minimally invasive biological fluids samples (as serum or plasma) with the required sensitivity and specificity (**Figure 5.36**). The implementation of such POC together the development of artificial intelligence in clinical practice would revolutionize cancer diagnosis, boosting personalised medicine, facilitating patient stratification, and providing and monitoring customized therapies which could end up in an increase in the recovery probabilities and survival rate.

In order to achieve such a biosensor-based sensitive and personalised diagnosis, further studies should be performed to optimise multiplex configuration in BiMW sensors. Also, innovative biosensing strategies for novel biomarkers detection should be studied. Although individual biosensor assays has been described in this chapter, the biofunctionalisation process and antifouling properties could be re-designed and optimised. APTES is one of the most commonly used silanes, but it is overly sensitive to environmental conditions such as O_2 atmosphere and water content. New silanisation and bionfunctionalisation protocols could be studied to achieve a less laboriuos and consistent biosensor methodology. In addition, new blocking agents should be tested to avoid dilution or pretreatment of body fluids and ensure proper performance of the biosensor assay.

The multiplexed biosensor methodology for lung cancer diagnosis proposed in this Chapter was awarded in the II Call for Innovation Project Awards for the early detection of lung cancer. This call was framed in the Lung Ambition Association (LAA), a strategic initiative of AstraZeneca. They highlighted the potential of our biosensing platform to provide a sensitive and specific tool for the early diagnosis and prognosis of the lung cancer.

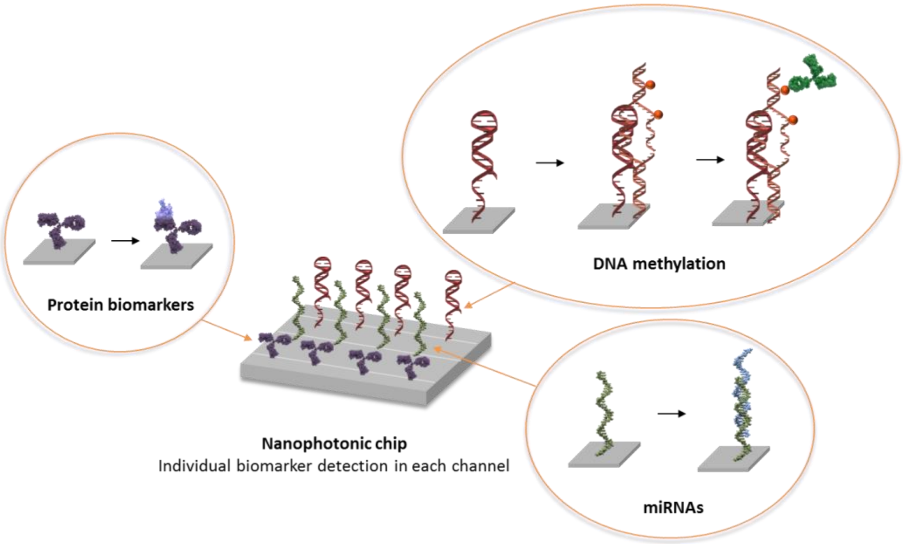

Figure 5.36. Multiplex analysis in BiMW. Scheme of a BiMW array showing the different types of biomarkers that will be potentially implemented in the POC device and the detection strategies.

General conclusions and future perspectives

General conclusions and future perspectives

This doctoral thesis demonstrates the potential applicability and versatility of the plasmonic and interferometric nanobiosensors for a more efficient clinical diagnosis of several respiratory diseases. New biosensor methodologies have been established in order to identify specific biomarkers involved in relevant diseases as COVID-19, Pneumocystis pneumonia and lung cancer. The rapid, sensitive, reliable and easy-to-use biosensor devices can provide an early and accurate diagnosis, enabling precise and prompt therapies.

Diverse analytical strategies have been designed and optimised to eventually perform the biosensor assays directly in human clinical samples. In each biosensor assay, we have selected the most appropriated and specific biorecognition elements such as viral antigens, DNA probes and antibodies for the direct detection of the analytes of interest (immunoglobulins, DNA sequences, miRNAs and proteins) present in human fluids such as serum, plasma and pulmonary specimens. Additionally, antifouling strategies such as blocking agents or additives included in the evaluation buffer have been implemented, showing an efficient reduction of the non-specific adsorptions of the components of these biological matrices. The rigorous optimisation and assessment of the biofunctionalisation and biosensor detection assays have demonstrated a reliable monitoring in terms of sensitivity, selectivity, and reproducibility comparable to standard analytical methodologies, reaching limits of detection within the clinical ranges reported for the three diseases studied. Finally, the analysis of clinical samples has demonstrated the complete feasibility of the proposed biosensor methodologies for their use in the biomedical and clinical practice.

The main general conclusions that can be drawn from this Thesis work are the following:

- A label-free-based methodology has been developed in a plasmonic biosensor for the detection of anti-SARS-CoV-2 antibodies in sera samples. The biorecognition layer was composed of a combination of viral antigens (N protein and RBD peptide). The main analytical parameters have been optimised to provide a biosensor able to operate in serum by applying a 1:10 dilution. The incorporation of a blocking step consisting of the surface coverage with PLL-g-PEG (0.5 mg·mL^{-1})

and the addition of detergents such as Tween 20 (0.5 %) and dextran sulfate (2 mg·mL^{-1}) in the PBS buffer have been crucial to avoid non-specific interactions and for achieving a LOD of 12.7 ng·mL^{-1} with excellent reproducibility and precision. The reported LOD reaches the detection levels and the working range within the clinical values required for COVID-19 serological assays. A large clinical validation with 120 sera samples has demonstrated the outstanding performance of the biosensor methodology, affording a diagnostic sensitivity and specificity of 99 % and 100 %, respectively. Compared to conventional serological techniques such as ELISA, CLIA and LFA, our biosensor approach offers a combination of the advantages of these methodologies, but operating in a simpler and faster format (≈ 15 min, as LFA) with superlative sensitivity and specificity (as ELISA/CLIA) for the convenient detection of anti-SARS-CoV2 antibodies. Our biosensor exhibits a strong potential to be implemented at the point-of-care and for a future technological transfer.

- An SPR biosensor has been established for the diagnosis of Pneumocystis pneumonia in pulmonary specimens like bronchoalveolar and nasopharyngeal lavages. The methodology is based on a label-free assay employing PPRH probes as bioreceptors for the direct capture of the gene mtLSU rRNA from *Pneumocystis jirovecii* fungus. The use of lateral spacers (SH-PEG-CH_3) in the biorecognition layer and the incorporation of formamide in the running buffer facilitated the target gene hybridisation and completely suppressed any non-specific adsorption, achieving a LOD of 2.11 nM. The previous purification of the clinical samples in a minute volume (≈ 30 µL) compromised the sensitivity of the hybridisation assay. However, the plasmonic biosensor device shows exceptional reproducibility, reliability and accuracy, demonstrated in the correlation analysis with a significant number of BAL and NPA real samples for patients infected with *P. jirovecii* and other microorganisms such as *Pseudomonas* and *Cladosporium* (Test Kruskal-Wallis p-value = 0.0012; $p\text{-value} < 0.05$). On-going work focuses on the incorporation of different pre-treatment protocols such as enzymatic cleavage for the validation of the strategy in non-purified pulmonary specimens.

- We have developed efficient and sensitive strategies for the detection of cancer-associated epigenetics biomarkers (miRNAs, DNA methylation profiling and proteins) directly in human plasma. The different methodologies have been carefully optimised using plasmonic biosensors. Additionally, the assays were transferred to the BiMW biosensors to improve the detection limits and to exploit the multiplexing capabilities of our interferometrictechnology. For miRNAs, a direct complementary hybridisation assay was conducted for the detection and quantification of miRNA-21-5p, miRNA-210-3p and miRNA-205-5p as biomarkers of lung cancer. The method is based on the use of complementary DNA probes immobilised on the sensor surface to allow selective miRNA detection without amplification steps. Limits of detection in the nM range have been reported by the plasmonic biosensor for the selected miRNAs (1.23 nM, 1.98 nM and 2.35 nM, respectively), reflecting the non-optimal performance of the SPR biosensor for the detection of these biomarkers within their estimated clinical range (fM-nM). Finally, the methodology has been successfully applied to the BiMW interferometric biosensor, improving the overall sensitivity by one order of magnitude. The feasibility of the methodology was demonstrated by the analysis of miRNA-21-5p in undiluted plasma. A blocking step consisting of a surface coverage with BSA (20 $mg \cdot mL^{-1}$), together with the introduction of lateral spacers, and the addition of detergents as Tween 20 (0.5 %) and CHAPS (10 mM) in SSC5X buffer, reduced the non-specific interactions and enable a LOD of 381 pM with excellent reproducibility. The biosensor assay has been validated with plasma samples from healthy and lung cancer patients, in which excellent discrimination between conditions was reported ($p\text{-value}<0.0001$). The epigenetic biosensor demonstrated a sensitivity and specificity of 80 %, operating similarly to the benchmark qRT-PCR methodology but in extraction and amplification-free format.

- We have set the basis for the identification of DNA methylation levels in promoter regions of lung cancer-related genes (*CDO1* and *ZNF177*) in plasma samples. Methylation assay relied on a two-step recognition process: (i) ds-DNA capture through PPRH probe attached to the sensor surface with lateral spacers (SH-PEG-CH_3, ratio 1:1) and (ii) 5-methylcytosines residues quantification by a specific anti-5-methylcytosine antibody. Using double strand synthetic targets of the *CDO1* and *ZNF177* sequences, the SPR biosensor has demonstrated a sensitivity of 4.29 nM and 3.90 nM, respectively, in SSC 5X buffer. Furthermore, 5-methylcytosines quantification revealed good performance, reflecting statistical differences depending on the number of 5-methylcytosines in the target sequences. The excellent execution and versatility of the strategy were confirmed by a preliminary analysis in 1:10 diluted human plasma in the SPR biosensor and in buffer conditions using the BiMW biosensor. In both cases, DNA methylation level discrimination was reached in synthetic sequences (p-value of 0.0138 and 0.0032, respectively). The bisulfite and amplification-free biosensor assay seems to be a promising alternative for the identification of hypermethylated genetic sequences as a future competitive tool for the early detection of lung cancer. However, further studies are required to confirm the feasibility and suitability of the assay for 5-methylcytosines quantification in human plasma samples. Alternative blocking steps and samples pre-treatment such as enzymatic cleavage to obtain shorter and more accessible sequences by the PPRH probes should be considered.

- We have proposed a biosensor methodology for the detection of lung cancer-associated protein biomarkers in plasma samples. The methodology is based on the direct detection of proteins (NSE) through their specific antibodies coupled over the sensor surface. Calibration curves using MES 50 mM + 0.1 % Tween 20 buffer in the plasmonic biosensor have allowed the direct quantification of this protein achieving LOD values of 5.33 ng·mL^{-1}. To carry out a future multiplexed biosensor assay for lung cancer diagnosis, the assay was transferred to the BiMW interferometric sensor, improving the sensitivity to 1.22 ng·mL^{-1}. The incorporation of a surface blocking step through BSA (50 mg·mL^{-1}) and the addition of Tween 20 (0.5 %) and dextran sulfate (10 mg·mL^{-1}) enabled the NSE analysis in 1:4 diluted plasma. Despite the plasma dilution, a very good sensitivity was reported for the BiMW biosensor, achieving a LOD of 2.18 ng·mL^{-1}, which is within the clinical range required for NSE analysis (≈ 11 ng·mL^{-1}). Further work is needed to elaborate a feasible protein biosensor assay in plasma conditions, avoiding matrix dilutions and minimising non-specific interaction over the sensor surface.

Overall, the proposed BiMW interferometric biosensor constitutes an extraordinary opportunity for the development of label-free, rapid, highly sensitive and multiplexed analytical tool that could afford a simultaneous detection of lung cancer-associated biomarkers of different nature (miRNA, proteins and DNA methylation panels) in human fluids. The implementation of such POC biosensors in clinical practice would boost the application of personalised medicine since they might drastically enhance the cancer diagnosis (even in early stages), the prognosis and the therapeutic monitoring, increasing the recovery probabilities and the overall survival rate.

This PhD Thesis has shown the extraordinary importance of developing new biofunctionalisation and reliable biosensor methodologies capable of being integrated into POC devices, competing and even improving the conventional analytical techniques.

Future perspectives may be directed to improve the anti-fouling strategies for the final stage of the clinical validation in which complex matrices can interfere with the biosensor surface or the biorecognition event. Also, further studies and optimisations should be carried out to elaborate a suitable validation of a complete epigenomic biomarker panel by using the biosensor methodologies developed in this Thesis. Additionally, to demonstrate the multiplexing capabilities of the BiMW biosensor, additional studies should be performed for simultaneously detect lung cancer-related biomarkers in the same patient plasma sample. Finally, a full engineering integration of the biosensor device has to be conducted in order to provide a technological transfer of compact POC biosensor devices to the clinical settings. The incorporation of advanced software, disposable biosensor cartridges and a multiplexed photonic design are required to position our biosensors close to their commercialization.

This PhD thesis represents a significant contribution to the respiratory diseases diagnosis field, demonstrating the immensurable potential of evanescent wave biosensors to be integrated into POC platforms for clinical diagnosis. Our biosensing technology could become a new addition to the existing bioanalytical tool kit for the early cancer diagnosis. Moreover, our technology could contribute to pave the way for a close-future personalised diagnosis and therapy follow-up for other cancer disorders, such as ovarian cancer.

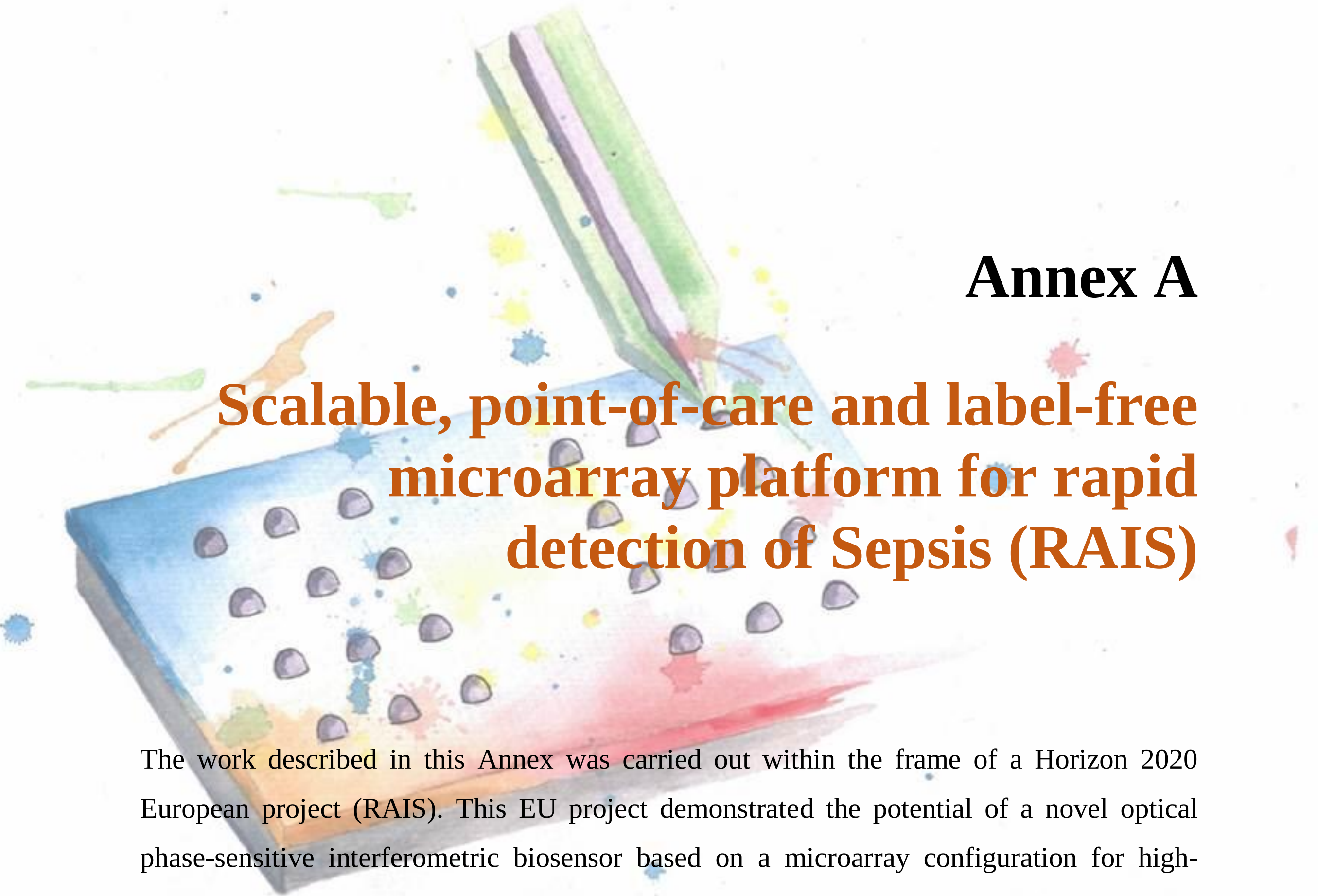

Annex A

Scalable, point-of-care and label-free microarray platform for rapid detection of Sepsis (RAIS)

The work described in this Annex was carried out within the frame of a Horizon 2020 European project (RAIS). This EU project demonstrated the potential of a novel optical phase-sensitive interferometric biosensor based on a microarray configuration for high-throughput detection of specific sepsis biomarkers. In particular, we have demonstrated the feasibility of this POC biosensor device for the detection of miRNA-16-5p biomarkers, besides the analysis of other relevant sepsis biomarkers as bacteria and specific proteins. For the miRNAs detection, we have performed an extended optimisation of the biofunctionalisation protocol based on the direct immobilisation of thiol DNA probes complementary to the sequence of the selected miRNAs. The biosensor assay includes an amplification step through an antibody specific against DNA/RNA hybrids.

A. Scalable, point-of-care and label-free microarray platform for rapid detection of Sepsis (RAIS)

A.1. Introduction

Sepsis is a clinical condition characterized by a whole-body inflammatory response caused by an infection. Sepsis involves several stages, firstly a systemic inflammatory response (SIRS) that could evolve into severe sepsis, characterized by organ dysfunction (liver, kidney, lung, and heart). The final stage is a sepsis shock that could cause hypotension and, ultimately, death[258]. At present, sepsis is the main cause of death in Intensive Care Units (ICU) with a mortality rate higher than 40 %[259]. A critical barrier for managing sepsis and antibiotic resistance is the lack of rapid diagnostics, resulting in either the use of unnecessarily broad first-line antibiotics, or in a long delay in administering the appropriate one. Late detection reduces the survival opportunity of the sepsis patients and implies a high economic cost for the healthcare system[260]. Thus, its early detection (< 5 h) increases dramatically the chances of survival.

Sepsis diagnosis is still challenging because it implies to find and identify the causative microorganism and determine its sensitivity to antibiotics. Currently, sepsis diagnosis is based on clinical examinations such as corporal temperature, breathing and heart and other general variables (organ dysfunction, haemodynamic…). Complementary to the physician observations, laboratory tests based on the identification of bacteria or biomarkers in body fluids could help to obtain a more complete and precise diagnosis[261]. Bacterial culture coupled to antibiotic susceptibility tests is the gold standard technique but requires several days. On the other hand, molecular and cellular detection methods (PCR, nanoparticle-based assays, or host-response based detection assays) have also been reported. Many of them involve bacteria resistance genes identification and can reduce the analysis to hours, but they still offer limited sensitivity which forces the use of a culture-enrichment step. Moreover, they require expensive equipment and complex, multiplex sample processing which affect their reliability. Therefore, the detection of key biomarkers of sepsis usually relies on immunoassays that, despite their sensitivity, require sophisticated instrumentation, tedious protocols and specialized personnel. More than 170 different biomarkers have been reported for sepsis diagnosis, prognosis and treatment monitoring[260]. Among these biomarkers, the most employed ones are C-reactive protein (CRP) and procalcitonin (PCT) as well as different proinflammatory cytokines (tumour necrosis factor (TNF), interleukin -1b (IL-1b), and interleukin-6 (IL-6)) due to their sensitivity and specificity. Additionally, some circulating miRNAs, which module the gene expression, have been identified for playing a relevant role in the progression, diagnosis and staging of sepsis (miRNA15a, miRNA-146a, miRNA-16 or miRNA-223, among others)[262–264]. As immunoassays techniques, genetic methodologies for miRNA detection such as RT-PCR, microarrays or Norther blot require centralized laboratories, long process and large amount of purified sample compromising their sensitivity or robustness[265].

The development of new technologies capable of providing a rapid and accurate diagnosis of sepsis in the first stages of the disease is crucial for the on-time selection of the most suitable treatment, improving patient outcomes. To overcome the inconvenience of standard techniques, biosensors have been proposed addressing such analytical needs (specificity, sensitivity, portability and speed), being the most promising the optical ones. Several optical biosensors have been reported, most of them based on SPR, for the detection of the protein biomarkers such as CRP, PCT and IL-6[266]. Regarding microarray formats for multiplexed assays, some sensors have been proposed although they employ conventional labelled strategies (fluorescence or chemiluminescence). Label-free sensors such as reflectometric interference spectroscopy, SPRi or arrayed imaging reflectometry (AIR)[267–269] have been also reported.

Within the frame of a Horizon 2020 European project (RAIS: Scalable, point-of-care and label-free microarray platform for rapid detection of Sepsis, Reference: 644956), an innovative POC biosensor platform have been designed and fabricated as a more efficient methodology for sepsis diagnosis providing a result in less than 30 minutes (**Figure A.1.**). The overall aim of RAIS was not only to develop a new fully integrated point-of-care label-free microarray platform but also validate it for quantifying levels of specific Sepsis' biomarkers. RAIS platform might identify sepsis biomarkers using a few microliters of serum or plasma samples, within 30 minutes (sample to result) and at a cost per patient of less than 50 €. The achievement of this project would provide an adequate and correct treatment to patients more rapidly, potentially reducing the mortality rate from sepsis by more than 70 %. In addition, the reduction of unnecessary drugs and shortenings hospital stays would result in cost saving, estimated at more than 10 € billion per year for healthcare systems.

In the first stages of the RAIS project, some partners of the consortium developed a novel optical phase-sensitive interferometric biosensor and custom-designed gold nanohole arrays chips (Au-NHA) for high-throughput analysis in a microarray format. On the other hand, and according to the suggestion of the clinical partner of the consortium, several biomarkers associated to sepsis were selected such as proteins (CRP, IL-6 and PCT), bacteria (*Escherichia coli* and *Staphylococcus aureus*) and miRNAs (miRNA-16-5p miRNA-15a-5p, miRNA-146a-5p). Our group at ICN2 has studied and optimised different biofunctionalisation strategies and performed clinical evaluations to demonstrate the feasibility of this new POC biosensor device for the diagnosis of those target sepsis biomerkers in less than 30 min[270,271].

In this Annex, we described the RAIS biosensor assay for the detection of miRNA-16-5p biomarkers related to sepsis. The clinical partner of the RAIS project selected miRNA-16-5p considering: (i) the diagnostic value rather than prognostic one, (ii) its over-expression in a sepsis condition, and (iii) it ability to distinguish between normal and sepsis/SIRS patients[264,272]. In addition, the partner reported that the clinical values in body fluids such as blood for miRNAs are within the fM-nM range. Therefore, a biofunctionalisation protocol based on the direct immobilisation of thiol complementary DNA probes was performed to identify the target miRNA. An amplification step through an antibody specific against the resulting DNA/RNA hybrids was carried out to achieve a sensitive detection of this sepsis biomarker. However, miRNA analysis has not been achieved yet in plasma samples due to the limited sensitivity of the novel sensor. The multiplexed potential of the RAIS platform and the demonstrated ability to detect other sepsis biomarkers in complex matrices, such as the detection of CRP, IL-6 and *E.coli* bacteria in plasma, would allow simultaneous analysis of a bunch of biomarkers in a fast manner (less than 30 min) with accurate results. These features position the RAIS POC biosensor device as a promising tool for clinical diagnosis of sepsis, overcoming the performance of conventional diagnosis techniques.

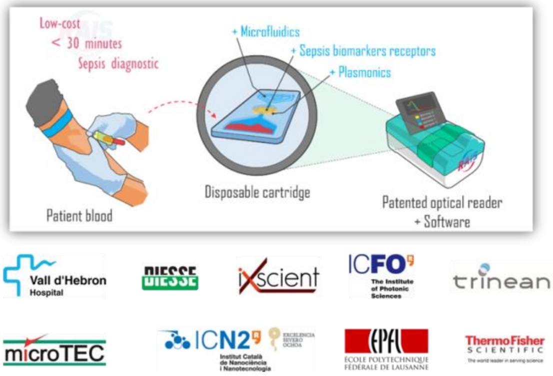

Figure A.1. RAIS project main concept for the fast diagnosis of sepsis and the EU consortium of the project.

A.2.Materials and methods

A.2.1. RAIS platform

A.2.1.1. Optical instrument, readout and data processing

The POC device (dimensions: 20 × 14 × 23 cm) (**Figure A.2A**) has been previously described[273] and is based on a novel lens-free interferometric microscopy (LIM). The device detects changes in the topography of transparent surfaces such as target-binding events. Briefly, the device working principle is based on an optical microarray reader with large-field-of-view (20 mm^2) (FOV), in which a polarized light beam is split into two beams (reference and signal) that pass through the sample. These two beams are then recombined and the final output light is recorded by a CMOS sensor (**Figure A.2B**). Any variation in the RI and thickness (such as biomarkers present in a sample), generates changes in the phase of the light beams when passing through a transparent substrate and produce an interferometric pattern over the full FOV of the camera, which is translated into an Optical Path Difference (OPD) map. An algorithm calculates, for each microarray spot, the difference between the maximum and the minimum phase-shift values, providing the final OPD value for each spot.

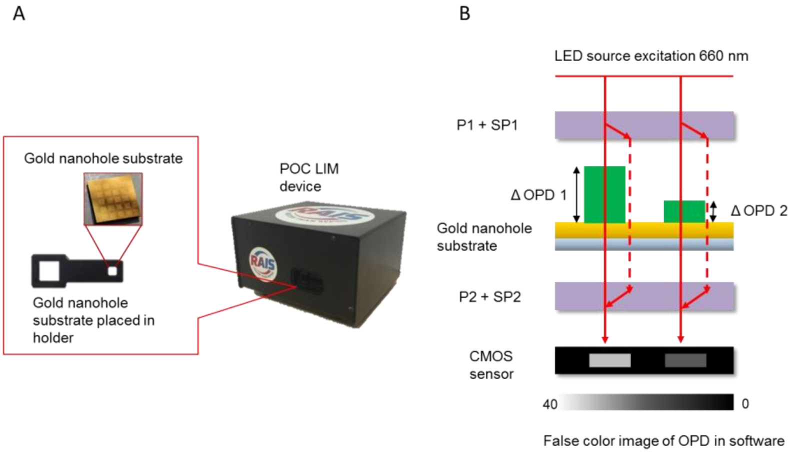

Figure A.2. RAIS POC technology. (A) Photograph of the POC device, gold-NHA plasmonic chips and sample holder. (B) Working principle of the LIM device.

A.2.1.2. Plasmonic gold nanohole array chips

Plasmonic Au-NHAs were fabricated at the Institute of Bioengineering, École Polytechnique Fédérale de Lausanne (EPFL, Lausanne, Switzerland)[274]. The fabrication process was reported by P. Buchegger and C.Preininger[275]. Briefly, plasmonic sensor chips (1×1 cm^2) are based on silica wafers coated with Ti/Au (10/120 nm) and patterned with 200 nm diameter and 600 nm period nanohole arrays. Symmetrically- and periodically-ordered Au-NHAs, nanohole diameter and metal film thickness were optimised to increase the transmission efficiency at narrow wavelength range, enhancing the sensor OPD. The presence of the nanoplasmonic structures improves the viability of the POC device for biosensing applications, reaching a LOD of 5.7×10^{-4} RIU[275]. Au-NHAs can be fabricated using large-area, low-cost and high-throughput nanofabrication methods. These features increase reproducibility and reduce time and cost during the nanofabrication process, leading to a mass production of the POC device.

Before use at ICN2, the Au-NHA chips were cleaned by consecutive sonicating for 1 min at 80° C and in solvents of increasing polarity (acetone, ethanol, and Milli-Q water). Then, they were dried with an N_2 flow and placed in a UV/O_3 chamber (Bioforce Nanoscience, Utah, USA) for 30 min. The sensor chips were finally rinsed with ethanol and Milli-Q water and dried with N_2 flow.

A.2.1.3. Optical path difference (OPD) and data analysis

OPD values and, therefore, the receptor-target binding events occurring on the Au-NHA chips surface were monitored with a home-made LabView software designed at The Institute of Photonic Sciences (ICFO, Barcelona, Spain). This software records the phase changes and renders an OPD map image. OPD was monitored before and after each step (receptor immobilisation, blocking step, miRNA hybridisation and antibody amplification). The plotted signal is the result of the difference in OPD value before (OPD_{t0}) and after incubation (OPD_{tt}) with the target analyte or the amplification antibody ($\Delta OPD = OPD_{tt} - OPD_{t0}$) (**Figure A.3**). OPD values do not correspond to a single spot, but to the mean value obtained for an array of 8 × 8 spots.

Calibration curves were obtained by evaluating anti-DNA/RNA antibody after the recognition of different concentrations of the miRNA in triplicate. Calibration curves were plotted as mean sensor signal (ΔOPD) and its standard deviation (SD) *versus* miRNA concentration. The data were fitted to a linear regression model (**Equation 3.1**) and one site-specific binding model regression (**Equation 4.1**) using Graphpad Prism (Graphpad Software, Inc., California, US)

The experimental LOD was determined as three times the standard deviation of the OPD obtained from a blank signal. The coefficients of variation were obtained as the ratio of the standard deviation of the mean, expressed in percentages (% CV).

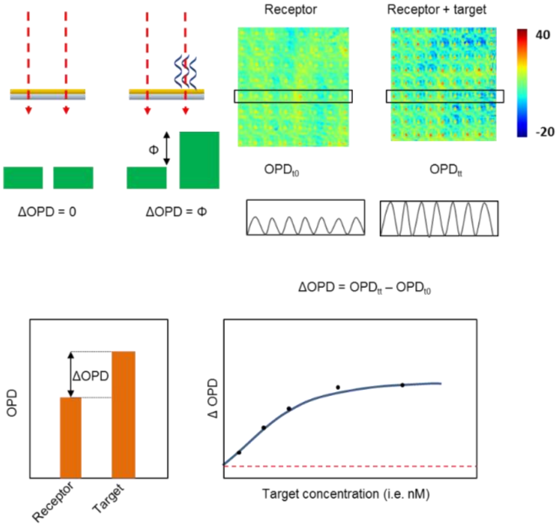

Figure A.3. OPD analysis. Images of the arrays generated after software processing. Differences in the OPD (ΔOPD=OPDtt−OPDt0) in each spot can be related to the analyte concentration, generating calibration curves.

A.2.2. Dip-pen nanolithography

The employment of a microarray format in the RAIS instrument allows the immobilisation of several bioreceptors in individual spots for diverse sepsis biomarkers detection The formation of the microarray-based platform was achieved by using a dip-pen nanolithography instrument (NanoInk, Illinois, USA) which ensures the appropriate spot size and high spatial accuracy in custom and well-defined patterns by using surface patterning tool (microcantilever with a dimeter of 10 – 60 µm) (BioForce, Utha, USA) (**Figure A.4.**). For miRNA experiments, 8 × 8 arrays (with a spot diameter of ~55 µm and an array pitch of 250 µm) were generated.

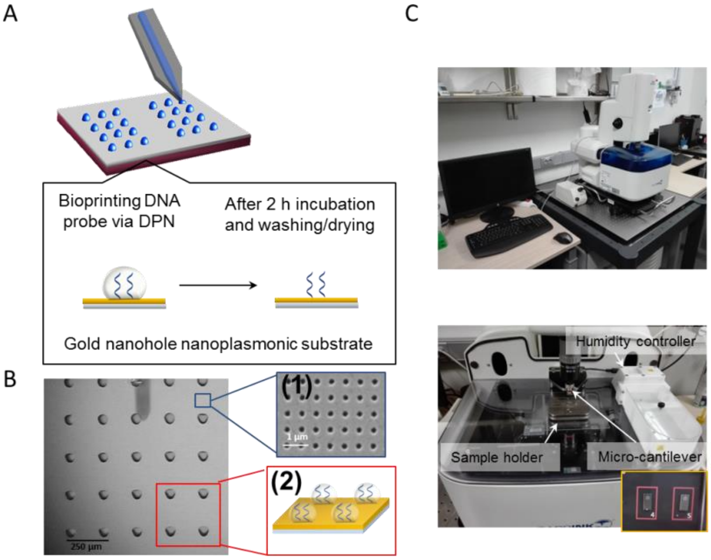

Figure A.4. Bioprinting microarrays. (A) Schematic representation of the bioprinting process of thiolated DNA probes with dip pen nanolithography (DPN) tip. (B) Image of the bioprinted microarrays of DNA probes in 5 × 5 arrays with 250 µm of spacing (scale bar = 250 µm), (1) underlying gold nanohole array (scale bar = 2 µm) and (2) schematic representation of the functionalised spots.(C) Photograph of the dip-pen nanolithography platform and the surface patterning tools.

A.2.3. Chemical and biological reagents

Organic solvents used for plasmonic sensor chip cleaning (acetone and ethanol) were purchase from Panreac (Barcelona, Spain). All the buffer compounds, PBS 50 mM (50 mM phosphate buffer, 0.75 M NaCl, 2 mM ethylenediaminetetraacetic acid (EDTA), pH 7), PBS 10mM (10 mM phosphate buffer, 0.15 M NaCl, pH 7), 5x SSC (0.75 M NaCl, 0.075M sodium citrate, 4 mM EDTA, pH 7), MES (2-(N-morpholino) ethanesulfonic acid) 0.1 M pH 6, Diethyl pyrocarbonate (DEPC), 16-mercaptohexadecanoic acid (MHDA), (1-ethyl-4(3-dimethylaminopropyl)carbodiimide hydrochloride (EDC), N-hydroxysulfosuccinimide (sulfo-NHS), ethanolamine hydrochloride,CM-dextran, glycerol and bovine serum albumin (BSA)were purchased from Sigma-Aldrich (Steinheim, Germany). HPDP-biotin (N-[6-(Biotinamido)hexyl]-3′-(2′-pyridyldithio)propionamide), neutravidin protein and amine-dextran were obtained from ThermoFisher Scientific (Massachusetts, US). Antibody against DNA/RNA duplex (Anti-DNA/RNA) was purchased from Kerafast (Boston, USA). Poly-L-lysine-graft-PEG (PLL-g-PEG) was obtained from SuSoS (Dübendorf, Switzerland). DNA capture probes incorporating thiol (SH-DNA) and biotin group at the 5'-end were purchased from IBIAN Technologies (Zaragoza, Spain) (**Table A.1.**) All the buffers and other solutions for miRNA detection were prepared using DEPC-H_2O (Milli-Q water incubated overnight with 0.1% DEPC and autoclaved for 1 h at 121 °C). All solid plastic and glass materials were autoclaved for 1 h at 121° C.

Table A.1. DNA capture probes and miRNAs nucleotide sequences used in the microarray assays

miRNA	Sequence	DNA-SH capture probe
miRNA-16-5p	5'UAGCAGCACGUAA AUAUUGGCG 3′	5′SH/biotin-T_{15}-CGCCAATATTTACGT 3′
miRNA-21-5p	5′UAGCUUAUCAGAC UGAUGUUGA 3′	5′SH/biotin-T_{15}-TCAACATCAGTCTGA 3′

A.2.4. Microarray biofunctionalisation

Due to the novelty of the POC biosensor device and in order to optimise the microarray assay to achieve a sensitive and specific miRNA detection, different biofunctionalisation protocols were studied. As usual in gold biofunctionalisation, all the strategies are based on the affinity between gold and thiolated compounds.

- Covalent immobilisation of biotinylated DNA probes on a carboxyl-modified surface (MHDA-NA) (Surface I) (**Figure A.5A**)

The sensor surface was incubated in MHDA 250 µM in ethanol overnight at RT. After rinsing and drying, the sensor was incubated with EDC/sulfo-NHS (0.2/0.05M in MES buffer 0.1 M pH 6) for 30 min and after rinsing, with NA 100 µg·mL^{-1} in PBS 1 h. Finally, ethanolamine 1 M pH 8 was incubated in order to block carboxylic reactive groups for 2 min. DNA-biotin probes (50 µM in PBS 50 mM with 5 % glycerol) are then spotted onto the sensor chip and incubated for 2 h.

- <u>Covalent immobilisation of biotinylated DNA probes on a biotin-modified surface (HPDP-biotin) (Surface II) (**Figure A.5B**)</u>

The sensor surface was incubated in HPDP-biotin 1mN in ethanol overnight at RT. After rinsing and drying, the sensor was incubated with NA 100 µg·mL^{-1} in PBS for 1 h. DNA-biotin probes (50 µM in PBS 50 mM with 5 % glycerol) are then spotted and incubated for 2 h.

- <u>Direct immobilisation of thiolated DNA probes (Surface III) (**Figure A.5C**)</u>

The sensor surface was directly biofunctionalised by spotting a solution of SH-DNA capture probes (50 µM in PBS 50 mM with 10% glycerol) over clean Au–NHAs chips and incubating them for 2 h at RT. The sensor chips were rinsed with DEPC-H_2O and incubated with BSA 0.01% in PBS 10 mM for 30 min to block the remaining gold area. The sensor chips were rinsed with DEPC-H_2O water and dried with N_2.

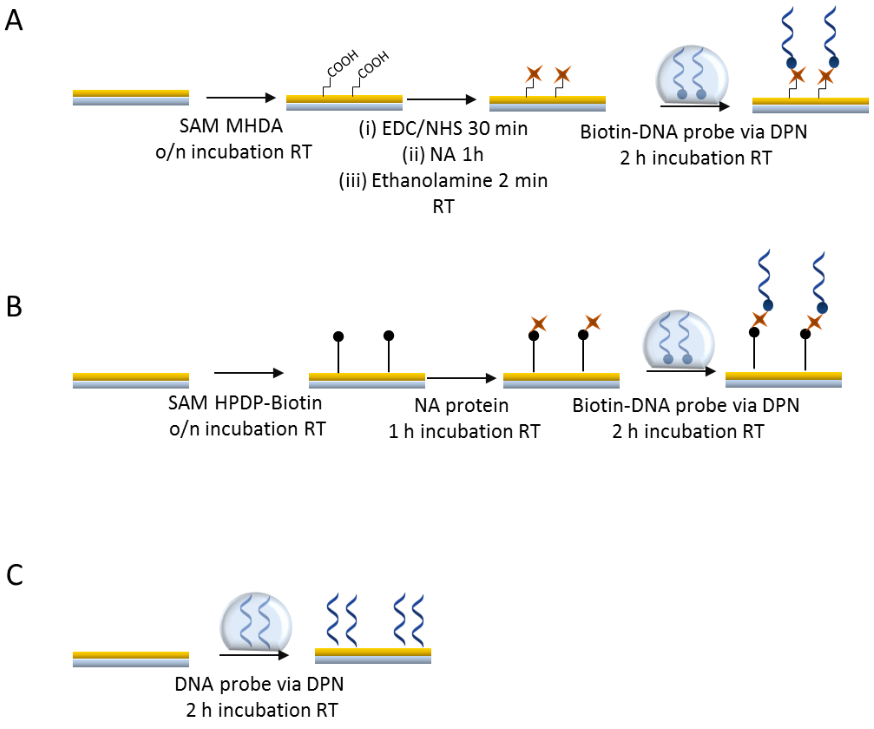

Figure A.5. Gold-NHA miRNA-based biofunctionalisation strategies. (A) Carboxyl-modified surface (B) Biotin-modified surface (C) Direct gold surface immobilisation.

A.2.5. miRNA detection and antibody amplification

Target miRNA (miRNA-16-5p) at different concentrations (0.1–50 µM in 5x SSC buffer) was incubated with DNA spotted sensor chips for 1 h at RT. After rinsing with DEPC-H_2O, the sensor chips were incubated with anti-DNA/RNA (at a fixed concentration of 80 µg·mL^{-1} diluted in 0.5x SSC) for 45 min at RT. Finally, the sensor chips were rinsed with DEPC-H_2O water and dried with N_2 flux. After each step of the assay, the rinsed and dried sensor chips were placed in the device to obtain the OPD value.

A.3. Design, optimisation and analytical parameters of the RAIS platform for miRNA detection.

A.3.1. Comparison of the RAIS biofunctionalisation approaches

Three different strategies were performed in order to demonstrate the capabilities of the RAIS device to identify miRNAs. The conventional thiol-gold approach was tested together with the bioaffinity between biotin-neutravidin. All the approaches were based on the immobilisation of DNA probes complementary to the miRNA-16-5p, following different gold surface and DNA probe modifications:

- Surface I. It implied the immobilisation of biotin-DNA probes through neutravidin-biotin affinity. Previously, NA was covalently bound to the gold surface by carboxyl-SAM activation and EDC/sulfo-NHS chemistry.
- Surface II. It was also based on biotin-neutravidin affinity. In this case, biotin-DNA probes were attached to the gold surface after a HPDP-biotin SAM formation and NA immobilisation.
- Surface III. A one-step and direct immobilisation of thiolated DNA probes was carried out over the gold surface.

Due to the novelty of the RAIS device, the three biofunctionalisation approaches were compared not in terms of sensitivity but in terms of visualization of the DNA probes spots on the sensor surface.

Figure A.6 shows the biofunctionalisation scheme and the OPD map read-out after each biofuntionalisation strategy. Surfaces I and II did not provide competitive results in terms of array formation, as no spots were observed on the OPD map. Due to the working principle of the RAIS device, the biotin strategies were expected to obtain higher OPD shifts due to the high molecular weight of biotinylated probes compared to thiolated ones. Although a well-known chemistry was employed for surface I, the short activation time of the EDC/sulfo-NHS reaction and the long handling and incubation time during thr biofunctionalisation protocol could hinder the covalent binding of the NA to the SAM. On the other hand, the proposed biotin-NA-biotin assay on surface II, could affect the free neutravidin binding sites, limiting or hampering the biotin-DNA probes unions. Finally, surface III was the simplest approach by the direct coupling of thiolated DNA probes onto the bare sensor chip. This strategy was successfully performed due to the excellent affinity between gold and thiol atoms, offering reproducible DNA arrays and being selected for the miRNA detection.

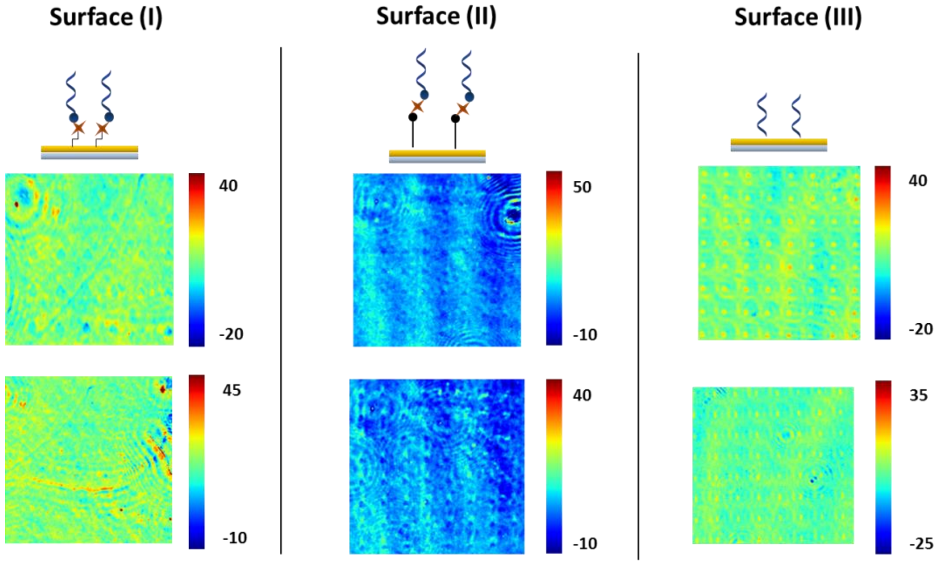

Figure A.6. Biofunctionalisation surfaces comparison. Surface (I) Biotin-probes were coupled in an NA-carboxyl-modified (II) Biotin-probes were coupled in an NA-biotin-modified (III) Thiol-probes were coupled in bare gold.

A.3.2. Influence of non-specific adsorptions in the RAIS sensor performance

The limited sensitivity of the plasmonic RAIS device (5.7 x 10^{-4} RIU) together to the small size (MW≈ 7 kDa) and low concentration in human real samples of the miRNAs biomarkers, made the identification of miRNA a challenge. In order to enhance the limit of detection of the biosensor for the miRNA detection, different strategies can be incorporated such as enzymatic reactions, antibodies or nanomaterials (e.g. nanoparticles)[87]. In our case, an amplification step by using a specific antibody against the DNA/RNA hybrids was carried out.

To avoid non-specific adsorptions on the gold surface due to the amplification step with the antibody and for future clinical analysis with plasma or serum, a blocking step was mandatory. Different blocking agents were added over the plasmonic sensor after the DNA immobilisation step (**Table A.2.**). The blocking agents differed in their chemical and charge properties, presenting neutral (BSA), positive (pLL-g-PEG and amino-dextran) or negative (CM-dextran) charge, respectively. All blocking agents were dissolved in PBS 10 mM and incubated over the sensor chips for 30 min at RT. After the blocking step, the corresponding hybridisation and amplification steps were carried out.

Table A.2. Blocking agents employed previously to the antibody amplification and their effect on the OPD value.

Blocking agent	OPD effect
BSA 0.1 mg·mL^{-1}	Decrease
PLL-g-PEG 0.1 mg·mL^{-1}	Increase
Amino-dextran 0.1 mg·mL^{-1}	Increase
CM-dextran 0.1 mg·mL^{-1}	Increase

As observed in **Table A.2.**, most of the blocking agents increase the OPD value after their incubation. The OPD value provides information about the biochemical interactions not only in the biofunctionalised spot but also in its surroundings, as it calculates the interference between the array (spots) and the reference (surrounding gold surface). The fact that OPD increases means that the blocking agents are interacting with the immobilised probes, increasing the molecular weight on the sport compared to the gold surface. DNA probes are negatively charged molecules, so using charged molecules to block the surface could more severely affect the biosensor assay by hindering miRNA accessibility. Only neutral blocking BSA causes a decrease of the OPD signal, related to its binding over the gold surface, increasing the thickness of the reference gold surface surrounding the spots (increase of the background signal and, therefore, a decrease of ΔOPD). BSA was deposited on the sensor surface without interfering with the DNA probes, being a good candidate for the blocking step in the miRNA biosensor assay.

A.3.3. Analytical parameters of the RAIS point-of-care

To evaluate the capabilities of the POC biosensor for miRNA identification, OPD values were monitored after each step assay (**Figure A.7**). **Figure A.7BC** shows the OPD map and the OPD values obtained after each stage for miRNA-16-5p detection in three different sensor chips. The direct and simple spotting of thiolated DNA probes onto bare chips ensures the presence of spots and a high OPD value (OPD ≈ 23) due to the excellent thiol-gold affinity. The BSA blocking step resulted in an OPD decrease, consistent with its adsorption over the gold surface (OPD ≈ 17). The direct detection of miRNA-16-5p was barely observed (OPD ≈ 17) given the relatively small size of the miRNA and the limited sensitivity of the RAIS POC. An amplification step was included by employing an antibody specific only to DNA/RNA hybrids[276]. A larger and detectable phase change was triggered by the high molecular weight of the antibodies (MW = 115 kDa), which enhanced the overall OPD signal (OPD ≈ 25) and improved the biosensor assay sensitivity.

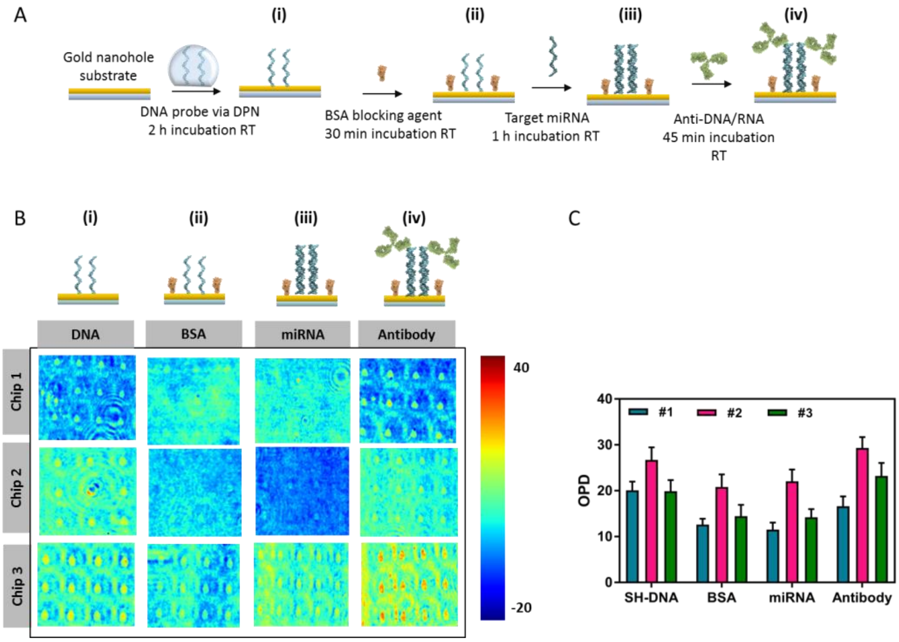

Figure A.7. MiRNA-16-5p detection assay using the RAIS POC. (A) Schematic representation of the steps for the miRNA identification (i) SH-DNA immobilisation (ii) BSA blocking (iii) miRNA-16-5p hybridisation and (iv) antibody amplification. (B) Representative interferometric images with the false colour image indicative of the OPD intensity maps of three microarrays in every assay step for miRNA-16-5p 10 mM detection (C) Mean OPD ± SD corresponding to images in Figure A7B.

Once the detection of miRNA-16-5p biomarker was optimised and achieved using the RAIS platform, the methodology was evaluated in terms of sensitivity, specificity and reproducibility.

By using the conditions previously detailed, a calibration curve for miRNA-16-5p was obtained to evaluate the sensitivity of the biosensor assay. The calibration curve shows the OPD sensor signal obtained after the anti-DNA/RNA antibody amplification step (**Figure A.8A**). Although a saturation region is observed for miRNA concentrations higher than 20 µM, a linear behaviour can be observed for the lowest analysed concentrations (0 – 20 µM), reflecting a LOD of 0.94 µM (R^2= 0.832). The clinical values of miRNAs in real samples commonly are within the fM - pM range in serum or plasma[201]. Therefore, the sensitivity achieved with the novel RAIS device is not enough for the clinical requirements of this family of biomarkers. However, one of the objectives of the EU project was to demonstrate the capabilities of the new instrument for the label-fee and selective microarray biosensing of biomarkers and this objective was fulfilled.

The specificity of the assay was also evaluated (**Figure A.8B**) by two negative control experiments. DNA probes were incubated with either a non-complementary miRNA (miRNA-21-5p) or simply buffer without miRNA. After the hybridisation step, the anti-DNA/RNA amplification was carried out. As shown in **Figure A.8B** a significantly higher enhancement of the OPD sensor signal was observed for the complementary miRNA-16-5p (**Figure A.8B(1)**). No significant OPD increase resulted when a non-complementary miRNA was present (**Figure A.8B(2)**) or in the absence of any miRNA (**Figure A.8(3)**). In these cases, the absence of miRNA or the impossibility of recognition of non-complementary analytes by the DNA probes prevented the formation of DNA/RNA hybrids and, therefore, the enhancement of the OPD sensor signal. Non-specific adsorptions due to anti-DNA/RNA antibody on the functionalised array were also not observed, showing the adequate surface blocking of BSA.

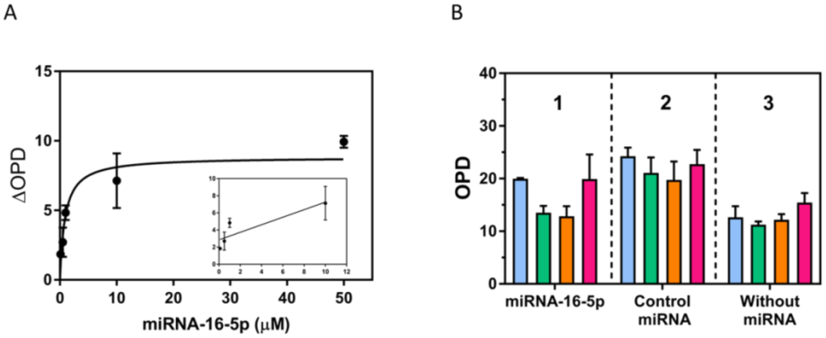

Figure A.8. (A) Calibration curve for miRNA-16-5p in PBS. Signals correspond to the amplification step. All data show mean ΔOPD ±SD of triplicate measurements obtained in three different chips (B) Specificity study for miRNA-16-5p assay showing the variation in the OPD in three different conditions: (1) specific assay with target miRNA-16-5p (10 mM) followed by anti-DNA/ RNA; (2) addition of non-complementary miRNA (miRNA-21-5p 10 mM) followed by anti-DNA/RNA (3) no addition of any miRNA (only buffer); followed by anti-DNA/RNA. All data show mean OPD ± SD of triplicate measurements.

Finally, reproducibility of the biofunctionalisation process was analysed by the calculation of the coefficient of variability (% CV) for DNA immobilisation and BSA blocking. The versatility of the plasmonic biosensor for different biomarker detection and the simple DNA probes immobilisation strategy enable the validation of this methodology not only with the miRNA-16-5p but also with other miRNA (miRNA-21-5p). Although miRNAs are composed of different nucleotide sequences, they exhibit similar behaviour under the same conditions, so an identical RAIS methodology was carried out for miRNA-21-5p. **Table A.3** shows the OPD sensor signal after the DNA probe immobilisation and BSA blocking steps. In both miRNA cases, the achieved OPD signal is similar for each step and the intra-chip variability is lower than the FDA recommended values (≈ 9 %) regardless of the DNA probe attached to the sensor surface. However, the inter-chip variability is slightly higher than the recommended values (15 %)[142] for clinical diagnostics. Several factors, such as dip-pen spotting conditions, incubation protocols and batch chip manufacturing, could increase assay variability. These factors should be studied and optimised to ensure better performance of the RAIS device and drive its integration into clinical practice.

Table A.3. Intra-chip and inter-chip variability in the two-step DNA-based biofunctionalisation protocol

Intra-chip variability				
	miRNA-16-5p		**miRNA-21-5p**	
	Mean ±SD	**%CV**	**Mean ±SD**	**%CV**
DNA-SH	22.5 ±1.86	8	27.7 ±0.98	3
BSA blocking	17.9 ±4.22	9	18.9 ±1.33	7
Inter-chip variability				
	miRNA-16-5p		**miRNA-21-5p**	
	Mean ±SD	**%CV**	**Mean ±SD**	**%CV**
DNA-SH	23.5 ±4.33	18	23.4 ±3.65	15
BSA blocking	17.9 ±4.22	23	17.9 ±4.51	26

A.4. Conclusions

A novel POC biosensor microarray device based on lens-free microscopy and light interferometry has been employed for the detection of miRNA-16-5p, a biomarker specific to sepsis. Implementing a microarray format through dip-pen technology, a miRNA biosensor assay was optimised. The biosensor assay based on the direct attachment of thiolated DNA probes onto the bare gold sensor surfaces, the hybridisation of the miRNA for base complementarity and an amplification step using an antibody specific against DNA/RNA hybrids, reported a LOD of 0.94 µM. This LOD is insufficient for its utilization in clinical applications, where an extreme sensitivity is required (fM - nM). However, the biofunctionalisation strategy developed allows a fast, one-step immobilisation and shows excellent specificity and reproducibility. In addition, its versatility makes it suitable for any miRNA, regardless of the nucleotide sequence.

This methodology was developed in the frame of a European project whose final aims was built up a new instrument for the label-fee microarray biosensing and demonstrated their capabilities using sepsis biomarkers. As we shown in this Anex, the objective has been fulfilled for miRNA identification. However, the RAIS instrument and the biomolecular methodology should undergo several cycles of upgrades to optimise the level of sensitivity and to be able to transfer the POC to the clinical practise. To boost the inherent optical resolution of the optical device, novel nanoplasmonic structures, and the incorporation of a multispectral source were studied in the last years. Moreover, the re-optimisation of some biological steps such as the amplification strategy through conjugated nanoparticles with the anti-DNA/RNA antibody would also increase the mass on the sensor surface, enhancing the final sensitivity of the device.

Annex B

Nanoplasmonic gold structures for LSPR biosensors: evaluation of a miRNA biomarker related to lung cancer diagnosis

In order to boost the sensitivity in LSPR biosensors, we have followed optimised hole-mask colloidal lithography protocols for the fabrication of the different plasmonic nanostructures. Nanostructures as round nanodisks (80 and 100 nm diameter), elliptical nanodisks (80 x 90 nm axes) and nanogap antennas (gap size ≈ 12 nm) have been designed, fabricated and fully characterised. We have evaluated the nanoplasmonic structures by analysing their bulk sensitivity and their biosensor capabilities. For that, we have studied and optimised the detection of a lung cancer biomarker (miRNA-210-3p) through a complementary hybridisation assay. Finally, surface sensitivities reported for each nanostructure were compared.

B. Nanoplasmonic gold structures for LSPR biosensors: evaluation of a miRNA biomarker ralted to lung cancer diagnosis.

B.1. Introduction

Plasmonic biosensors are powerful diagnosis tools due to their potential for monitoring biorecognition events taking place in the close vicinity of the plasmonic metal surface. Although SPR biosensors are the most employed biosensing platforms, other configurations such as localised surface plasmon resonance (LSPR) are gaining prominence.

LSPR sensors are characterized by the excitation of sub-wavelength-sized metal nanostructures and the exploitation of localised plasmons highly confined on the surface of those nanostructures. In contrast to SPR sensors, the evanescent field of LSPR is tightly confined at a short distance from the surface of the nanostructure, exhibiting a penetration depth in the dielectric medium around 10 - 30 nm[277,278]. The penetration depth range is of the same order as the typical size of the target biomolecules (proteins, DNA sequences…) leading to increased sensitivity to minute RI changes in the immediate vicinity of the nanostructure and obviating bulky RI changes occurring in nanostructure environment due complex matrices or solutions with a high RI[279,280]. The outstanding sensitivity together the small size and minimal detection area of the nanostructures make the LSPR-based biosensors excellent candidates for point-of-care integration and multiplexed analysis. Some LSPR sensors have been reported for the identification of analytes such as miRNAs[281], bacteria[282], drugs[100] among others, even at single molecule level[283–286].

In LSPR-based sensors, the shape, size and distribution of the nanostructures determine the spectral signature of its plasmonic resonance[278]. By using simple sphere-shaped nanoparticles, the first LSPR nanostructures studied was round nanodisks. The symmetry of round nanostructures limited the confinement and strength of the evanescent field, and innovative nanostructures and distributions emerged to enhance the electromagnetic field[287]. The shape of the nanostructures can determine the polarizability of the field. The spherical symmetry of round nanodisks exhibits dipolar resonance with generates a weak evanescent field. However, the modification of the dimensions of a nanostructure (nanorods or elliptical nanodisks) could generate anisotropy and multipole resonances, increasing the polarizability of the field and enhancing the LSPR. The distribution also affects the LSPR since the inter-coupling between two nanostructures leads to a stronger field enhancement. The evanescent field can be more powerful as the nanostructures get closer to each other since the fields coupling at the nano gap surrounded by them[288]. Nanogap antennas (two nanostructures separated by a nanogap of a few nanometers) are highlighted since they support the confinement of a high local electromagnetic field within the nanogap formed by the arms of a dipole antenna[289]. The proximity of the metallic nanoantennas induces plasmon coupling between them and forms a hybrid plasmon mode that generates a strong field enhancement[290], being this phenomenon remarkably observed for gap sizes below 20 nm[291,292].

In this work, we have studied the effect of the shape, size and distribution of gold nanostructures in LSPR-based biosensors in order to achieve the optimised configuration for lung cancer diagnosis. We have selected the simplest and traditional round nanodisks, an elongated elliptical shape and the inter-coupling of nanogap antennas. Plasmonic sensor chips with different gold nanostructures (round nanodisks (80 and 100 nm diameter), elliptical nanodisks (80 x 90 axes) and nanogap antennas (gap size ≈12 nm)) have been fabricated by colloidal lithography, which offers a versatile and affordable strategy to fabricate nanostructures with different characteristics at the chip or even at wafer level. Experimental characterisation and comparison of the nanoplasmonic sensor chips were performed, including Scanning Electron Microscope (SEM) images and the assessment of their bulk sensitivity. Finally, biosensing capabilities of each plasmonic nanostructures were evaluated and compared by a label-free and direct complementary hybridisation assay for the detection of miRNA-210-3p biomarker. MiRNA-210-3p is involved in the expression of HIF-1 factor, indispensable for cancerous cells environment[209]. As we commented in **Chapter 5**, this miRNA biomarker is up-regulated during a cancerous process, and is present in concentrations of fM-nM in body fluids.

B.2. Materials and methods

B.2.1. Chemical and biological reagents

The buffers employed were Phosphate buffer saline PBS 50 mM (750 mM NaCl, 33 mM Na_2HPO_4, 17 mM NaH_2PO_4, and 2 mM EDTA , pH 7) and Sodium citrate buffer saline (SSC-5X) (75 mM SSC, 750 mM NaCl, 4 mM EDTA pH 7). All the buffer compounds, anisol and poly(diallyldimethylammonium) chloride (PDDA 20 %wt, Mw 400-500 K), diethyl pyrocarbonate (DEPC), ethylenediaminetetraacetic acid (EDTA), sodium dodecyl sulfate(SDS) were acquired from Sigma-Aldrich (Steinheim, Germany). Glass substrates (No. 4, 22 x 22 mm) were purchased from Thermo Scientific Menzel-Glaser (Braunschweig, Germany). Organic solvents (acetone, absolute ethanol, toluene, and 2-propanol) and hydrochloric acid (HCl) were purchased from Panreac–Applichem (Barcelona, Spain). Polymethyl methacrylate 950 K (PMMA A8), was obtained from Microchem, (Westborough, USA). Polystyrene sulfate latex beads 8 %wt, 0.1 μm or 0.08 μm diameters were purchased from Invitrogen (Eugene, USA). Lateral spacers SH-PEG-COOH, SH-PEG-NH_2, and SH-PEG-CH_3 (MW 2000 g/mol) were purchased from Laysan Bio (Alabama, US). Bond-Breaker™ TCEP Solution (Tris(2-carboxyethyl)phosphine hydrochloride solution) was purchased from ThermoFisher (Massachusetts, US).

DNA capture probes incorporating a thiol group (SH-) at the 5′-end and the miRNA nucleotide sequence (**Table B.1**) were obtained from Ibian (Zaragoza, Spain).

In order to work in RNAase conditions, DEPC-H_2O was employed (Milli-Q water incubated overnight with 0.1% DEPC and autoclaved at 121° C for 1 h). All solid plastic and glass materials were sterile.

Table B.1. Nucleotide sequence of the miRNAs sequences employed in the nanoplasmonic biosensors

miRNA name	DNA probe (5’→3’)	miRNA sequence(5’→3’)
miRNA-210-3p	[Thiol]TTT TTT TTT TTT TTT TCA GCC GCT GTC ACA	CUG UGC GUG UGA CAG CGG CUG A

miRNA-205-5p	-	UCC UUC AUU CCA CCG GAG UCU G

B.2.2. Nanoplasmonic structures fabrication: Colloidal nanolithography process

Nanoplasmonic chips were fabricated over glass substrates following a modified protocol of the colloidal hole-mask lithography (HCL) process described by B. Hans Fredriksson *et al.*[293] (**Figure B.1**). Firstly, glass slides were cleaned using SDS, HCl, and Milli-Q water. After rising and drying under N_2 flow, they were sonicated for 5 min at 50 °C sequentially in acetone and isopropanol and finally dried under N_2 flow. A thin layer (thickness ≈ 210 nm) of PMMA diluted at 4% in anisole was spin-coated (4000 rpm, 1500 $r{\cdot}s^{-2}$), onto the glass-treated substrate, and immediately baked at 165 °C for 5 min. Then, an O_2 plasma treatment (10 s, 75 W, 75 mTorr) was applied to increase the hydrophilicity of the PMMA layer. A cationic solution of PDDA 0.2 wt % in water was deposited over the PMMA-treated glass for 1 min, then the chips were rinsed with Milli-Q water and dried under N_2 flow. A solution of nanoparticles (NPs) of sulfate latex beads is diluted in water (0.01 wt %) and drop-coated in the glass for 1 min. The chip was then immersed in water at 95 °C for 3 min) to fix the NPs on the PMMA layer before rinsing again with Milli-Q water and drying under N_2 flow.

Afterward, a titanium (Ti) sacrificial layer of 20 nm thickness was evaporated (EB273, Telemark, Germany) generating a round (normal 90° evaporation) or an elliptical shape mask by tilting the sample stage concerning to the normal 90° evaporation. Tape-stripping was carried out to remove the NPs, leaving the Ti-hole mask with differential shape characteristics. Using a reactive ion etcher (RIE) (Oxford PlasmaPro®100 Cobra Oxford Instruments, UK), a selective etching of the thin PMMA layer was achieved (O_2 plasma: 5 min 400 W, 75 mTorr, O_2-flux = 50 sccm). Now the glass substrate is exposed and accessible for the Au evaporation due to small cavities underneath the Ti layer left by the etched PMMA.

Finally, e-beam evaporation of 19 nm of gold is carried out. For round and elliptical nanodisks, an unique evaporation without angle modification is sufficient. For nanogap antennas, e-beam evaporation was performed two times, using equal values of opposite angles concerning to the normal evaporation. To improve the gold adhesion to the glass surface, a thin Ti layer (1 nm) using the same angles was deposited previously to the gold one. To remove any remaining Au and Ti coated on top of the PMMA layer, a lift-off process was done by sonicating the chips in acetone for short cycles of less than 5 s. The sensor chips were rinsed with isopropanol and dried under N_2 flow, eventually.

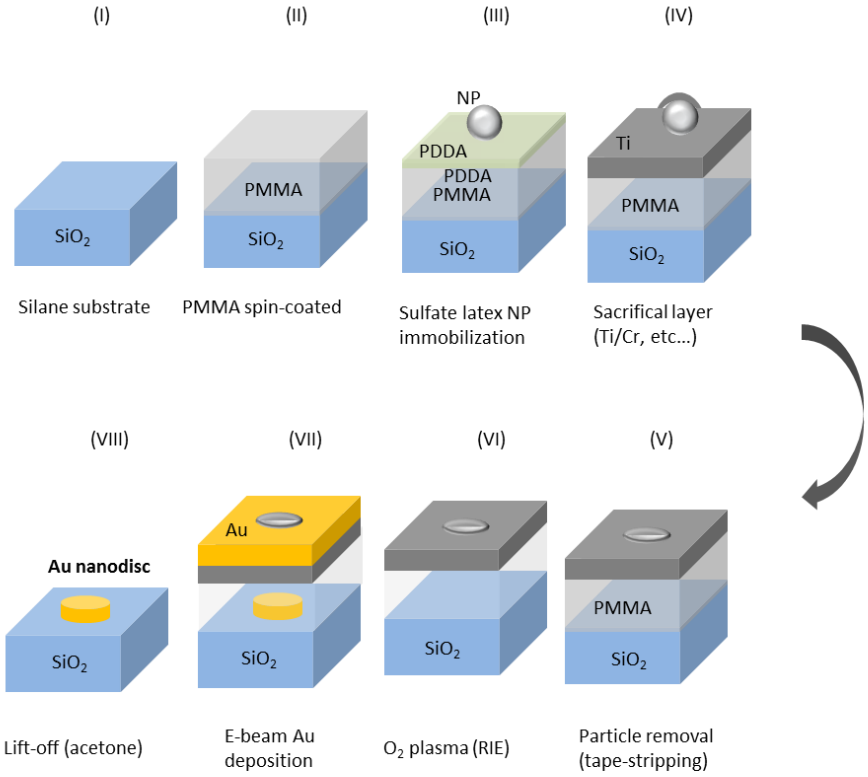

Figure B.1. Schematic representation of the nanofabrication process of gold nanodisks non-ordered arrays based on hole-mask lithography.

B.2.3. Localised Surface Plasmon Resonance experimental platform

We employed the in-house plasmonic platform previously described in **Chapter 2** at a fixed angle of $\theta=80^{\circ}$. The light was set in transverse-electric (TE) polarization mode.

B.2.4. Bulk sensitivity evaluation

As we commented in the **Introduction (1.2.1.Optical biosensors)**, the sensitivity represents the magnitude change of the transducer response to any change in the refractive index and it corresponds to the slope of the linear calibration curve, expressed in nm·RIU^{-1}. In the case of the LOD, we calculate it applying the **Equation 1.1**.

In order to analyse the bulk sensitivity for the different plasmonic nanostructures, PBS solutions with different refractive indexes previously evaluated by a digital refractometer J57 from RUDOLPH (Hackettstown, USA) were flowed over the sensor surface at a constant rate of 20 µL·min^{-1}. **Table B.2** shows the RI of the PBS solutions employed for the bulk sensitivity experiment.

Table B.2. Refractive index of solutions employed for bulk sensitivity calculation

PBS solution	Refractive index (RIU)	$\Delta\eta$ (RIU)
20 X	1.36248	2.9×10^{-2}
10 X	1.34759	1.5×10^{-2}
5 X	1.33987	6.8×10^{-3}
1 X	1.33428	1.6×10^{-3}
0.5 X	1.33364	7.4×10^{-4}
0.1 X	1.33314	1.7×10^{-4}

B.2.5. MiRNA complementary assay

B.2.5.1. DNA probes immobilisation

For the *in-situ* immobilisation of the DNA probes, the sensor chips were placed in the experimental set-up and a constant flow (10 µL·min^{-1}) of DEPC–H_2O was employed. Then, a solution of the DNA probe 1 µM (or a combination with lateral spacers) prepared in 50 mM PBS was flowed at a constant flow rate. Previous to the immobilisation, the DNA probe solution was incubated with 100 nM of TCEP for 20 min at 37 ºC to reduce eventual disulfide bonds formed between the thiol groups.

B.2.5.2. miRNA detection

Different miRNA solutions (from 0.5 nM to 100 nM, 150 µL) were dissolved in SSC 5X buffer (0.75 M in NaCl, 0.075 M in sodium citrate) and flowed over the plasmonic biofunctionalised biosensor surface at a 10 µL·min^{-1} rate, using SSC 5X as running buffer.

B.2.6. Data analysis

For bulk sensitivity, calibration curves were plotted as mean sensor signal ($\Delta\lambda$) and its standard deviation (SD) *versus* variation in the refractive index ($\Delta\eta$). The data were fitted to a linear regression (**Equation 3.1**) using Graphpad Prism (Graphpad Software, Inc., California, US).

For surface sensitivity, calibration curves were plotted as mean sensor signal ($\Delta\lambda$) and its standard deviation (SD) *versus* miRNA concentration. The data were fitted to one site-specific binding model regression (**Equation 4.1**) using Graphpad Prism (Graphpad Software, Inc., California, US).

The experimental LOD was determined as three times the SD of the sensor signal obtained from a blank signal.

B.3. Round gold nanodisks

Round gold nanodisks are the most traditional nanostructures. They were fabricated through conventional hole-mask lithography and e-beam evaporation (**Figure B.2**), without any modification to the protocol. In order to evaluate the effect of the size in the LSPR, NPs characterised by different diameters were used: 80 and 100 nm. After the nanofabrication process, nanodisks of 20 nm height and 6 – 7% density were achieved.

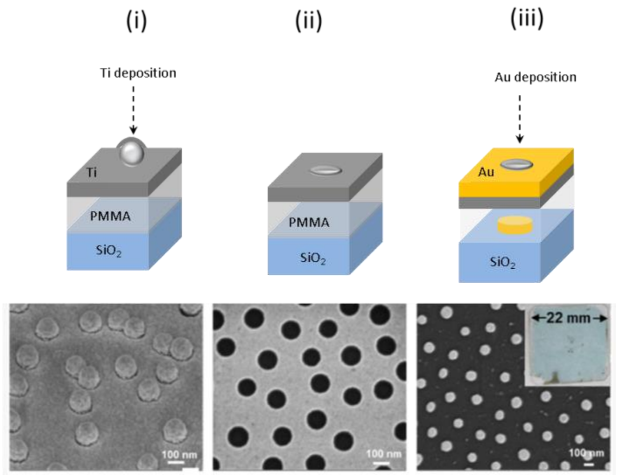

Figure B.2. SEM images of round gold nanodisks after the key steps of the fabrication process: (i) sacrificial layer deposited over NPs; (ii) tape-stripping of NPs, and (iii) acetone lift-off. The insets show a photograph and dimensions of a representative sensor chip.

B.3.1. Round gold nanodisks: Bulk and surface sensitivity evaluation

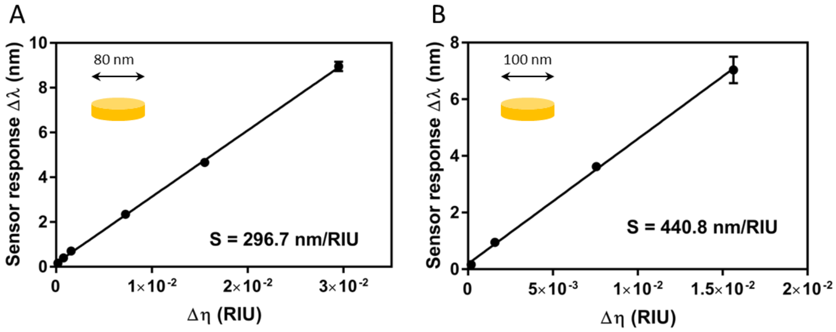

Figure B.3. Calibration curve of the bulk sensitivity for round gold nanodisks sensors of (A) 80 and (B) 100 nm diameter. Each signal corresponds to the mean ± SD of triplicate measurements.

Figure B.3 shows the calibration curve obtained by injecting a solution with different refractive indexes over the nanoplasmonic sensors of 80 and 100 nm diameters. Sensitivity related to each nanostructure was determined by the slope of the calibration curve, being S =

296.7 nm·RIU^{-1} in the case of 80 nm round nanodisks and S=440.8 nm·RIU^{-1} for 100 nm round nanodisks. Considering the achieved sensitivity, we could affirm that the bigger nanostructures (100 nm) allow a better performance of the LSPR biosensor. However, the limits of detection in both cases are vastly similar (LOD = 2.46x10^{-5} RIU for 80 nm round nanodisks and LOD = 2.27x10^{-5} RIU for 100 nm).

Regarding the surface sensitivity for biosensing, we evaluated the detection of the miRNA-210-3p biomarker. Based on a complementary hybridisation assay (**Figure B.4A**), we first optimised the condition for the highest bioreceptor surface coverage and miRNA detection in 100 nm nanodisks. The optimised protocol was employed for biosensing analysis in all the selected nanostructures. Combinations of DNA probes and lateral spacers (MCH, thiol-PEG with different functional groups) were immobilised in different concentrations and ratios onto the sensor surface. Then, the hybridisation signal from miRNA-210-3p 100 nM was noted. **Figure B.4B** reflects the sensor signal depending on the bioreceptor layer immobilised over the gold nanostructures and the corresponding sensor signal to the hybridisation of miRNA-210-3p 100 nM. As can be observed, the monolayer composed of a 1 µM concentration of DNA probes, without lateral spacers, is the best approach for the miRNA assay. This condition reported the highest immobilisation ($\Delta\lambda \approx 7$ nm) and analyte recognition signal ($\Delta\lambda \approx 0.6$ nm). The cited monolayer enabled to completely cover the available gold surface with the bioreceptors, reflecting immobilisation signals similar to those of more concentrated monolayers (2 µM $\Delta\lambda \approx 6$ nm and 5 µM $\Delta\lambda \approx 7$ nm). Moreover, the increase of DNA probes concentration and, therefore, the bioreceptor density, hindered the accessibility of the miRNA analyte, showing sensor signals lower than 0.6 nm. Compared to conventional SPR, with a continuous gold surface, in the LSPR-based biosensor the use of lateral spacers is not required. The small gold surface available together with the low bioreceptor density if there are lateral spacers could reduce the miRNA detection. Thus, in **Figure B.4B**, the incorporation of lateral spacers generated a lower sensor response related to miRNA detection ($\Delta\lambda \approx 0.3$ nm). The monolayer composed of a 1 µM of complementary DNA probes was the best approach for miRNA-210-3p hybridisation in LSPR-based biosensor, ensuring adequate surface coverage and bioreceptor density.

As can be seen in **Figure B.4C**, regardless of the NP's size, the sensor signal rose when the miRNA concentration increased. An evaluation of different miRNA concentrations enabled to obtain calibration curves and calculate the LOD for each round nanodisks size, being 3.49 nM for 100 nm, and 1.86 for 80 nm. Although both nanostructures showed the same round shape and density on the sensor surface, a difference was manifested in the LOD achieved and the 80 nm gold round nanodisks reported a slightly better limit of detection.The smaller gold structure fabricated in the case of 80 nm nanodisks could generate and confine a stronger evanescent field, being more sensitive to any RI change in the gold surface such as the miRNA hybridisation. Since 80 nm round nanodisks showed better performance, NPs of this size were used to fabricate gold elliptical and nanogap antennas.

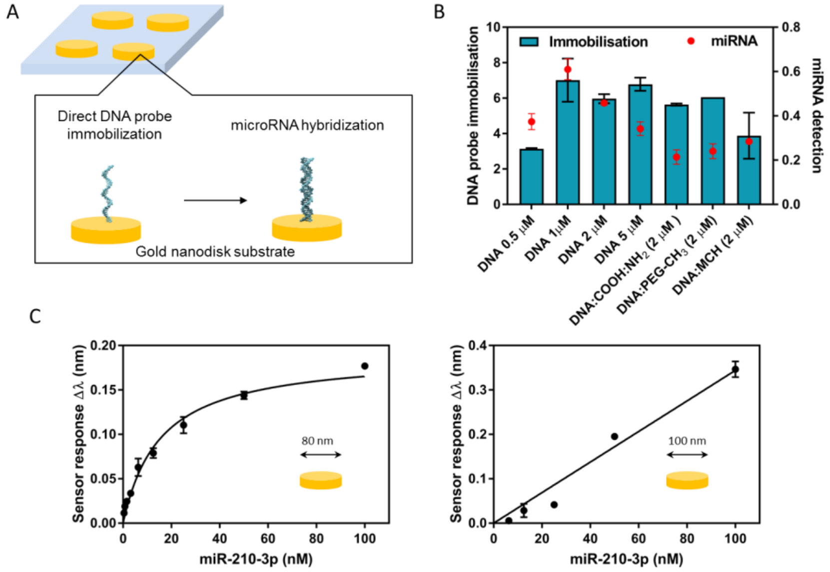

Figure B.4. Round gold nanodisks surface sensitivity. (A) Scheme of the complementary hybridisation assay (B) Biosensor response obtained during the immobilisation of different DNA probes and lateral spacers combinations and their respective miRNA capture signals using 100 nm gold nanodisks sensors. (C) Calibration curve of the miRNA-210-3p detection for round nanodisks. Each signal corresponds to the mean ± SD of triplicate measurements.

B.4. Elliptical gold nanodisks

Elliptical nanodisks can be fabricated by evaporating the Ti sacrificial layer over the sample (glass slides) with a rotation angle (Ɣ) concerning to its vertical axis. The rotation angle would determine the length of the long axis. In our case, NPs of 80 nm and an angle Ɣ of 5° were employed, resulting in elliptical nanodisks with long radii of 90 nm and short radii of 80 nm. **Figure B.5** shows an SEM image of the elliptical nanodisks, characterised by 20 nm height and located with a 6 – 7% density over the sensor surface.

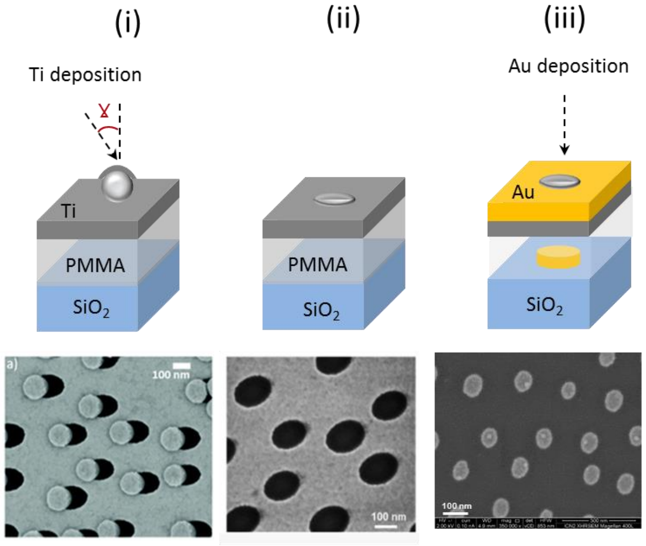

Figure B.5. SEM images of elliptical gold nanodisks after the key steps of the fabrication process: (i) sacrificial layer deposited over NPs; (ii) tape-stripping of NPs, and (iii) acetone lift-off.

B.4.1. Elliptical gold nanodisks: Bulk and surface sensitivity evaluation

The calibration curve showed in **Figure B.6A** reported a sensitivity of 307.8 nm·RIU^{-1} and a bulk sensitivity for elliptical nanodisks of 3.59 x10^{-5} RIU. Concerning the surface sensitivity for miRNA-210-3p detection, **Figure B.6B** shows the sensorgram where the LSPR signal increases when the miRNA concentration increases. In addition, a non-complementary miRNA (miRNA-205-5p) was evaluated, exhibiting a null signal when was flowed over the sensor surface. This evaluation demonstrates the excellent specificity of the biosensor assay. Different concentrations of miRNA-210-3p were evaluated with the elliptical nanodisks, showing a limit of detection of 1.53 nM (**Figure B.6BC**).

All three parameters (sensitivity, bulk and surface sensitivity) were close to those reported for the 80 nm round nanodisks sensors. The slight difference in size and shape between the elliptical (80 x 90 nm radii) and the round gold nanodisks (80 nm diameter) did not excessively improve the plasmonic shift and thus both exhibited a similar behaviour.The elliptical radii hardly differ in length, and perhaps more elongated elliptical nanodisks (e.g. 60 x 100 nm radii) could increase the field polarizability and improve the LSPR performance.

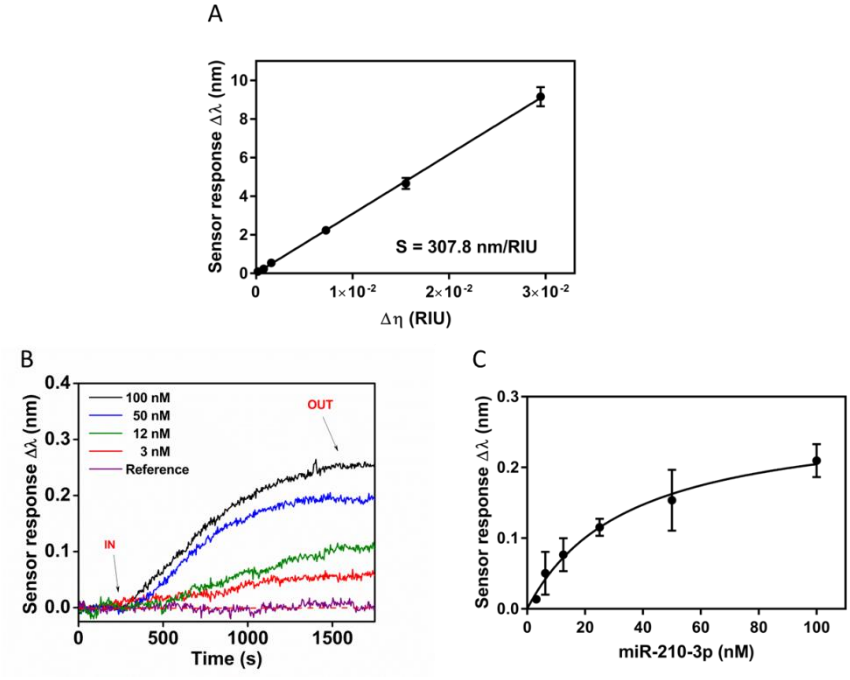

Figure B.6. (A) Bulk sensitivitycalibration curve for elliptical gold nanodisks. Each signal corresponds to the mean ± SD of triplicate measurements. (B) Real-time sensorgrams showing the specific interaction of DNA probe with different miRNA-210-3p concentrations. Non-specific miRNA-205-5p (reference) was measured at a concentration of 100 nM. (C) Calibration curve in hybridisation buffer (SSC 5X) for miRNA-210-3p. Each signal corresponds to the mean ± SD of triplicate measurements.

B.5. Gold Nanogap antennas

Nanogap gold antennas were fabricated by creating a hole-mask equal to the elliptical nanodisks (Ti sacrificial layer with a rotation angle (Ɣ) of 5°). In addition, the evaporation of the gold layer was also conducted with the same rotation angle. Following this protocol, randomly distributed arrays of gold nanogap antennas (two nanodisks of variable shape and diameter, height = 20 nm, separated by a nanogap of 12 nm) were achieved (**Figure B.7**).

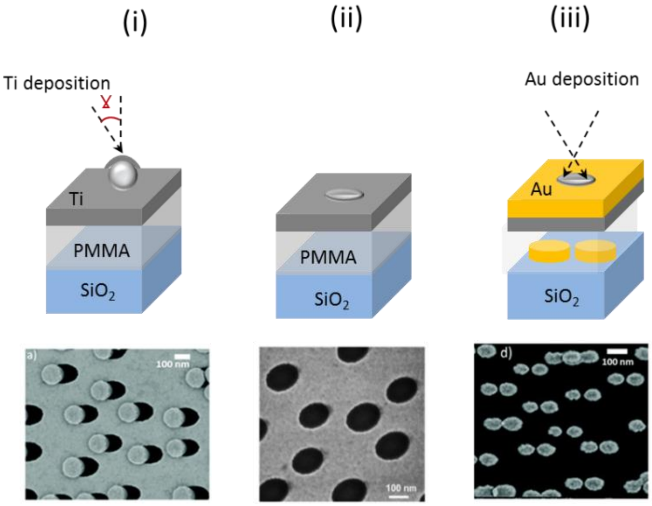

Figure B.7. SEM images of gold nanogap antennas after the key steps of the fabrication process: (i) sacrificial layer deposited over NPs; (ii) tape-stripping of NPs, and (iii) acetone lift-off.

B.5.1. Gold nanogap antennas: Bulk and surface sensitivity evaluation

In the case of the gold nanogap antennas, the sensitivity and bulk sensitivity were 427.4 nm·RIU^{-1} and 5.11 x 10^{-5}, respectively (**Figure B.8A**). These values coincide with the behaviour of all the nanostructures fabricated. However, the detection of the miRNA-210-3p showed a better performance. As in the case above, there was a direct relationship between the sensor signal and the miRNA concentration, increasing proportionally until the DNA probes saturation (**Figure B.8B**). The LOD reached with the gold nanogap antennas was 0.75 nM, the best sensitivity reported with the proposed gold nanostructures (**Figure B.8C**).

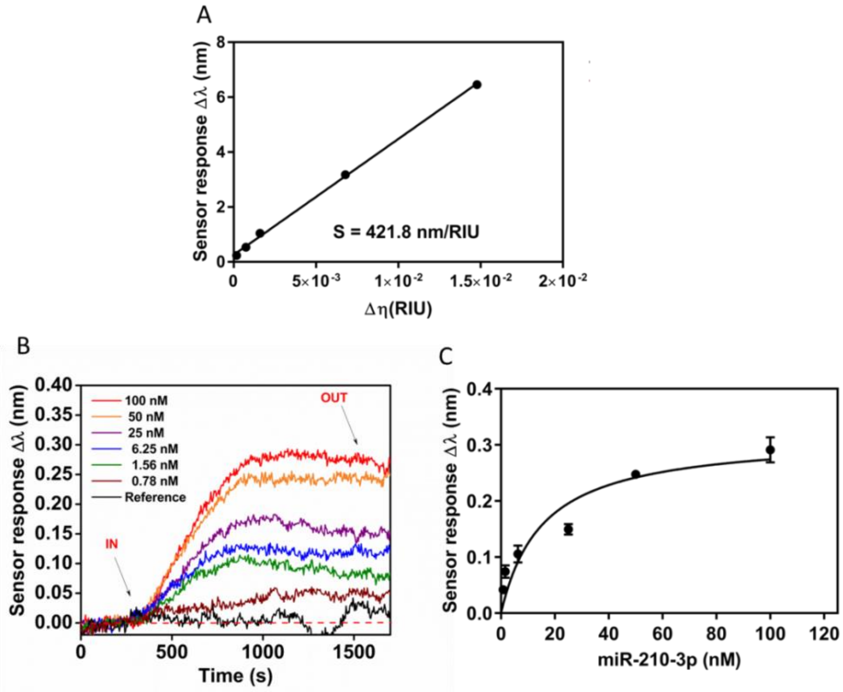

Figure B.8. (A) Calibration curve of the bulk sensitivity for gold nanogap antennas. Each signal corresponds to the mean ± SD of triplicate measurements (B) Real-time sensorgrams showing the specific interaction of the DNA probes with different miRNA-210-3p concentrations. Non-specific miRNA-205-5p (reference) was evaluated at a concentration of 100 nM (C) Calibration curve in hybridisation buffer (SSC 5X) for the detection of miRNA-210-3p. Each signal corresponds to the mean ± SD of triplicate measurements.

The proximity of the gold nanoantennas (≈ 12 nm), allowed plasmonic coupling of both nanostructures and generated a stronger field. Although this enhancement could not be observed for bulk changes in the RI, reflecting similar values as for previous nanostructures, it was demonstrated for RI changes close to the gold surface. Thus, the surface sensitivity for miRNA-210-3p detection was improved to values below 1 nM.

A summary of the fabricated nanostructures and their corresponding sensitivity, bulk and surface sensitivities are collected in **Table B.3**. Four all nanostructures manifest a bulk sensitivity in the range of 10^{-5} RIU, a common value for an LSPR sensor. Regarding the detection of the miRNA biomarker, the nanoplasmonic structures also exhibit similar values, with limits of detection in the nM range. However, we should highlight the gold nanogap antenna behaviour since it reported a LOD twice better as compared with the elliptical or 80 nm round nanodisks and three times better than the 100 nm round nanodisks. This demonstrates that the fabrication of sophisticated and inter-coupling nanostructures as the nanogap antennas could improve the performance of LSPR biosensors. In fact, some studies have reported the use of these structures for biological applications[294,295].

Table B.3. Plasmonic nanostructures, bulk and surface sensitivity values.

Nanostructure	**Sensitivity (nm·RIU^{-1})**	**Bulk sensitivity (RIU)**	**Surface sensitivity miRNA (nM)**
Round 100 nm	440.8	2.27x10^{-5}	3.49
Round 80 nm	296.7	2.46x10^{-5}	1.86
Elliptical	307.8	3.59x10^{-5}	1.53
Nanogap antennas	427.4	5.11x10^{-5}	0.75

B.6. Conclusions

Plasmonic biosensors are the most widely evanescent wave-based sensors employed due to their robustness, simplicity and versatility, among other excellent characteristics. Specifically, localised surface plasmon resonance has drawn attention for its potential to confine the field in tiny metallic nanostructures, enhancing the sensitivity of this type of biosensors. The shape, size and distribution of the nanostructures determine the spectral signature of its resonance and the overall biosensor performance. Following a previously reported hole-mask colloidal lithography method, we have fabricated four gold nanostructures: round nanodisks of 80 and 100 nm diameter, elliptical (80 x 90 nm radii) and nanogap antennas (gap size ≈12 nm). The biosensing behaviour of the nanoplasmonic structures was assessed in order to select the best one. We verified the size, shape and distribution of the nanostructures by SEM images. In addition, we analysed solutions of different refractive index (sensitivity and bulk sensitivity) and the detection of a lung cancer biomarker, the miRNA-210-3p. Comparing the bulk sensitivity, all the nanostructures reported a LOD within the expected values for an LSPR sensor, in the range of 10^{-5} RIU. However, for the miRNA detection, the limits of detection varied. Nanogap antennas showed the best sensitivity, with a LOD of 0.78 nM, twice better as compared to round 80 nm and elliptical nanodisks and three times better than round 100 nm. This result can be explained due to the stronger electromagnetic filed confinement in the nanogap. Gold nanogap antennas are a promising candidate nanostructure for LSPR sensors. A more extensive study with gold nanogap antennas should be explored to reveal the full potential of these nanostructures for identifying analytes with low molecular weight and/or present in low concentrations in biological samples.

List of publications

- **JOURNAL ARTICLES**

One-step and real-time detection of miRNA-21 in human samples for lung cancer biosensing diagnosis
O. Calvo-Lozano, P. García-Aparicio, L. Z. Raduly, M.C. Estévez, I. Berindan-Neagoe, M. Ferracin and L. M. Lechuga
2022 Analytical Chemistry (*submitted*)

Label-Free Plasmonic Biosensor for Rapid, Quantitative, and Highly Sensitive COVID-19 Serology: Implementation and Clinical Validation
O. Calvo-Lozano, M. Sierra, M. Soler, M. C. Estévez, L. Chiscano-Camón, A. Ruiz-Sanmartin, J. C. Ruiz-Rodriguez, R. Ferrer, J. J. González-López, J. Esperalba, C. Fernández-Naval, L. Bueno, R. López-Aladid, A. Torres, L. Fernández-Barat, S. Attoumani, R. Charrel, B. Coutard, and L. M. Lechuga
2021 Analytical chemistry, 94(2), 975-984

Fast and Accurate Pneumocystis Pneumonia Diagnosis in Human Samples Using a Label-Free Plasmonic Biosensor
O. Calvo-Lozano, A. Aviñó, V. Friaza, A. Medina-Escuela, C. S. Huertas, E. J. Calderón, R. Eritja and L. M. Lechuga
2020 Nanomaterials, 10 (6), 1246

Coating Bioactive Microcapsules with Tannic Acid Enhances the Phenotype of the Encapsulated Pluripotent Stem Cells
D. Choi, K. Gwon, H. J. Hong, H. Baskaran, O. Calvo-Lozano, A. M. Gonzalez-Suarez, K. Park, J. M. de Hoyos-Vega, L. M. Lechuga, J. Hong, G. Stybayeva and Alexander Revzin
2022 ACS Applied Materials & Interfaces, 14 (23), 27274–27286

Optical nanogap antennas as plasmonic biosensors for the detection of miRNA biomarkers
A. Portela, O. Calvo-Lozano, M. C. Estevez, A. M. Escuela and L. M. Lechuga
2020 Journal of Materials Chemistry B, 8 (19), 4310-4317

Early Sepsis Diagnosis via Protein and miRNA Biomarkers using a novel Point-of-Care Photonic Biosensor
N. Fabri-Faja, O. Calvo-Lozano, P. Dey, R. A. Terborg, M.-C. Estévez, A. Belushkin, F. Yesilköy, L. Duempelmann, H. Altug, V. Pruneri and L. M. Lechuga
2019 Analytica Chimica Acta, 1077, 232-242

Label-free Bacteria Quantification in Blood Plasma by a Bioprinted Microarray Based Interferometric Point-of-Care Device

P. Dey, N. Fabri-Faja, O. Calvo-Lozano, R. Terborg, A. Belushkin, F. Yesilkoy, A. Fàbrega, J.C. Ruiz-Rodriguez, R. Ferrer, J.J. González-López, M.C. Estévez, H. Altug, V. Pruneri and L.M. Lechuga

2019 ACS Sensors, 4 (1), 52-60

A CO2 optical sensor based on self-assembled metal–organic framework nanoparticles

B. Chocarro-Ruiz, J. Pérez-Carvajal, C. Avci, O. Calvo-Lozano, M. I. Alonso, D. Maspoch and L. M. Lechuga

2018 Journal of Materials Chemistry A, 6 (27), 13171-13177

- **JOURNAL REVIEW**

Advanced Evanescent-Wave Optical Biosensors for the Detection of Nucleic Acids: An Analytic Perspective

C. S. Huertas, O. Calvo-Lozano, A. Mitchell1 and L. M. Lechuga

2019 Frontiers in chemistry, 7, 724

- **BOOK CHAPTER**

Label-free Nanoplasmonic Biosensing of Cancer Biomarkers for Clinical Diagnosis

A. Portela, E. C. Peláez, O. Calvo-Lozano, M. C. Estévez and Laura M. Lechuga

2019 Biomimetic Sensing. Methods and Protocols in Molecular Biology. Editorial Humana Press, 2027 (10), 115-140

- **SCIENTIFIC DIVULGATION**

Nanophotonic biosensors: driving personalized medicine

M. Soler, O. Calvo-Lozano, M. C. Estevez and L. M. Lechuga

2020 Optics and Photonics News, 31(4), 24-31

- **PROCEEDINGS**

Lens-Free Interferometric Microscope for Point-of-Care Label-Free Detection of Sepsis Biomarkers

R. A. Terborg, L. Duempelmann, J. Pello, A. Noyan, F. Yesilkoy, A. A. Belushkin, Y. Jahani, N. Fabri-Faja, P. Dey, O. Calvo-Lozano, M.C. Estevez, A. Fàbrega, J. J. González-López, L. M. Lechuga, H. Altug and Valerio Pruneri

2019 Frontiers in Optics. Optical Society of America, FM3F-6

Label-free, scalable and point-of-care imaging platform for rapid analysis of biomarker

L. Duempelmann, R. A. Terborg, J. Pello, I. Mannelli, F. Yesilkoy, A. A. Belushkin, Y. Jahani, N. Fabri-Faja, P. Dey, O. Calvo-Lozano, M. C. Estevez, A. Fàbrega, J. J. González-López, L. M. Lechuga, H. Altug and V. Pruneri

2019 European Conference on Biomedical Optics. Optical Society of America, 11076_46

- **CONFERENCES**

Label-free plasmonic biosensor for covid-19 serology
O. Calvo-Lozano, M. Sierra, M. Soler, M.C. Estévez, L.Chiscano, A. Ruiz-Sanmartin, J. C. Ruiz-Rodriguez, R. Ferrer, J. J. González-López, J. Esperalba, C. Fernández-Naval, L. Bueno, R. López-Aladid, A. Torres, L. Fernández-Barat, S. Attoumani, R. Charrel, B. Coutard and L. M. Lechuga
XV Conference on Optical Chemical Sensors and Biosensors EUROPT(R)ODE, Warsaw (Poland) 28th November – 1st December 2021**Oral presentation**

Label-free detection of micro-RNA-21 in plasma human samples for lung cancer diagnosis using an advanced nanophotonic biosensor
O. Calvo-Lozano, P. García-Aparicio, L. Z. Raduly, I. Berindan Neagoe, M. Ferracin and L. M. Lechuga
IV Young Researchers Meeting CiberONC-CiberBBN, Barcelona (Spain) 13th – 14th December 2021 **Poster presentation**

Direct and sensitive COVID-19 serology based on a plasmonic biosensor
O. Calvo-Lozano, M. Sierra, M. Soler, M. C. Estévez and L. M. Lechuga
XIII National Meeting of Optics RNO2021, On-line 22nd -24th November 2021**Oral presentation**

Rapid detection of sepsis with a point-of care and label free microarray platform - Poster N. Fabri-Faja, O. Calvo-Lozano, M.C. Estévez, J. Pello, R. A. Terborg, A. Belushkin, F. Yesilköy, P. Soetaert, M. Rabaey, H. Altug, V. Pruneri and L.M. Lechuga
VIII International Congress on Analytical Nanoscience and Nanotechnology, Barcelona (Spain) 3th – 5th July 2017 **Poster presentation**

RAIS: Scalable, point-of-care and label free microarray platform for rapid detection of Sepsis - WP5: Laboratory Validation
N. Fabri-Faja, O. Calvo-Lozano, P. Dey, M.C. Estévez and L.M. Lechuga
RAIS open workshop H2020, Barcelona (Spain) 6th – 7th November 2017 **Poster presentation**

Use of a microarray reader for the fast, label-free and multiplexed measurement of biomarkers for Sepsis
N. Fabri-Faja, R.A. Terborg, F.Yesilköy, O. Calvo-Lozano, P. Dey, M.C. Estévez, J. Pello, A. Fàbrega, J.C. Ruiz-Rodriguez, A. Belushkin, J. Götzen, P. Soetaert, M. Rabaey, J.J. González-López, H. Altug, V. Pruneri and L.M. Lechuga
XIV Conference on Optical Chemical Sensors and Biosensors EUROPT(R)ODE, Naples (Italy) 25th – 28th March 2018 **Oral presentation**

Fast, multiplex and label-free quantification of sepsis biomarkers with an innovative optical point-of-care platform

N. Fabri-Faja, O. Calvo-Lozano, P. Dey, R. A. Terborg, M.C. Estévez, F. Yesilköy, J. Pello, A. Fàbrega, J. C. Ruiz-Rodriguez, A. Belushkin, J. González-López, H. Altug, V. Pruneri and L. M. Lechuga
XI Ibero-American Congress on Sensors IBERSENSORS, Barcelona (Spain) 17th – 20th September 2018 **Oral presentation**

Label-free, scalable and point-of-care imaging platform for rapid analysis of biomarker
L. Duempelmann, R.A Terborg, J. Pello, I. Mannelli, F. Yesilkoy, A.A. Belushkin, Y. Jahani, N. Fabri-Faja, P. Dey, O. Calvo-Lozano, M.-C. Estevez, L.M. Lechuga, H. Altug and V. Pruneri SPIE Photonics West, San Francisco (US) 2nd – 7th February 2019 **Poster presentation**

Label-free imaging platform for rapid analysis of biomarker
L. Duempelmann, R.A Terborg, J. Pello, I. Mannelli, F. Yesilkoy, A.A. Belushkin, Y. Jahani, N. Fabri-Faja, P. Dey, O. Calvo-Lozano, M.-C. Estevez, Anna Fàbrega, Juan J. González-López, L.M. Lechuga, H. Altug and V. Pruneri
45th International Conference on Micro & Nano Engineering, Rhodes (Greece) 23rd – 26th September 2019 **Poster presentation**

Lens-free Interferometric Microscope for Point-of-Care Label-free Detection of Sepsis Biomarkers
R.A. Terborg, L. Duempelmann, J. Pello, A. Noyan, F. Yesilkoy, A. Belushkin, Y. Jahani, N. Fabri-Faja, P. Dey, O. Calvo-Lozano , M.-C. Estevez, A. Fàbrega, J.J. González-López, L.M. Lechuga, H. Altug, V. Pruneri
Frontiers in Optics and Laser Science, Washington DC (US) 15th – 19th September 2019

Oral presentation

Abbreviations and acronyms

5hmC	5-hydroxymethylcytosine
5mC	5-methylcytosine
Ab	Antibody
AIDS	Acquired Immunodeficiency Syndrome
AIR	Arrayed Imaging Reflectometry
Anti-5mC	Antibody against 5-methylcytosine
Anti-5hmC	Antibody against 5-hydroxymethylcytosine
Anti-DNA/RNA	Antibody against DNA/RNA hybrid
Anti-CRP	Antibody against CRP protein
Anti-NSE	Antibody against NSE protein
ANX-A2	Annexin A2
APTES	3-Aminopropyltriethoxy silane
AUC	Area Under Curve
Au-NHA	Gold Nanoholes Array chips
BAL	Bronchoalveolar Lavage
BAU	Binding Antibody Unit
BiMW	Bimodal Waveguide
BSA	Bovine Serum Albumin
CA15.3	Cancer Antigen 15-3
CCD	Charge-Coupled Device
CEA	Carcino Embryonic Antigen
CH	Clinic Hospital
CHAPS	3-[3-Cholamidopropyldimethylammonio]-1-propane sulfonate
ChIP	Chromatin Immunoprecipitation
CLIA	Chemiluminescence Immunoassay
CMOS	Complementary Metal-Oxide Semiconductor
COI	Cut-off index
COPD	Chronic Obstructive Pulmonary Disease
COVID-19	Coronavirus Disease 2019
CT	Computed Tomography
CTES	Carboxyethylsilanetriol sodium salt

CV	Coefficient of Variation
CYFRA21-1	Cytokeratin 19 Fragment
DEPC	Diethylpyrocarbonate
DIPEA	N, N-diisopropylethylamine
DMF	Dimethylformamide Anhydrous
DNA	Deoxyribonucleic Acid
DNMTs	DNA Methyltransferases
DPN	Dip-pen Nanolithography
DS	Dextran Sulfate sodium salt
Ds-DNA	Double Strand DNA
E protein	Envelop protein of SARS-CoV-2 virus
EBL	Electron Beam Lithography
EDC	1-Ethyl-3-(3-dimethylaminopropyl)-carbodiimide
EDTA	Ethylenediaminetetraacetic Acid
ELISA	Enzyme-linked Immunosorbent Assay
EW	Evanescent Wave
FA	Formamide
Fab	Fragment antigen-binding
Fc	Fragment crystallisable
FIB	Focused Ion Beam
FISH	Fluorescence In Situ Hybridisation
FN	False Negative
FP	False Positive
FOV	Field-Of-View
GC	Guanine-Cytosine content
GOPTS	3- Glycidyloxypropyltrimethoxysilane
HCL	Hole-mask Colloidal Lithography
HEPES	4-(2-Hydroxyethyl)piperazine-1-ethanesulfonic acid
HIF-1	Hypoxia Inducible Factor-1
HIV	Human Immunodeficiency Virus
HPDP-biotin	N-[6-(Biotinamido)hexyl]-3′-(2′-pyridyldithio)propionamide
HR	Hoogsteen-Reverse bond
ICPTS	Isocyanatepropyltriethoxysilane

ICU	Intensive Care Unit
Ig	Immunoglobulin
IL-1b	Interleukin -1b
IL-6	Interleukin-6
IUPAC	International Union of Pure and Applied Chemistry
LC	Lung Cancer
LFA	Lateral Flow Assay
LIM	Lens-free Interferometric Microscopy
LNA	Locked- Nucleic Acids
LOD	Limit Of Detection
LSPR	Localised Surface Plasmon Resonance
M protein	Membrane protein of SARS-CoV-2 virus
mAb	Monoclonal antibody
MBD	Methyl-CpG-Binding Domain
MCH	6-mercapto-1-hexanol
MECP2	Methyl-CpG Binding Protein 2
MeOH	Methanol
MERS	Middle East Respiratory Syndrome
MES	2-(N-Morpholino)ethanesulfonic Acid
MHDA	16-Mercaptohexadecanoic Acid
MiRNA	MiRNA
MPTMS	3- Mercaptopropyltrimethoxysilane
MRI	Magnetic Resonance Imaging
mRNA	Messenger RNA
mtLSU rRNA	Mitochondrial Large Subunit Ribosomal RNA gene
MUOH	11-Mercapto-1-undecanol
MW	Molecular weight
N protein	Nucleocapsid protein of SARS-CoV-2 virus
NA	Neutravidin
NP	Nanoparticle
NPA	Nasopharyngeal Aspirates
NPV	Negative Predictive Value
NSCLC	Non-Small Cell Lung Cancer

NSE	Neuron Specific Enolase
NTA	Nitrilotriacetic Acid
OPD	Optical Path Difference
ORF	Open Reading Frame
pAb	Polyclonal Antibody
pAb-N	Polyclonal Antibody against N protein
pAb-RBD	Polyclonal Antibody against RBD domain
pAb-S1	Polyclonal Antibody against S1 subunit
PBS	Phosphate Buffered Saline
PCR	Polymerase Chain Reaction
PCT	Procalcitonin
PcP	Pneumocystis Pneumonia
PDDA	Poly(diallyldimethylammonium) chloride
PDITC	ρ-phenylene diisothiocyanate
PDMS	Polydimethylsiloxane
PEG	Polyethylene Glycol
PET	Positron Emission Tomography
PLL-g-PEG	Poly-L-lysine-graft-Polyethylene Glycol
PMMA	Polymethyl Methacrylate
PMO	Phosphorodiamidate Morpholino Oligos
PNAs	Peptide Nucleic Acids
POC	Point Of Care
PPRH	Polypurine Reverse-Hoogsteen hairpins
PPV	Positive Predictive Value
(q)RT-PCR	(quantitative) Reverse Transcription Polymerase Chain Reaction
RBD	Receptor Binding Domain
RI	Refractive Index
RIE	Reactive Ion Etcher
RIU	Refractive Index Unit
RNA	Ribonucleic Acid
S protein	Spike protein of SARS-CoV-2 virus
S1	Subunit 1of Spike protein
SAM	Self-Assembled Monolayer

SARS-CoV-2	Severe Acute Respiratory Syndrome Coronavirus 2
SCLC	Small Cell Lung Cancer
SD	Standard Deviation
SDS	Sodium Dodecyl Sulfate
SE	Diagnostic Sensitivity
SELEX	Systematic Evolution of Ligands by Exponential Enrichment
SEM	Scanning Electron Microscope
Silane-PEG-COOH	Triethoxysilane Polyethylene Glycol Carboxylic Acid
SIRS	Systemic Inflammatory Response
SP	Diagnostic Specificity
SPP	Surface Plasmon Polariton
SPR(i)	Surface Plasmon Resonance (imaging)
SSC	Saline-Sodium Citrate buffer
Ss-DNA	Single Strand DNA
Sulfo-NHS	N-hydroxysulfosuccinimide
TCEP	Tris(2-Carboxyethyl)phosphine hydrochloride solution
TE	Transverse-Electric
TIR	Total Internal Reflection
TM	Transverse-Magnetic
TN	True Negative
TNF	Tumor Necrosis Factor
TP	True Positive
TP53INP1	p53 Inducible Nuclear Protein 1
Tris-HCl	Tris(hydroxymethyl)aminomethane hydrochloride
UTR	Untranslated Region
VH	Vall D’Hebron Hospital
WC	Watson-Crick bond
WHO	World Health Organization

Bibliography

1. WHO Global Health Estimates. The top 10 causes of death. https://www.who.int/news-room/fact-sheets/detail/the-top-10-causes-of-death (2020) (Accessed 30/06/2022).
2. Levine, S. *et al*. Forum of International Respiratory Societies. The global impact of respiratory disease. *ERS* 3^{th} *ed.* (2021).
3. Soriano, J. B. *et al.* Prevalence and attributable health burden of chronic respiratory diseases, 1990–2017: a systematic analysis for the Global Burden of Disease Study 2017. *Lancet Respir. Med.* **8**, 585–596 (2020).
4. Csikesz, N. G. & Gartman, E. J. New developments in the assessment of COPD: early diagnosis is key. *Int. J. Chron. Obstruct. Pulmon. Dis.* **9**, 277 (2014).
5. Meghji, J. *et al.* Improving lung health in low-income and middle-income countries: from challenges to solutions. *Lancet* **397**, 928–940 (2021).
6. Hargreave, F. E. & Nair, P. The definition and diagnosis of Asthma. *Clin. Exp. Allergy* **39**, 1652–1658 (2009).
7. The Global Asthma Report 2018. *Global Asthma Network* http://globalasthmareport.org/ (2018).
8. What is Cancer? Cancer Basics. *American Cancer Society*. https://www.cancer.org/treatment/understanding-your-diagnosis/what-is-cancer.html (2022) (Accesed 30/06/2022).
9. Sung, H. *et al.* Global Cancer Statistics 2020: GLOBOCAN Estimates of Incidence and Mortality Worldwide for 36 Cancers in 185 Countries. *CA. Cancer J. Clin.* **71**, 209–249 (2021).
10. Latimer, K. M. & Mott, T. F. Lung Cancer: Diagnosis, Treatment Principles, and Screening. *Am. Fam. Physician* **91**, 250–256 (2015).
11. Global tuberculosis report 2020. *World Health Organization* https://www.who.int/publications/i/item/9789240013131 (2020) (Accesed 30/06/2022)
12. Campbell, I. A. & Bah-Sow, O. Pulmonary tuberculosis: diagnosis and treatment. *BMJ* **332**, 1194–1197 (2006).
13. Hoare, Z. & Lim, W. S. Pneumonia: update on diagnosis and management. *BMJ* **332**, 1077–1079 (2006).
14. Ottosen, J. & Evans, H. Pneumonia: Challenges in the Definition, Diagnosis, and Management of Disease. *Surg. Clin. North Am.* **94**, 1305–1317 (2014).
15. WHO Influenza (seasonal). *World Health Organization* https://www.who.int/news-room/fact-sheets/detail/influenza-(seasonal) (2018) (Accessed 30/06/2022).
16. COVID-19 Map - Johns Hopkins Coronavirus Resource Center. https://coronavirus.jhu.edu/ (2022) (Accessed 05/09/2022).
17. WHO Coronavirus (COVID-19) Dashboard. *WHO Coronavirus* https://covid19.who.int/ (2022) (Accessed 05/09/2022)
18. Kung, S. *et al.* Underestimation of COVID-19 mortality during the pandemic. *ERJ Open Res.* **7**, 00766–02020 (2021).
19. Shrestha, J. *et al.* Lung-on-a-chip: the future of respiratory disease models and pharmacological studies. *Crit. Rev. Biotechnol.* **40**, 213–230 (2020).

20. Gibson, G. J., *et al*. The economic burden of lung disease in *European Lung White Book. ERS;2018* https://www.erswhitebook.org/chapters/the-economic-burden-of-lung-disease/ (2019) (Accessed 05/09/2022).
21. Zarei, M. Infectious pathogens meet point-of-care diagnostics. *Biosens. Bioelectron.* **106**, 193–203 (2018).
22. Chin, C. D., Linder, V. & Sia, S. K. Commercialization of microfluidic point-of-care diagnostic devices. *Lab Chip* **12**, 2118–2134 (2012).
23. Aryasomayajula, A., Bayat, P., Rezai, P. & Selvaganapathy, P. R. Microfluidic devices and their applications in *Springer handbook of nanotechnology* 487–536 (Springer Berlin, 2017).
24. Monošík, R. & Lúcio A. Utilisation of micro-and nanoscaled materials in microfluidic analytical devices. *Microchem. J.* **119**, 159-168 (2015).
25. Drain, P. K. *et al.* Diagnostic point-of-care tests in resource-limited settings. *Lancet Infect. Dis.* **14**, 239–249 (2014).
26. Sia, S. K. & Whitesides, G. M. Microfluidic devices fabricated in poly(dimethylsiloxane) for biological studies. *Electrophoresis* **24**, 3563–3576 (2003).
27. Whitesides, G. M. The origins and the future of microfluidics. *Nature* **442**, 368–373 (2006).
28. Becker, H. & Gärtner, C. Polymeric Microfluidic Devices for High Performance Optical Imaging and Detection Methods in Bioanalytics. *Optical Nano-and Microsystems for Bioanalytics* 271–288 (2012).
29. Land, K. J., Boeras, D. I., Chen, X. S., Ramsay, A. R. & Peeling, R. W. REASSURED diagnostics to inform disease control strategies, strengthen health systems and improve patient outcomes. *Nat. Microbiol.* **4**, 46–54 (2018).
30. Nagel, B., Dellweg, H. & Gierasch, L. M. Glossary for chemists of terms used in biotechnology. *Pure Appl. Chem.* **64**, 143–168 (1992).
31. Bhalla, N., Jolly, P., Formisano, N. & Estrela, P. Introduction to biosensors. *Essays Biochem.* **60**, 1–8 (2016).
32. Heidt, B. *et al.* Point of Care Diagnostics in Resource-Limited Settings: A Review of the Present and Future of PoC in Its Most Needed Environment. *Biosens.* **10**, 133 (2020).
33. Romeo, A., Leung, T. S. & Sánchez, S. Smart biosensors for multiplexed and fully integrated point-of-care diagnostics. *Lab Chip* **16**, 1957–1961 (2016).
34. Kalyani, N., Goel, S. & Jaiswal, S. On‑site sensing of pesticides using point‑of‑care biosensors: a review. *Environ. Chem. Lett.* **19**, 345–354 (2020).
35. Wang, J. Electrochemical glucose biosensors. *Chem. Rev.* **108**, 814–825 (2008).
36. Ehrenkranz, J. R. L. Home and point-of-care pregnancy tests: a review of the technology. *Epidemiology* S15-S18 (2002).
37. Narayanaswamy, R. & Wolfbeis, O. S. Optical sensors: industrial, environmental and diagnostic applications **1** (Springer Berlin, 2004).
38. González-Guerrero, A. B., Maldonado, J., Herranz, S. & Lechuga, L. M. Trends in photonic lab-on-chip interferometric biosensors for point-of-care diagnostics. *Anal. Methods* **8**, 8380–8394 (2016).
39. Estevez, M. C., Alvarez, M. & Lechuga, L. M. Integrated optical devices for lab-on-a-chip biosensing applications. *Laser Photon. Rev.* **6**, 463–487 (2012).

40. Kozma, P., Kehl, F., Ehrentreich-Förster, E., Stamm, C. & Bier, F. F. Integrated planar optical waveguide interferometer biosensors: A comparative review. *Biosens. Bioelectron.* **58**, 287–307 (2014).
41. Passaro, V. M. N., Dell'Olio, F., Casamassima, B. & De Leonardis, F. Guided-Wave Optical Biosensors. *Sensors* **7**, 508–536 (2007).
42. Puiu, M. & Bala, C. SPR and SPR Imaging: Recent Trends in Developing Nanodevices for Detection and Real-Time Monitoring of Biomolecular Events. *Sensors* **16**, 870 (2016).
43. Cottier, K., Wiki, M., Voirin, G., Gao, H. & Kunz, R. E. Label-free highly sensitive detection of (small) molecules by wavelength interrogation of integrated optical chips. *Sens. Actuators B Chem.* **91**, 241–251 (2003).
44. Luchansky, M. S. *et al.* Characterization of the evanescent field profile and bound mass sensitivity of a label-free silicon photonic microring resonator biosensing platform. *Biosens. Bioelectron.* **26**, 1283–1291 (2010).
45. Gavela, A. F., García, D. G., Ramirez, J. C. & Lechuga, L. M. Last Advances in Silicon-Based Optical Biosensors. *Sensors* **16**, 285 (2016).
46. Soler, M. & Lechuga, L. M. Principles, technologies, and applications of plasmonic biosensors. *J. Appl. Phys.* **129**, 111102 (2021).
47. Masson, J. F. Surface Plasmon Resonance Clinical Biosensors for Medical Diagnostics. *ACS Sensors* **2**, 16–30 (2017).
48. Homola, J. Surface plasmon resonance sensors for detection of chemical and biological species. *Chem. Rev.* **108**, 462–493 (2008).
49. Nguyen, H. H., Park, J., Kang, S. & Kim, M. Surface Plasmon Resonance: A Versatile Technique for Biosensor Applications. *Sensors* **15**, 10481–10510 (2015).
50. Hill, R. T. Plasmonic biosensors. *Wiley Interdiscip. Rev. Nanomed. Nanobiotechnology* **7**, 152–168 (2015).
51. Homola, J. & Piliarik, M. Surface Plasmon Resonance (SPR) Sensors in *Surface plasmon resonance based sensors* 45–67 (Springer Berlin, 2006).
52. Lopez, G. A., Estevez, M. C., Soler, M. & Lechuga, L. M. Recent advances in nanoplasmonic biosensors: Applications and lab-on-a-chip integration. *Nanophotonics* **6**, 123–136 (2017).
53. Prabowo, B. A., Purwidyantri, A. & Liu, K. C. Surface Plasmon Resonance Optical Sensor: A Review on Light Source Technology. *Biosens.* **8**, 80 (2018).
54. Cytiva. https://www.cytivalifesciences.com/en/us.
55. Biosensing Instrument - Biosensing Instrument. https://biosensingusa.com/.
56. XanTec bioanalytics GmbH | Sensors and surfaces. https://www.xantec.com/.
57. BioNavis | Manufacturer of MP-SPR instruments. https://www.bionavis.com/en/.
58. Gao, Y., Gan, Q. & Bartoli, F. J. Breakthroughs in Photonics 2013: Research Highlights on Biosensors Based on Plasmonic Nanostructures. *IEEE Photonics J.* **6**, 1-5 (2014).
59. Wang, J. *et al.* Silicon-based integrated label-free optofluidic biosensors: latest advances and roadmap. *Adv. Mater. Technol.* **5**, 1901138 (2020).
60. Xu, Y. *et al.* Silicon-based sensors for biomedical applications: a review. *Sensors* **19**, 2908 (2019).
61. Chocarro-Ruiz, B., *et al.* Nanophotonic label-free biosensors for environmental monitoring. *Curr. Opin. Biotechnol.* **45**, 175-183 (2017).

62. Luan, E., Shoman, H., Ratner, D. M., Cheung, K. C. & Chrostowski, L. Silicon photonic biosensors using label-free detection. *Sensors* **18**, 3519 (2018).
63. Zinoviev, K. E., *et al*. Integrated bimodal waveguide interferometric biosensor for label-free analysis. *J. Light. Technol.* **29**, 1926-1930 (2011).
64. Bassols-Cornudella, B. *et al.* Novel Sensing Algorithm for Linear Read-Out of Bimodal Waveguide Interferometric Biosensors. *J. Light. Technol.* **40**, 237–244 (2022).
65. Chocarro-Ruiz, B. *et al.* Interferometric nanoimmunosensor for label-free and real-time monitoring of Irgarol 1051 in seawater. *Biosens. Bioelectron.* **117**, 47–52 (2018).
66. Ramirez-Priego, P. *et al.* Real-time monitoring of fenitrothion in water samples using a silicon nanophotonic biosensor. *Anal. Chim. Acta* **1152**, 338276 (2021).
67. Maldonado, J. *et al.* Label-free detection of nosocomial bacteria using a nanophotonic interferometric biosensor. *Analyst* **145**, 497–506 (2020).
68. Huertas, C. S., Fariña, D. & Lechuga, L. M. Direct and Label-Free Quantification of Micro-RNA-181a at Attomolar Level in Complex Media Using a Nanophotonic Biosensor. *ACS Sensors* **1**, 748–756 (2016).
69. González-Guerrero, A. B., Maldonado, J., Dante, S., Grajales, D. & Lechuga, L. M. Direct and label-free detection of the human growth hormone in urine by an ultrasensitive bimodal waveguide biosensor. *J. Biophotonics* **10**, 61–67 (2017).
70. Bañuls, M. J., Puchades, R. & Maquieira, Á. Chemical surface modifications for the development of silicon-based label-free integrated optical (IO) biosensors: A review. *Anal. Chim. Acta* **777**, 1-16 (2013).
71. Choi, M. M. F. Progress in Enzyme-Based Biosensors Using Optical Transducers. *Microchim. Acta* **148**, 107–132 (2004).
72. Conroy, P. J., Hearty, S., Leonard, P. & O’Kennedy, R. J. Antibody production, design and use for biosensor-based applications. *Semin. Cell Dev. Biol.* **20**, 10–26 (2009).
73. Bora, U., Arghya S., & Deepika S. Nucleic acid based biosensors for clinical applications. *Biosens. J* **2**, 1-8 (2013).
74. Song, S., Wang, L., Li, J., Fan, C. & Zhao, J. Aptamer-based biosensors. *TrAC Trends Anal. Chem.* **27**, 108–117 (2008).
75. Chiu, M. L., Goulet, D. R., Teplyakov, A. & Gilliland, G. L. Antibody Structure and Function: The Basis for Engineering Therapeutics. *Antibodies* **8**, 55 (2019).
76. Padoa, C. J., & Nigel J. C. Engineered antibodies: A new tool for use in diabetes research. *Diabetes Res. Clin. Pract.* **74**, S51-S62 (2006).
77. Lipman, N. S., Jackson, L. R., Trudel, L. J. & Weis-Garcia, F. Monoclonal Versus Polyclonal Antibodies: Distinguishing Characteristics, Applications, and Information Resources. *ILAR J.* **46**, 258–268 (2005).
78. Hughes, R. A., & Ellington A. D. Synthetic DNA synthesis and assembly: putting the synthetic in synthetic biology. *Cold Spring Harb. Perspect. Biol.* **9**, a023812 (2017).
79. Ermini, M. L., *et al*. A rational approach in probe design for nucleic acid-based biosensing. *Biosens. Bioelectron* **26**, 4785-4790 (2011).
80. Hormeno, S., *et al*. Mechanical Properties of High-G· C Content DNA with A-Type Base-Stacking. *Biophys. J.* **100**, 1996-2005 (2011).

81. Fontenete, S. *et al.* Application of locked nucleic acid-based probes in fluorescence in situ hybridization. *Appl. Microbiol. Biotechnol.* **100**, 5897–5906 (2016).
82. Bakthavathsalam, P., *et al*. Locked nucleic acid molecular beacon for multiplex detection of loop mediated isothermal amplification. *Sens. Actuators B Chem*. **268**, 255-263 (2018).
83. Annoni, C., *et al*. Triplex-forming peptide nucleic acid modified with 2-aminopyridine as a new tool for detection of A-to-I editing. *Chem. Comm.* **52**, 7935-7938 (2016).
84. Sahu, B. *et al.* Synthesis and characterization of conformationally preorganized, (R)-diethylene glycol-containing γ-peptide nucleic acids with superior hybridization properties and water solubility. *J. Org. Chem.* **76**, 5614–5627 (2011).
85. Liao, T. *et al.* Ultrasensitive Detection of MicroRNAs with Morpholino-Functionalised Nanochannel Biosensor. *Anal. Chem.* **89**, 5511–5518 (2017).
86. Aviñó, A., Eritja, R., Ciudad, C. J. & Noé, V. Parallel Clamps and Polypurine Hairpins (PPRH) for Gene Silencing and Triplex-Affinity Capture: Design, Synthesis, and Use. *Curr. Protoc. Nucleic Acid Chem.* **77**, e78 (2019).
87. Huertas, C. S., Calvo-Lozano, O., Mitchell, A. & Lechuga, L. M. Advanced Evanescent-Wave Optical Biosensors for the Detection of Nucleic Acids: An Analytic Perspective. *Front. Chem.* **7**, 724 (2019).
88. Welch, N. G., Scoble, J. A., Muir, B. W. & Pigram, P. J. Orientation and characterization of immobilised antibodies for improved immunoassays. *Biointerphases* **12**, 02D301 (2017).
89. Rabe, M., Verdes, D. & Seeger, S. Understanding protein adsorption phenomena at solid surfaces. *Adv. Colloid Interface Sci.* **162**, 87–106 (2011).
90. Cosnier, S. & Holzinger, M. Electrosynthesized polymers for biosensing. *Chem. Soc. Rev.* **40**, 2146–2156 (2011).
91. Trilling, A. K., Beekwilder, J. & Zuilhof, H. Antibody orientation on biosensor surfaces: a minireview. *Analyst* **138**, 1619–1627 (2013).
92. Jung, Y., Jeong, J. Y. & Chung, B. H. Recent advances in immobilisation methods of antibodies on solid supports. *Analyst* **133**, 697–701 (2008).
93. Samanta, D. & Sarkar, A. Immobilisation of bio-macromolecules on self-assembled monolayers: methods and sensor applications. *Chem. Soc. Rev.* **40**, 2567–2592 (2011).
94. Strong, L. & Whitesides, G. M. Structures of Self-Assembled Monolayer Films of Organosulfur Compounds Adsorbed on Gold Single Crystals: Electron Diffraction Studies. *Langmuir* **4**, 546–558 (1988).
95. Ulman, A. Formation and structure of self-assembled monolayers. *Chem. Rev.* **96**, 1533–1554 (1996).
96. Soler, M. & Lechuga, L. M. Biochemistry strategies for label-free optical sensor biofunctionalisation: advances towards real applicability. *Anal. Bioanal. Chem.* **414**, 5071–5085 (2021).
97. Vericat, C., Vela, M. E., Benitez, G., Carro, P. & Salvarezza, R. C. Self-assembled monolayers of thiols and dithiols on gold: new challenges for a well-known system. *Chem. Soc. Rev.* **39**, 1805–1834 (2010).
98. Sassolas, A., Blum, L. J. & Leca-Bouvier, B. D. Immobilisation strategies to develop enzymatic biosensors. *Biotechnol. Adv.* **30**, 489–511 (2012).

99. Satjapipat, M., Sanedrin, R. & Zhou, F. Selective desorption of alkanethiols in mixed self-assembled monolayers for subsequent oligonucleotide attachment and DNA hybridization. *Langmuir* **17**, 7637–7644 (2001).
100. Peláez, E. C. *et al.* Nanoplasmonic biosensor device for the monitoring of acenocoumarol therapeutic drug in plasma. *Biosens. Bioelectron.* **119**, 149–155 (2018).
101. Fischer, M. J. E. Amine coupling through EDC/NHS: a practical approach in *Surface plasmon resonance* **627**, 55–73 (Humana Press, 2010).
102. Vashist, S. K., Lam, E., Hrapovic, S., Male, K. B. & Luong, J. H. T. Immobilisation of antibodies and enzymes on 3-aminopropyltriethoxysilane-functionalised bioanalytical platforms for biosensors and diagnostics. *Chem. Rev.* **114**, 11083–11130 (2014).
103. Vaisocherová, H., Brynda, E. & Homola, J. Functionalizable low-fouling coatings for label-free biosensing in complex biological media: advances and applications. *Anal. Bioanal. Chem.* **407**, 3927–3953 (2015).
104. D'Agata, R., Bellassai, N., Jungbluth, V. & Spoto, G. Recent Advances in Antifouling Materials for Surface Plasmon Resonance Biosensing in Clinical Diagnostics and Food Safety. *Polym.* **13**, 1929 (2021).
105. Brogan, K. L., Shin, J. H. & Schoenfisch, M. H. Influence of surfactants and antibody immobilisation strategy on reducing nonspecific protein interactions for molecular recognition force microscopy. *Langmuir* **20**, 9729–9735 (2004).
106. Krishnan, S., Weinman, C. J. & Ober, C. K. Advances in polymers for anti-biofouling surfaces. *J. Mater. Chem.* **18**, 3405–3413 (2008).
107. Bergstrand, A., Rahmani-Monfared, G., Östlund, Å., Nydén, M. & Holmberg, K. Comparison of PEI-PEG and PLL-PEG copolymer coatings on the prevention of protein fouling. *J. Biomed. Mater. Res. Part A* **88A**, 608–615 (2009).
108. Al-Ani, A. *et al.* The influence of PEG-thiol derivatives on controlling cellular and bacterial interactions with gold surfaces. *Appl. Surf. Sci.* **462**, 980–990 (2018).
109. Vogt, M. B. A. T. U. D., & Hauptmann, R. B. A. T. U. D. Plasma-deposited passivation layers for moisture and water protection. *Surf. Coat. Technol.* **74**, 676-681(1995).
110. Wang, M. Y. *et al.* SARS-CoV-2: Structure, Biology, and Structure-Based Therapeutics Development. *Front. Cell. Infect. Microbiol.* **10**, 724 (2020).
111. Hu, B., Guo, H., Zhou, P. & Shi, Z. L. Characteristics of SARS-CoV-2 and COVID-19. *Nat. Rev. Microbiol.* **19**, 141-154 (2020).
112. Wu, D., Wu, T., Liu, Q. & Yang, Z. The SARS-CoV-2 outbreak: What we know. *Int. J. Infect. Dis.* **94**, 44–48 (2020).
113. Wiersinga, W. J., Rhodes, A., Cheng, A. C., Peacock, S. J. & Prescott, H. C. Pathophysiology, Transmission, Diagnosis, and Treatment of Coronavirus Disease 2019 (COVID-19): A Review. *JAMA* **324**, 782–793 (2020).
114. Hasell, J. *et al.* A cross-country database of COVID-19 testing. *Sci. Data* **7**, 1–7 (2020).
115. Zhang, N. *et al.* Recent advances in the detection of respiratory virus infection in humans. *J. Med. Virol.* **92**, 408–417 (2020).
116. Hirotsu, Y. *et al.* Comparison of automated SARS-CoV-2 antigen test for COVID-19 infection with quantitative RT-PCR using 313 nasopharyngeal swabs, including from

seven serially followed patients. *Int. J. Infect. Dis.* **99**, 397–402 (2020).

117. Nagura-Ikeda, M. *et al.* Clinical evaluation of self-collected saliva by quantitative reverse transcription-PCR (RT-qPCR), Direct RT-qPCR, reverse transcription-loop-mediated isothermal amplification, and a rapid antigen test to diagnose COVID-19. *J. Clin. Microbiol.* **58**, e01438-20 (2020).
118. Qu, J. *et al.* Profile of Immunoglobulin G and IgM Antibodies Against Severe Acute Respiratory Syndrome Coronavirus 2 (SARS-CoV-2). *Clin. Infect. Dis.* **71**, 2255–2258 (2020).
119. Long, Q. X. *et al.* Antibody responses to SARS-CoV-2 in patients with COVID-19. *Nat. Med.* **26**, 845–848 (2020).
120. Post, N. *et al.* Antibody response to SARS-CoV-2 infection in humans: A systematic review. *PLoS One* **15**, e0244126 (2020).
121. Leung, G. M. *et al.* Seroprevalence of IgG antibodies to SARS-coronavirus in asymptomatic or subclinical population groups. *Epidemiol. Infect.* **134**, 211–221 (2006).
122. Krammer, F. & Simon, V. Serology assays to manage COVID-19. *Science* **368**, 1060–1061 (2020).
123. Carter, L. J. *et al.* Assay Techniques and Test Development for COVID-19 Diagnosis. *ACS Cent. Sci.* **6**, 591–605 (2020).
124. Mekonnen, D. *et al.* Diagnostic accuracy of serological tests and kinetics of severe acute respiratory syndrome coronavirus 2 antibody: A systematic review and meta-analysis. *Rev. Med. Virol.* **31**, e2181 (2020).
125. Rashid, Z. Z., *et al*. Diagnostic performance of COVID-19 serology assays. *Malays. J. Pathol.* **42**, 13-21 (2020).
126. Whitman, J. D. *et al.* Evaluation of SARS-CoV-2 serology assays reveals a range of test performance. *Nat. Biotechnol.* **38**, 1174–1183 (2020).
127. Zhang, X. *et al.* Viral and host factors related to the clinical outcome of COVID-19. *Nature* **583**, 437–440 (2020).
128. Grifoni, A. *et al.* Targets of T Cell Responses to SARS-CoV-2 Coronavirus in Humans with COVID-19 Disease and Unexposed Individuals. *Cell* **181**, 1489-1501 (2020).
129. Lisboa Bastos, M. *et al.* Diagnostic accuracy of serological tests for covid-19: Systematic review and meta-analysis. *BMJ* **370**, 2516 (2020).
130. Jahanshahi, P., Zalnezhad, E., Sekaran, S. D. & Adikan, F. R. M. Rapid immunoglobulin M-based dengue diagnostic test using surface plasmon resonance biosensor. *Sci. Rep.* **4**, 1–7 (2014).
131. Kumbhat, S., Sharma, K., Gehlot, R., Solanki, A. & Joshi, V. Surface plasmon resonance based immunosensor for serological diagnosis of dengue virus infection. *J. Pharm. Biomed. Anal.* **52**, 255–259 (2010).
132. Chung, J. W., Kim, S. D., Bernhardt, R. & Pyun, J. C. Application of SPR biosensor for medical diagnostics of human hepatitis B virus (hHBV). *Sens. Actuators B Chem.* **111**, 416–422 (2005).
133. Riedel, T. *et al.* Diagnosis of Epstein-Barr virus infection in clinical serum samples by an SPR biosensor assay. *Biosens. Bioelectron.* **55**, 278–284 (2014).
134. Park, T. J., Hyun, M. S., Lee, H. J., Lee, S. Y. & Ko, S. A self-assembled fusion protein-based surface plasmon resonance biosensor for rapid diagnosis of severe

acute respiratory syndrome. *Talanta* **79**, 295–301 (2009).

135. Djaileb, A. *et al.* A rapid and quantitative serum test for SARS-CoV-2 antibodies with portable surface plasmon resonance sensing. *ChemRxiv* (2020) doi:10.26434/chemrxiv.12118914.v1.
136. Basso, C. R. *et al.* Fast and reliable detection of SARS-CoV-2 antibodies based on surface plasmon resonance. *Anal. Methods* **13**, 3297–3306 (2021).
137. Schasfoort, R. B. M. *et al.* Presence and strength of binding of IgM, IgG and IgA antibodies against SARS-CoV-2 during CoViD-19 infection. *Biosens. Bioelectron.* **183**, 113165 (2021).
138. Knecht, S., Ricklin, D., Eberle, A. N. & Ernst, B. Oligohis-tags: Mechanisms of binding to Ni2+-NTA surfaces. *J. Mol. Recognit.* **22**, 270–279 (2009).
139. Burbelo, P. D. *et al.* Sensitivity in Detection of Antibodies to Nucleocapsid and Spike Proteins of Severe Acute Respiratory Syndrome Coronavirus 2 in Patients With Coronavirus Disease 2019. *J. Infect. Dis.* **222**, 206–213 (2020).
140. Premkumar, L. *et al.* The receptor-binding domain of the viral spike protein is an immunodominant and highly specific target of antibodies in SARS-CoV-2 patients. *Sci. Immunol.* **5**, eabc8413 (2020).
141. Ma, H. *et al.* COVID-19 diagnosis and study of serum SARS-CoV-2 specific IgA, IgM and IgG by chemiluminescence immunoanalysis. *medRxiv* (2020) doi:10.1101/2020.04.17.20064907.
142. Food and Drug Administration. *Bioanalytical Method Validation - Guidance for Industry* (2018).
143. GeurtsvanKessel, C. H. *et al.* An evaluation of COVID-19 serological assays informs future diagnostics and exposure assessment. *Nat. Commun.* **11**, 1–5 (2020).
144. Phipps, W. S. *et al.* SARS-CoV-2 Antibody Responses Do Not Predict COVID-19 Disease Severity. *Am. J. Clin. Pathol.* **154**, 459–465 (2020).
145. Yongchen, Z. *et al.* Different longitudinal patterns of nucleic acid and serology testing results based on disease severity of COVID-19 patients. *Emerg. Microbes Infect.* **9**, 833–836 (2020).
146. Edouard, S. *et al.* Evaluating the serological status of COVID-19 patients using an indirect immunofluorescent assay, France. *Eur. J. Clin. Microbiol. Infect. Dis.* **40**, 361–371 (2021).
147. Garcia-Beltran, W. F. *et al.* COVID-19-neutralizing antibodies predict disease severity and survival. *Cell* **184**, 476-488 (2021).
148. Okba, N. M. A. *et al.* Severe Acute Respiratory Syndrome Coronavirus 2-Specific Antibody Responses in Coronavirus Disease Patients. *Emerg. Infect. Dis.* **26**, 1478–1488 (2020).
149. Zhao, J. *et al.* Antibody Responses to SARS-CoV-2 in Patients With Novel Coronavirus Disease 2019. *Clin. Infect. Dis.* **71**, 2027–2034 (2020).
150. Pereira-Díaz, E. *et al.* Changing Trends in the Epidemiology and Risk Factors of Pneumocystis Pneumonia in Spain. *Front. Public Heal.* **7**, 275 (2019).
151. Morris, A. & Norris, K. A. Colonization by pneumocystis jirovecii and its role in disease. *Clin. Microbiol. Rev.* **25**, 297–317 (2012).
152. Wang, H. W., Lin, C. C., Kuo, C. F., Liu, C. P. & Lee, C. M. Mortality predictors of Pneumocystis jirovecii pneumonia in human immunodeficiency virus-infected patients at presentation: Experience in a tertiary care hospital of northern Taiwan. *J.*

Microbiol. Immunol. Infect. **44**, 274–281 (2011).

153. Calderón, E. J. Pneumocystis Infection: Seeing beyond the Tip of the Iceberg. *Clin. Infect. Dis.* **50**, 354–356 (2010).
154. Tasaka, S. & Tokuda, H. Pneumocystis jirovecii pneumonia in non-HIV-infected patients in the era of novel immunosuppressive therapies. *J. Infect. Chemother.* **18**, 793–806 (2012).
155. Tasaka, S. Recent advances in the diagnosis and management of Pneumocystis pneumonia. *Tuberc. Respir. Dis.* **83**, 132 (2020).
156. Procop, G. W. *et al.* Detection of Pneumocystis jiroveci in Respiratory Specimens by Four Staining Methods. *J. Clin. Microbiol.* **42**, 3333–3335 (2004).
157. Durand-Joly, I. *et al.* Molecular diagnosis of Pneumocystis pneumonia. *FEMS Immunol. Med. Microbiol.* **45**, 405–410 (2005).
158. Karageorgopoulos, D. E. *et al.* Accuracy of β-D-glucan for the diagnosis of Pneumocystis jirovecii pneumonia: a meta-analysis. *Clin. Microbiol. Infect.* **19**, 39–49 (2013).
159. Respaldiza, N. *et al.* Usefulness of oropharyngeal washings for identifying Pneumocystis jirovecii carriers. *J. Eukaryot. Microbiol.* **53**, (2006).
160. Robberts, F. J. L., Liebowitz, L. D. & Chalkley, L. J. Polymerase chain reaction detection of Pneumocystis jiroveci: evaluation of 9 assays. *Diagn. Microbiol. Infect. Dis.* **58**, 385–392 (2007).
161. Wakefield, A. E. *et al.* Amplification of mitochondrial ribosomal RNA sequences from Pneumocystis carinii DNA of rat and human origin. *Mol. Biochem. Parasitol.* **43**, 69–76 (1990).
162. Brancart, F., Rodriguez-Villalobos, H., Fonteyne, P. A., Peres-Bota, D. & Liesnard, C. Quantitative TaqMan PCR for detection of Pneumocystis jiroveci. *J. Microbiol. Methods* **61**, 381–387 (2005).
163. White, P. L., Backx, M. & Barnes, R. A. Diagnosis and management of Pneumocystis jirovecii infection. **15**, 435–447 (2017).
164. Barbosa, J., Costa-De-Oliveira, S., Silva, A. T., Rodrigues, A. G. & Pina-Vaz, C. Specific detection of Pneumocystis jirovecii in clinical samples by flow cytometry. *Methods Mol. Biol.* **968**, 203–211 (2013).
165. Tomás, A. L. *et al.* Development of a Gold Nanoparticle-Based Lateral-Flow Immunoassay for Pneumocystis Pneumonia Serological Diagnosis at Point-of-Care. *Front. Microbiol.* **10**, 2917 (2019).
166. Pla, L. *et al.* Triplex Hybridization-Based Nanosystem for the Rapid Screening of Pneumocystis Pneumonia in Clinical Samples. *J. Fungi* **6**, 292 (2020).
167. Hu, Y., Cecconello, A., Idili, A., Ricci, F. & Willner, I. Triplex DNA Nanostructures: From Basic Properties to Applications. *Angew. Chemie - Int. Ed.* **56**, 15210–15233 (2017).
168. Rodríguez, L. *et al.* Improved design of PPRHs for gene silencing. *Mol. Pharm.* **12**, 867–877 (2015).
169. Aviñó, A., Huertas, C. S., Lechuga, L. M. & Eritja, R. Sensitive and label-free detection of miRNA-145 by triplex formation. *Anal. Bioanal. Chem.* **408**, 885–893 (2016).
170. Carrascosa, L. G. *et al.* Sensitive and label-free biosensing of RNA with predicted secondary structures by a triplex affinity capture method. *Nucleic Acids Res.* **40**, e56-

e56 (2012)

171. Nadal, A. *et al.* Efficient Sequence-Specific Purification of Listeria innocua mRNA Species by Triplex Affinity Capture with Parallel Tail-Clamps. *ChemBioChem* **7**, 1039–1047 (2006).

172. Huertas, C. S. *et al.* Label-free DNA-methylation detection by direct ds-DNA fragment screening using poly-purine hairpins. *Biosens. Bioelectron.* **120**, 47–54 (2018).

173. Cancer Today. https://gco.iarc.fr/today/home.(Accesed 30/06/2022)

174. Cryer, A. M. & Thorley, A. J. Nanotechnology in the diagnosis and treatment of lung cancer. *Pharmacol. Ther.* **198**, 189–205 (2019).

175. Siegel, R. L., Miller, K. D. & Jemal, A. Cancer statistics, 2020. *CA. Cancer J. Clin.* **70**, 7–30 (2020).

176. Rodriguez-Canales, J., Parra-Cuentas, E. & Wistuba, I. I. Diagnosis and molecular classification of lung cancer. *Cancer Treat. Res.* **170**, 25–46 (2016).

177. Wang, L. Screening and Biosensor-Based Approaches for Lung Cancer Detection. *Sensors* **17**, 2420 (2017).

178. Usman, F. *et al.* Plasmonic Biosensors for the Detection of Lung Cancer Biomarkers: A Review. *Chemosens.* **9**, 326 (2021).

179. Da Cunha Santos, G., Shepherd, F. A. & Tsao, M. S. EGFR Mutations and Lung Cancer. *Annu. Rev. Pathol.* **6**, 49–69 (2011).

180. Korpanty, G. J., Graham, D. M., Vincent, M. D. & Leighl, N. B. Biomarkers that currently effect clinical practice in lung cancer: EGFR, ALK, MET, ROS-1 and KRAS. *Front. Oncol.* **4**, 204 (2014).

181. Pisapia, P. *et al.* ALK and ROS1 testing on lung cancer cytologic samples: Perspectives. *Cancer Cytopathol.* **125**, 817–830 (2017).

182. Roointan, A. *et al.* Early detection of lung cancer biomarkers through biosensor technology: A review. *J. Pharm. Biomed. Anal.* **164**, 93–103 (2019).

183. Grunnet, M. & J. B. Sorensen. Carcinoembryonic antigen (CEA) as tumor marker in lung cancer. *Lung cancer* **76**, 138-143 (2012).

184. Ferrigno, D., Gianfranco B. & Cristina G. Neuron-specific enolase is an effective tumour marker in non-small cell lung cancer (NSCLC). *Lung Cancer* **41**, 311-320 (2003).

185. Altintas, Z. & Tothill, I. Biomarkers and biosensors for the early diagnosis of lung cancer. *Sens. Actuators B Chem.* **188**, 988–998 (2013).

186. Molina, R. *et al.* Assessment of a combined panel of six serum tumor markers for lung cancer. *Am. J. Respir. Crit. Care Med.* **193**, 427–437 (2016).

187. Wang, B., *et al.* Clinical utility of haptoglobin in combination with CEA, NSE and CYFRA21-1 for diagnosis of lung cancer. *APJCP* **15**, 9611-9614 (2014).

188. Lu, H. Y. *et al.* EGFR, KRAS, BRAF, PTEN, and PIK3CA mutation in plasma of small cell lung cancer patients. *Onco. Targets. Ther.* **11**, 2217 (2018).

189. Diaz-Lagares, A. *et al.* A novel epigenetic signature for early diagnosis in lung cancer. *Clin. Cancer Res.* **22**, 3361–3371 (2016).

190. Zhang, Y. *et al.* Methylation of multiple genes as a candidate biomarker in non-small cell lung cancer. *Cancer Lett.* **303**, 21–28 (2011).

191. Kulis, M. & Esteller, M. DNA Methylation and Cancer. *Adv. Genet.* **70**, 27–56 (2010).

192. Iqbal, M. A., Arora, S., Prakasam, G., Calin, G. A. & Syed, M. A. MicroRNA in lung cancer: role, mechanisms, pathways and therapeutic relevance. *Mol. Aspects Med.* **70**, 3–20 (2019).
193. Pio, R. & Montuenga, L. M. Alternative Splicing in Lung Cancer. *J. Thorac. Oncol.* **4**, 674–678 (2009).
194. Misquitta-Ali, C. M. *et al.* Global Profiling and Molecular Characterization of Alternative Splicing Events Misregulated in Lung Cancer. *Mol. Cell. Biol.* **31**, 138–150 (2011).
195. Ouyang, T., Liu, Z., Han, Z. & Ge, Q. MicroRNA Detection Specificity: Recent Advances and Future Perspective. *Anal. Chem.* **91**, 3179–3186 (2019).
196. Yong, S. L. & Dutta, A. MicroRNAs in cancer. *Annu. Rev. Pathol.* **4**, 199 (2009).
197. Oliveto, S., Mancino, M., Manfrini, N. & Biffo, S. Role of microRNAs in translation regulation and cancer. *World J. Biol. Chem.* **8**, 45 (2017).
198. Ardekani, A. M. & Naeini, M. M. The Role of MicroRNAs in Human Diseases. *Avicenna J. Med. Biotechnol.* **2**, 161 (2010).
199. Rosenfeld, N. *et al.* MicroRNAs accurately identify cancer tissue origin. *Nat. Biotechnol.* **26**, 462–469 (2008).
200. Pencheva, N. & Tavazoie, S. F. Control of metastatic progression by microRNA regulatory networks. *Nat. Cell Biol.* **15**, 546–554 (2013).
201. Mitchell, P. S. *et al.* Circulating microRNAs as stable blood-based markers for cancer detection. *Proc. Natl. Acad. Sci. U. S. A.* **105**, 10513–10518 (2008).
202. Schmieder, S., Weißpflog, J., Danz, N., Klotzbach, U. & Sonntag, F. Detection of miRNA using a surface plasmon resonance biosensor and antibody amplification. *Curr. Dir. Biomed. Eng.* **2**, 135–138 (2016).
203. Liu, R. *et al.* Surface plasmon resonance biosensor for sensitive detection of microRNA and cancer cell using multiple signal amplification strategy. *Biosens. Bioelectron.* **87**, 433–438 (2017).
204. Li, X. *et al.* A novel surface plasmon resonance biosensor for enzyme-free and highly sensitive detection of microRNA based on multi component nucleic acid enzyme (MNAzyme)-mediated catalyzed hairpin assembly. *Biosens. Bioelectron.* **80**, 98–104 (2016).
205. Graybill, R. M., Cardenosa-Rubio, M. C., Yang, H., Johnson, M. D. & Bailey, R. C. Multiplexed microRNA expression profiling by combined asymmetric PCR and label-free detection using silicon photonic sensor arrays. *Anal. Methods* **10**, 1618–1623 (2018).
206. Liu, Q. *et al.* Mach–Zehnder interferometer (MZI) point-of-care system for rapid multiplexed detection of microRNAs in human urine specimens. *Biosens. Bioelectron.* **71**, 365–372 (2015).
207. Zhang, J. G. *et al.* MicroRNA-21 (miR-21) represses tumor suppressor PTEN and promotes growth and invasion in non-small cell lung cancer (NSCLC). *Clin. Chim. Acta* **411**, 846–852 (2010).
208. Zhao, Y. L. *et al.* MiR-205-5p promotes lung cancer progression and is valuable for the diagnosis of lung cancer. *Thorac. Cancer* **13**, 832–843 (2022).
209. Puisségur, M. P. *et al.* miR-210 is overexpressed in late stages of lung cancer and mediates mitochondrial alterations associated with modulation of HIF-1 activity. *Cell Death Differ.* **18**, 465–478 (2010).

210. Tsou, J. A., Hagen, J. A., Carpenter, C. L. & Laird-Offringa, I. A. DNA methylation analysis: A powerful new tool for lung cancer diagnosis. *Oncogene* **21**, 5450–5461 (2002).
211. Esteller, M. Epigenetics in Cancer. *NEJM* **358**, 1148–1159 (2008).
212. Saxonov, S., Berg, P. & Brutlag, D. L. A genome-wide analysis of CpG dinucleotides in the human genome distinguishes two distinct classes of promoters. *Proc. Natl. Acad. Sci. U. S. A.* **103**, 1412–1417 (2006).
213. Lyko, F. The DNA methyltransferase family: a versatile toolkit for epigenetic regulation. *Nat. Rev. Genet.* **19**, 81–92 (2017).
214. Feinberg, A. P. & Vogelstein, B. Hypomethylation distinguishes genes of some human cancers from their normal counterparts. *Nature* **301**, 89–92 (1983).
215. Paz, M. *et al.* A systematic profile of DNA methylation in human cancer cell lines. *Cancer res.* **63**, 1114-1121 (2003).
216. Wade, P. A. Methyl CpG binding proteins: coupling chromatin architecture to gene regulation. *Oncogene* **20**, 3166–3173 (2001).
217. Herman, J. G. & Baylin, S. B. Gene Silencing in Cancer in Association with Promoter Hypermethylation. *NEJM* **349**, 2042–2054 (2003).
218. Heyn, H. & Esteller, M. DNA methylation profiling in the clinic: applications and challenges. *Nat. Rev. Genet.***13**, 679–692 (2012).
219. Maxwell, A., McCudden, C. R., Wians, F. & Willis, M. S. Recent Advances in the Detection of Prostate Cancer Using Epigenetic Markers in Commonly Collected Laboratory Samples. *Lab. Med.* **40**, 171–178 (2009).
220. Costello, J. F. *et al.* Aberrant CpG-island methylation has non-random and tumour-type–specific patterns. *Nat. Genet.* **24**, 132–138 (2000).
221. Esteller, M., *et al*. A gene hypermethylation profile of human cancer. *Cancer res.* **61**, 3225-3229 (2001).
222. Duruisseaux, M. & Esteller, M. Lung cancer epigenetics: From knowledge to applications. *Semin. Cancer Biol.* **51**, 116–128 (2018).
223. Sandoval, J. *et al.* A Prognostic DNA Methylation Signature for Stage I Non-Small-Cell Lung Cancer. *J. Clin. Oncol.* **31**, 4140-4147 (2013).
224. Brock, M. V. *et al.* DNA Methylation Markers and Early Recurrence in Stage I Lung Cancer. *N. Engl. J. Med.* **358**, 1118–1128 (2008).
225. Toyooka, S., *et al.* The relationship between aberrant methylation and survival in non-small-cell lung cancers. *Br. J. Cancer* **91**, 771-774 (2004).
226. Kneip, C. *et al.* SHOX2 DNA Methylation Is a Biomarker for the Diagnosis of Lung Cancer in Plasma. *J. Thorac. Oncol.* **6**, 1632–1638 (2011).
227. Wrangle, J. *et al.* Functional identification of cancer-specific methylation of CDO1, HOXA9, and TAC1 for the diagnosis of lung cancer. *Clin. Cancer Res.* **20**, 1856–1864 (2014).
228. Nikolaidis, G. *et al.* DNA methylation biomarkers offer improved diagnostic efficiency in lung cancer. *Cancer Res.* **72**, 5692–5701 (2012).
229. Kim, H. *et al.* Tumor-Specific Methylation in Bronchial Lavage for the Early Detection of Non-Small-Cell Lung Cancer. *J Clin Oncol* **22**, 2363–2370 (2004).
230. Tian, T., Wang, S., Wu, J. & Zhou, X. Review: Advances in methodology of DNA methylation assay. *Sci. China Chem.* **54**, 1233–1243 (2011).
231. Nazmul Islam, M. *et al.* Optical biosensing strategies for DNA methylation analysis.

Biosens. Bioelectron. **92**, 668–678 (2017).

232. Kurinomaru, T., Kojima, N. & Kurita, R. An alkylating immobilisation linker for immunochemical epigenetic assessment. *Chem. Commun.* **53**, 8308–8311 (2017).
233. Nguyen, A. H. & Sim, S. J. Nanoplasmonic biosensor: Detection and amplification of dual bio-signatures of circulating tumor DNA. *Biosens. Bioelectron.* **67**, 443–449 (2015).
234. Sina, A. A. I. *et al.* Methylsorb: A simple method for quantifying DNA methylation using DNA-gold affinity interactions. *Anal. Chem.* **86**, 10179–10185 (2014).
235. Carrascosa, L. G. *et al.* Molecular inversion probe-based SPR biosensing for specific, label-free and real-time detection of regional DNA methylation. *Chem. Commun.* **50**, 3585–3588 (2014).
236. Kurita, R., Yanagisawa, H., Yoshioka, K. & Niwa, O. On-Chip Sequence-Specific Immunochemical Epigenomic Analysis Utilizing Outward-Turned Cytosine in a DNA Bulge with Handheld Surface Plasmon Resonance Equipment. *Anal. Chem.* **87**, 11581–11586 (2015).
237. Pan, S. *et al.* Double recognition of oligonucleotide and protein in the detection of DNA methylation with surface plasmon resonance biosensors. *Biosens. Bioelectron.* **26**, 850–853 (2010).
238. Yoon, J., Park, M. K., Lee, T. Y., Yoon, Y. J. & Shin, Y. LoMA-B: a simple and versatile lab-on-a-chip system based on single-channel bisulfite conversion for DNA methylation analysis. *Lab Chip* **15**, 3530–3539 (2015).
239. Hawk, R. M. & Armani, A. M. Label free detection of 5′hydroxymethylcytosine within CpG islands using optical sensors. *Biosens. Bioelectron.* **65**, 198–203 (2015).
240. Maki, W. C. *et al.* Nanowire-transistor based ultra-sensitive DNA methylation detection. *Biosens. Bioelectron.* **23**, 780–787 (2008).
241. Kang, Y. P. *et al.* Cysteine dioxygenase 1 is a metabolic liability for non-small cell lung cancer. *Elife* **8**, (2019).
242. Liu, X. *et al.* Knockdown of neuron-specific enolase suppresses the proliferation and migration of nci-h209 cells. *Oncol. Lett.* **18**, 4809–4815 (2019).
243. Xu, C. M. *et al.* Multifunctional neuron-specific enolase: its role in lung diseases. *Biosci. Rep.* **39**, 20192732 (2019).
244. Schneider, J. Tumor Markers in Detection of Lung Cancer. *Adv. Clin. Chem.* **42**, 1–41 (2006).
245. Harmsma, M., Schutte, B. & Ramaekers, F. C. S. Serum markers in small cell lung cancer: Opportunities for improvement. *Biochim. Biophys. Acta - Rev. Cancer* **1836**, 255–272 (2013).
246. Zha, Z. *et al.* Neuron specific enolase promotes tumor metastasis by activating the Wnt/β-catenin pathway in small cell lung cancer. *Transl. Oncol.* **14**, 101039 (2021).
247. Shibayama, T. *et al.* Complementary roles of pro-gastrin-releasing peptide (ProGRP) and neuron specific enolase (NSE) in diagnosis and prognosis of small-cell lung cancer (SCLC). *Lung Cancer* **32**, 61–69 (2001).
248. Ando, S., Suzuki, M., Yamamoto, N., Iida, T., & Kimura, H. The Prognostic Value of Both Neuron-specific Enolase (NSE) and Cyfra21-1 in Small Cell Lung Cancer. *Anticancer Res.* **24**, 1941-1946 (2004).
249. Satoh, H. *et al.* Cut-off levels of NSE to differentiate SCLC from NSCLC. *Oncol. Rep.* **9**, 581–583 (2002).

250. Akoun, G. M., Scarna, H. M., Milleron, B. J., Bénichou, M. P. & Herman, D. P. Serum Neuron-Specific Enolase: A Marker for Disease Extent and Response to Therapy for Small-Cell Lung Cancer. *Chest* **87**, 39–43 (1985).
251. Jørgensen, L. G. M. *et al.* Serum neuron-specific enolase (S-NSE) and the prognosis in small-cell lung cancer (SCLC): a combined multivariable analysis on data from nine centres. *Br. J. Cancer* **74**, 463–467 (1996).
252. Liu, X. *et al.* The prognostic value of the serum neuron specific enolase and lactate dehydrogenase in small cell lung cancer patients receiving first-line platinum-based chemotherapy. *Medicine* **96**, e8258 (2017).
253. Van Gool, A. *et al.* Analytical techniques for multiplex analysis of protein biomarkers. *Expert Rev. Proteom.* **17**, 257–273 (2020).
254. Yang, G. *et al.* Recent advances in biosensor for detection of lung cancer biomarkers. *Biosens. Bioelectron.* **141**, 111416 (2019).
255. Sun, L. *et al.* Aptamer based surface plasma resonance assay for direct detection of neuron specific enolase and progastrin-releasing peptide (31-98). *RSC Adv.* **11**, 32135–32142 (2021).
256. Toma, M., Izumi, S. & Tawa, K. Rapid and sensitive detection of neuron specific enolase with a polydopamine coated plasmonic chip utilizing a rear-side coupling method. *Analyst* **143**, 858–864 (2018).
257. Liu, B. *et al.* High Performance, Multiplexed Lung Cancer Biomarker Detection on a Plasmonic Gold Chip. *Adv. Funct. Mater.* **26**, 7994–8002 (2016).
258. Essandoh, K. & Guo-Chang F. Role of extracellular and intracellular microRNAs in sepsis. *Biochim. Biophys. Acta Mol. Basis Dis.* **1842**, 2155-2162 (2014).
259. Napolitano, L. M. Sepsis 2018: Definitions and Guideline Changes. *Surg. Infect. (Larchmt).* **19**, 117–125 (2018).
260. Prucha, M., Bellingan, G. & Zazula, R. Sepsis biomarkers. *Clin. Chim. Acta* **440**, 97–103 (2015).
261. Faix, J. d. Biomarkers of Sepsis. *Crit. Rev. Clin. Lab. Sci.* **50**, 23–26 (2013).
262. Wang, H. *et al.* Four serum microRNAs identified as diagnostic biomarkers of sepsis. *J. Trauma Acute Care Surg.* **73**, 850–854 (2012).
263. Caserta, S. *et al.* Circulating plasma microRNAs can differentiate human sepsis and systemic inflammatory response syndrome (SIRS). *Sci. Rep.* **6**, 1-13 (2016).
264. Huang, J. *et al.* Identification of MicroRNA as sepsis biomarker based on miRNAs regulatory network analysis. *Biomed Res. Int.* **2014**, (2014).
265. Hruštincová, A., Votavová, H., Dostálová Merkerová, M. & Merkerová, M. D. Circulating microRNAs: methodological aspects in detection of these biomarkers. *Folia Biol.* **61**, 203 (2015).
266. Kumar, S., Tripathy, S., Jyoti, A. & Singh, S. G. Recent advances in biosensors for diagnosis and detection of sepsis: A comprehensive review. *Biosens. Bioelectron.* **124**, 205–215 (2019).
267. Kemmler, M., Sauer, U., Schleicher, E., Preininger, C. & Brandenburg, A. Biochip point-of-care device for sepsis diagnostics. *Sens. Actuators B Chem.* **192**, 205–215 (2014).
268. Tsounidi, D., Petrou, P. S. & Raptis, I. Current Progress on Biosensors and Point-of-Care Devices for Sepsis Diagnosis. *IEEE Sens. J.* **21**, 12840–12855 (2021).
269. Mace, C. R., Striemer, C. C. & Miller, B. L. Detection of human proteins using

arrayed imaging reflectometry. *Biosens. Bioelectron.* **24**, 334–337 (2008).

270. Fabri-Faja, N. *et al.* Early sepsis diagnosis via protein and miRNA biomarkers using a novel point-of-care photonic biosensor. *Anal. Chim. Acta* **1077**, 232–242 (2019).
271. Dey, P. *et al.* Label-free Bacteria Quantification in Blood Plasma by a Bioprinted Microarray Based Interferometric Point-of-Care Device. *ACS Sensors* **4**, 52–60 (2019).
272. Wang, H. *et al.* Evidence for serum miR-15a and miR-16 levels as biomarkers that distinguish sepsis from systemic inflammatory response syndrome in human subjects. *Clin. Chem. Lab. Med.* **50**, 1423–1428 (2012).
273. Terborg, R. A., Pello, J., Mannelli, I., Torres, J. P. & Pruneri, V. Ultrasensitive interferometric on-chip microscopy of transparent objects. *Sci. Adv.* **2**, (2016).
274. Yesilkoy, F. *et al.* Phase-sensitive plasmonic biosensor using a portable and large field of view interferometric microarray imager. *Light Sci. Appl.* **7**, 17152-17152 (2018).
275. Buchegger, P. & Preininger, C. Four assay designs and on-chip calibration: Gadgets for a sepsis protein array. *Anal. Chem.* **86**, 3174–3180 (2014).
276. Phillips, D. D. *et al.* The sub-nanomolar binding of DNA–RNA hybrids by the single-chain Fv fragment of antibody S9.6. *J. Mol. Recognit.* **26**, 376–381 (2013).
277. Estevez, M. C., Otte, M. A., Sepulveda, B. & Lechuga, L. M. Trends and challenges of refractometric nanoplasmonic biosensors: A review. *Anal. Chim. Acta* **806**, 55–73 (2014).
278. Mazzotta, F. *et al.* Influence of the evanescent field decay length on the sensitivity of plasmonic nanodisks and nanoholes. *ACS Photonics* **2**, 256–262 (2015).
279. Unser, S., Bruzas, I., He, J. & Sagle, L. Localized Surface Plasmon Resonance Biosensing: Current Challenges and Approaches. *Sensors* **15**, 15684–15716 (2015).
280. Tokel, O., Inci, F. & Demirci, U. Advances in plasmonic technologies for point of care applications. *Chem. Rev.* **114**, 5728–5752 (2014).
281. Joshi, G. K. *et al.* Highly specific plasmonic biosensors for ultrasensitive MicroRNA detection in plasma from pancreatic cancer patients. *Nano Lett.* **14**, 6955–6963 (2014).
282. Yoo, S. M., Kim, D. K. & Lee, S. Y. Aptamer-functionalised localized surface plasmon resonance sensor for the multiplexed detection of different bacterial species. *Talanta* **132**, 112–117 (2015).
283. Taylor, A. B. & Zijlstra, P. Single-Molecule Plasmon Sensing: Current Status and Future Prospects. *ACS Sensors* **2**, 1103–1122 (2017).
284. Raghu, D. *et al.* Nanoplasmonic pillars engineered for single exosome detection. *PLoS One* **13**, (2018).
285. Mauriz, E., Priyanka D., & L. M. Lechuga. Advances in nanoplasmonic biosensors for clinical applications. *Analyst* **144**, 7105-7129 (2019).
286. Sepúlveda, B., Angelomé, P. C., Lechuga, L. M. & Liz-Marzán, L. M. LSPR-based nanobiosensors. *Nano Today* **4**, 244–251 (2009).
287. Wang, Y., Zhou, J. & Li, J. Construction of Plasmonic Nano-Biosensor-Based Devices for Point-of-Care Testing. *Small Methods* **1**, 1700197 (2017).
288. Chung, T., Lee, S. Y., Song, E. Y., Chun, H. & Lee, B. Plasmonic Nanostructures for Nano-Scale Bio-Sensing. *Sensors* **11**, 10907–10929 (2011).
289. Mühlschlegel, P., Eisler, H. J., Martin, O. J. F., Hecht, B. & Pohl, D. W. Applied

physics: Resonant optical antennas. *Science* **308**, 1607–1609 (2005).

290. Prodan, E., Radloff, C., Halas, N. J. & Nordlander, P. A Hybridization Model for the Plasmon Response of Complex Nanostructures. *Science.* **302**, 419–422 (2003).
291. Portela, A., Yano, T. & Santschi, C. Spectral tunability of realistic plasmonic nanoantennas. *Appl. Phys. Lett.***105**, 91105 (2014).
292. Fischer, H., & Olivier J. F. M. Engineering the optical response of plasmonic nanoantennas. *Optics express* **16**, 9144-9154 (2008).
293. Hans Fredriksson, B. *et al.* Hole-mask colloidal lithography. *Adv. Mater.* **19**, 4297–4302 (2007).
294. Zhang, W., Huang, L., Santschi, C. & Martin, O. J. F. Trapping and sensing 10 nm metal nanoparticles using plasmonic dipole antennas. *Nano Lett.* **10**, 1006–1011 (2010).
295. Righini, M. *et al.* Nano-optical trapping of rayleigh particles and Escherichia coli bacteria with resonant optical antennas. *Nano Lett.* **9**, 3387–3391 (2009).